Searching for High-Energy Neutrinos from Transient Sources with IceCube

Dissertation
zur Erlangung des akademischen Grades
doctor rerum naturalium
(Dr. rer. nat.)

im Fach: Physik
Spezialisierung: Experimentalphysik

eingereicht an der
Mathematisch-Naturwissenschaftlichen Fakultät
der Humboldt-Universität zu Berlin

von
Jannis Necker M. Sc.

Präsidentin der Humboldt-Universität zu Berlin
Prof. Dr. Julia von Blumenthal

Dekanin der Mathematisch-Naturwissenschaftlichen Fakultät
Prof. Dr. Caren Tischendorf

Gutachter:
Prof. Dr. Marek Kowalski, Humboldt-Universität zu Berlin
Prof. Dr. Sara Buson, Universität Würzburg
Prof. Dr. Jörn Wilms, Friedrich-Alexander-Universität Erlangen-Nürnberg

Tag der mündlichen Prüfung: 04.04.2025

Colophon
This document was typeset with the help of KOMA-Script and LaTeX using the open-source kaobook template class.

The source code of this thesis is available at:
https://github.com/JannisNe/thesis,
while the scripts used to generate the plots are available at:
https://github.com/JannisNe/thesis_plots

Image Credit: Enikö Katalin Eged

Abstract

The IceCube neutrino observatory, the largest operating neutrino detector located at the South Pole, discovered a diffuse flux of high-energy astrophysical neutrinos in 2013. Although single sources have been identified, the sources of the majority of this flux remain unknown. The goal of this thesis is to probe astrophysical transients as neutrino sources using IceCube neutrino observations along with observations of other telescopes. Bright flares from enhanced accretion onto supermassive black holes (SMBHs) were reported to be correlated with IceCube's high-energy (> 100 TeV) neutrino alerts. They are characterized by bright, transient infrared emission, called dust echos. For the first time, this work probes the general population of accretion flares using the full IceCube muon neutrino sample with a stacking analysis. The non-detection is consistent with the reported correlation only if neutrino production happens by hadronic interaction with optical-UV photons, or the infrared photons from the dust echo. Neutrino production through interaction with X-ray photons from the accretion disk is excluded. Assuming that all accretion flares are Tidal Disruption Events (TDEs), their contribution to the diffuse neutrino flux is constrained to below around 7.1% for a spectral index of $\gamma = 2.5$, following the diffuse flux. This is around four times more constraining than a previous result. Although high-energy neutrino production through proton interaction with the infrared photons can still not be excluded, model parameters such as the dissipation efficiency are constrained to below optimistic values. An improved re-simulation method for calibration of the localization uncertainty for IceCube's high-energy neutrino alerts is also developed, applicable to through-going muon events. It is the first method that works for events with unusual energy deposition patterns in the detector and can improve the runtime per event from thousands to tens of seconds. Results for the neutrinos reported in coincidence with accretion flares indicate that the corresponding uncertainty contours need robust calibration. To enable a more sensitive search for neutrinos from accretion flares with bright dust echos, a catalog of dust-echo-like flares is compiled. This is the widest and deepest such catalog to date, increasing the sample size compared to the previous analysis by a factor of ten. Assuming the sample is dominated by TDEs, it is the first one to provide enough statistics at higher redshifts to probe the evolution of their rate. At least for black hole masses that enable the disruption of a solar mass star, the evolution is consistent with expectations from number density evolutions of SMBHs.

Zusammenfassung

IceCube, der größte in Betrieb befindliche Neutrinodetektor am Südpol, entdeckte 2013 einen diffusen Fluss von hochenergetischen, astrophysikalischen Neutrinos. Obwohl einzelne Quellen identifiziert wurden, is der Ursprung des Großteils dieses Flusses weiterhin unbekannt. Das Ziel dieser Arbeit ist es, astrophysikalische Transienten als Neutrinoquellen zu untersuchen. Dazu werden IceCube-Neutrinobeobachtungen zusammen mit Beobachtungen anderer Teleskope verwendet. Vorhergehender Arbeit zufolge sind Helligkeitsausbrüche, die mit der verstärkten Materieakkretion von supermassiven Schwarzen Löchern (SMBHs) zusammenhängen, sogenannte Akkretionsflares, mit hochenergetischen (> 100 TeV) Neutrinos korreliert, deren Messung IceCube in Echtzeit publiziert. Diese Ausbrüche zeichnen sich durch helle, vorübergehende Infrarotemissionen aus, die als Staubechos bezeichnet werden. Zum ersten Mal wird diese Population mit dem gesamten IceCube Datensatz an Muonneutrinos analysiert. Das Ergebnis ist mit der Nullhypothese konsistent. Das ist nur dann mit der berichteten Korrelation vereinbar, wenn die Neutrinoproduktion durch die Wechselwirkung von Hadronen mit optischen UV-Photonen oder den Infrarot-Photonen des Staubechos erfolgt. Eine Neutrinoproduktion durch Wechselwirkung mit Röntgenphotonen aus der Akkretionsscheibe ist ausgeschlossen. Unter der Annahme, dass es sich bei allen Akkretionsflares um die Zerstörung eines Sterns durch die Gezeitenkräfte des SMBH (TDEs) handelt, liegt ihr Beitrag zum diffusen Neutrinofluss bei einem Spektralindex von $\gamma = 2.5$ unter 7.1%. Dieser Grenzwert ist etwa viermal kleiner als ein früheres Ergebnis. Obwohl eine hochenergetische Neutrinoproduktion durch Hadronenwechselwirkung mit den Infrarotphotonen noch nicht ausgeschlossen werden kann, werden Modellparameter wie die Dissipationseffizienz auf wenig optimistische Werte eingeschränkt. Es wurde auch eine verbesserte Re-Simulationsmethode zur Kalibrierung der Lokalisierungsunsicherheit für die hochenergetischen IceCube Neutrinos entwickelt, die auf durchgehende Myonenereignisse anwendbar ist. Es ist die erste Methode, die auf Ereignisse mit ungewöhnlichen Energiedepositionsmustern im Detektor anwendbar ist und die Laufzeit von tausenden auf weniger als hundert Sekunden verbessern kann. Die Ergebnisse für die Neutrinos, die im Zusammenhang mit Akkretionsflares gemeldet wurden, zeigen, dass die entsprechenden Unsicherheitskonturen einer robusten Kalibrierung bedürfen. Um in Zukunft eine empfindlichere Suche nach Akkretionsflares mit hellen Staubechos zu ermöglichen, wird ein Katalog von staubechoähnlichen Helligkeitsausbrüchen zusammengestellt. Dies ist der bisher umfangreichste Katalog dieser Art, und erhöht die Stichprobengröße im Vergleich zur vorherigen Analyse um den Faktor zehn. Wenn man davon ausgeht, dass der Katalog hauptsächlich TDEs enthält, ist es der erste, der eine genügende Anzahl an Beobachtungen bei höheren Rotverschiebungen liefert, um die Entwicklung der TDE Rate zu untersuchen. Zumindest für Massen von Schwarzen Löchern, die die Zerstörung eines sonnenähnlichen Sterns ermöglichen, stimmt das Ergebnis mit der Erwartung überein, die sich aus der Entwicklung der Anzahldichte von SMBHs ergibt.

Contents

List of Figures

List of Tables

Introduction 1

In 1912, Victor Hess set off in a hot air balloon to measure the level of ionizing radiation at different altitudes. He expected the intensity to decrease with increasing distance from the ground as all radioactivity was thought to come from material in the Earth's crust. The surprising discovery was that at an altitude above around 3000 m, the amount of ionization started to increase again. Hess concluded that ionizing radiation must be entering Earth's atmosphere from above [1]. This was the beginning of what is known today as *multimessenger astronomy*.

[1]: Hess (1912), *Über Beobachtungen Der Durchdringenden Strahlung Bei Sieben Freiballonfahrten*

It is well established now that what Victor Hess observed is the product of highly energetic particles hitting the atmosphere, called cosmic rays. These particles can reach energies of 10^{20} eV, which will never be achievable by human made particle accelerators. The question of which processes can transfer this amount of energy to a single particle is therefore interesting for particle physics and astronomy. Particle physics can use these cosmic accelerators to study regimes that would otherwise be inaccessible. Astronomy can in return infer properties of the environment from the presence of such an accelerator.

Unfortunately, cosmic rays are electrically charged and thus do not travel straight from their origin to Earth. Other tracers, or messengers, have to be used instead to find the sources of cosmic rays. Photons in the visible wavelength range have been used to do astronomy for thousands of years. However, since Victor Hess discovered cosmic rays, also the accessible electromagnetic (EM) wavelength range has expanded dramatically and now extends from radio up to the highest energy gamma-rays, constituting what is known as *multiwavelength astronomy*. Additionally, also optical astronomy is undergoing a transformation of its own. Robotically operated survey telescopes with a large field-of-view (FoV) scan the sky autonomously, producing datasets that are too large to analyze each object individually. Instead, decisions such as object classifications have to be automated. These large datasets enable astronomers to shift from focusing on individual objects to analyzing entire populations, particularly in transient science, where the repeated, wide-field scans of the sky are essential for exploring changes over time.

Multimessenger astronomy only started to live up to its name[1] with the discovery of astrophysical high-energy neutrinos by IceCube in 2013 [2]. This particle's interaction cross-section is so small that Wolfgang Pauli worried it might never be detectable [3] after he proposed its existence in 1933 [4]. The same property, however, makes it a valuable cosmic messenger: It escapes dense environments that would absorb photons and then travels the universe unimpeded. Neutrino observation therefore offers information complementary to photons.

Connecting observations of multiple messengers rapidly after detection has become possible lately with the progressing automation

1: *Astronomy* translated from greek means *arrangement of the stars*. Although cosmic rays were the first other cosmic messenger to be discovered, they can not be used to study any arrangement on the sky because they do not point back to their source.

[2]: IceCube Collaboration (2013), *Evidence for High-Energy Extraterrestrial Neutrinos at the IceCube Detector*

[3]: Reines (1996), *The Neutrino: From Poltergeist to Particle*

[4]: (1934), *Structure et propriétés des noyaux atomiques: rapports et discussions du septième Conseil de physique tenu à Bruxelles du 22 du 29 octobre 1933, sous les auspices de l'Institut international de physique Solvay*

of data processing and distribution, consequently called *real-time multimessenger astronomy*. This enables timely follow-up observations of transient events across multiple messengers and wavelengths to create rich datasets to better study their physical properties.

Based on these recent achievements, this thesis aims at studying transient neutrino sources using both EM and IceCube observations. It further narrows down which sources contribute to the high-energy neutrino flux as well as infer properties of the astrophysical transients.

It first introduces the cosmic messengers, possible transient neutrino sources, and the detection by IceCube:

Chapter 2 introduces multimessenger astronomy, the combined observation of cosmic rays, photons, neutrinos, and gravitational waves. The physics of the respective emission mechanisms is discussed briefly as well as the information each messenger carries to highlight the synergy of combining their detections.

Chapter 3 introduces candidate transient neutrino sources. The potential acceleration sites of cosmic rays and potential interaction targets are presented, along with their multi-wavelength picture.

Chapter 4 introduces neutrino astronomy with the IceCube neutrino observatory. The principles of astrophysical neutrino detection are introduced in general along with the specific implementation in the case of IceCube. The full chain from detection to reconstruction and statistical analysis is presented.

Chapter 5 presents IceCube's real-time system, enabling timely follow-up observations for transient neutrino events. The chapter details the technical setup with an emphasis on the uncertainty of the directional reconstruction. A new method for addressing calibration issues of these uncertainties is presented.

The second part of the thesis deals with follow-up observations of IceCube realtime alert neutrinos with optical telescopes:

Chapter 6 describes the optical follow-up of high-energy neutrino alerts using the *All-Sky Automated Survey for SuperNovae* (ASAS-SN). This chapter reviews the observational capabilities and results of ASAS-SN's follow-up program, including its performance metrics and the constraints it places on potential neutrino source populations.

Chapter 7 introduces a similar program by the more sensitive *Zwicky Transient Facility* (ZTF). In particular, the association of tidal disruption events (TDEs) with IceCube alerts is discussed.

The possible connection between infrared flares and high-energy neutrino emission is discussed in the third part:

Chapter 8 extends the discussion from TDEs to a more general population of flares from enhanced accretion onto supermassive black holes (SMBHs). The role of dust around the SMBH is emphasized, and models for the origin of the corresponding infrared signal are explained. The report of a correlation between IceCube alerts and accretion flares is investigated. The method from Chapter 5 is used to test the robustness of the

neutrino uncertainty areas. An analysis using the full IceCube data sample is performed but is consistent with background expectations. Implications for neutrino production models in TDEs are discussed.

Chapter 9 presents a comprehensive catalog of infrared flares, compiled to aid in the search for neutrino sources. The chapter describes the methodology used to identify and classify flares, assesses the completeness of the catalog, and discusses implications for the observed flare rates and their potential evolution over cosmic time.

Chapter 10 then synthesizes the results of this thesis, summarizing the advances in multimessenger follow-up strategies, and the constraints on transient neutrino source populations. The chapter concludes with an outlook into the future of multimessenger astronomy.

Multimessenger Astronomy in the Time Domain

Cosmic Messengers 2

Although astronomy has been practiced for many centuries, the only messenger used for observations was the photon. This only changed about 100 years ago when Victor Hess discovered cosmic rays [1]. Around sixty years ago, extraterrestrial neutrinos were first measured [5], and the discovery of extragalactic neutrinos is only about a decade old [2], and the most recent addition is gravitational waves [6]. Today many facilities exist to measure these messengers in a wide range of energies. Akin to multi-wavelength astronomy, the combined observation of photons of different energies, multi-messenger astronomy seeks to infer complementary information from observations of multiple messengers. This chapter introduces the characteristics of each messenger, and the specific information each one provides.

[1]: Hess (1912), *Über Beobachtungen Der Durchdringenden Strahlung Bei Sieben Freiballonfahrten*

[5]: Davis et al. (1968), *Search for Neutrinos from the Sun*

[2]: IceCube Collaboration (2013), *Evidence for High-Energy Extraterrestrial Neutrinos at the IceCube Detector*

[6]: LIGO Scientific Collaboration and Virgo Collaboration et al. (2016), *Observation of Gravitational Waves from a Binary Black Hole Merger*

2.1 Cosmic Rays

Cosmic rays (CRs) are energetic particles that originate beyond the Earth's atmosphere with energies from MeV to hundreds of EeV [1], far beyond what can be achieved with human-made particle accelerators. A broad distinction can be made into primary CRs that originate in astrophysical sources, and secondary CRs that are the product of interaction of the primaries with interstellar gas. The spectrum is steeply falling towards higher energies, approximately following a power-law. Up to around 100 TeV they can be detected directly by balloon or space borne instruments [9]. Up to this energy at least, the CRs are mainly free protons ($\sim 70\%$), and alpha particles ($\sim 18\%$), while the rest are heavier nuclei [10, Chapter 30]. At higher energies, the flux becomes so low and the necessary collection areas so large, that direct detection becomes impractical. Instead, they can indirectly be observed by measuring the particle showers they produce when interacting in the atmosphere, called *air showers*. The inference of the composition is not as straightforward as in direct detection, so it is not conclusively determined whether the light composition dominates up until the highest energies [10]. In any case, the particles are charged, so they will be deflected by interstellar, intra-, and intergalactic magnetic fields, so their arrival direction does not necessarily reveal their origin.

Composition

1: The two most energetic particles detected to date have energies of around 250 EeV and 320 EeV [7, 8].

[9]: Spurio (2018), *Probes of Multimessenger Astrophysics : Charged Cosmic Rays, Neutrinos, γ-Rays and Gravitational Waves / Maurizio Spurio*

[10]: Particle Data Group et al. (2022), *Review of Particle Physics*

Since the discovery of CRs a whole suite of instruments is characterizing the particles over more than eleven orders of magnitude. The full spectrum is shown in Figure 2.1. There are three distinct features above PeV energies: The *first* and *second knee* are spectral hardenings occuring at around $10^{6.5}$GeV and 10^{8} GeV, respectively. The *ankle* is the feature around $10^{9.5}$GeV. A possible explanation for the ankle is that a more energetic population starts to dominate at these very high energies, for example, an extragalactic component beginning to dominate over a galactic one. In this case, the first knee might indicate that most galactic sources cannot accelerate protons

Spectrum

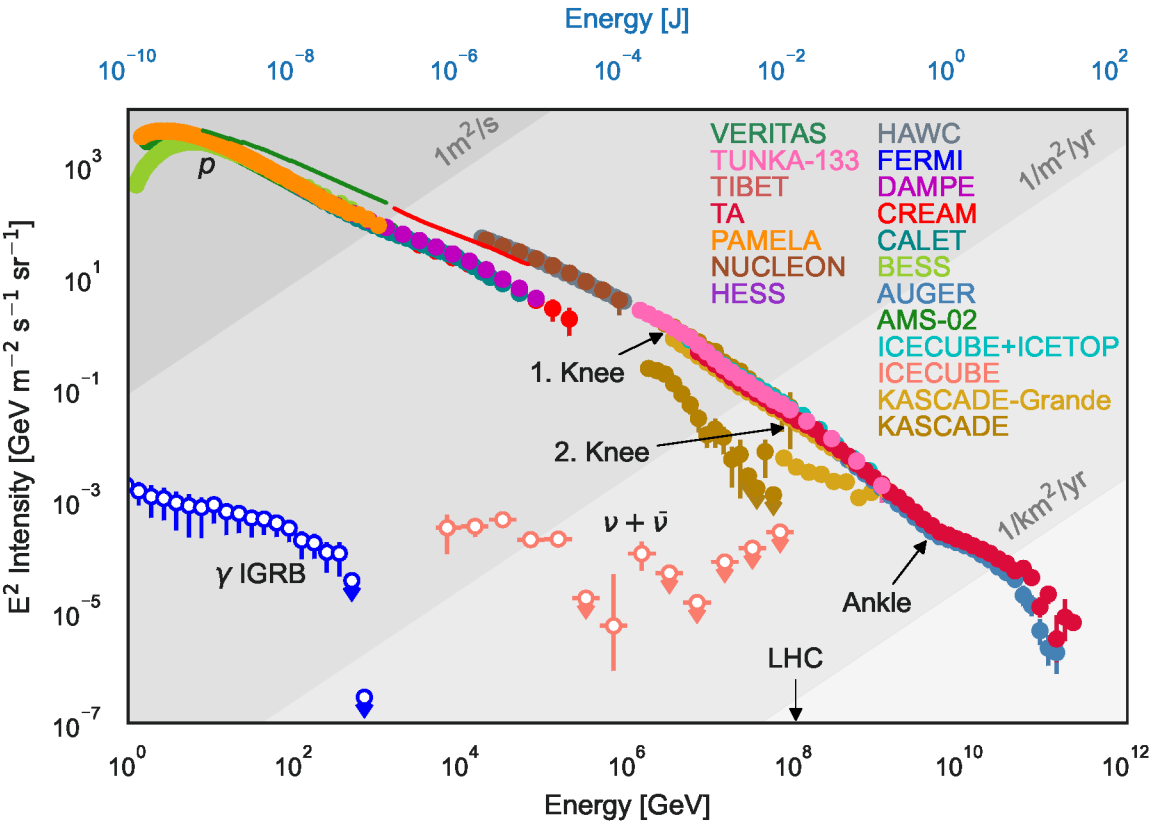

Figure 2.1: The cosmic ray spectrum. The energy scaled flux is shown against the energy. The color of the datapoints indicates the experiment. Grey shaded areas indicate number flux per area and time. In addition to the proton and all particle cosmic ray measurements, the diffuse, measured by Fermi, and the diffuse astrophysical neutrino flux measured by IceCube are shown. Adapted from Evoli [12]

beyond around $10^{6.5}$GeV. Similarly, the second knee might indicate the same cutoff for heavier nuclei [10]. Indeed, it will be explained later that promising galactic sources have the right combination of size and magnetic field strength to enable particle acceleration up to about 1 PeV. However, another explanation for the knee features is that the galactic magnetic fields cannot confine the CRs anymore so that they start to leak out. Again, this happens at different energies for light and heavy particles, explaining the two knees [11].

[11]: Giacinti et al. (2014), *Explaining the Spectra of Cosmic Ray Groups above the Knee by Escape from the Galaxy*

GZK cutoff

It is expected that there is an upper limit to the CR energy and a respective attenuation should be visible in the spectrum. CRs above energies of around 10^9 GeV are generally referred to as Ultra-High Energy Cosmic Rays (UHECRs), coinciding roughly with the ankle and the supposed extragalactic origin. These can interact with the photons of the cosmic microwave background (CMB) (see Equation 2.3a and Equation 2.3b). The expected spectral feature is called the *Greisen-Zatsepin-Kuzmin* (GZK) cutoff [13, 14]. For protons, this can happen at an energy of about 5×10^{10} GeV [9]. The two largest experiments measuring the UHECR flux are the *Telescope Array* (TA)[15] and the *Pierre Auger Observatory* (PAO) [16]. Both experiments have observed a steepening of the spectrum that is consistent with the GZK cutoff [17, 18], although photo-dissociation of heavy nuclei and a maximum energy of extragalactic accelerators can also contribute to the cutoff [10].

[13]: Greisen (1966), *End to the Cosmic-Ray Spectrum?*
[14]: Zatsepin et al. (1966), *Upper Limit of the Spectrum of Cosmic Rays*

[15]: Abu-Zayyad et al. (2012), *The Surface Detector Array of the Telescope Array Experiment*

[16]: (2015), *The Pierre Auger Cosmic Ray Observatory*

[17]: Ivanov (2019), *Energy Spectrum Measured by the Telescope Array*
[18]: The Pierre Auger Collaboration et al. (2020), *Measurement of the Cosmic-Ray Energy Spectrum above* 2.5×10^{18} eV *Using the Pierre Auger Observatory*

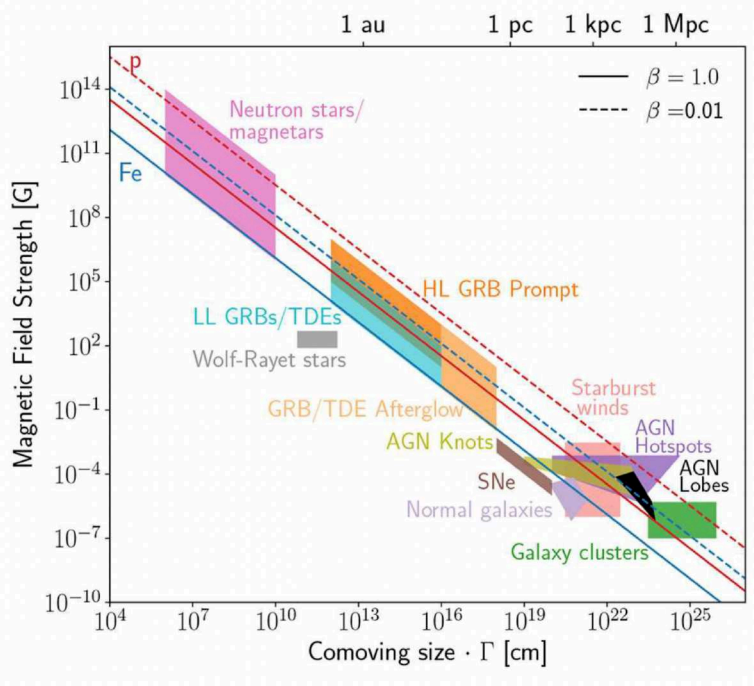

Figure 2.2: Hillas plot to visualize the Hillas criterion for particle acceleration up to 10^{11} GeV. The diagonal lines indicate the relation defined by Equation 2.1 for proton and iron for different shock velocities β. The excluded parameter space is at the bottom left of the lines. The colored regions show the parameter space for different classes of potential CR sources. Taken from Alves Batista et al. [21].

A possible mechanism to provide cosmic rays with their high energies is stochastic acceleration of low-energy particles in the vicinity of a shock front [19], called *diffusive shock acceleration*. The particles repeatedly cross the shock front and get reflected back by irregular magnetic fields, sometimes called magnetic mirrors, gaining energy each time. This mechanism naturally provides a power-law energy spectrum. The exact spectral index depends on the details of the shock, like its speed and the material density, but is in general close to $\gamma \approx 2$ [9].

Diffusive shock acceleration

[19]: Fermi (1954), *Galactic Magnetic Fields and the Origin of Cosmic Radiation.*

Potential sources of CRs can be considered by realizing that particles have to be magnetically confined in the acceleration region. The maximum energy a particle can reach in a region of size R with a magnetic field with strength B is given by [20]

Possible sources

[20]: Hillas (1984), *The Origin of Ultra-High-Energy Cosmic Rays*

$$E_{\max} \approx \beta_{\mathrm{sh}} Z \left(\frac{B}{\mu\mathrm{G}}\right)\left(\frac{R}{\mathrm{kpc}}\right) \mathrm{EeV}. \tag{2.1}$$

Z is the charge of the particle, and β_{sh} is the velocity of the shock front in units of the speed of light. This is called the *Hillas criterion*. For a value of $E_{\max}$ it gives the relation between size and magnetic field strength. This is shown in Figure 2.2 for $E_{\max} = 10^{11}$ GeV, where potential CR sources are indicated. The ones relevant to this thesis will be introduced in detail in the next chapter. Although this is a necessary criterion, it is not sufficient because the existence of shocks to enable diffusive shock acceleration is still not guaranteed. Observations of CR from a source indicate this acceleration takes place.

However, as already mentioned above, because of their charge CRs are deflected by magnetic fields and do in general not point back to their origin. But for higher energies the deflection is weaker, so for UHECRs some correlation could be expected. In addition, at these high energies the GZK attenuation takes effect so that

Anisotropy

particles from far away sources get attenuated, and the observed sources should be close ($\lesssim 100\,\mathrm{Mpc}$) [10]. Indeed, the PAO reported a large-scale dipole in the observed UHECR arrival directions, supporting the idea of an extragalactic origin [22, 23]. However, no source or source population could be conclusively identified. Similarly, the TA reported intermediate-scale anisotropies that point to an extragalactic origin of UHECRs [24, 25]. The PAO also found an excess of UHECR in the direction of the closest active galaxy Centaurus A [26, 27] and both PAO and TA reported a correlation with nearby galaxies with intense star forming activity at a statistical significance above 4σ [27, 28]. However, even if the excess is real, it can only explain around 10% of the UHECR flux [27]. Therefore, other tracers of hadronic particle acceleration are necessary to identify the bulk of CR sources. Luckily, the accelerated particles will interact while still in their acceleration environment and produce secondary particles, which can be used as tracers.

[22]: THE PIERRE AUGER COLLABORATION et al. (2017), *Observation of a Large-Scale Anisotropy in the Arrival Directions of Cosmic Rays above* 8×10^{18} eV
[23]: Abdul Halim et al. (2023), *An Update on the Arrival Direction Studies Made with Data from the Pierre Auger Observatory*
[24]: Abbasi et al. (2014), *Indications of Intermediate-Scale Anisotropy of Cosmic Rays with Energy Greater than 57 EeV in the Northern Sky Measured with the Surface Detector of the Telescope Array Experiment*
[25]: Kim et al. (2023), *Anisotropies in the Arrival Direction Distribution of Ultra-High Energy Cosmic Rays Measured by the Telescope Array Surface Detector*
[27]: Abreu et al. (2022), *Arrival Directions of Cosmic Rays above 32 EeV from Phase One of the Pierre Auger Observatory*
[28]: Tkachev et al. (2021), *Telescope Array Anisotropy Summary*

Cosmic ray interactions

The production sites of UHECRs are typically dense environments with gas or dust in the vicinity of the acceleration. The interaction with the highest cross-section is the collision with other nuclei, producing pions and heavier hadronic particles X [9]:

$$p + p \rightarrow \pi^{\pm},\, \pi^{0},\, X. \tag{2.2}$$

The protons can also interact with photons through *photohadronic* interactions with a similar decay chain:

$$p + \gamma \rightarrow \Delta^{+} \rightarrow \begin{cases} \pi^{+} + n & \text{(2.3a)} \\ \pi^{0} + p. & \text{(2.3b)} \end{cases}$$

The photohadronic interaction has a threshold center-of-mass energy equivalent to the mass of the Δ^+ resonance $m_{\Delta^+} = 1232\,\mathrm{MeV}$. Although the cross-section is much lower than the proton-proton collision, the number density of ambient photons is usually much higher so that the photohadronic interaction is typically dominating the production of pions [9]. Charged pions decay into muons and neutrinos, and the muon subsequently decays into an electron and neutrinos, while the neutral pion decays into two photons:

$$\begin{aligned} \pi^{\pm} &\rightarrow \mu^{\pm} + \nu_{\mu}(\bar{\nu}_{\mu}) && \text{(2.4a)} \\ &\hookrightarrow e^{\pm} + \nu_{\mathrm{e}}(\bar{\nu}_{\mathrm{e}}) + \bar{\nu}_{\mu}(\nu_{\mu}) \\ \pi^{0} &\rightarrow \gamma + \gamma. && \text{(2.4b)} \end{aligned}$$

The resulting neutrinos and gamma rays are not magnetically confined and can potentially escape the acceleration site and be detected. Because they do not carry charge, they have the potential to reveal the sources of CRs. Both messengers are discussed in the following sections, but a promising observation can already be made in Figure 2.1, where the isotropic gamma-ray background (iGRB) and the diffuse high-energy neutrino flux are shown next to the CR spectrum: The energy flux carried by gamma-rays, neutrinos and UHECRs is remarkably similar, so that a common origin is indeed plausible.

2.2 Photons

Long before the discovery of CRs, photons in the form of visible light were used to observe the sky. Today the observations in many more electromagnetic bands from radio to gamma-rays constitute modern multi-wavelength astronomy, where each regime can provide information about different physical processes.

Thermal radiation

Infrared (IR) and optical light usually comes from objects emitting blackbody radiation due to their temperature, also referred to as *thermal radiation*. The peak wavelength of the blackbody spectrum is related to the temperature [29, Chapter 6]:

[29]: Bradt (2008), *Astrophysics Processes: The Physics of Astronomical Phenomena*

$$\lambda_{\text{peak}} \approx \left(\frac{T}{\text{K}}\right)^{-1} \cdot 3\,\text{mm}. \tag{2.5}$$

For example, the mid-infrared (MIR) (10 to 2.5 µm or around 10^2 to 10^3 K) is the domain of warm or hot dust, whereas the optical (750 to 380 nm or 10^3 to 10^4 K) is the regime where the surface of stars is visible. However, some sources are even hotter, like the corona of the sun or accretion disks around SMBHs. Consequently, these can be observed in the soft X-ray regime (around 10 to 0.1 nm or 10^5 to 10^7 K). Colder bodies would radiate at even longer wavelengths in the radio regime. This is true for the CMB, which follows the blackbody spectrum nearly perfectly. With a temperature today of $T_{\text{CMB}} \approx 2.7\,\text{K}$ its peak wavelength is about 1 mm [30].

[30]: Neronov (2019), *Introduction to Multi-Messenger Astronomy*

Non-thermal radiation

In contrast, light from other processes is referred to as *non-thermal*. Of particular relevance for high-energy astrophysics are those processes involved in the cooling of accelerated particles. A prominent example is the *synchrotron radiation*, emitted by charged particles that get deflected in a magnetic field. Because the energy loss depends on the inverse squared of the particle's mass, this is particularly efficient for the light electrons. Prominent extragalactic sources exhibiting synchrotron emission are accreting SMBHs with large particle jets, while galactic sources include remnants of supernova (SN) explosions or rapidly rotating neutron stars, called pulsars. The energy of synchrotron emission depends on the energy of the parent electron and the magnetic field strength and can stretch from radio to X-rays [9]. The same accelerated electrons can also scatter on photons and transfer their energy in a process called *inverse compton scattering*. This and other non-thermal processes are observed at X-ray energies and above, even to high (> MeV) and very high energy (VHE; > 10^2 GeV) gamma-rays [30].

Synchrotron radiation

Leptonic emission

Hadronic emission

Up until know, these non-thermal processes only involve electrons. Because protons are more massive, their contribution to radiative processes is usually negligible. However, in their interaction with other protons or photons, they can produce gamma-rays through π^0 decay (see Equation 2.2, Equation 2.3b, and Equation 2.4b), resulting in a characteristic spectral shape called the *pion bump* [9]. Recently, the VHE gamma-ray detection of the recurring stellar explosion (nova) RS Ophiuci provided evidence that the emission came from pion decay, favoring hadronic over leptonic particle acceleration [31]. Another example is the diffuse gamma-ray emission from the Milky Way, produced in interaction between CRs and interstellar

[31]: H.E.S.S. Collaboration et al. (2022), *Time-Resolved Hadronic Particle Acceleration in the Recurrent Nova RS Ophiuchi*

gas [32]. This shows that identifying hadronic emission is possible with gamma-rays, but the distinction to purely leptonic scenarios is not trivial.

[32]: Ackermann et al. (2012), *Fermi-LAT Observations of the Diffuse Gamma-Ray Emission: Implications for Cosmic Rays and the Interstellar Medium*

Extragalactic gamma-rays

Beyond the galaxy, an isotropic, extragalactic component can be identified at high energies [33], called the iGRB, shown together with the CR spectrum in Figure 2.1. As already pointed out above, the energy flux is similar to the CRs which makes a common origin plausible. Unfortunately, more energetic photons get attenuated by interaction with the CMB, so that the universe becomes opaque to gamma-rays above around 10 TeV at distances of more than $\mathcal{O}(10)$ Mpc. For reference, the closest active galaxy, Centaurus A, is 3.5 Mpc away [9]. So while VHE gamma-ray astronomy can be useful in directly identifying CR sources in our own galaxy, its potential to do so for the big extragalactic population of UHECRs sources is limited. And even for a close-by source, there is still the possibility that gamma-rays, even if produced alongside CRs, get absorbed on their way to Earth.

[33]: Ackermann et al. (2015), *The Spectrum of Isotropic Diffuse Gamma-Ray Emission Between 100 MeV and 820 GeV*

Spectroscopy

The measurements described so far are typically conducted over wide wavelength ranges. More detailed information can be obtained when scanning the intensity in finer wavelength steps, revealing the spectrum of the object. Because the energy levels of electrons in atoms are quantized, they emit a photon of specific energy when transitioning between two states. Atoms get excited in hot gas, and if the ambient pressure is low, the electrons de-excite producing an emission line in the spectrum. The same line shows up as an absorption feature if cold gas is observed against a bright source. Because the sequence of lines is specific to the atoms, these emission and absorption lines can reveal the chemical composition of the source. For extragalactic objects, the spectrum appears shifted towards longer wavelengths, which is called *redshift*, an effect due to the expansion of the universe and related to the distance. Determining which lines are present in the spectrum and comparing the observed to the rest frame wavelengths therefore gives a handle on the object's distance [34]. Spectroscopy can, in principle, be performed at any wavelength but is frequently used in the optical. Not only is optical astronomy practical because it is possible from the ground, but the Balmer lines of the abundant element Hydrogen occupy the optical regime, with the prominent Hα line at around $\lambda_{\mathrm{H}\alpha} = 656\,\mathrm{nm}$ [35].

Redshift

[34]: Karttunen et al. (2007), *Fundamental Astronomy*

[35]: A. Kramida et al. (2023), *NIST Atomic Spectra Database (Ver. 5.11)*

Time-domain astronomy

Modern astronomy has just transitioned into the field of big, robotic sky surveys, allowing the automatic scan of the full sky [30]. Scanning the sky repeatedly enables the study of transient phenomena by comparing each image with previous ones and looking for a change in flux. Trying to identify transient sources with two of these optical survey instruments and looking for high-energy neutrino emission is part of Chapter 7 and Chapter 6. Chapter 8 and Chapter 9 discuss and perform equivalent searches in the MIR. Transient surveys usually name discovered transients with the acronym of the survey appended typically with the year of discovery and continuing alphabetical letters. Since January 2016, the *Transient Name Server* (TNS)* is the official International Astronomical Union platform for reporting new astrophysical transients. Reported events receive the

* https://www.wis-tns.org/

prefix AT, followed by the year and continuing alphabetical letters, for example AT 2019dsg.

2.3 Neutrinos

Neutrinos do not carry charge and only interact weakly, so they do not get deflected by magnetic fields like CRs and also do not interact electromagnetically in contrast to photons. As a result, they travel unimpeded through the universe. Because they can escape dense environments and are exclusively produced in hadronic interactions, they can give insight into different processes than the ones accessible with observations of photons only. For example, at high energies they provide a smoking gun signature of hadronic acceleration and can pin down the sources of CRs. To fully understand the role of astrophysical neutrinos, it is helpful to consider the broader spectrum of their origins across different processes.

The spectrum of neutrino sources is shown in Figure 2.3. The lowest energy neutrinos from μeV to meV are relics from the Big Bang, analogous to the CMB photons. There is currently no feasible method for detecting these neutrinos. First, their interaction cross-section at such low energies is extremely small. Second, even if an interaction were to occur, the energy transferred to the detection volume would be minimal, making any signal exceedingly difficult to measure.

Cosmological neutrinos

In the keV to MeV range, neutrinos come from the sun, nuclear reactors and supernovae [36]. The neutrinos produced in the sun by the nuclear fusion reactions were already discovered in 1968 [5], but with a deficit with respect to the expected flux. This was later solved by the introduction of neutrino oscillation: The neutrino flavor, electron, muon or tau neutrino, changes during propagation, a consequence of the fact that neutrinos apparently have mass. The tightest bound on the neutrino mass comes from cosmological observations. Cosmological models are sensitive only to the sum of the masses of the three neutrino flavors: $\sum m_\nu \lesssim 0.5\,\mathrm{eV}$ [10]. However, these are dependent on the cosmological model. Current experiments are getting close to probing neutrino masses at eV scale in a model independent way, using the kinematics of the tritium β-decay [37, 38].

Solar neutrinos

[36]: Spiering (2012), *Towards High-Energy Neutrino Astronomy*

[5]: Davis et al. (1968), *Search for Neutrinos from the Sun*

Neutrino oscillation

[37]: Formaggio et al. (2021), *Direct Measurements of Neutrino Mass*

[38]: Aker et al. (2022), *Direct Neutrino-Mass Measurement with Sub-Electronvolt Sensitivity*

During the explosions of massive stars, called supernova (SN), neutrinos of MeV energies are released in a burst (see Chapter 3). This signal was observed for the galactic SN SN 1987A. There should also be a diffuse background due to the ensemble of SNe in the universe, called the diffuse supernova background (DSNB) [36]. Although the sensitivity of the current generation of neutrino detectors optimized for this energy range is close to the predicted flux, searches have only resulted in upper limits up until now [for example 39].

Supernova neutrinos

[39]: Suliga (2023), *Diffuse Supernova Neutrino Background*

The most abundant artificial source of neutrinos are nuclear reactors. The detection of anti-neutrinos produced in the fission reactions actually provided the first confirmation of the existence of neutrinos [40]. More recently, neutrinos from radioactive decays in the Earth have been detected [41].

Reactor neutrinos

[40]: Cowan et al. (1956), *Detection of the Free Neutrino: A Confirmation*

Terrestrial neutrinos

[41]: Bellini et al. (2010), *Observation of Geo-Neutrinos*

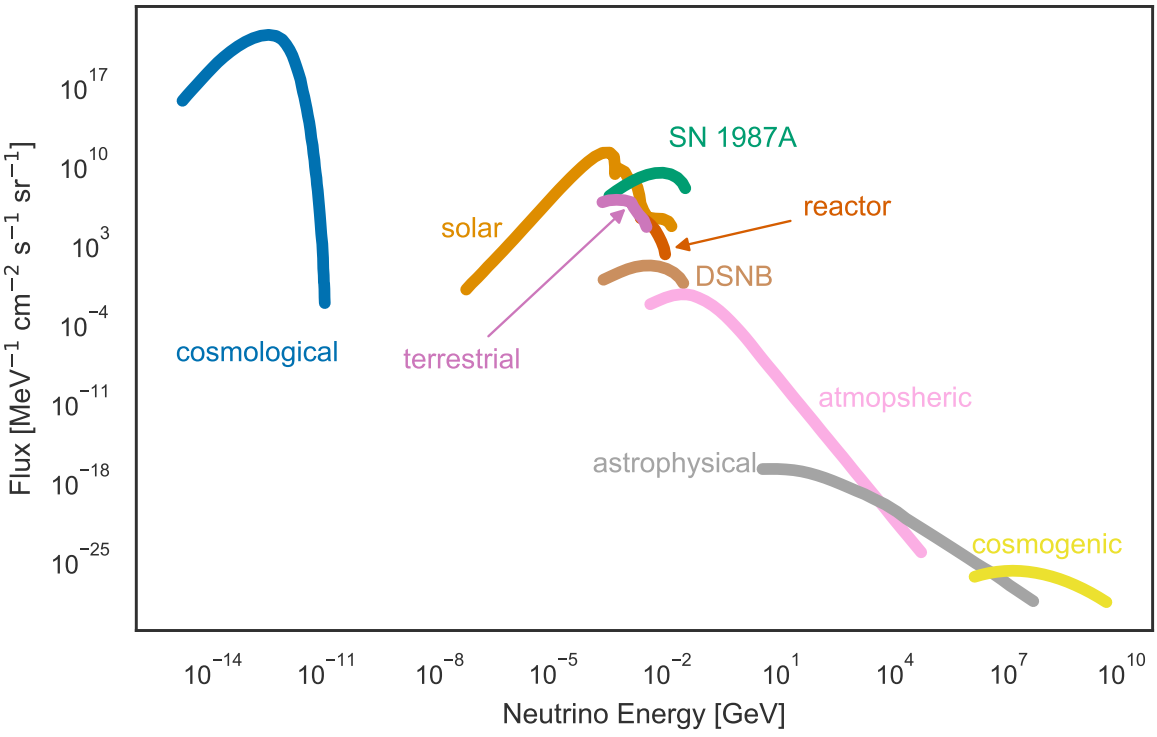

Figure 2.3: Fluxes from natural neutrino sources and reactors. Cosmological, cosmogenic, and diffuse supernova background (DSNB) fluxes are expectations. Adapted from Spiering [36]

Atmospheric neutrinos

Cosmogenic neutrinos

[42]: Aguilar et al. (2019), *The Next-Generation Radio Neutrino Observatory – Multi-Messenger Neutrino Astrophysics at Extreme Energies*

Astrophysical neutrinos

[2]: IceCube Collaboration (2013), *Evidence for High-Energy Extraterrestrial Neutrinos at the IceCube Detector*

[43]: Aartsen et al. (2015), *A Combined Maximum-likelihood Analysis of the High-energy Astrophysical Neutrino Flux Measured with IceCube*

[45]: Abbasi et al. (2022), *Improved Characterization of the Astrophysical Muon–Neutrino Flux with 9.5 Years of IceCube Data*

[44]: Naab et al. (2023), *Measurement of the Astrophysical Diffuse Neutrino Flux in a Combined Fit of IceCube's High Energy Neutrino Data*

For this work, neutrinos roughly above GeV energies are referred to as high-energy neutrinos. The most abundant component is produced in CR air showers (see Section 2.1). These atmospheric neutrinos predominantly come from the decay of charged pions produced by the interaction of a CR with an atomic nucleus in the atmosphere, as shown in Equation 2.2 and Equation 2.4a. At the very highest energies, cosmogenic neutrinos are expected due to the interaction of UHECRs with the CMB photons [36]. This was already introduced in Section 2.1 as the GZK mechanism. However, due to their low flux, they were not observed so far but are a prime target for future neutrino observatories [42].

When CRs interact in their source with ambient photons or other hadrons, they can produce charged pions (see Section 2.1). For photohadronic interactions (see Equation 2.3a) the neutrinos carry on average 5% of the parent proton energy, but their spectrum does not have to follow the parent proton spectrum but also depends on the target photons. For proton-proton interactions, the neutrino spectrum also follows a power-law with the parent spectral index [9]. In 2013, IceCube discovered a diffuse, isotropic high-energy neutrino flux, consistent with being of astrophysical origin [2]. The spectrum between TeV to PeV energies was characterized as a power-law with a most likely spectral index between 2.4 and 2.9 (see Figure 2.4) [43, 45]. Because this matches the CR spectrum above the ankle, this is consistent with the hypothesis that neutrinos are produced in the same sources as UHECRs. Recent preliminary IceCube results suggest that a broken power-law provides a better description of the neutrino flux [44], which could indicate that there are multiple populations of UHECR sources.

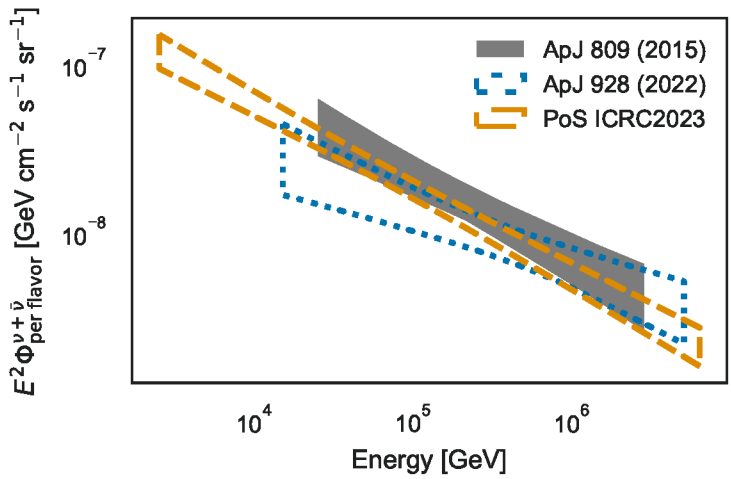

Figure 2.4: Measurements of the diffuse astrophysical neutrino flux by the IceCube observatory. Here the 68% uncertainty contours of three measurements are shown. The analyses presented in ApJ 809 [43] and at ICRC 2023 [44] use all neutrino flavors, while the analysis in ApJ 928 [45] uses only muon neutrinos.

The flavor composition is consistent with pion decay in distant sources, which predicts an intrinsic neutrino flavor proportion $\nu_e : \nu_\mu : \nu_\tau$ of $1 : 2 : 0$ (see Equation 2.4a). Due to oscillation, this changes to almost equal parts when observing the combined flux from astrophysical sources at Earth. Because of cooling of the interacting particles in the source, this intrinsic flavor composition might be different. Current analyses do net yet have the sensitivity to conclusively differentiate between these scenarios [46].

IceCube has conclusively identified two active galaxies as high-energy neutrino emitters, the flaring blazar TXS 0506+056 [47] and the core of the nearby galaxy NGC 1068 [48]. Recently, also a galactic plane contribution was confirmed, produced by CR interactions with interstellar material [49], which is the neutrino counterpart to the diffuse galactic gamma-ray emission introduced in the previous section. And although there is a hint from a large population of active galaxies [50], the majority of the extragalactic neutrino flux is still unexplained. Chapter 8 and Chapter 9 investigate TDEs and flares from active galaxies as potential contributors to this flux.

[46]: Abbasi et al. (2022), *Detection of Astrophysical Tau Neutrino Candidates in IceCube*

[47]: IceCube Collaboration et al. (2018), *Multimessenger Observations of a Flaring Blazar Coincident with High-Energy Neutrino IceCube-170922A*

[48]: IceCube Collaboration et al. (2022), *Evidence for Neutrino Emission from the Nearby Active Galaxy NGC 1068*

[49]: IceCube Collaboration et al. (2023), *Observation of High-Energy Neutrinos from the Galactic Plane*

[50]: Abbasi et al. (2022), *Search for Neutrino Emission from Cores of Active Galactic Nuclei*

2.4 Gravitational Waves

The newest addition to the pool of cosmic messengers is gravitational waves. They are a distortion in spacetime traveling at the speed of light, emitted by a changing gravitational quadrupole moment. The most common example for such a system is two objects orbiting each other. This was first confirmed indirectly by observing the decrease of a nearby binary pulsar system's orbital period [51, 52]. The measured decrease matched the expectation of energy being carried away by gravitational waves. The contraction and stretch ΔL induced by a gravitational wave passing through an object of length L can be characterized as the *strain*:

$$h = \Delta L / L, \tag{2.6}$$

which is of the order of 10^{-21} [9].

Pulsar binary

[51]: Hulse et al. (1975), *Discovery of a Pulsar in a Binary System.*

[52]: Taylor et al. (1982), *A New Test of General Relativity - Gravitational Radiation and the Binary Pulsar PSR 1913+16*

Since then, efforts were made to facilitate direct detection through

Laser intereferometers

ground-based laser interferometers. A laserbeam is split, sent down two perpendicular arms, reflected, and the interference between both beams is measured. If a gravitational wave passes through, it will alter the lengths of the two perpendicular beam paths differently, such that the intensity at the interference point is a measure of the strain. The currently operating interferometers are the *Laser Interferometer Gravitational-Wave Observatory* (LIGO)[†], *Virgo*[‡] and the *Kamioka Gravitational Wave Detector* (KAGRA)[§], collectively called the LVK collaboration. The four observation sites (LIGO consists of two interferometers) are distributed around the globe (USA, Europe and Japan), so that multi-interferometer detection allows for directional reconstruction of the signal [9]. The interferometer arms have kilometer lengths so that following Equation 2.6, variations of 10^{-18} m have to be measured. In 2016 LIGO and Virgo announced the first direct detection of a gravitational wave that was emitted by the merger of two stellar-mass black holes [6], opening a new window to the universe. Binary black hole mergers, however, do not emit other messengers. In contrast, if at least one of the compact objects is a neutron star, other messengers can also escape. This was confirmed by the first observation of a binary neutron star merger in gravitational waves along with the corresponding electromagnetic emission [53]. In general, the current generation of interferometers is sensitive to compact objects from 1 to 10^2 $M_\odot$.

[6]: LIGO Scientific Collaboration and Virgo Collaboration et al. (2016), *Observation of Gravitational Waves from a Binary Black Hole Merger*

[53]: Abbott et al. (2017), *Multi-Messenger Observations of a Binary Neutron Star Merger*

SMBH binaries

To detect the mergers of the massive SMBHs in the center of galaxies, arm lengths of $\mathcal{O}(10^6)$ km are necessary. This is only possible with a space-based mission like the planned *Laser Interferometer Space Antenna* (LISA)[¶]. So-called pulsar timing arrays can also indirectly detect the combined signal of the population of SMBH binaries. The presence of the gravitational wave ensemble affects the timing of the pulsar signals. Precise measurements of the timing of many pulsars can reveal the gravitational wave imprint. The *North American Nanohertz Observatory for Gravitational Waves* (NANOGrav) has recently found evidence for this signal in their dataset [54] which indicates the presence of SMBH binaries that can potentially be observed and located with future observatories like LISA.

[54]: Agazie et al. (2023), *The NANOGrav 15 Yr Data Set: Evidence for a Gravitational-wave Background*

[†] https://ligo.org
[‡] https://www.virgo-gw.eu
[§] https://gwcenter.icrr.u-tokyo.ac.jp/en/
[¶] https://lisa.nasa.gov/index.html

Candidate Transient Neutrino Source Populations

3

The only confirmed sources of high-energy neutrinos are a diffuse emission from the galactic plane [49] and the active galaxies TXS 0506+056 [47] and NGC 1068 [48]. The only astrophysical population that showed hints of neutrino emission are Active Galactic Nuclei [50]. They all emit at different energy ranges: the galactic plane and NGC 1068 below around 30 TeV, and TXS 0506+056 and Active Galactic Nuclei (AGN) above. Both NGC 1068 and TXS 0506+056 contribute around 1% of the diffuse flux in their respective energy ranges [48], and the galactic plane around 6 to 10%. Active Galactic Nuclei could be the sources of most neutrinos above 30 TeV, based on the distribution of AGN in the universe and their luminosities, but probably contribute at least 27% [50]. That leaves 89 to 93% of the flux unaccounted for below 30 TeV and 0 to 72% at higher energies.

This chapter introduces the classes of potential transient neutrino sources to review their potential for contributing to the missing neutrino flux. It is not a comprehensive list but rather focuses on those extragalactic populations with a potentially detectable optical signal, which are relevant to this thesis. Novae, Magnetars and supernova remnants do not fall within this category because they would only be detectable in the Milky Way. Powerful radio transients, called fast radio bursts, have not yet been associated with an accompanying optical signal.

Furthermore, the transients are introduced based on their physical origin rather than observational characteristics where possible. As an example, there is no dedicated section for gamma-ray bursts, but they will instead be discussed as signatures of Core-collapse Supernovae and neutron star mergers.

3.1 Active Galactic Nuclei

The most efficient form of energy release from normal matter occurs through accretion onto compact objects, such as SMBHs. These SMBHs, located at the centers of galaxies [55], accrete matter that forms luminous disks. As gravitational energy is converted into radiation, these disks emit light across the entire electromagnetic spectrum [56, 57], which is observed as an active galactic nucleus (AGN). Although all galaxies have a SMBH at their center, only a small fraction is active.

[55]: Magorrian et al. (1998), *The Demography of Massive Dark Objects in GalaxyCenters*

[56]: Lynden-Bell (1969), *Galactic Nuclei as Collapsed Old Quasars*
[57]: Rees (1984), *Black Hole Models for Active Galactic Nuclei*

AGN unification model

The characteristics of the observed emission can vary widely. The AGN *unification model* describes these effects as a result of viewing angle effects, the presence of a jet, and the power of the central engine (see Figure 3.1) [58]. According to this, the SMBH in the center is surrounded by an accretion disk formed by infalling matter, a region of dense, compact clouds or outflow producing broad spectral lines (*broad line region*), and an extended, diffuse region producing narrow

[58]: Urry et al. (1995), *Unified Schemes for Radio-Loud Active Galactic Nuclei*

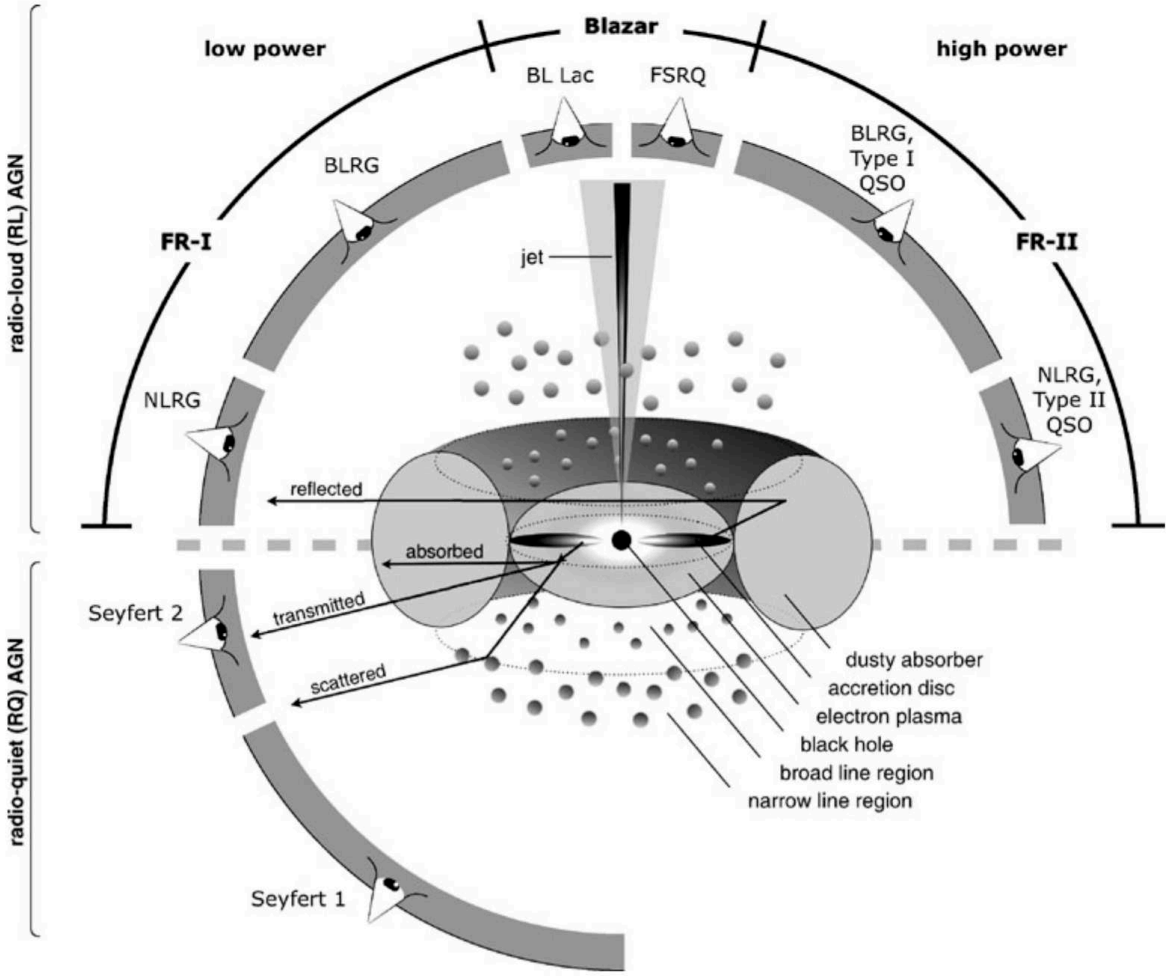

Figure 3.1: The AGN unification model. The central SMBH is surrounded by an accretion disk, a dense and compact region producing broad spectral lines, an extended, diffuse one producing narrow lines, and a dusty torus. The viewing angle determines which of these components are observed directly or indirectly or if their emission is absorbed. Typically, radio-loud AGN have a jet while radio-quiet ones do not. Taken from Beckmann [60]

spectral lines (*narrow line region*). Depending on the viewing angle, the different components can be absorbed or reflected by the dusty torus and manifest accordingly in the observed spectrum. This leads to a distinction into two general classes: Type I exhibit broad lines while type II do not. Following the paradigm that the dusty torus can obscure the broad line region, type I are usually interpreted as an unobscured view onto the disk and the broad line region, while they are obscured in type II, where only the narrow line region is visible. The presence of a jet determines the radio properties. If it points directly towards earth, the beamed emission can reach gamma-ray energies and is observed as a blazar. The optical emission of blazars is also likely dominated by synchrotron emission in these cases rather than coming from the disk [59].

AGN have long been predicted to be acceleration sites of cosmic rays and sources of high-energy neutrinos. Especially blazars were thought to be promising candidates [61, 62]. They show very high energy gamma-ray emission, which was thought to be a tracer of the neutrino emission. Indeed, the first confirmed neutrino source is the blazar TXS 0506+056. It was flaring in gamma-rays at the same time as a high-energy neutrino was observed from the same direction [47].

[59]: Ulrich et al. (1997), *Variability of Active Galactic Nuclei*

Blazars

[61]: Mannheim (1993), *The Proton Blazar.*
[62]: Mannheim (1995), *High-Energy Neutrinos from Extragalactic Jets*

Blazar flares

[47]: IceCube Collaboration et al. (2018), *Multimessenger Observations of a Flaring Blazar Coincident with High-Energy Neutrino IceCube-170922A*

The flare was accompanied by an increase of around 0.5 $\mathrm{mag_{AB}}$ over 50 days in the optical. However, an earlier neutrino flare at lower energies turned out to not be accompanied by gamma-rays [63]. It turns out that efficient neutrino production is not even expected to be accompanied by gamma-rays because the latter are absorbed [64]. The blazar PKS 1502+106 was also observed in coincidence with another high-energy neutrino alert during a quiescent EM state [65]. Based on IceCube results, gamma-ray blazar flares were constrained to contribute no more than 50% to the diffuse neutrino flux, based on their flaring duty cycle and an assumed neutrino power-law spectrum. For a more realistic model or an X-ray proxy, this limit can go down as low as around 7% [66]. The time-independent constraint by IceCube allows a maximal contribution of gamma-ray blazars to the diffuse flux of 27% if each blazar contributes equally, independent of its properties [67]. If the neutrino flux is proportional to the gamma-ray flux, this limit even goes down to 10%. Although recently, a significant correlation was found between IceCube neutrinos and a general compilation of blazars [68], it was later suggested that this is due to the specific choice of catalog and dataset [69].
There is evidence for neutrino production in some blazars, but the properties that separate them from the rest of the population are still not clear. Especially gamma-rays do not seem to be a good tracer for neutrino emission. Blazar variability is observed at all wavelengths [59], but there is no prediction that the optical signal would be correlated to a neutrino signal.

[63]: IceCube Collaboration et al. (2018), *Neutrino Emission from the Direction of the Blazar TXS 0506+056 Prior to the IceCube-170922A Alert*

[64]: Halzen et al. (2019), *On the Neutrino Flares from the Direction of TXS 0506+056*

[65]: Rodrigues et al. (2021), *Multiwavelength and Neutrino Emission from Blazar PKS 1502 + 106*

[66]: Yoshida et al. (2023), *Flare Duty Cycle of Gamma-Ray Blazars and Implications for High-energy Neutrino Emission*

[67]: Aartsen et al. (2017), *The Contribution of Fermi-2LAC Blazars to Diffuse TeV–PeV Neutrino Flux*

[68]: Buson et al. (2022), *Beginning a Journey Across the Universe: The Discovery of Extragalactic Neutrino Factories*

[69]: Bellenghi et al. (2023), *Correlating High-energy IceCube Neutrinos with 5BZCAT Blazars and RFC Sources*

[59]: Ulrich et al. (1997), *Variability of Active Galactic Nuclei*

Other AGN

Even if the AGN does not have a strong jet pointed at earth, particle acceleration can still occur, for example, in an accretion shock [70]. This is thought to be the case for the second identified source of high-energy neutrinos, the core of NGC 1068 [48]. It is a Seyfert 2 galaxy and highly obscured by dust, absorbing the accompanying gamma radiation. X-rays from the hot plasma above the disk, the corona, might be a good tracer instead, because they could be the target for photo-meson pion production leading to high-energy neutrinos [71]. Indeed, an AGN selection probing AGN cores based on soft X-rays and mid-infrared was found to be correlated with the IceCube data at 2.6σ [50]. Hard X-ray AGN, however, did not show a significant correlation with high-energy neutrinos, although a major contribution to the diffuse flux at energies up to 30 TeV cannot be ruled out [72]. And although even those Seyfert galaxies similar to NGC 1068 did not show significant correlation, a subsample did, indicating that at least part of the population is contributing to the diffuse flux [73]. Still, more data is necessary for the characterization of their physical parameters. Therefore, similar to blazars, non-blazar AGN are promising high-energy neutrino sources, while it is not yet clear what distinguishes efficient from inefficient neutrino emitters.

[70]: Stecker et al. (1991), *High-Energy Neutrinos from Active Galactic Nuclei*

[48]: IceCube Collaboration et al. (2022), *Evidence for Neutrino Emission from the Nearby Active Galaxy NGC 1068*

[71]: Murase et al. (2023), *High-Energy Neutrinos from Active Galactic Nuclei*

[50]: Abbasi et al. (2022), *Search for Neutrino Emission from Cores of Active Galactic Nuclei*

[72]: Abbasi et al. (2024), *Search for Neutrino Emission from Hard X-ray AGN with IceCube*

[73]: Abbasi et al. (2024), *IceCube Search for Neutrino Emission from X-ray Bright Seyfert Galaxies*

Giant AGN flares

Instead of emission over a long period of time, giant AGN flares were suggested as the sources of UHECRs [74] and high-energy neutrinos [75]. Variability is inherent to the AGN emission on timescales from hours to years [59] typically within tens of percent [76]. In recent years, a distinct population of giant flares emerged that shows more dramatic changes. Among them, the *changing-look* AGN seem to

[74]: Farrar et al. (2009), *Giant AGN Flares and Cosmic Ray Bursts*

[75]: Bednarek et al. (1999), *Gamma-Ray and Neutrino Flares Produced by Protons Accelerated on an Accretion Disc Surface in Active Galactic Nuclei*

transition from type I to type II or the other way around, accompanied by extreme flares in the X-ray of optical and ultraviolet (OUV). At least in the latter case, this is attributed to enhanced accretion events rather than changing obscuration (see Ricci and Trakhtenbrot [77] for a recent overview), as for example, derived from reprocessed emission by circumnuclear dust in the MIR [78]. Another class of flares is characterized by a certain set of transient emission lines, called Bowen fluorescence lines. These flares are believed to be due to sudden rejuvenation of accretion onto the SMBH [79]. What exactly triggers both of these flare classes is uncertain. Possibilities include disk instabilities, an outflow from the broad line region or tidal disk deformation, for example by a TDE [77], as introduced in the next section. Recently, a sample of flares connected to extreme accretion events was found to be correlated at 3.6σ with IceCube's high-energy neutrinos [80]. Some of them are TDEs but for most of them, the classification is uncertain because of the underlying AGN activity. This will be discussed in detail in Chapter 8.

[77]: Ricci et al. (2023), *Changing-Look Active Galactic Nuclei*

[78]: Sheng et al. (2017), *Mid-Infrared Variability of Changing-look AGNs*

[79]: Trakhtenbrot et al. (2019), *A New Class of Flares from Accreting Supermassive Black Holes*

[80]: van Velzen et al. (2024), *Establishing Accretion Flares from Supermassive Black Holes as a Source of High-Energy Neutrinos*

In summary, AGN are promising acceleration sites for UHECRs and sources of high-energy neutrinos. IceCube identified single AGN as neutrino sources, but the respective populations still elude detection. Giant AGN flares due to enhanced accretion might temporarily provide the right conditions for high-energy production, but their nature remains unclear.

3.2 Tidal Disruption Events

TDEs were first thought of as a result of the idea that galaxies harbor SMBHs in their center [81]. If a star got too close, the gravitational forces exerted by the SMBH would at some point be greater than the ones holding the star together, ripping the star apart [82]. Parts of the star debris would remain bound to the SMBH and get accreted, and the radiation outburst was suggested to be the observable signature of a TDE. However, if the SMBH is too massive, the disruption would happen inside the event horizon and no flare would be visible. The corresponding mass limit for a solar type star is called the *Hills mass* and is around $10^8 m_\odot$ [81].

[81]: Hills (1975), *Possible Power Source of Seyfert Galaxies and QSOs*

[82]: Rees (1988), *Tidal Disruption of Stars by Black Holes of 106–108 Solar Masses in Nearby Galaxies*

X-ray emission

If the EM emission is indeed powered by the accretion, and the accretion is proportional to the fallback rate of the debris, the luminosity declines with a characteristic rate of $L \propto t^{-5/3}$ [83]. This was indeed used to identify the first TDE candidates in archival soft X-ray observations [84]. Since then, more candidates have been selected in X-rays, all sharing a soft spectrum that fits a blackbody of around 2×10^5 to 15×10^5 K.

[83]: Gezari (2021), *Tidal Disruption Events*

[84]: Komossa et al. (1999), *The Giant X-ray Outbursts in NGC 5905 and IC 3599: Follow-up Observations and Outburst Scenarios*

Optical and ultraviolet signal

Today TDEs are mainly discovered in the optical, owing to the advent of large optical time domain surveys like, for example, ZTF [83]. The OUV spectrum also fits a blackbody with lower temperature of around 10^4 K, stable over hundreds of days [83]. Superimposed are broad emission lines, specifically those of HeII. The OUV light curve also broadly falls with $t^{-5/3}$ [85].

[83]: Gezari (2021), *Tidal Disruption Events*

[85]: van Velzen et al. (2020), *Optical-Ultraviolet Tidal Disruption Events*

Radio emission

In 2011, the high-luminosity hard X-ray transient Swift J1644+57 was discovered, together with transient radio emission [87], which was

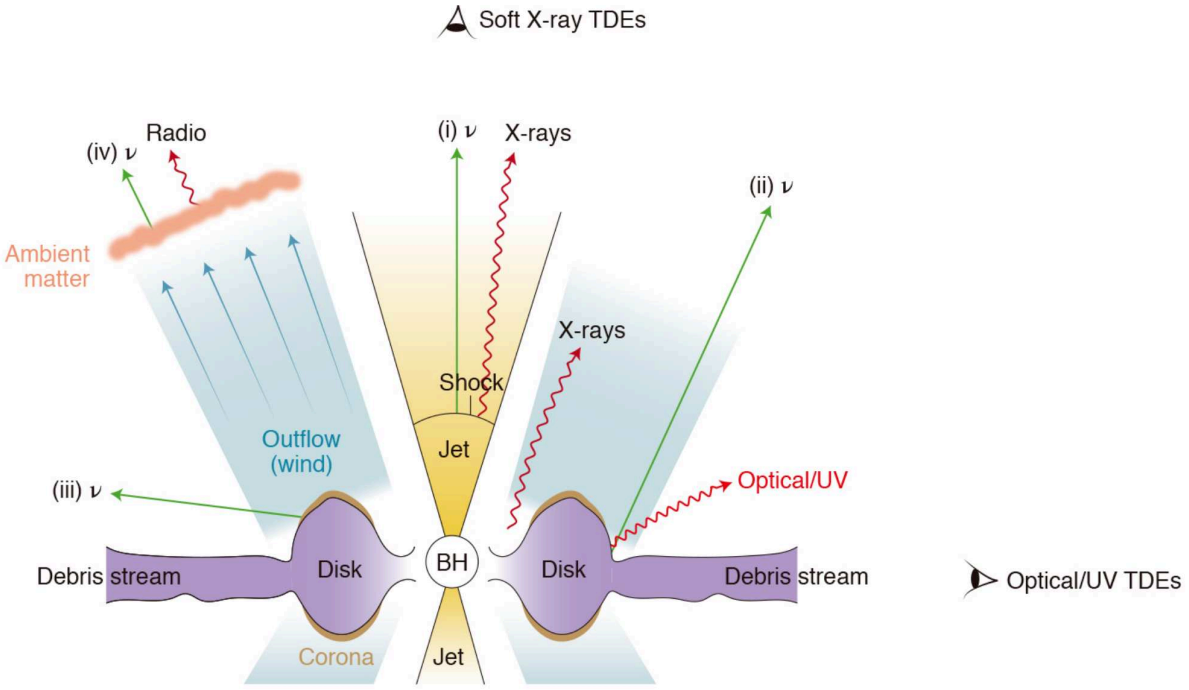

Figure 3.2: The TDE unification model, including sites for possible neutrino production. The viewing angle determines the spectral properties of the observed flare. Taken from Hayasaki [86].

interpreted as the non-thermal emission by a relativistic jet launched by a TDE. This confirmed that at least leptonic particle acceleration takes place in some TDEs. Only a few such radio-loud or hard X-ray transients have been observed, suggesting that only a few percent of TDEs have a relativistic jet pointing towards Earth. However, also radio emission with lower luminosity has been observed, attributed to a lower energetic outflow [88].

[88]: Alexander et al. (2020), *Radio Properties of Tidal Disruption Events*

Unification model

This does not necessarily mean, however, that there are distinct populations of TDEs. A unification model, akin to the one for AGN introduced in the previous section, can describe the different spectral properties dependent on the viewing angle as shown in Figure 3.2 [89]: The soft X-rays are produced by the inner accretion disk and only visible when looking down the funnel close to the disk axis. If the system is viewed edge-on, the X-rays are reprocessed by a slow outflow to the OUV. Gradually varying from the one extreme to the other gradually shifts the observed X-ray-to-optical ratio. However, recent simulations suggest that the OUV emission is instead powered by shocks between the stream of returning star debris and the forming accretion disk [90], so late-time X-ray detections could then be due to delayed accretion [83].

[89]: Dai et al. (2018), *A Unified Model for Tidal Disruption Events*

[90]: Steinberg et al. (2024), *Stream–Disk Shocks as the Origins of Peak Light in Tidal Disruption Events*

Neutrinos from TDEs

TDEs jets have been suggested as promising sources of UHECR by accelerating protons in internal shocks or at the interaction with the interstellar medium (ISM) [74], and subsequent high-energy neutrino production is possible [91]. IceCube has since constrained the contribution of jetted TDEs to the diffuse astrophysical neutrino flux to less than 1.3% [92]. Even if no jet is present, neutrino production is possible in an outflow from the disk, the disk corona [93], or in the disk itself [94]. IceCube has also limited the contribution by non-jetted TDEs to no more than 26% assuming a the neutrino

[74]: Farrar et al. (2009), *Giant AGN Flares and Cosmic Ray Bursts*

[91]: Biehl et al. (2018), *Tidally Disrupted Stars as a Possible Origin of Both Cosmic Rays and Neutrinos at the Highest Energies*

[92]: Stein (2019), *Search for High-Energy Neutrinos from Populations of Optical Transients*

spectrum is a power-law with spectral index $\gamma = 2.5$ [92].

However, three coincidences were identified between IceCube high-energy neutrino alerts (see Chapter 5) and three (candidate) TDEs, and a sample of similar events shows correlation with the IceCube alerts [80]. Although many of the flares cannot be classified unambiguously as TDEs due to underlying AGN activity and dust obscuration, they are extreme accretion events onto SMBHs that could be connected to TDEs. They are characterized by bright IR emission lagging the OUV signal that comes from a re-processing of the initial flare by the dusty region around the SMBH, called dust echos. In Chapter 8, this thesis presents the first limits on neutrino emission from this population. If they are indeed TDEs, the limit is four times stricter than the previous result for a soft spectral index of $\gamma = 2.5$. Although the most promising model that connects high-energy neutrino production to the dust echo and would primarily explain neutrinos above around 10 PeV, as explained in Chapter 8. However, it is not at all clear how this population ties in to the border class of giant AGN flares discussed in the previous section. To address this, this thesis compiles a catalog of such flares (see Chapter 9).

[80]: van Velzen et al. (2024), *Establishing Accretion Flares from Supermassive Black Holes as a Source of High-Energy Neutrinos*

3.3 Supernovae

Massive stellar explosions, called Supernovae (SNe), are the most commonly observed type of extragalactic transient [for example 96]. They have traditionally been classified based on their spectrum, which does not necessarily follow the underlying physical system [95], as shown in Figure 3.3. This scheme sorts SNe based on the presence of hydrogen lines (type I or II), silicon lines (type Ia), and helium lines (type Ib or Ic). However, in principle, two underlying physical scenarios exist.

[96]: Perley et al. (2020), *The Zwicky Transient Facility Bright Transient Survey. II. A Public Statistical Sample for Exploring Supernova Demographics**

[95]: Turatto (2003), *Classification of Supernovae*

3.3.1 Explosion mechanism

Thermonucelar supernovae

The first explosion mechanism is a thermonuclear explosion. During the main phase of its life, the star is supported by pressure produced by nuclear fusion in its core. If the mass of the star is below around $8m_\odot$, the heaviest element it is able too use in the fusion reaction is helium [34], and the fusion stops once the nuclear fuel is expended. The stellar core starts to contract until the electron degeneracy pressure is large enough to support it against the gravitational forces. The outer star layers are driven away, and the core remains, called a *White Dwarf*. These White Dwarfs can accumulate matter on their surface from a companion star, and once this matter exceeds the *Chandrasekhar* mass limit [97] of around $1.4m_\odot$ [34], fusion instantly sets in, completely destroying the White Dwarf. The resulting explosion is observed as a SN type Ia, which comprises about 24% of all SNe[1] [98], but is not expected to generate shocks to enable particle acceleration and high-energy neutrino production. It turns out that their brightness is correlated with the timescale on which they rise and fade, so they can be used as standard candles in cosmology.

[34]: Karttunen et al. (2007), *Fundamental Astronomy*

[97]: Chandrasekhar (1931), *The Maximum Mass of Ideal White Dwarfs*

1: Considering a magnitude limited survey instead of a volume limited one, SNe Ia will actually dominate the observed transients [96]

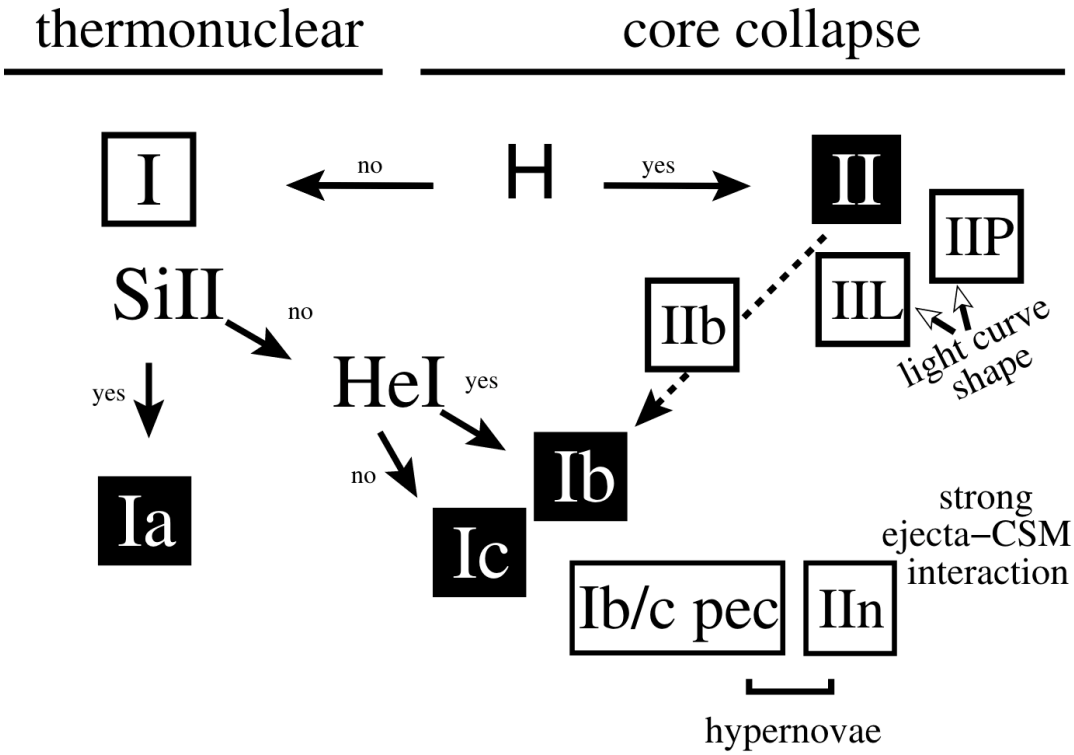

Figure 3.3: The supernova classification scheme based on the transient spectrum. The decision flow is based on the presence of hydrogen, helium, and silicon spectral lines. Strong CSM interaction is indicated by narrow line in the spectrum as explained in the text. Taken from Turatto [95].

Core-collapse supernovae

If a star is heavier than around $8m_\odot$ [34], it produces heavier elements up to iron. Because iron does not release energy in further fusion processes, the fusion stops, and the core begins to collapse. In this case, the gravitational forces are stronger than the electron degeneracy pressure, so the contraction continues until the density gets so high that protons capture electrons and produce neutrons:

$$p + e^- \rightarrow n + \nu_e. \tag{3.1}$$

If the mass of the core is below around $2m_\odot$ [34], the neutron degeneracy pressure eventually balances the gravitational forces and suddenly stabilizes the core to form a *Neutron Star*. The material from the outer star shells bounces off the surface of the neutron star, creating an outgoing shockwave that heats the material and eventually leads to the explosion of the star. Large amounts of ^{56}Ni are ejected and its decay (and that of the decay product ^{56}Co) heat the material and power its expansion so that the supernova is visible over months. Because they are triggered by the collapse of the core they are called Core-collapse Supernovae (CCSNe).

The neutrinos produced in the electron capture by protons have an energy of several MeV, and can escape the dense nuclear environment[2]. For an individual supernovae, this signal can only be observed if it happens in the Milky Way or a satellite dwarf galaxy. Since detectors looking for neutrinos in this energy range are taking data, this has only happened once: The IMB detector and the Kamiokande detector observed the MeV neutrino burst from SN 1987A [100, 101]. Today many more detectors that are sensitive

MeV neutrinos

2: Before they escape, the MeV neutrinos might play a crucial role in actually triggering the supernova explosion by re-heating the outgoing shock, that would otherwise stall [99].

[100]: Bionta et al. (1987), *Observation of a Neutrino Burst in Coincidence with Supernova 1987A in the Large Magellanic Cloud*

[101]: Hirata et al. (1987), *Observation of a Neutrino Burst from the Supernova SN1987A*

to this energy range are in operation, and even neutrino detectors optimized for higher energies like IceCube have some sensitivity to this signal (see Section 4.2.2). Thus, the next galactic supernova is going to be observed in much more detail.

Supernovae type II

CCSNe are, in contrast to the SNe of type Ia, a very diverse class, dependent on the progenitor star. In the last stages of the star's life, it has an onion-like structure with the nuclear fusion taking place in shells that burn successively heavier elements. If it has retained all the shells, hydrogen emission lines from the outer shell are visible in the supernova spectrum, which is defined as a SN type II. The most common type shows a plateau in the lightcurve (type IIP), followed by the ones with linear decay (type IIL). A rare subclass shows narrow lines in the spectrum (type IIn) that result from interaction with circumstellar material (CSM). These are typically longer lived as this interaction transforms some of the ejecta's kinetic energy into radiation.

Stripped-envelope Supernovae

If the star has lost its outer hydrogen layer, emission lines from the exposed helium shell are visible in the spectrum instead of the hydrogen ones (type Ib). If the helium layer also got stripped off the star, and the corresponding lines are missing from the spectrum, the supernova is of type Ic. Collectively, these are called stripped-envelope Supernovae (SESNe). Some SNe type II show hydrogen lines in the beginning, but they disappear over time, making them a transitional type between II and Ib, called IIb. Also, some SESNe show narrow lines in their spectrum, indicating CSM interaction, and are consequently called Ibn or Icn.

Superluminous Supernovae

In recent years, it became clear that there is a population of very luminous supernovae, brighter than $-21\,\mathrm{mag_{AB}}$ in the optical, called superluminous supernovae (SLSNe). They seem to be powerful extensions of the SN type IIn and type Ic populations. The origin of their extreme luminosity is not yet clear. Suggestions include intense CSM interaction, a larger amount of ^{56}Ni than in normal SNe, or the spin-down of a magnetar, a highly magnetized neutron star [102].

[102]: Moriya et al. (2018), *Superluminous Supernovae*

Fast Blue Optical Transients

Another transient population that is so far only defined by the observational properties are Fast Blue Optical Transients (FBOTs). They are characterized by a fast rise and fade, with a time above half-maximum brightness of only around twelve days [103]. The likely underlying mechanism is (shock) interaction of SN ejecta with CSM, similar to SNe IIb or Ibn [104].

[103]: Drout et al. (2014), *Rapidly Evolving and Luminous Transients from Pan-STARRS1*

[104]: Ho et al. (2023), *A Search for Extragalactic Fast Blue Optical Transients in ZTF and the Rate of AT 2018cow-like Transients*

3.3.2 High-energy Neutrinos from Supernovae

CSM interaction

There are two scenarios how CCSNe can potentially accelerate hadrons and subsequently produce high-energy neutrinos. The interaction of ejecta and CSM can produce strong shocks that enable hadronic particle acceleration. Protons then interact with the CSM or UV to gamma ray photons from the SN emission to produce neutrinos [105]. The neutrino flux depends on the explosion energy and the parameters of the CSM, like mass, extension, and density [105, 106]. As the shock loses energy, the neutrino production is expected to be efficient on a timescale of months after the explosion, gradually declining over time. As narrow lines are an indication for CSM interaction, any supernova showing this spectral feature is a promising neutrino source candidate. Moreover, there are indications

[105]: Murase et al. (2011), *New Class of High-Energy Transients from Crashes of Supernova Ejecta with Massive Circumstellar Material Shells*

[106]: Zirakashvili et al. (2016), *Type IIn Supernovae as Sources of High Energy Astrophysical Neutrinos*

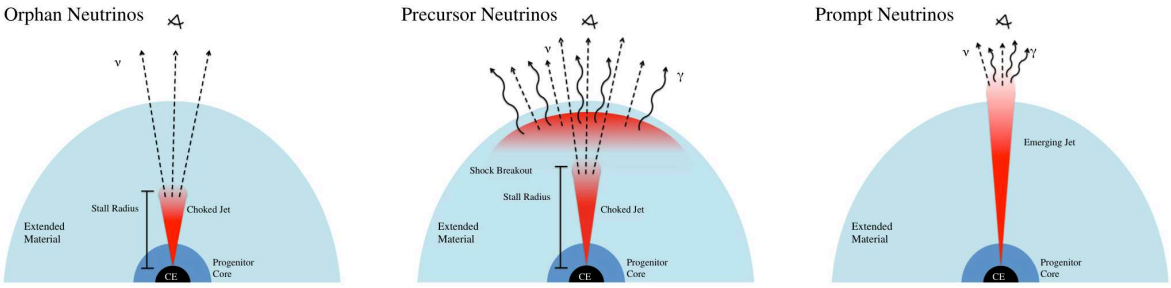

Figure 3.4: Illustration of the connection between (choked) jets, GRBs and high-energy neutrino production in supernovae. *Left*: A jet stalls within the stellar envelope and gets choked. The only high-energy messengers escaping are the neutrinos. *Center*: For a slightly more energetic jet, the shock from the jet interaction with the stellar envelope manages to break out, producing a low-luminosity GRB. The neutrinos produced in the jet arrive slightly before the gamma ray photons. *Right*: The jet is powerful enough to emerge from the stellar material, producing a long GRB. Taken from Senno, Murase, and Mészáros [110]

that also regular type IIP SNe are surrounded by a more confined CSM shell [107]. Thus, IceCube searched for the high-energy neutrino signature on a timescale of hundreds of days after the explosion using a catalogs of type IIn, IIP, and SESNe SNe, resulting in constraints on the contribution to the diffuse neutrino flux of 34%, 60%, and 27%, respectively [108]. However, recent modeling indicates that the optical signal alone might not be a good tracer of the neutrino production and multi-wavelength properties must be correctly taken into account [109].

[107]: Bruch et al. (2023), *The Prevalence and Influence of Circumstellar Material around Hydrogen-rich Supernova Progenitors*

[108]: Abbasi et al. (2023), *Constraining High-energy Neutrino Emission from Supernovae with IceCube*

[109]: Pitik et al. (2023), *Optically Informed Searches of High-Energy Neutrinos from Interaction-Powered Supernovae*

Long GRBs

The second scenario is connected to gamma-ray bursts (GRBs), extremely luminous gamma ray transients caused by beamed emission in a relativistic jet. Specifically, long GRBs with a duration of more than about two seconds were observed in coincidence with supernovae[3] [111, 112]. The generally accepted model is that the collapsing stellar core launches a jet that is powerful enough to break through the remaining stellar envelope (see Figure 3.4 on the right). For a long time, they were considered promising sources of high-energy neutrinos [113]. However, by now they are one of the best constrained source candidates. IceCube has repeatedly looked for the signal in the TeV to PeV range and constrained the contribution to the diffuse flux to below 12% [for example 114] in the prompt phase (first 100 s) and to below around 24% within 10^4 s. There is also no indication for a sub-TeV neutrino signal [115]. After the initial prompt burst of photons, most GRBs exhibit continuing emission called the afterglow, which is often also detected other wavelengths, from radio to X-ray [116]. IceCube also provided limits on the neutrino emission during the afterglow phase to be below around 80% of the diffuse flux within fourteen days [114]. Recently, the brightest GRB of all time was detected, GRB 221009A [117], with an estimated rate of only one in 10,000 years. Nevertheless, no neutrino emission was found, which provides better constraints on neutrino emission models from GRBs than the combined rest of the GRB population [118]. In addition, this thesis presents general constraints on the optical luminosity function of a neutrino source population, applicable to GRBs (see Chapter 6). So although GRBs have a large EM energy output, they do not seem to be efficient hadronic particle accelerators.

3: Short GRBs are connected to neutron star mergers as discussed in the next section.

[111]: Galama et al. (1998), *An Unusual Supernova in the Error Box of the γ-Ray Burst of 25 April 1998*

[112]: Woosley et al. (2006), *The Supernova Gamma-Ray Burst Connection*

[113]: Waxman et al. (1997), *High Energy Neutrinos from Cosmological Gamma-Ray Burst Fireballs*

[114]: Abbasi et al. (2022), *Searches for Neutrinos from Gamma-Ray Bursts Using the IceCube Neutrino Observatory*

[115]: Abbasi et al. (2024), *Search for 10–1000 GeV Neutrinos from Gamma-Ray Bursts with IceCube*

[116]: Vedrenne et al. (2009), *Gamma-Ray Burst Afterglows*

[117]: Burns et al. (2023), *GRB 221009A: The BOAT*

[118]: Abbasi et al. (2023), *Limits on Neutrino Emission from GRB 221009A from MeV to PeV Using the IceCube Neutrino Observatory*

Choked jet

In contrast to the successful jet breakout in the long GRB scenario, it is possible that the jet stalls or gets *choked* while still within the

expanding ejecta (see Figure 3.4 on the left). High-energy neutrinos would then be the only messengers to escape the dense environment, in contrast to the gamma ray photons that get absorbed [119]. The only observable EM counterpart to the neutrino emission would be the supernova itself. It is expected that there exists a continuum between successful and completely choked jets, where at least the termination shock of the jet manages to break out of the ejecta, producing a GRB of lower luminosity (see Figure 3.4 in the center). Fast-moving jet material leads to broad lines in the spectrum. Indeed, these were observed in some SNe type Ic [112], dubbed broad-line supernovae (SNe Ic-BL). This is in concordance with the picture that heavier stars are both more likely to launch a jet and develop strong winds that can strip their outer layers [120]. The prediction of the neutrino signal time is around a day from the shock breakout and the visible onset of the explosion [110]. For this scenario, IceCube constrained the contribution to the diffuse flux to less than 15% using a catalog of SESNe and a time window of 20 days prior to the first detection to ensure that the explosion time is included [108]. The non-detection of neutrinos can also be used to constrain the fraction of supernovae with a jet pointed towards Earth as a function of the energy deposited in cosmic rays [121, 122].

[119]: Mészáros et al. (2001), *TeV Neutrinos from Successful and Choked Gamma-Ray Bursts*

[112]: Woosley et al. (2006), *The Supernova Gamma-Ray Burst Connection*

[120]: Smartt (2009), *Progenitors of Core-Collapse Supernovae*

[110]: Senno et al. (2016), *Choked Jets and Low-Luminosity Gamma-Ray Bursts as Hidden Neutrino Sources*

[121]: Senno et al. (2018), *Constraining High-Energy Neutrino Emission from Choked Jets in Stripped-Envelope Supernovae*

[122]: Chang et al. (2024), *High-Energy Neutrinos from Choked-Jet Supernovae: Searches and Implications*

Despite the non-detections, the transient AT 2023uqf was recently found in coincidence with a high-energy neutrino alert that IceCube sent out, and later classified as a SN type Ibn with similarities to luminous FBOTs [123, 124]. Because it is both a SESN and shows CSM interaction, both neutrino production scenarios are possible. This association might indicate that at least a subpopulation of CCSNe does in fact produce high-energy neutrinos, even if their contribution to the diffuse flux is subdominant.

[123]: Reusch et al. (2023), *IceCube-231004A: One Candidate Counterpart from the Zwicky Transient Facility*

[124]: Stein et al. (2023), *IC231004A: Classification of AT2023uqf/ZTF23abidzvf as a Rapidly-Evolving Supernova with CSM Interaction*

3.4 Compact object mergers

Neutron star mergers

The merger of a neutron star with another neutrino star, or a stellar mass black hole produces a black hole in the final state, accreting the leftover debris. This can produce a signature over a wide range of EM wavelengths together with gravitational waves. The only case so far where both messengers were observed together was the observation of the binary neutron star merger GW170817 [53].

[53]: Abbott et al. (2017), *Multi-Messenger Observations of a Binary Neutron Star Merger*

Kilonovae

In the optical and near IR, the transient is called a *kilonova*. It fades faster in bluer bands (within days in the optical and within tens of days in the near IR) and is powered by the decay of heavy elements produced in the explosion [125]. AT 2017fgo, the optical counterpart to GW170817 is the first and only such transient ever observed, so kilonova lightcurve predictions heavily rely on this object. Because the emission is longer lived in the near IR, more telescopes are being built to survey the sky in this wavelength range for independent discoveries of more such transients, for example WINTER [126], PRIME*, and VISTA [127].

[125]: Cowperthwaite et al. (2017), *The Electromagnetic Counterpart of the Binary Neutron Star Merger LIGO/Virgo GW170817. II. UV, Optical, and Near-infrared Light Curves and Comparison to Kilonova Models*

Short GRBs

Mergers involving at least one neutron star had long been speculated to be the engines behind short GRBs with a duration of typically less than two seconds[4] [128]. Also in this case, GW170817 provided

4: Long GRBs are connected to supernovae as discussed in the previous section.

[128]: Eichler et al. (1989), *Nucleosynthesis, Neutrino Bursts and γ-Rays from Coalescing Neutron Stars*

* http://www-ir.ess.sci.osaka-u.ac.jp/prime/index.html

confirmation of this scenario with the first direct observational link. As already mentioned, GRBs in general were one of the promising sources of high-energy neutrinos, even before the distinction of long and short GRBs was established [113]. Searches for high-energy neutrinos are still often carried out for the combined sample of long and short GRBs. The contribution to the diffuse high-energy neutrino flux was constrained by IceCube to be less than around 1% at high energies [114], and also no excess was found at sub TeV energies [115]. The additional limits derived in this thesis on the luminosity function of a neutrino transient population mentioned above also apply for short GRBs (see Chapter 6).
IceCube together with ANTARES and Auger also looked for a high-energy neutrino signal from GW170817 within 500 seconds of the prompt GRB signal and within two weeks of the merger. The non-detection is consistent with an off-axis jet [129].

[115]: Abbasi et al. (2024), *Search for 10–1000 GeV Neutrinos from Gamma-Ray Bursts with IceCube*

[129]: Albert et al. (2017), *Search for High-energy Neutrinos from Binary Neutron Star Merger GW170817 with ANTARES, IceCube, and the Pierre Auger Observatory*

Binary black hole mergers

If the two merging objects are black holes, only gravitational waves are emitted but no other messengers. If, however, this merger does not take place in vacuum, accretion of gas or dust surrounding the merging black holes can launch a jet [130] or wind [131]. This could create EM signatures and possibly accelerate hadrons when interacting with the surrounding medium. A promising environment is the accretion disk of an AGN with the relatively high densities of both gas and stellar mass black holes. Several optical candidates were identified with ZTF, but the understanding of explosive phenomena in AGN disks is not developed enough to rule out other origins of these flares [132]. IceCube conducted a search for high-energy neutrinos from the binary black hole mergers detected by LIGO and Virgo up until their third observing run without detecting any signal [133]. The search is also continuing during the ongoing fourth observing run [134].

[130]: Zhou et al. (2023), *High-Energy Neutrino Emission Associated with GWs from Binary Black Hole Mergers in AGN Accretion Disks*

[131]: Ma et al. (2024), *High-Energy Neutrinos from Outflows Powered by the Kicked Remnants of Binary Black Hole Mergers in Active Galactic Nucleus Accretion Disks*

[132]: Graham et al. (2023), *A Light in the Dark: Searching for Electromagnetic Counterparts to Black Hole–Black Hole Mergers in LIGO/Virgo O3 with the Zwicky Transient Facility*

[133]: Abbasi et al. (2023), *IceCube Search for Neutrinos Coincident with Gravitational Wave Events from LIGO/Virgo Run O3*

[134]: Thwaites et al. (2023), *Searches for IceCube Neutrinos Coincident with Gravitational Wave Events*

3.5 Summary

This section reviewed the possible candidate transient high-energy neutrino source populations. Some important conclusions can be drawn from this compilation:

1. The detection of a blazar, a radio-quiet AGN, and at least TDE-like flares from SMBHs show that there are multiple populations contributing to the diffuse high-energy neutrino flux.
2. The constraint on blazars and GRBs suggests that gamma-rays are not necessarily a good tracer for high-energy neutrino emission. Although they can be observed in coincidence, like in the flare from TXS 0506+056, the sources might be more efficient neutrino emitters in periods when the gamma-rays are obscured [64].
3. The most promising sources are accreting SMBHs, although the characteristics that identify the efficiently emitting subpopulation are not yet clear.
4. Multiple giant flares from accreting SMBHs have been detected in neutrinos. Whether they form a common population,

[64]: Halzen et al. (2019), *On the Neutrino Flares from the Direction of TXS 0506+056*

however, is uncertain. If they do, it is the only transient population with more than one detected example, and is a promising source class, especially for the neutrinos above around 100 TeV.

As mentioned in the introduction of this chapter, this is not a comprehensive list of all potential neutrino source candidate populations but biased towards optically detectable transients. Nevertheless, it provides an overview of objects that can be expected when looking for counterparts to high-energy neutrinos with optical telescopes (see Chapter 6 and Chapter 7), and motivates closer investigation of giant AGN flares (see Chapter 9).

Neutrino Astronomy with the IceCube Neutrino Observatory

4

Because of their small cross-section, detection of neutrinos needs a large detection volume. This is especially true when trying to measure the small diffuse astrophysical neutrino flux which is. To estimate how large the detector has to be, an upper limit on the neutrino flux can be derived from cosmic ray observations [135]. Assuming all cosmic rays produce pions through proton-photon interaction before escaping their production site, the muon neutrino flux is constrained to $E_\mu^2 \Phi_\mu < 2 \times 10^{-8}\,\mathrm{GeV\,s^{-1}\,cm^{-2}\,sr^{-1}}$. To detect around 20 muons from muon neutrino interactions, a detector with an area of around $1\,\mathrm{km}^2$ is necessary. Additionally, that detector has to observe the full sky at all time, implying an instrumented volume of around $1\,\mathrm{km}^3$. IceCube is currently the only operating neutrino detector at this scale, detecting the astrophysical signal through Cherenkov radiation.

This chapter first introduces the detection principle in Section 4.1 and the IceCube detector in Section 4.2, before discussing reconstruction algorithms (Section 4.3) and a likelihood approach to searching for neutrino sources (Section 4.4).

[135]: Waxman et al. (1998), *High Energy Neutrinos from Astrophysical Sources: An Upper Bound*

4.1 Astrophysical Neutrino Detection in Cherenkov Detectors

The detection principle behind all neutrino detectors looking for the astrophysical diffuse signal is the measurement of Cherenkov radiation emitted by particles produced in the interaction of the neutrinos inside or close to the detector medium. For this, a large volume of a transparent medium is necessary, with an overburden of several thousand meters to shield off background radiation. The two naturally occurring options are deep glacial ice or deep sea water. This section first introduces the relevant neutrino interactions, the Cherenkov radiation, and the muon energy losses before discussing the nature of the background.

4.1.1 Neutrino Interaction

Neutrinos with energy above $E_\nu \approx 0.5\,\mathrm{TeV}$ passing through Earth interact primarily via deep inelastic scattering [136], where the interaction happens with a single quark in an atomic nucleus. The mediator particle can be a charged $W^\pm$-boson (charged current interaction) or a neutral Z^0-boson (neutral current interaction). In both cases, the final state consists of a lepton and a hadronic shower. In the neutral-current interaction, the lepton is the neutrino itself, and the corresponding charged lepton in the charged-current interaction.

Deep inelastic scattering

[136]: Formaggio et al. (2012), *From eV to EeV: Neutrino Cross Sections across Energy Scales*

An exception is electron antineutrinos interacting with electrons,

Glashow resonance

producing a W^--boson, called the *Glashow resonance*. This process has a greater cross-section than deep inelastic scattering at around the resonance energy of $s = 6.3\,\text{PeV}$ [136–138].

Secondaries

The final state particles lose their energy on very different length scales. The hadronic shower has a typical length of around 10 m. The electron immediately initiates an electromagnetic cascade with a comparable length [139]. The tau typically travels $\mathcal{O}(10^1\,\text{m})$ through the ice until it decays, initiating another hadronic shower [10]. The muon is the only charged particle that escapes the interaction site and travels $\mathcal{O}(10^3\,\text{m})$ through the ice. This feature makes the muon well suited for astronomy purposes, because it enables a good reconstruction of the neutrino arrival direction. This will be explained in more detail in Section 4.2.4.

[139]: Aartsen et al. (2014), *Energy Reconstruction Methods in the IceCube Neutrino Telescope*

[10]: Particle Data Group et al. (2022), *Review of Particle Physics*

Kinematic angle

If a muon neutrino undergoes a charged-current interaction, the direction of the resulting muon usually deviates from the direction of the incoming neutrino. The median of the deviation depends on the neutrino energy E_ν and can be approximated by [140]

$$\Psi = 0.7^\circ \left(\frac{E_\nu}{\text{TeV}}\right)^{-0.7}, \tag{4.1}$$

which is referred to as the *kinematic angle*.

[140]: Learned et al. (2000), *High-Energy Neutrino Astrophysics*

4.1.2 Cherenkov Radiation

The secondary particles are generally relativistic after the interaction of neutrinos in the relevant energy range of $E_\nu \gtrsim 1\,\text{TeV}$. If they are charged and their speed exceeds the speed of light in the medium $c \cdot n$, where n is the refractive index, they emit so-called Cherenkov radiation. The polarizable molecules of the medium get excited and emit electromagnetic waves upon de-excitation with coherent superposition at an angle that depends on the velocity, equivalent to the sonic boom of a fast-moving vehicle. The corresponding angle is called the Cherenkov angle [141, Chapter 13]:

$$\cos(\theta_\text{C}) = (n \cdot \beta)^{-1}. \tag{4.2}$$

For example, for ice with $n \approx 1.33$ [142], the angle is $\theta_\text{C} \approx 41^\circ$, and the spectrum peaks in the visible and near-UV. Integration from 300 to 600 nm gives a total number of around 3×10^4 photons emitted per meter by a relativistic ($\beta \approx 1$) charged particle [143].

[141]: Jackson (2011), *Klassische Elektrodynamik*

[142]: Warren (1984), *Optical Constants of Ice from the Ultraviolet to the Microwave*

[143]: van Santen (2014), *Neutrino Interactions in IceCube above 1 TeV: Constraints on Atmospheric Charmed-Meson Production and Investigation of the Astrophysical Neutrino Flux with 2 Years of IceCube Data Taken 2010–2012*

4.1.3 Muon Energy Losses

As mentioned above, muons produced in muon neutrino charge-current interactions are well suited for astronomy purposes, so understanding their energy loss as they travel through the ice is important. Although Cherenkov radiation is the mechanism to detect these charged particles, the energy loss through this process is negligible compared with the four main processes: ionization, electron pair production, bremsstrahlung, and photo-nuclear interactions. Ionization happens smoothly along the track, meaning that

the muon is continuously losing the same amount of energy. The other, radiative processes happen stochastically and dominate over ionization above around 1 TeV [10], initiating particle cascades that also emit Cherenkov radiation and contribute to the overall light yield of the muon. This means that energy depositions by the muon can happen in irregular intervals with irregular amounts of energy. The average loss can still be parameterized linearly [144]:

[144]: Barrett et al. (1952), *Interpretation of Cosmic-Ray Measurements Far Underground*

$$-\frac{\mathrm{d}E}{\mathrm{d}x} = a + b \cdot E, \tag{4.3}$$

where a describes the ionization loss and b the linear scaling factor for the stochastic losses. Although these two parameters depend in general on the muon energy, a good approximation for energies of 20 to 10^{11} GeV is $a = 0.246\,\mathrm{GeV\,m^{-1}}$ and $b = 4.31 \times 10^{-3}\,\mathrm{m^{-1}}$ [145].

[145]: Chirkin et al. (2004), *Propagating Leptons through Matter with Muon Monte Carlo (MMC)*

4.1.4 Atmospheric Background

As discussed in Chapter 2, the search for the astrophysical neutrino signal is typically a search for the needle in the haystack. The reason is the overwhelming background produced in the Earth's atmosphere, which has several components.

Atmospheric muons

For any Cherenkov detector looking for high-energy astrophysical neutrinos, the dominant background is muons, produced in cosmic ray air showers in the Earth's atmosphere (see Chapter 2). Their energy is high enough to penetrate kilometers underground, while other shower particles can only reach the surface. However, for much larger distances the Earth provides an effective shield, which is why they are observed as downgoing events for a detector with a large overburden. Their rate gradually declines going from vertical to higher inclinations. Because their spectrum is softer than the astrophysical neutrino flux, they can be excluded by only selecting events of high energy, where the exact threshold depends on the inclination angle and ranges from around 10 to 100 TeV [146].

[146]: Aartsen et al. (2017), *All-Sky Search for Time-integrated Neutrino Emission from Astrophysical Sources with 7 Yr of IceCube Data*

Muon bundles

Still, muons can be produced with high multiplicity in air showers, and travel in parallel with only slight offsets in so-called muon bundles. A kilometer scale detector with sparse instrumentation on the order of tens of meters cannot resolve the individual muons, so the combined light yield looks like one highly energetic muon. The difference is that one high energy muon is expected to deposit energy stochastically while the low energy muons will lose energy smoothly along their path (see the previous section), which can be used to differentiate the two cases.

Atmospheric Neutrinos

Cosmic ray air showers also produce neutrinos that can interact in the ice and produce the same event pattern as astrophysical neutrinos. In contrast to the atmospheric muons, they can travel through the Earth and are thus an isotropic background. Their rate is much higher than the astrophysical one, at least below the highest energies (see Chapter 2). The individual events themselves are indistinguishable from astrophysical ones, but can be accompanied by coincident muons from the same air shower which can serve as a veto.

An efficient event selection rejects the atmospheric background as good as possible while maintaining as much of the astrophysical

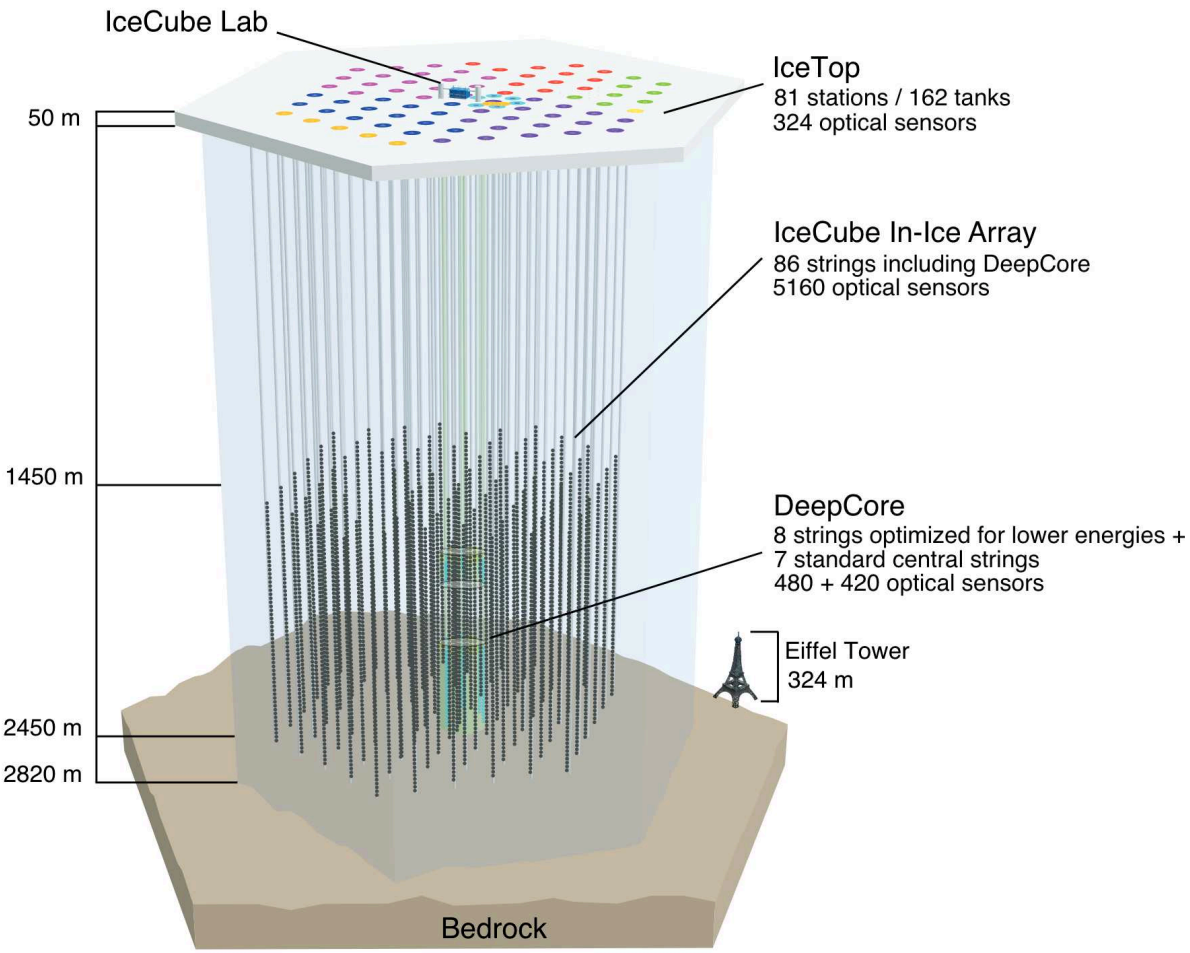

Figure 4.1: Overview of the IceCube components, the in-ice array, the DeepCore subarray, the IceTop stations, and the IceCube Lab building. The gray lines show the strings and black dots represent DOMs. The Eiffel Tower is shown for scale reference. Taken from Aartsen et al. [147].

signal as possible, weighing purity against efficiency. Examples are introduced in Section 4.2.5.

4.2 The IceCube Detector

IceCube was built to detect the interaction of astrophysical neutrinos in the TeV to PeV range through the detection of Cherenkov light emitted by charged secondary particles as described in the previous section. 1 km^3 of instrumented glacial ice at the South Pole constitutes the main part of the detector. An overview of all components is given in Figure 4.1. The detection unit is the *Digital Optical Module* (DOM). The main in-ice array is made up of 5160 DOMs, deployed on 86 strings between 1450 to 2450 m. The strings are arranged in a hexagonal pattern, have a distance of 125 m, and consist of 60 DOMs each, where the vertical spacing between them is 17 m. A hot water drill was used to melt the 86 holes into the ice to the required depth, and the instrumentation was lowered into the water-filled boreholes and re-frozen in place [147].

Main in-ice array

[147]: Aartsen et al. (2017), *The IceCube Neutrino Observatory: Instrumentation and Online Systems*

Eight strings in the center of the hexagon at depths from 2100 to 2450 m form a denser infill array called *DeepCore* [148]. Because the

DeepCore

[148]: Abbasi et al. (2012), *The Design and Performance of IceCube DeepCore*

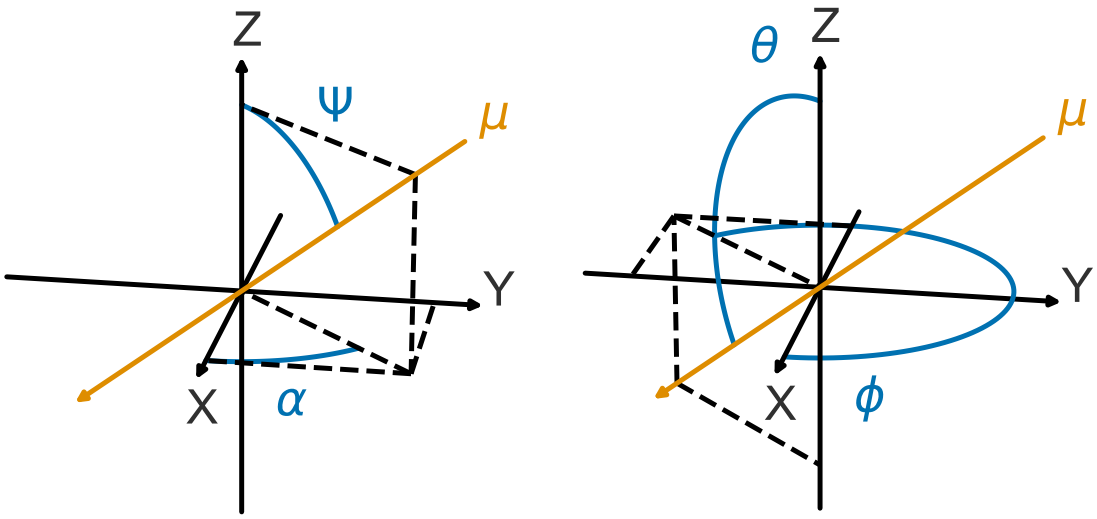

(a) Zenith Ψ and Azimuth α

(b) Spherical coordinates θ and Φ

Figure 4.2: The IceCube coordinate system with its origin at the geometrical center of the in-ice array at a depth of around 1950 m. The two versions show two different sets of angle coordinates used for direction measurements. The orange arrow indicates the direction of an exmaple muon track.

DOMs are closer together, the energy threshold is only about 10 GeV in this area.

IceTop

IceTop is a cosmic ray air shower detector array at the surface of the glacial ice at an altitude of about 2835 m above sea level. It consists of 162 ice-filled tanks, that each contain two DOMs [149]. The Cherenkov light produced by the shower particles is a measure of the deposited energy and can be used to reconstruct the primary cosmic ray with an energy threshold of PeV to EeV [150]. It can also serve as a veto for down-going neutrino events [147].

[149]: Abbasi et al. (2013), *IceTop: The Surface Component of IceCube*

[150]: IceCube Collaboration et al. (2013), *Measurement of the Cosmic Ray Energy Spectrum with IceTop-73*

IceCube Lab

In the *IceCube Lab* (ICL), the surface cables connecting to all DOMs of the observatory end in the corresponding computers for read-out and controlling.

Coordinate System

Any low-level geometrical measurements in IceCube are described in a detector-native coordinate system, with the origin at the geometrical center of the in-ice array at a depth of around 1950 m (see Figure 4.2). The y-axis is aligned along the Prime Meridian, pointing towards Greenwich, UK, the x-axis points 90° clockwise from the y-axis, and the z-axis is pointing upwards, normal to the surface. The zenith angle Ψ refers to the angle formed between the particle direction and the z-axis. The azimuth α is defined as the projection within the xy-plane, measured counterclockwise from the positive x direction, with the positive y direction corresponding to an azimuth of 90° (see Figure 4.2a). The angles Φ and Θ are also sometimes used, describing the outgoing instead of the incident direction, such that

$$\begin{aligned} \Psi &= \pi - \theta \\ \alpha &= (\pi + \phi) \mod 2\pi, \end{aligned} \tag{4.4}$$

as shown in Figure 4.2b.

4.2.1 The Digital Optical Module

[151]: Abbasi et al. (2010), *Calibration and Characterization of the IceCube Photomultiplier Tube*

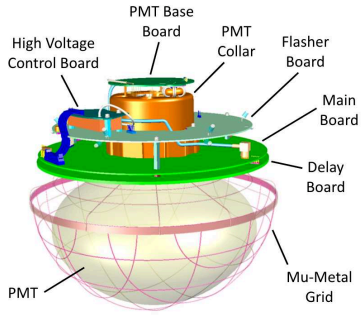

Figure 4.3: A schematic view of the IceCube DOM. Taken from Aartsen et al. [147].

[139]: Aartsen et al. (2014), *Energy Reconstruction Methods in the IceCube Neutrino Telescope*

The *Digital Optical Module* (DOM), the detection unit of IceCube, consists of a 10 inch Photo-Multiplier Tube (PMT) [151] for detection of Cherenkov light and circuit boards for readout and calibration. They are surrounded by a spherical glass pressure vessel. The components inside the glass sphere are illustrated in Figure 4.3. The PMT faces downward and is surrounded by a mu-metal cage for shielding of the ambient magnetic field. It is secured in a silicon gel for mechanical support and optical coupling [147]. The main electronics board around the PMT neck is responsible for data acquisition, control, calibration, communication, and low-voltage power conversion. A so-called Flasher Board controls LEDs for calibration purposes. The other circuit boards generate PMT voltage supply and delay PMT signals [152].

The PMTs are operated at a gain of 10^7. If a photon produces a photoelectron (PE) at the cathode via the photoelectric effect, it is accelerated towards the anode via ten dynodes, producing an electron avalanche that results in a measurable current. Integration leads to the total collected *charge*, which is the elementary quantity for energy estimation in IceCube and is measured in units of PE, defined as around 1.6 pC, the most likely deposition by a single PE [139]. The exact value is calibrated in-situ and per DOM, using the flasher LEDs as primary references [147].

Three wire pairs are connected to the DOM. One is responsible for power supply and communication with the data acquisition (DAQ) computers in the ICL, the other two connect to the nearest and next-to-nearest DOMs up and down along the string. They carry digital pulses for the detection of a local coincidence as explained in the following section.

4.2.2 Data Acquisition

Waveform Capture

The basic function of the DOMs is to generate so-called hits, containing a timestamp and the waveform of charge per time. The basic signal flow is illustrated in Figure 4.4. The waveform capture and digitization are launched when the collected charge exceeds the threshold of 0.25 PEs. There are two types of circuits for the digitization. The Analog Transient Waveform Digitizer (ATWD) has a sampling speed of around 3 ns and records the waveform for 427 ns, capturing light produced within $\mathcal{O}(10)$m of the DOM. The signal is routed through the Delay Board to achieve a delay of 75 ns, so that the waveform can be recorded starting before the charge threshold crossing. Three separate amplifiers providing factors of 16, 2, and 0.25 capture the dynamic range of the PMT output and ensure that no waveform features are lost due to saturation. Signals from distant depositions arrive over a longer time period due to scattering in the ice, so the fast Analog to Digital Converter (fADC), records the waveform for 6.4 µs with a coarser sampling of around 25 ns [147]. The launch of the waveform capture is immediately signaled to the nearest and next-to-nearest DOMs along the same string (two DOMs up and two DOMs down). A hard local coincidence (HLC) is defined by a coincident hit in a neighboring DOM within ±1 µs. In that case,

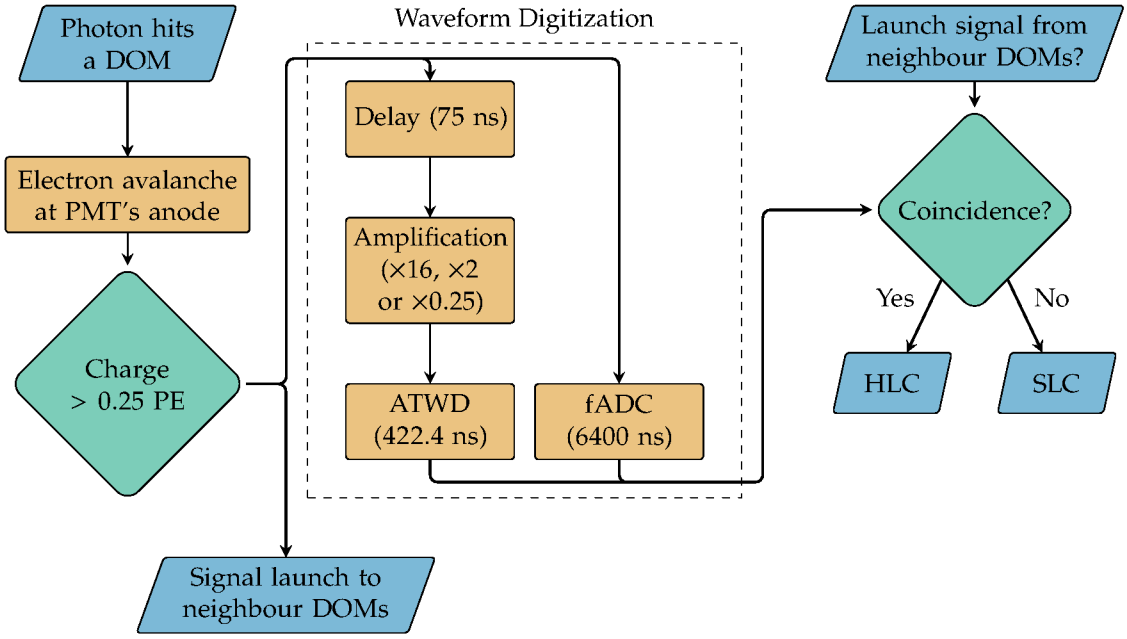

Figure 4.4: Signal flow of the DOM data aquisition as explained in Section 4.2.2. Green squares a decisions, blue parallelograms are in- and outputs, and orange rectangles are processing steps. Simplified and adapted from Abbasi et al. [152] and Bradascio [153].

the full ATWD and fADC waveforms are sent to the DAQ computers at the ICL. If there is no coincident hit (soft local coincidence, SLC), only a compressed version of the fADC waveform is sent [147].

The DAQ system is constantly looking for a coincidence of HLC hits in space and time [147]. Once these trigger criteria are met, the corresponding HLC and SLC are read out, combined with the trigger information and saved as an event. The relevant trigger for this work is the Single Multiplicity Trigger, which looks for a certain number of HLC hits within a specified time window. For the in-ice array DOMs, eight hits are required within 5 µs, which results in a trigger rate of around 2.8 kHz [146], amounting to a data rate of around 1 TB per day. In addition, the PMT hit rate is recorded in 1.6384 ms intervals. A collective increase of that rate throughout the detector can indicate an MeV neutrino burst from a galactic supernova [154]

4.2.3 The Antarctic Ice

An important part of the IceCube detector and yet the least understood is the antarctic ice itself. It is the medium in which the neutrinos interact, but most importantly, also the medium the Cherenkov photons propagate through. During propagation, photons are subject to scattering and absorption, which has to be taken into account when reconstructing particles. The strength of scattering and absorption can be described by the average distance a photon travels between successive scatters and before being absorbed, respectively [155]. In the deep glacial ice below around 1350 m, embedded dust grains are responsible for most of the scattering, while also contributing to the absorption along with embedded soot [155, 156]. These particles are deposited on the surface and slowly covered in snow, forming new ice over time, such that the dust is layered in the deep ice. Layers

Event trigger

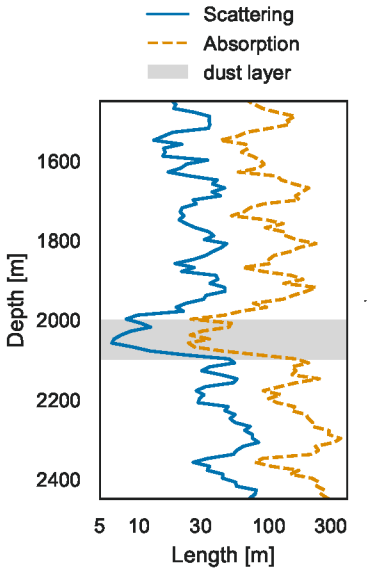

Figure 4.5: Depth dependent absorption and scattering lengths of the antarctic ice for light at 400 nm at the depths of the main in-ice array as used in SPICE 3.2.1. The gray-shaded area is the dust layer, where the strongest absorption and scattering happens.

[155]: Ackermann et al. (2006), *Optical Properties of Deep Glacial Ice at the South Pole*
[156]: Price et al. (1997), *Optical Properties of Deep Ice at the South Pole: Scattering*

with more particles thus correspond to periods of high dust and soot concentration at the surface. A major layer between 2000 to 2100 m was deposited around 65,000 years ago during a cold period and usually referred to as the *dust layer* (see Figure 4.5). In the boreholes used for the string deployment, a central column of air bubbles formed during the re-freezing. These bubbles significantly scatter photons, and consequently this so-called hole-ice has to be treated separately when modeling the ice [157].

Dust layer

[157]: Collaboration et al. (2022), *A Calibration Study of Local Ice and Optical Sensor Properties in IceCube*

The model describing the ice properties is called the *South Pole Ice* (SPICE) model, and is calibrated in-situ using data obtained with the DOM LED flashers [158]. It describes the photon scattering off the dust particles with the Mie theory [159]. The dust layers are not perfectly horizontal but follow the structure of the underlying bedrock to some extent. The relevant model version for this work, SPICE 3.2.1, takes this into account using a one-dimensional parameterization of the ice tilt along the tilt axis. Additionally, the scattering was observed to be anisotropic with respect to the flow axis of the ice, which is phenomenologically incorporated. Only the latest iteration of the model includes a full description of this effect due to birefringence caused by the polycrystalline ice microstructure [160]. The absorption and scattering profile of SPICE 3.2.1 is shown in Figure 4.5, where the prominent dust layer at 2000 to 2100 m is clearly visible.

SPICE model

[158]: Aartsen et al. (2013), *Measurement of South Pole Ice Transparency with the IceCube LED Calibration System*

[159]: Mie (1908), *Beiträge Zur Optik Trüber Medien, Speziell Kolloidaler Metallösungen*

[160]: Abbasi et al. (2024), *In Situ Estimation of Ice Crystal Properties at the South Pole Using LED Calibration Data from the IceCube Neutrino Observatory*

During the deployment of the in-ice array, the stratigraphy of eight boreholes was measured using so-called dust-loggers [161], devices that measure the fraction of re-scattered photons emitted by a 404 nm laser to reconstruct the dust content in the ice with a resolution of about one meter. This data was used to derive the tilt map and serves as a reference for the SPICE scattering profile [155].

Dust logger

[161]: Collaboration (2013), *South Pole Glacial Climate Reconstruction from Multi-Borehole Laser Particulate Stratigraphy*

4.2.4 Event Morphologies

The neutrino interactions described in Section 4.1 can produce three principal shapes in the detector.

Track

If a muon neutrino undergoes charged-current interaction, producing a muon, the muon travels kilometer distances through the ice. Due to the emitted Cherenkov radiation, they leave elongated light patterns in the detector, called a *track* (Figure 4.6, left). Because of the long lever arm, directional reconstruction is typically possible to sub-degree scale[1] [see for example 48, 146], which makes them well suited for the search for sources of astrophysical neutrinos. Of course, any muon traversing the detector will produce a track event, so also atmospheric muons produced in cosmic ray air showers. It is up to an effective event selection to distinguish these components as explained in the next section. However, the atmospheric muons can be used to verify the muon track reconstruction: The "shadow" the moon casts in the cosmic ray flux can be reconstructed within of around 0.2° [162]. Because the atmospheric component is of lower energy, this result only relates to muons from 1 to 10 TeV, but no other equivalent calibration source exists at higher energies. It is also only valid for an ensemble of events instead of single tracks.

1: This is still well above the limiting kinematic angle given by Equation 4.1.

[48]: IceCube Collaboration et al. (2022), *Evidence for Neutrino Emission from the Nearby Active Galaxy NGC 1068*

[146]: Aartsen et al. (2017), *All-Sky Search for Time-integrated Neutrino Emission from Astrophysical Sources with 7 Yr of IceCube Data*

[162]: IceCube Collaboration et al. (2014), *Observation of the Cosmic-Ray Shadow of the Moon with IceCube*

Cascade

A charged-current interaction of electron or tau neutrinos or a

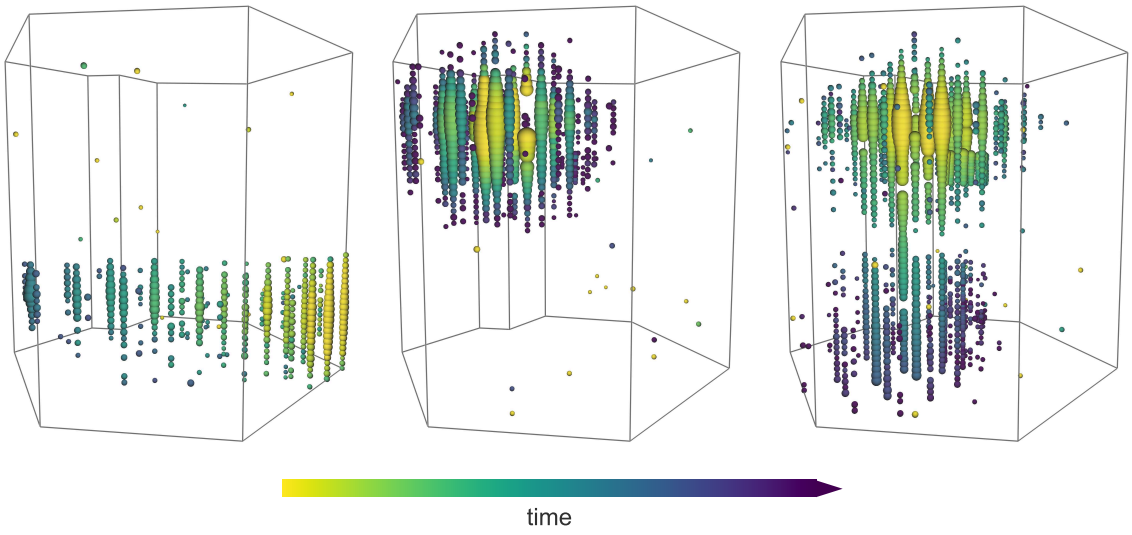

Figure 4.6: Examples of the three basic event morphologies. In these IceCube event views, each sphere represents light detection by a DOM, where the size represents the amount of charge, and the color encodes the arrival time. The gray lines are the outlines of the in-ice array. Left: The elongated light pattern of a muon track. Center: The point like deposition of a particle shower is observed as a cascade. Right: Two point like depositions connected by a track by a ν_τ charged current interaction and the subsequent τ decay produces a double-bang event.

neutral-current interaction of any neutrino produces a shower inside the detector. As mentioned in Section 4.1.1, these showers - hadronic or electromagnetic - reach a length of around 10 m in the ice. The DOM spacing in the main in-ice array is too coarse to resolve this, so they can be treated as an isotropically emitting point source within the detector, called *cascades* (see Figure 4.6, center) [139]. This means that they are spatially much more confined, well suited for reconstructing the deposited energy with around 10% resolution, but the reconstruction of the neutrino arrival direction is only possible within 10 to 15° [49].

[139]: Aartsen et al. (2014), *Energy Reconstruction Methods in the IceCube Neutrino Telescope*

[49]: IceCube Collaboration et al. (2023), *Observation of High-Energy Neutrinos from the Galactic Plane*

Double bang

In a ν_τ charged-current interaction, a tauon is produced next to a hadronic cascade. Dependent on the energy, the tauon travels several to tens of meters through the ice before decaying, producing another cascade. This leads to a characteristic signature of two cascades connected by the tauon track, called a double-bang event (Figure 4.6, right). However, the separation of the two cascades is still small compared to the horizontal string spacing in the main in-ice array, which makes the detection possible above around 60 TeV, albeit still challenging [46].

[46]: Abbasi et al. (2022), *Detection of Astrophysical Tau Neutrino Candidates in IceCube*

4.2.5 Event Selections

Online filter

After the DAQ system records events as described in Section 4.2.2, they are further processed at the South Pole. First, the digitized waveforms are calibrated and deconvolved [139] using constants obtained during the DOM's self-calibration. The extracted charge and photon arrival times are used to run basic, fast reconstructions (some muon track-specific ones are discussed in Section 4.3.1). Based on the results, the events are filtered to extract candidates for further, more advanced event selections. There are several filters tailored to different analyses, but the relevant one for this work is the muon

[139]: Aartsen et al. (2014), *Energy Reconstruction Methods in the IceCube Neutrino Telescope*

filter, which rejects events that are unlikely muon track events and ends up with an event rate of around 40 Hz [163]. In total, the event rate after filtering is around 300 Hz, so the corresponding data rate of around 100 GB per day is small enough to be transmitted via satellite to the data center in the Northern Hemisphere for further processing [147].

[163]: Kintscher (2020), *Rapid Response to Extraordinary Events: Transient Neutrino Sources with the IceCube Experiment*

Point Source Tracks

Two event selections are relevant for this work. The first one is the *Point Source Tracks* sample, composed of muon track events likely due to neutrino interactions [146, 164, 165]. After passing the muon filter, another, more sophisticated selection for muon track events is applied, reducing the event rate to a few Hertz. This makes it possible to run the *SplineMPE* directional and *MuEX* energy reconstruction on the events, explained in the next section. Some pre-cuts are applied on derived quantities, like the track length, number of hit DOMs, and length along the track without any hit. These cuts were developed separately for the Northern and Southern Hemisphere to accommodate the different contribution from the atmospheric muon background (see Section 4.1.4). Finally, a Boosted Decision Tree (BDT) [166, 167], trained on simulated data, performs a multivariate selection in an 11 dimensional parameter space. After this, the sample is dominated by atmospheric neutrinos, and it is up to statistical analysis to find the astrophysical component [168]. The Version 4.0 of this dataset is used in this work, which includes data up until the 2019 season (the latest data event is on May 29th, 2020).

[146]: Aartsen et al. (2017), *All-Sky Search for Time-integrated Neutrino Emission from Astrophysical Sources with 7 Yr of IceCube Data*
[164]: Aartsen et al. (2019), *Search for Steady Point-like Sources in the Astrophysical Muon Neutrino Flux with 8 Years of IceCube Data*
[165]: Aartsen et al. (2020), *Time-Integrated Neutrino Source Searches with 10 Years of IceCube Data*

[166]: Hastie et al. (2009), *Boosting and Additive Trees*
[167]: Keerthi et al. (2001), *Improvements to Platt's SMO Algorithm for SVM Classifier Design*

[168]: Carver (2019), *Time Integrated Searches for Astrophysical Neutrino Sources Using the IceCube Detector and Gender in Physics Studies for the Genera Project*

Also relevant is the track selection used for the IceCube realtime system, introduced in Chapter 5. It is based on three separate selections that all have the common goal to suppress the atmospheric neutrino background in addition to the atmospheric muons. An additional filter is applied for use in real-time, which is introduced in Chapter 5.

HESE

The *High-Energy Starting Events* (HESE) selection [169, 170] reduces the atmospheric background by choosing charge-current muon neutrino events, where the interaction vertex is contained inside the detector volume. Other parts of the detector can then be used as a veto region. Atmospheric muons will only be detected as through-going tracks and atmospheric neutrinos will be accompanied by muons from the same air shower.

[169]: Aartsen et al. (2014), *Observation of High-Energy Astrophysical Neutrinos in Three Years of IceCube Data*
[170]: IceCube Collaboration et al. (2021), *IceCube High-Energy Starting Event Sample: Description and Flux Characterization with 7.5 Years of Data*

EHE

Because the astrophysical component of the neutrino flux has a harder spectrum, it dominates at higher energies. The *Extremely High Energy* (EHE) selection [171] makes use of this by selecting events with very high charge depositions based on a zenith-dependent threshold, effectively reducing the background event expectation to about 0.01 per year .

[171]: IceCube Collaboration et al. (2016), *Constraints on Ultrahigh-Energy Cosmic-Ray Sources from a Search for Neutrinos above 10 PeV with IceCube*

GFU

The *Gamma-ray Follow-Up* (GFU) selection uses BDTs to select through-going muon tracks from the whole sky with an energy of $\mathcal{O}(10^2\,\text{TeV})$ [163].

[163]: Kintscher (2020), *Rapid Response to Extraordinary Events: Transient Neutrino Sources with the IceCube Experiment*

4.3 Reconstruction of Muon Track Events

4.3.1 Directional Reconstruction

The reconstruction of the arrival direction in IceCube relies on the nanosecond timing information of pulses recorded by the DOMs [147]. There exist several algorithms in a wide complexity range with a tradeoff between fast but crude and slow but precise. Typically, slow algorithms are seeded with the result of a faster one to successively improve the reconstruction. In the following, the ones relevant to this work will be discussed ordered by increasing complexity.

[147]: Aartsen et al. (2017), *The IceCube Neutrino Observatory: Instrumentation and Online Systems*

LineFit: The Plane Wave approximation

The simplest approximation is projecting the position of the DOMs onto the muon track [172]. If the DOM i at the position $\boldsymbol{r}_\mathrm{i}$ is hit with the first photon at the time t_i, the track can be parameterized by a line

$$\boldsymbol{r}_\mathrm{i} = \boldsymbol{r} + \boldsymbol{v} \cdot t_\mathrm{i}. \tag{4.5}$$

$\boldsymbol{r}$ and $\boldsymbol{v}$ are free parameters representing the vertex and the direction, respectively[2]. The solution can be found analytically:

$$\boldsymbol{r} = \langle \boldsymbol{r}_\mathrm{i} \rangle - \boldsymbol{v} \cdot \langle t_\mathrm{i} \rangle \qquad \boldsymbol{v} = \frac{\langle \boldsymbol{r}_\mathrm{i} \cdot t_\mathrm{i} \rangle - \langle \boldsymbol{r}_\mathrm{i} \rangle \cdot \langle t_\mathrm{i} \rangle}{\langle t_\mathrm{i}^2 \rangle - \langle t_\mathrm{i} \rangle^2}. \tag{4.6}$$

Here, $\langle x_\mathrm{i} \rangle$ denotes the mean of all x. This simplification is ignoring the geometry of the Cherenkov cone, the optical properties of the medium, and all but the first photon per DOM. It can therefore only give a rough approximation of the true muon direction. Consequently, the resolution of this reconstruction is only about 5° for a muon energy of $E_\mu = 10\,\mathrm{TeV}$ [173]. Nevertheless, the analytical solution is extremely fast to compute and serves as a good starting point for more sophisticated reconstructions.

[172]: Stenger (1990), *Track Fitting For Dumand-II Octagon Array (Technical Report)*

2: The norm of $\boldsymbol{v}$ also represents the velocity of the muon in the plane wave approximation. In practice, only the direction $\boldsymbol{v}/|\boldsymbol{v}|$ is used

[173]: Schatto (2014), *Stacked Searches for High-Energy Neutrinos from Blazars with IceCube*

The maximum likelihood method

More elaborate reconstructions are not solvable analytically anymore but try to find the track parameters that match the data best. Given a set of N independent measurements $\boldsymbol{x}$, the maximum likelihood (ML) estimation provides a method to determine model parameters $\boldsymbol{\theta}$ that optimally describe the data. The probability of a single measurement x_i is given by a probability density function (PDF), assuming a parameter set $\boldsymbol{\theta}$. The so-called *likelihood function* $\mathcal{L}$ gives the combined probability as a product over all PDFs:

$$\mathcal{L}(\boldsymbol{x}|\boldsymbol{\theta}) = \prod_i^N p(x_i|\boldsymbol{\theta}). \tag{4.7}$$

A specific problem is then encoded in the PDFs. If the number of observations N itself is the result of a counting experiment, an additional poisson term has to be included. The corresponding likelihood is called *extended likelihood function* [174]:

[174]: Barlow (1990), *Extended Maximum Likelihood*

$$\mathcal{L}(\boldsymbol{x}|\boldsymbol{\theta}) = \frac{e^{-\lambda}\lambda^N}{N!}\prod_i^N p(x_i|\boldsymbol{\theta}). \tag{4.8}$$

The ML estimation is used in the following for more refined track direction and energy reconstructions, as well as for neutrino point source searches in Section 4.4.

SplineMPE: The infinite Muon approximation

To improve upon the results of *Linefit*, more details of the photon emission, propagation and detection have to be taken into account. A likelihood function can be defined with the problem encoded in the PDFs. The free parameters $\boldsymbol{\theta}$ are again the track vertex $\boldsymbol{r}$ and direction $\boldsymbol{p}$. The PDFs should then give the probability of the photon arriving at the measured time given a set of parameters. It is convenient to formulate this in terms of the *time residual*: the arrival time t_{hit} relative to the time t_{geo} a photon would need to travel from the track in a straight line to the DOM:

$$t_{\text{res}} \equiv t_{\text{hit}} - t_{\text{geo}}. \tag{4.9}$$

It is enough to consider the arrival time of the first photon[3]. Accounting for the fact that all other photons arrived after the first, the Multi-Photoelectron (MPE) likelihood is:

$$\mathcal{L}_{\text{MPE}} = \prod_i^{N_{\text{DOM}}} n_i \cdot p(t_{\text{res,i}}|\boldsymbol{\theta}) \cdot [1 - P(t_{\text{res,i}}|\boldsymbol{\theta})]^{n_i - 1}, \tag{4.10}$$

where $p(t_{\text{res,i}}|\boldsymbol{\theta})$ is the PDF giving the probability that DOM i is hit at the time $t_{\text{res,i}}$. $P(t_{\text{res,i}}|\boldsymbol{\theta})$ is the cumulative distribution function (CDF) of $p(t_{\text{res,i}}|\boldsymbol{\theta})$, N_{DOMS} is the number of DOMs that recorded at least one PE, and n_{i} the number of PEs detected by DOM i. Equation 4.10 is not solvable analytically. Instead, the numerical maximization of the likelihood yields the best fit track $\hat{\boldsymbol{\theta}}$. The problem is now reduced to finding PDFs that describe the emission and propagation of the photons.

SplineMPE [173] uses Monte-Carlo (MC) simulations to build these PDFs. Muons traversing the detector and their corresponding energy losses are simulated. The resulting photons are propagated through the ice until they are recorded at a DOM. The tabulated results could be used as the PDFs. However, instead of accessing the tables directly, using stored interpolations with B-splines is computationally much cheaper [176]. This yields high performance, and a much improved result compared to *Linefit*. The biggest improvement is at the highest energies, where the angular resolution is around 0.4°. Even at 10 TeV, the resolution is still below 1°.

Although *SplineMPE* provides good results for through-going, smooth muon tracks, it does not necessarily do so for events with large stochastic energy losses or starting tracks. Because the simulations are explicitly built on a smooth muon track, photons from stochastic losses or the starting cascade are not accounted for and can result in reconstructions far worse than the resolution quoted above.

3: Although taking into account the arrival times of all PEs should theoretically give the best result, it turns out that this is not the case. The reason is not entirly clear. Presumably, late photons scattered so many times that they do not carry much information about the event but are rather sensitive to impurities in the ice [175].

[173]: Schatto (2014), *Stacked Searches for High-Energy Neutrinos from Blazars with IceCube*

[176]: Whitehorn et al. (2013), *Penalized Splines for Smooth Representation of High-Dimensional Monte Carlo Datasets*

B-Splines

Splines are piecewise defined polynomials typically used for interpolation. Here, B-splines describe a basis of splines, formed through iterative self-convolution.

The minimization can also get stuck in a local minimum (see Section 8.2.2 for an example). This is already included in the average resolution quoted above, which is derived from a large sample of events. *SplineMPE* is thus often used as the final directional reconstruction for large muon track event samples (for example as used in Section 8.3). However, to get reliable reconstructions for a single event, additional steps have to ensure the convergence into a global minimum, for example, with a sky scan [177].

Millipede: The sky scan method

To correctly take into account stochastic energy losses, or the starting cascade of a muon track, it is necessary to look at individual segments along the track. *Millipede* formulates a likelihood that takes into account the contribution from each light deposition for every DOM, modeling the losses as individual cascades along the track [139]. Although this was originally developed as an energy reconstruction (see the next section), the resulting likelihood value also depends on the seed track hypothesis. Changing the seed direction across a grid[4] and maximizing the likelihood every time, the highest likelihood value found gives the best fit direction. Iteratively increasing the grid resolution around the previous best fit can successively increase the precision.
Because in each iteration the complex *Millipede* likelihood has to be maximized, this can take thousands of CPU hours. It is therefore not possible to reconstruct the direction of a large event sample with *Millipede*. It is typically only used for promising individual events in the real-time program (see Chapter 5).
This sky scan can, in principle, be used with any algorithm that evaluates a likelihood. Notably, it was implemented and tested for *SplineMPE* [177].

4: Defining pixels with equal area on a spehere is not trivial an in practice done using *HEALPix* [178]

4.3.2 Angular Uncertainty Estimation

Besides the reconstruction of the best fit arrival direction, the estimation of its uncertainty plays a crucial role in finding the sources of astrophysical neutrinos. It indicates the maximum distance at which a neutrino can be linked to a potential source.

Several algorithms exist, but the relevant for this work is the *Paraboloid* method [179]. If the best-fit arrival direction was obtained by a maximum-likelihood fit, like for example, in *SplineMPE*, the likelihood space around the best-fit position holds the appropriate information. The faster the likelihood falls when deviating from the best-fit, the better the problem is constrained. *Paraboloid* scans the likelihood in azimuth and zenith while treating the vertex coordinates as nuisance parameters. In the ideal gaussian case, the likelihood follows a paraboloid around the maximum. The parameters of this paraboloid are determined with a least squares fit and describe an ellipse in the parameter space with the axis σ_1 and σ_2. It is convention to use the circularized error instead, defined as

$$\sigma = \sqrt{\frac{\sigma_1 + \sigma_2}{2}}. \tag{4.11}$$

Paraboloid

[179]: Neunhoffer (2006), *Estimating the Angular Resolution of Tracks in Neutrino Telescopes Based on a Likelihood Analysis*

Pull correction

This gives a good uncertainty estimate for the muon direction reconstruction. For astrophysical analysis, however, what matters is the direction of the incident neutrino rather than the outgoing muon. These can differ, and the median is given by the kinematic angle, which depends on the neutrino energy (see Equation 4.1). If the neutrino energy was known, calculating the kinematic angle and convolving it with σ would give the uncertainty on the neutrino arrival direction. Because this is not the case, the so-called pull σ/Ψ between the directional muon uncertainty and the difference Ψ between reconstructed direction and true neutrino direction is determined using simulations. This can be used as an energy-dependent correction to the *Paraboloid* error. Because of the simplicity, this method is used for large neutrino datasets like the Point Source Tracks introduced in Section 4.2.5.

Robustly determining the uncertainty region in the form of detailed likelihood contours is also possible with a likelihood scan. Because this takes considerable more computational resources, it is only possible for individual events. It is used in the IceCube real-time system and in detail introduced in Chapter 5.

4.3.3 Energy Estimation

While the fact that muons of TeV energies can traverse long distances in the ice plays in favor of the directional reconstruction, it is a major downside for the estimation of its energy. Because the length of a track far exceeds the dimensions of the detector, most of the muon's energy will be deposited outside the instrumented volume[5]. Fortunately, the differential energy loss scales linearly with the total energy (see Equation 4.3 in Section 4.1.3) and can therefore be used as a proxy. Because the number of observed PEs is expected to increase linearly with the energy losses, scaling a reference quantity is the basis for the algorithms below. Like in the previous section, the following are the relevant techniques for this work, ordered by their complexity.

5: Muons at lower energies ($E \lesssim 100\,\mathrm{GeV}$) can be fully contained in the detector and a calorimetric measurement is possible. [139]

MuEX: Scaling a Muon Template

The simplest approach to the energy estimation of a muon track is counting all observed PEs and comparing it to the value expected from a reference muon with an energy loss of $1\,\mathrm{GeV\,m^{-1}}$. The differential energy loss is then just the observed number divided by the expected number times the reference energy loss. *MuEX* uses an analytic approximation to get the expectation for the reference track. [139]

[139]: Aartsen et al. (2014), *Energy Reconstruction Methods in the IceCube Neutrino Telescope*

This method works well on average, although there is a large spread when comparing true values from simulations to the measurement. This is primarily due to the stochastic processes that can cause large losses which are not included in the assumption of a smooth muon and skew the estimate [180].

***TruncatedEnergy*: The segmented Muon Template**

To deal with the stochastic energy losses discussed above, it is possible to estimate the differential energy loss in segments along a track instead of considering the full detector at once. The goal is then to identify these segments with a stochastic energy loss and exclude them when calculating the mean differential energy loss. The ratio of expected to observed PEs can be calculated for each segment individually. The highest ratios will be the ones with large stochastic losses, and discarding them leads to a more robust measurement, the so-called truncated mean. This approach is implemented in *TruncatedEnergy*, which uses a bin size of 120 metres and disregards the 40% highest ratios. Compared to *MuEX*, it also refines the PE expectation by using spline surface fits of tabulated results (see Section 4.3.1) from muon and photon propagation simulations [180].

[180]: Abbasi et al. (2013), *An Improved Method for Measuring Muon Energy Using the Truncated Mean of dE/Dx*

***Millipede*: Unfolding all Hits**

Stochastic energy losses can occur on scales much smaller than the 120 m bins used in *TruncatedEnergy*. Also, because the segments are a-posteriori made up according to a specific track hypothesis and have no physical counterpart in the detector, light emitted in one segment can also be detected in another. The light from all energy depositions can potentially be detected everywhere in the detector and so sums up in every single DOM. Because this happens linearly, and the individual losses can be described as electromagnetic cascades, it is possible to reconstruct the individual light depositions from all DOM signals. The *Millipede* algorithm does this by varying energy losses, and the initial muon energy to maximize a likelihood function. Each DOM is described as an individual counting experiment following the Poisson distribution. The PE expectation is given by the sum of expectations from every cascade plus a constant noise rate. For a typical separation between the cascades of 2.5 m, the resolution of the deposited energy is about 10–15% [139].

4.4 Neutrino Point-Source Likelihood Method

This chapter has so far introduced the collection, compilation, and reconstruction of neutrino events. But as already mentioned in Section 4.2.5, for large neutrino samples, there is an overwhelming contribution of atmospheric neutrinos, so statistical methods are necessary to tell if a potential source or population is associated with the astrophysical component. This section introduces the appropriate method for point source searches, first for a single source and then for a source population, before discussing the evaluation of significance and the statistical power of an analysis. For an application of this method refer to Chapter 8.

4.4.1 Single Point-Source Likelihood

The reason why neutrino astronomy has to be treated statistically in the first place is the large background. The likelihood should therefore incorporate probabilities for any neutrino to be signal or background. The simplest, normalized combination of a signal PDF, $\mathcal{S}$, and background PDF, $\mathcal{B}$, is the *standard point-source likelihood*:

$$\mathcal{L}(n_s, \gamma|\boldsymbol{\theta}) = \prod_i^N \left(\frac{n_s}{N} \mathcal{S}(\gamma|\theta_i) + \frac{N - n_s}{N} \mathcal{B}(\theta_i) \right). \tag{4.12}$$

It depends on the properties $\boldsymbol{\theta}$ of all N neutrino events, usually their arrival direction, angular uncertainty, and energy. Because this work is concerned with transient sources, it also depends on the arrival time. It has two free parameters that describe the signal:

n_s: This parameter encodes the signal strength. If the analysis yields a significant signal detection, it can be interpreted as the number of signal neutrinos [181, Chapter 9]. It is restricted to $n_s \geq 0$.

γ: This is the assumed neutrino spectrum's spectral index and is restricted to the interval $\gamma = [1, 4]$.

[181]: Glüsenkamp (2016), *Search for a Cumulative Neutrino Flux from 2LAC-blazar Populations Using 3 Years of IceCube Data*

It is generally assumed that the spatial, energy, and temporal part of the PDFs are independent, and so the PDFs can be written as their products:

$$\begin{aligned} \mathcal{S} &= \mathcal{S}_{\text{space}} \times \mathcal{S}_{\text{time}} \times \mathcal{S}_{\text{energy}}, \\ \mathcal{B} &= \mathcal{B}_{\text{space}} \times \mathcal{B}_{\text{time}} \times \mathcal{B}_{\text{energy}}. \end{aligned} \tag{4.13}$$

Once these PDFs are defined according to the signal and background hypotheses, the maximum of the likelihood function gives the values of n_s and γ that best fit the data $\boldsymbol{\theta}$. For computational reasons, this is done in practice by numerically minimizing the negative logarithm $-\ln \mathcal{L}$.

4.4.2 Stacking Likelihood

If there is a whole population of candidate sources instead of a single one, looking for a combined excess from this population improves the sensitivity of the analysis [67]. This modifies the signal PDF to become a weighted sum over all M sources:

$$S(\gamma|\theta_i) = \sum_j^M \omega_j \mathcal{S}_j(\gamma|\theta_i). \tag{4.14}$$

[67]: Aartsen et al. (2017), *The Contribution of Fermi-2LAC Blazars to Diffuse TeV–PeV Neutrino Flux*

The weights are determined by the effective area of the detector A_{eff} and model assumptions about the flux ϕ_j:

$$\omega_j = \int \phi_j(E)\, A_{\text{eff}}(\delta_j, E)\, \mathrm{d}E. \tag{4.15}$$

Model weights

This can be simplified assuming a global neutrino energy spectrum

that follows a power-law with spectral index γ:

$$\omega_j = C \cdot \omega_{j,\text{model}} \cdot \omega_{j,\text{acc}}(\delta_j, \gamma). \tag{4.16}$$

All model assumptions are now encoded in the model weight $\omega_{j,\text{model}}$ while all detector-specific effects are left to the *acceptance* $\omega_{j,\text{acc}}$.

The final stacking likelihood is then given by inserting Equation 4.14 into Equation 4.12:

$$\mathscr{L}(n_s, \gamma|\boldsymbol{\theta}) = \prod_i^N \left(\frac{n_s}{N} \sum_j^M \omega_j \mathcal{S}_j(\gamma|\theta_i) + \frac{N - n_s}{N} \mathcal{B}(\theta_i) \right). \tag{4.17}$$

4.4.3 Floating Weights

If there is no clear model for the distribution of the neutrino signal between a catalog of sources, the weights can be included as free parameters in the fit:

$$\mathscr{L}(\boldsymbol{n_s}, \gamma|\boldsymbol{\theta}) = \prod_i^N \left(\frac{1}{N} \sum_j^M n_{s,j} \mathcal{S}_j(\gamma|\theta_i) + \frac{N - n_s}{N} \mathcal{B}(\theta_i) \right). \tag{4.18}$$

The signal strength parameter is now a vector $\boldsymbol{n_s}$ with an entry $n_{s,j}$ per source. This drastically increases the size of the parameter space from two to $M+1$ dimensions. The model-independence thus comes with higher computational costs of the minimization.

4.4.4 Hypothesis Testing

Although maximizing the likelihood will give the best-fit parameters n_s and γ, the likelihood value alone cannot inform about the significance of the result. For that, it has to be compared to the value expected from background only. In general, this means comparing the hypothesis $\mathscr{H}_1$ that the data does contain signal with the background hypothesis $\mathscr{H}_0$. It turns out that the likelihood ratio provides the optimal comparison of both hypotheses [182]. This is also true for the logarithm of the ratio which is used to define the test statistic:

[182]: Neyman et al. (1997), *IX. On the Problem of the Most Efficient Tests of Statistical Hypotheses*

$$\lambda = 2 \log_{10} \left[\frac{\mathscr{L}(\mathscr{H}_1)}{\mathscr{L}(\mathscr{H}_0)} \right]. \tag{4.19}$$

This particular choice has the advantage that λ is expected to follow a χ^2 distribution with degrees of freedom equal to the number of independent parameters [183]. The significance of a test statistic value could then in principle easily be calculated from the χ^2 CDF.

[183]: Wilks (1938), *The Large-Sample Distribution of the Likelihood Ratio for Testing Composite Hypotheses*

Background trials

This is, however, only true in the limit of a large sample and for unbounded parameters. The test statistic's degrees of freedom are also not obvious because $\boldsymbol{n_s}$ and γ are correlated: Depending on the spectral index, more or less signal is expected in the IceCube dataset. To circumvent this, many background datasets are simulated, and the likelihood is maximized under the signal and background hypotheses. So each of these *background trials* yields a test statistic

value that together form the background test statistic distribution. This can now be used instead of the χ^2 distribution.

Scrambling

How the background datasets are simulated depends in general on the dataset. In this work, the approach taken is called *scrambling*. Exploiting that the signal contribution in the dataset is negligible, and the background is uniform in time and right ascension (see Section 8.3), random values can be assigned to the neutrino events in these dimensions to simulate a background dataset.

4.4.5 Statistical Power

To prevent personal biases and tweaking of analysis choices and parameters such as weighting schemes, IceCube analyses are developed blindly. The relevant PDFs, all parameters, and all final variables are defined before the test statistic are calculated for the unmodified, or *unblinded* data. No change is allowed after that.

Assessing the capabilities of an analysis is still possible beforehand. It can be quantified by the probabilities to accept the background hypothesis, although there is signal (false negative), or accept the signal hypothesis although there is only background (false positive). For a given test statistic value $\hat{\lambda}$, the probability α for a false negative is given by the integral over the background test statistic distribution $H_0(\lambda)$:

$$\alpha = \int_{\hat{\lambda}}^{\infty} H_0(\lambda)\,\mathrm{d}\lambda. \tag{4.20}$$

The probability β for a false positive is instead based on the distribution under the signal hypothesis $H_1(\lambda)$:

$$\beta = \int_{0}^{\hat{\lambda}} H_1(\lambda)\,\mathrm{d}\lambda. \tag{4.21}$$

Signal trials

How to obtain the background test-statistic distribution was already discussed in the previous section. To get the distribution $H_1(\lambda)$ under varying signal hypotheses is only possible using MC simulations of signal neutrinos, but in principle follows the same steps as a background trial. A scrambled background dataset is created as described above. Then the appropriate number of signal neutrinos is chosen from a set of simulations. For a single source, this is trivial and only influenced by the choice of signal strength. For a catalog of sources in a stacking analysis, the source hypothesis also must specify the weighting of the signal between the sources, which determines how the signal neutrinos are distributed. The selected signal is then added to the dataset, and the likelihood maximization performed.

Different quality metrics are defined based on values for α and β. Adjusting the signal hypothesis and generating signal trials, such that the chosen values are reached, yields the corresponding signal parameters. Two metrics are relevant for this work:

Sensitivity: $\alpha = 0.5$ and $\beta = 0.1$. This means that $\hat{\lambda}$ is the median of the background distribution λ_{bkg}, and the signal hypothesis

is excluded at 90% confidence level. It is therefore also called the median sensitivity at 90% confidence level.

90% upper limit: $\beta = 0.1$, so this is similar to the sensitivity. However, $\hat{\lambda}$ is the background median λ_{bkg} only if it is larger than the observed value λ_{obs}. If λ_{obs} is larger, then it is used instead. This means that the upper limits can be weaker than the sensitivity suggests.

In practice, successively more signal is injected in steps. The resulting values of β are used to fit an empiric function:

$$\beta(\phi) = 1 - b \cdot \exp(-a \cdot \phi). \tag{4.22}$$

As illustrated in Figure 4.7, the flux value where this fit reaches the β threshold is the sensitivity.

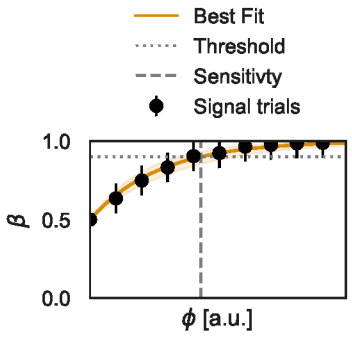

Figure 4.7: Illustration of the sensitivity fit. The probability β from Equation 4.21 is shown against the flux normalization. The data points from signal trials are shown together with the best fit of Equation 4.22. The gray dashed line indicates thes flux value where the best fit reaches the threshold (dotted gray line).

Real-Time Neutrino Astronomy

5

Real-time astronomy relies on modern telecommunication infrastructure to communicate interesting observations as soon as possible to other observatories. They can follow up the detection with observations of their own with the goal to produce rich datasets of transient phenomena. Because many observatories like optical telescopes have a limited FoV and operate under pointed observation, the sky localization of the initial transient detection is crucial. The previous section already introduced the IceCube neutrino observatory with its neutrino detection and reconstruction methods. This chapter first explains the global infrastructure for communicating interesting detections in real-time (Section 5.1) and then the corresponding IceCube system to promptly distribute the observation of high-energy neutrinos (Section 5.2). Different algorithms for the directional reconstruction than in offline analyses are necessary (Section 5.3) and special methods need to be employed to get robust directional uncertainties (Section 5.4). A method to improve the uncertainty calculation was developed by the author, which is introduced and evaluated in Section 5.5.

5.1 Coordinating Multimessenger Real-Time Follow-Up

With the advent of time domain astronomy, it became possible to study transient astronomical phenomena. Consequently, with improving timing resolution, the accessible timescales become shorter allowing the study of faster transients. To facilitate timely follow-up by many observatories across multiple messengers, it is necessary to distribute the detection of such transients with low latency. Especially the fast-fading GRB afterglows set the timescale for this distribution.

General Coordinates Network

Consequently, NASA introduced the Gamma-ray Coordinates Network* which was recently updated into the *General Coordinates Network* (GCN)†. This system allows observatories to rapidly send information on detected transients as so-called alerts in the form machine-readable Notices‡ shortly after detection. These are widely used, for example, by the Fermi and Swift satellites to announce GRBs but also by the gravitational wave interferometers LIGO, Virgo and KAGRA. The initial alert Notices can later be supplemented by bulletins issued as Circulars§. These can further elaborate on the event, contain information on follow-up observations, near-term predictions or future observation plans, mostly in the form of continuous text.

GCN Notice

GCN Circular

* https://gcn.gsfc.nasa.gov
† https://gcn.nasa.gov
‡ https://gcn.nasa.gov/notices
§ https://gcn.nasa.gov/circulars

The only neutrino observatory currently issuing high-energy neutrino detections in real-time is IceCube. The alerts distributed rapidly after detection via GCN are followed up by many observatories (see for example Chapter 6 and Chapter 7). The following sections will discuss the details of this realtime program including possible improvements.

5.2 The IceCube Real-Time System

IceCube started publicly distributing information on single neutrino events in real-time as alerts through the GCN system in 2016 [147]. These contain information about energy, arrival time and arrival direction of the incident neutrino, as well as uncertainties on the direction. The latter is often dubbed the event localization area, and is crucial for follow-up observatories as it describes the area in the sky they need to observe. Originally, the alerts were based on the HESE and EHE event selections (see Section 4.2.5) with additional requirements to select track events rather than cascades [184]. There is a separate stream for high-energy cascade events[1], but they are less useful for astronomy purposes (see Section 4.2.4) and will not be discussed here.

[147]: Aartsen et al. (2017), *The IceCube Neutrino Observatory: Instrumentation and Online Systems*

[184]: Aartsen et al. (2017), *The IceCube Realtime Alert System*

1: https://gcn.gsfc.nasa.gov/doc/High_Energy_Neutrino_Cascade_Alerts.pdf

The alert stream was substantially revised in 2019 with two major changes.
Firstly, a consistent *signalness* parameter $\mathcal{S}$ was introduced for all alerts. It is the probability to be an astrophysical neutrino, calculated for every single event. It depends on the energy E_{reco} and declination δ and assumes an astrophysical neutrino spectrum of $E^{-2.19}$ [185] to calculate the expected number of signal and background events, N_{sig} and N_{bkg}:

Signalness

[185]: Haack et al. (2018), *A Measurement of the Diffuse Astrophysical Muon Neutrino Flux Using Eight Years of IceCube Data.*

$$\mathcal{S}(E_{\text{reco}}, \delta) = \frac{N_{\text{sig}}(E \geq E_{\text{reco}}, \delta)}{N_{\text{sig}}(E \geq E_{\text{reco}}, \delta) + N_{\text{bkg}}(E \geq E_{\text{reco}}, \delta)}. \tag{5.1}$$

Based on this parameter, alerts are classified as Gold or Bronze: Bronze events have an average signalness between 30% and 50%, while Gold events are on average above 50%.
Secondly, the GFU event selection was adapted for use in real-time. It is based on its offline counterpart (see Section 4.2.5) with an additional threshold on the reconstructed energy, tuned to achieve the Gold and Bronze selection criteria. This results in only the highest energy (above around 100 TeV) GFU neutrinos being selected in real-time, significantly elevating the alert rate and providing most of the events sent out since 2019.
Additionally, the HESE selection improved to reject poorly reconstructed events.

As mentioned in Chapter 4, the online selection of promising events happens at a dedicated computing center at the South Pole. The detection receives an alias composed by the UTC date of detection, the prefix "IC" and an alphabetical letter to differentiate between neutrinos detected within the same day[2], for example, IC170922A. After a fast reconstruction algorithm is run, a Notice with the results is distributed via GCN typically within 30 s [184]. In parallel, the

2: There were only ever maximum two events detected within one day.

event information is sent north for a refined analysis. These results are typically available within hours and are communicated in a GCN Circular. The next section details the algorithms and construction of the associated uncertainty regions.

5.3 Directional Reconstruction and Uncertainties

An introduction to the various reconstruction algorithms relevant to this work was already presented in Section 4.3. However, compared to the offline data processing, the requirements for directional reconstruction for single alert neutrinos and large offline datasets there are two main differences:

1. For a single neutrino it is possible to run an expensive reconstruction algorithm that takes more than seconds.
2. The convergence into a local minimum is acceptable for a large data sample as long as on average, the global minimum is found. For a single neutrino, this has to be mitigated.

In addition, the online reconstruction must perform well also for edge cases such as events with exceptionally high energy. The *Millipede* sky scan complies with these requirements (see Section 4.3.1) and is used to provide the refined reconstruction sent out in the GCN Circular. Although it takes a lot of computational resources, ran in parallel, the results are available typically hours after the neutrino detection. To also provide a first estimate with low latency, the result of *SplineMPE* with the *Paraboloid* uncertainty (see Section 4.3.2) is sent out with the first GCN Notice.

Wilk's Theorem

The *Millipede* sky scan provides a skymap of likelihood values $\mathscr{L}$. The ratio to the best fit value is the best test for alternative directions [182] and can be used to construct detailed uncertainty contours (see Figure 5.1). However, the conversion from likelihood ratio to confidence level is not trivial. A theorem formulated by Wilks [183] states that if the distribution of the likelihood values is purely based on statistical fluctuations, $-2\Delta\ln(\mathscr{L})$ follows a χ^2 distribution. The sky scan has two independent parameters, zenith and azimuth, so the corresponding χ^2 distribution has two degrees of freedom. For 1.4 (4.6) the respective CDF is 0.5 (0.9). In this case, the pixels where $-2\Delta\ln(\mathscr{L}) = 1.4\,(4.6)$ form the 50% (90%) uncertainty contour.

[182]: Neyman et al. (1997), *IX. On the Problem of the Most Efficient Tests of Statistical Hypotheses*

[183]: Wilks (1938), *The Large-Sample Distribution of the Likelihood Ratio for Testing Composite Hypotheses*

Resimulations

Wilk's Theorem does not hold if systematic uncertainties have a significant impact. Resimulating individual events and reconstructing these resimulations while varying detector and ice parameters takes this into account (in detail, discussed in the next section). The position of the resimulations on the original likelihood map then gives a likelihood distribution that can be used instead of the χ^2 distribution (see Figure 5.2).

Coverage

The calibration of the likelihood contour using resimulations ensures correct coverage: the percentage of resimulations that is within a corresponding likelihood ratio value. However, this can be very computationally intensive. Remember that the *Millipede* sky scan

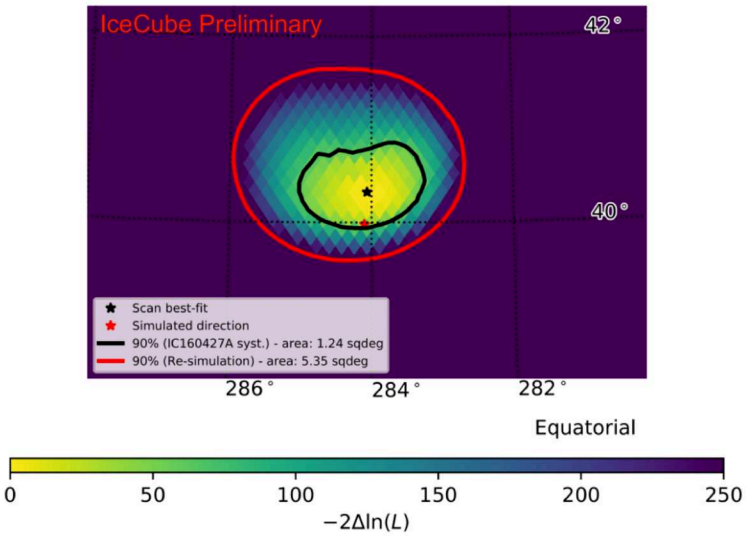

Figure 5.1: An example of a *Millipede* sky scan, and the correpsonding uncertainties derived from resimulations and simulations of IC160427A for simulated event. The colorscale indicates value of $-2\Delta\log(\mathcal{L})$ Taken from Abbasi et al. [187]

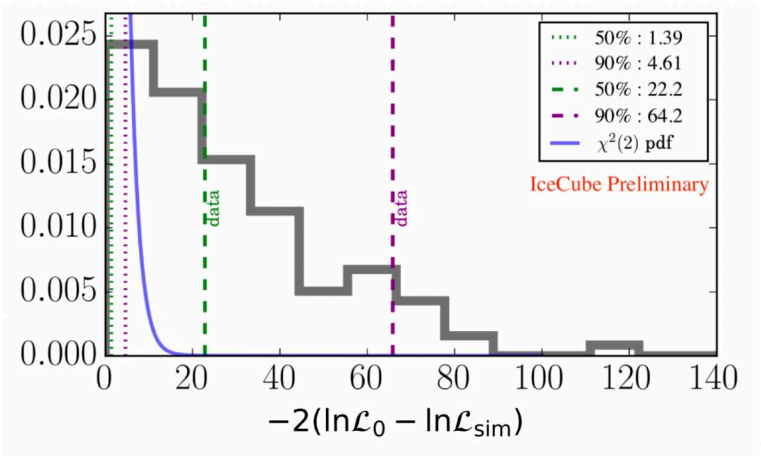

Figure 5.2: Likelihood distribution for resimulations of IC160427A. The gray histogram is the distribution derived from resimulations, and the solid blue line the χ^2 distribution expected from Wilks' theorem. The dashed and dotted vertical lines indicate the percentiles for the resimulation and χ^2 distribution, respectively. Taken from Abbasi et al. [187]

has to be performed for each resimulations to find its best fit direction. Therefore, this analysis is only performed in special cases, for example, for the first public alert ever issued, IC160427A [186]. It resulted in likelihood values about ten times larger than the ones derived from the χ^2 distribution. In general, these values are reused for every alert, assuming that the mapping between likelihood ratio values and confidence level does not change. In many cases, this assumption does not hold. This results in uncertainty contours that do not have the claimed coverage (see Figure 5.1). Unfortunately, the exact difference and even its sign (i.e., whether the contours should be bigger or smaller) seem to depend on the individual event [187].

The following sections will detail the resimulation method, and a possible solution to the coverage problem.

[186]: Kankare et al. (2019), *Search for Transient Optical Counterparts to High-Energy IceCube Neutrinos with Pan-STARRS1*

[187]: Abbasi et al. (2021), *Studies of Systematic Uncertainty Effects on IceCube's Real-Time Angular Uncertainty*

5.4 Resimulating Neutrino Alert Events

As discussed in Section 5.3, resimulations of realtime alert events are necessary to calibrate the likelihood maps and get uncertainty contours. These are simulated events that look similar to the original detection. In principle, this is not different to any other simulation

typically performed in particle physics experiments. These follow the general steps of generating the primary particle, simulating the interaction with the target, generating the secondary particles and simulating their detection, including the detector response. However, using the original event as a starting point, some shortcuts are possible. The scheme outlined below [188] was first used for IC160427A [186]. In the context of this work, the crucial step is the detection of the secondary particle, in this case a muon. The preceding steps can be summarized as the muon generation. The second column of Table 5.2 gives an overview of the explanations below.

[188]: Lagunas Gualda (2024), *Realtime Detection of High-Energy Neutrinos and Search for Correlations with Candidate Source Classes*

Muon Generation

The software for generating the incoming neutrino and simulating the particle interaction is called *LeptonInjector* [189]. Incoming muon neutrinos are simulated within a ±2° range of the original zenith and azimuth, and only the events that are actually within an angular offset of 2° are selected for further processing. The simulated energy is between 10^{-1} and 100 times the originally inferred neutrino energy. The secondary particles are generated, selecting only events with an outgoing muon. The muon is propagated through the ice using *Muon Gun* [143].

[143]: van Santen (2014), *Neutrino Interactions in IceCube above 1 TeV: Constraints on Atmospheric Charmed-Meson Production and Investigation of the Astrophysical Neutrino Flux with 2 Years of IceCube Data Taken 2010–2012*

Geometric Track Selection

To make sure that the resimulated events pass through similar parts of the detector, the simulated track has to be within 30 m from the original one [186]. This simulate-and-select approach is very inefficient with only 10^{-4} of events passing the selection (see Section 5.5.3). A more effective way of sampling will be introduced in the nest section.

Muon Propagation

The energy losses of the muon are simulated using *PROPOSAL* [190]. These include all processes introduced in Section 4.1. This is not necessary for electrons or taus where the resulting signature is point-like and detected as a cascade, and no track is observed.

Ice Systematics, Photon Propagation and Detector Response

The Cherenkov photons emitted by all energy depositions (muon track and cascades alike) are propagated through the ice until they reach a DOM. The properties of the ice influence the photon propagation and the efficiency and noise rate of the DOM the detection efficiency and threshold. Both have to be taken into account (see Section 4.2). For IC160427A this was done by varying the parameters of the ice model *SPICE MIE* following a multivariate gaussian distribution (see Section 4.2 for more details on ice models). The more refined approach used in this work is the *SnowStorm* method [191], which varies the ice parameters continuously based on user

[191]: Aartsen et al. (2019), *Efficient Propagation of Systematic Uncertainties from Calibration to Analysis with the SnowStorm Method in IceCube*

SnowStorm

[160]: Abbasi et al. (2024), *In Situ Estimation of Ice Crystal Properties at the South Pole Using LED Calibration Data from the IceCube Neutrino Observatory*

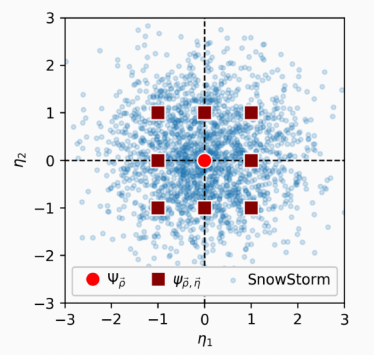

Figure 5.3: Illustration of the *SnowStorm* method. The red squares represent discrete MC datasets, each with a different set of nuisance parameters, abd the blue dots a single *SnowStorm* dataset with continuously varied parameters. Taken from Aartsen et al. [191].

Table 5.1: Ice model paremeters varied in the photon propagation.

Parameter	Range
Scattering	[0.9, 1.1]
Absorption	[0.9, 1.1]
Anisotropy	[0, 2]
DOM Efficiency	[0.9, 1.1]
Hole Ice	[-0.84, +0.3] [-0.134, 0.05]

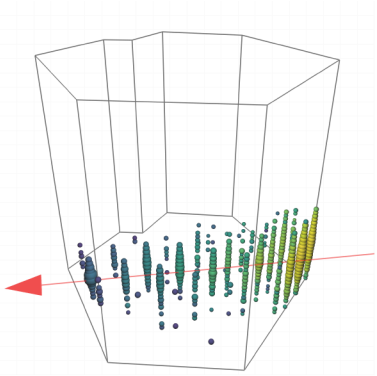

Figure 5.4: IC170922A, a good example of a smooth, through-going muon track event.

defined ranges as illustrated in Figure 5.3. Table 5.1 summarizes the values of the updated *SPICE 3.2.1* model. The global absorption, scattering, and the efficiency with which DOMs detect photons are varied within 10% of the nominal value. The anisotropy parameter determines the strength to which ice birefringence affects the direction of photon propagation [160]. The hole ice parameterizes the effects of the re-frozen ice in the boreholes.

Basic Processing

To compare the simulations to the original event, they are processed and filtered like actual data at the South Pole up to level 2. This involves triggers, hit cleaning and basic directional and energy reconstruction (see Section 4.2).

Energy Selection

The definition of similarity between simulation and data event up until now is limited to geometrical constraints, i.e., the distance between the muon tracks and angular offset in arrival direction. This does not guarantee that the event looks similar in the detector because statistical losses can create a large amount of light in a certain part of the detector. To at least have a handle on the total amount of energy deposited within the detector volume, the total charge of the simulated event is required to be within ±20% of the original. Although this works well, especially for smooth track events, large statistical fluctuations cannot easily be reproduced [188]. Furthermore, typically only ~ 5% of simulations pass this selection, although they already underwent the expensive photon propagation simulation leading to a waist of resources. The next section will introduce a method to also address this issue.

5.5 Improved Resimulations for Through-Going Track Events

The approach for resimulating events presented in the previous section works well if they can be reproduced easily by random MC processes. This is the case as long as the muon track is smooth. However, if large statistical losses are present in the data event, they appear by chance only in a tiny number of simulations. All other simulations will not produce the right number of photoelectrons and do not pass the energy selection. And even if the total amount of deposited charge is within the selection constraints, the depositions are likely distributed more evenly than in the measured event with one large energy loss.

Because this happens after the computationally expensive step of photon propagation, it can become unfeasible to run enough simulations to produce even a single event that represents the original. But already before the photon propagation, analyzing the muon's simulated energy deposition can give an idea whether the event is promising. Limiting the procedure to through-going

tracks of which a representative example is shown in Figure 5.4, performance improvements in the sampling of the muon tracks are also introduced in Section 5.5.1 before explaining the energy selection in Section 5.5.2. The third column of Table 5.2 gives an overview of the improvements.

5.5.1 Direct Sampling of the Muon Track

In the previous resimulation scheme, the neutrino arrival direction is sampled from a ±2° range within the original arrival direction, and the geometric constraints are achieved by selecting resulting muon tracks. This brute force simulate-and-select approach is inefficient, and it turns out that usually not even 1% of initially generated events pass the geometric constraints [188, Table 6.1]. Because the kinematic angle at the energies relevant for alert events can be neglected (see Section 4.1), simulating the muon track directly is equivalent to simulating the angular offset of the incident neutrino. So directly sampling muon tracks from the constrained parameter space is possible, and the extra selection step after the fact becomes unnecessary.

The two constraining parameters are still the maximum allowed distance from the original track d_{max} and the angular offset α_{max}. These are not independent, however. As illustrated in Figure 5.5, the maximum angular separation allowed by the constraint on the distance between the two tracks is reached when the tracks cross exactly in the middle of the detector. This angle is then

$$\alpha_{\text{d}} = \tan^{-1}\left(\frac{d_{\text{max}}}{L/2}\right), \tag{5.2}$$

where L is the length of the original track in the detector.

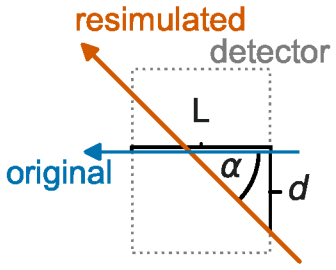

Figure 5.5: Schematic of the geometric constraints for resimulations. α is the angle between the original, and the resimulated track and d the distance between the two tracks.

The sampling of the simulated direction is then straight forward. The angular offset between simulated and original direction is sampled from a uniform distribution so that $\alpha \in [0, \min(\alpha_{\text{max}}, \alpha_{\text{d}})]$ along with a position angle p so that $p \in [0, 2\pi]$. Offsetting the original coordinates according to α and p gives the simulated direction.

Sampling the position of the track becomes more difficult because there is no single distribution to draw from. Instead, for a specific simulated direction, it is constrained by the allowed distance d_{max}. If the track satisfies this constraint at the entry and exit points of the detector, it also does so inside the detector volume. As a simplification, this distance is measured perpendicular to the original event at its detector entry (d in Figure 5.5) and exit. In other words, the simulation has to be within a radius d_{max} of the original track at detector entry and exit, effectively placing it inside a cylinder with radius d_{max} around the original track. In the following, the top and bottom of this cylinder will be called entry and exit target. Projected into a frame F', with the base of the cylinder at the origin and the original direction along the z'-axis, these targets are shown in Figure 5.6. The circle indicating the constraint at detector exit is projected along the simulated direction into the x'-y'-plane. In this reference frame, the points that satisfy the distance constraint lie in the area where both circles overlap. Sampling this area is easiest in

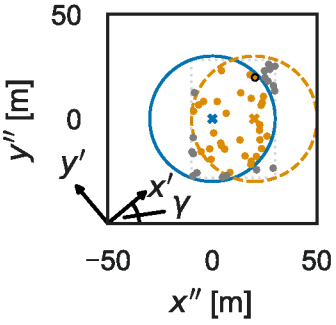

Figure 5.6: Visualization of the fix point generation for an allowed distance of 30 m. The circles indicate the parameter constraints at the detector entry (blue solid) and exit (orange dashed). Grey points are discarded, orange ones are potential fix points of which one is chosen (black solid outline).

the reference frame F'' rotated along the z'-axis such that the center of the projected exit target lies on the x''-axis. The rotation angle γ is given by the coordinates of the projected exit target:

$$\gamma = \tan^{-1}\left(\frac{x'_{\text{exit}}}{y'_{\text{exit}}}\right). \tag{5.3}$$

The x''-coordinate of the projected exit target is just

$$x''_{\text{exit}} = \sqrt{x'^2_{\text{exit}} + y'^2_{\text{exit}}}. \tag{5.4}$$

Because directly sampling the overlapping area is not trivial, sampling from the bounding rectangle (gray dashed in Figure 5.6) instead and subsequently selecting points in the targeted area is the best option. The rectangle is constrained in x'' in between $x''_{\text{exit}} - d_{\text{max}}$ and d_{max}. The circles intersect in the middle between the two centers at $x''_{\text{exit}}/2$ and the corresponding y'' values are

$$y''_{\text{intersect}} = \pm\sqrt{d^2_{\text{max}} - \frac{x''^2_{\text{exit}}}{4}}. \tag{5.5}$$

So sampling from uniform distributions such that

$$x'' \in [x''_{\text{exit}} - d_{\text{max}},\ d_{\text{max}}] \tag{5.6}$$
$$y'' \in [-y''_{\text{intersect}},\ y''_{\text{intersect}}] \tag{5.7}$$

will give points in the bounding rectangle of the region where the two targeted areas overlap (all points in Figure 5.6). Sampling 100 points, one lying inside the overlapping region can be selected. z'' can always be set to zero because the only important thing is the track itself and not its starting point. With these three coordinates, all components of the position r'' are sampled. The rotation back to the detector system is then described by three rotations

$$\boldsymbol{r} = \mathcal{R}_z(-\phi)\,\mathcal{R}_y(-\theta)\,\mathcal{R}_z(-\beta)\,\boldsymbol{r}'', \tag{5.8}$$

where $\mathcal{R}_i$ is the rotation matrix around dimension i. θ and ϕ are IceCube coordinates of the original direction representing zenith and azimuth (see Section 4.2). Figure 5.7 shows an example for a randomly chosen initial direction and randomly selected resimulations.

5.5.2 Energy Deposition Pattern

As mentioned above, the resimulation scheme introduced in Section 5.4 works well if the muon track is smooth. However, if energy losses that happen only rarely by chance are present, the scheme breaks down. Firstly, because a large statistical energy loss inside the detector leads to a high charge which simulations without depositions that large cannot reproduce and will not pass the energy selection. The energy selection only happens at the end of the simulation chain, so to get only a limited number of resimulations, a huge number of events has to be produced initially. Secondly, even if the total amount of charge is reproduced due to a large loss, it is likely that this does not happen in the same part of the detector, altering the structure of

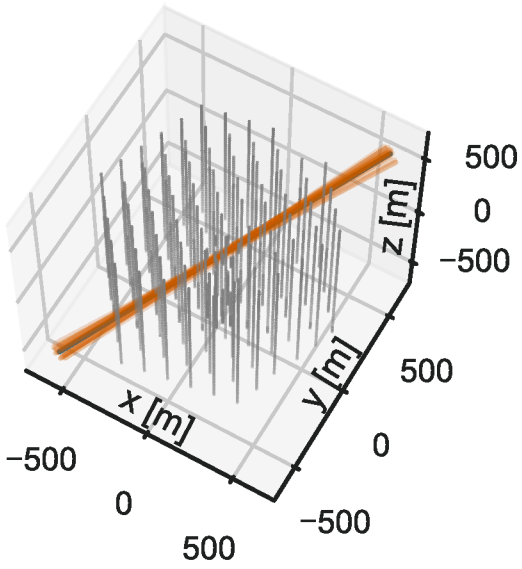

Figure 5.7: Resimulations (orange lines) of a toy event (blue line) with a maximum allowed distance of $d_{\text{max}} = 50\,\text{m}$ and sampled from an angular offset of $\alpha = 5°$ for better visualization. The gray dots represent the DOMs, and the axes indicate detector coordinates.

the event significantly. This leads to high computation consumption and results that do not necessarily represent the original event. Figure 5.8a shows the case of IC200530A that suffers a large energy loss early in the detector, but very little light is observed later on[3]. Figure 5.8b shows a representative example of a resimulation attempt from [188] that exhibits too much charge in the second half of the track. For a sample of 36 resimulated events from [188], this gets clear when looking at the measured charge as a function of the height in the detector (see Figure 5.9). The resimulations do not follow the energy deposition pattern of the original event. Especially in and around the dust layer, even on average, there is too much light detection simulated.

Introducing a selection based on the simulated energy deposition pattern right after the simulation of the muon propagation addresses both issues. To have a baseline to compare to, a measurement of the original event's energy deposition in segments along the track is necessary. In principle, both *Millipede* and *TruncatedEnergy* estimate the energy in separate intervals (see Section 4.3.3 for more details). However, *TruncatedEnergy* is a lot faster. Additionally, the segmentation should not be too small to avoid overconstraining the light pattern, and the 120 m segments are better suited than the meter scale ones used by *Millipede*.

The segments k are separated by $k + 1$ planes j. They are perpendicular to the original track and given by the original direction $\hat{\boldsymbol{d}}$ and support vectors $\boldsymbol{r}_j$:

$$(\boldsymbol{x} - \boldsymbol{r}_j) \cdot \hat{\boldsymbol{d}} = 0. \tag{5.9}$$

Knowing the distance D_0 from the starting point of the muon $\boldsymbol{p}$ to the first plane, the support vectors are

$$\boldsymbol{r}_j = \boldsymbol{p} + (120\,\text{m} \cdot j + D_0) \cdot \hat{\boldsymbol{d}}. \tag{5.10}$$

A simulated track with a direction $\hat{v}$ through a point $\boldsymbol{r}$ is given by

$$\boldsymbol{x} = \boldsymbol{r} + D \cdot \hat{v}, \tag{5.11}$$

3: A more detailed disucssion of IC200530A including dust layer effects can be found in Section 8.2

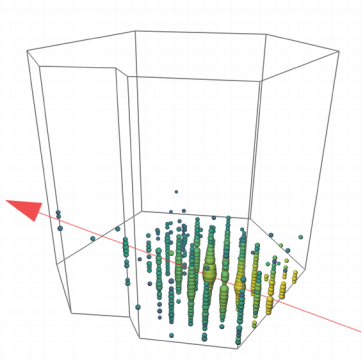

(a) Original

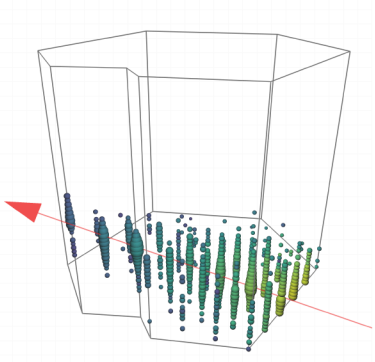

(b) Resimulation

Figure 5.8: IC200530A, an example of a track event dominated by a large stochastical energy loss. The original observed event (a) and an example of a resimulated event (b) produced with the scheme introduced in Section 5.4.

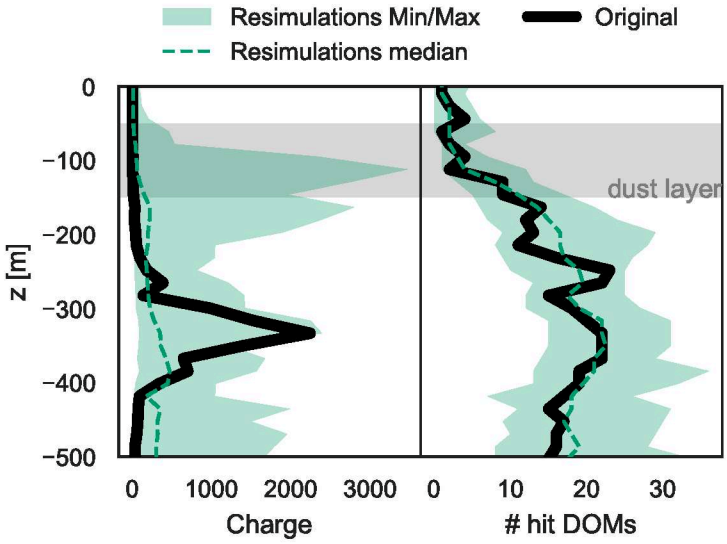

Figure 5.9: The distribution of charge and number of hit DOMs as a function of height in the detector for the original event and resimulations of IC200530A. The black solid line marks the original event, the green dashed line the median from the resimulations, and the green-shaded area their minimum and maximum.

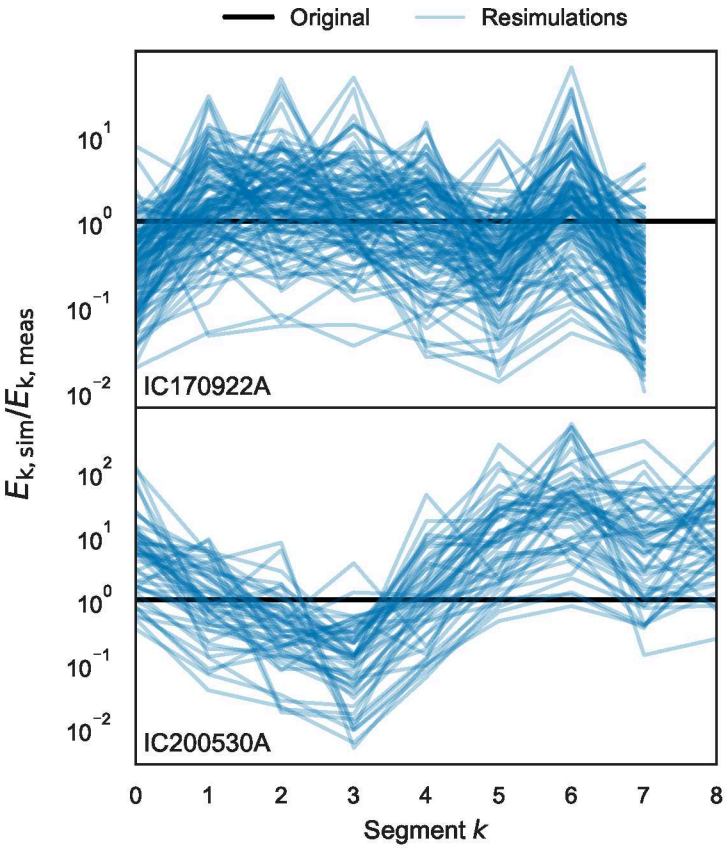

Figure 5.10: Ratio of simulated to measured energy deposition of IC170922A and IC200530A and previous simulations. The black solid line shows the depositions measured by *Truncated Energy*. The blue lines show the simulated energy.

where D is the distance along the track. Inserting Equation 5.11 into Equation 5.9 provides the value where a line intersects plane j:

$$D_j = \frac{(r_j - r) \cdot \hat{d}}{\hat{v} \cdot \hat{d}}. \tag{5.12}$$

The energy deposited in segment k is then

$$E_{k,sim} = E_\mu(D_{k+1}) - E_\mu(D_k), \tag{5.13}$$

where the energy of the simulated muon as a function of traveled distance $E_\mu(D)$ is accessed using *Muon Gun*.
As explained in Section 4.3.3, *TruncatedEnergy* compares the observed number of photoelectrons to the expectation from a 1 GeV muon to get the differential energy loss $(\mathrm{d}E/\mathrm{d}x)_\mathrm{k}$ in segment k. The measured energy deposition is then simply

$$E_{\mathrm{k,meas}} = \left(\frac{\mathrm{d}E}{\mathrm{d}x}\right)_\mathrm{k} \cdot 120\,\mathrm{m}. \tag{5.14}$$

TruncatedEnergy had to be modified to return the position of the first segment D_0 and the individual $(\mathrm{d}E/\mathrm{d}x)_\mathrm{k}$. The simulated value can then be compared to the measurements to assess how well the pattern agrees.

Figure 5.10 shows this comparison for IC170922A and IC200530A, and the simulations performed without the direct sampling and energy deposition pattern selection. Both are through-going tracks but IC200530A had a large stochastical energy deposition that was not reproduced by the resimulations. The discrepancy is immediately visible. The mean offset per segment varies little for the smooth track IC170922A. But almost all simulated events of IC200530A produce less light in and around segment three and too much in and around segment six by factors of tens to hundreds.

To solve this, it is necessary to define a metric M that assesses the compatibility with the original event. The maximum ratio between simulation and measurement in any segment captures at least the biggest outlier and can be used to select successful simulations. In a functional form this can be written as

$$M = \max_\mathrm{k} \left| \log_{10}\left(\frac{E_{\mathrm{k,sim}}}{E_{\mathrm{k,meas}}}\right)\right|. \tag{5.15}$$

So the smaller M the better the agreement is between original and simulated event.

Figure 5.11a shows the cumulative distribution of this ratio for IC170922A and its successfully resimulated events. Figure 5.11b shows the same for the failed case of IC200530A. Because the distribution for IC200530A is concentrated and extends towards higher values, these confirm that M does contain information about the agreement with the original event.

Comparing them can gauge a threshold value M_thresh that separates simulations that represent the original in terms of energy deposition pattern from the ones that do not. Defining the purity as one minus the CDF of IC200530A and the efficiency as the CDF of IC170922A, a suitable value for M_thresh can be estimated. This is shown in Figure 5.12. For $M_\mathrm{thresh} = 0.8$, corresponding to a maximum deviation between simulation and original of a factor around six, no resimulations of IC200530A pass, indicating good purity[4]. And although only around 20% of the IC170922A simulations remain, their simulation is already performant with the scheme in Section 5.4 and will only improve with the direct spatial sampling introduced in Section 5.5.1, so the focus is on optimizing purity.

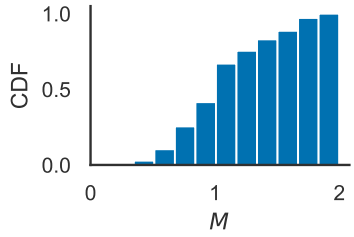

(a) IC170922A

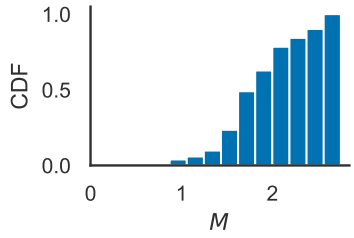

(b) IC200530A

Figure 5.11: Maximum ratio distribution of simulated to measured energy deposition for IC170922A (top) and IC200530A (bottom). The x-axis shows the maximum of the ratio logarithm such that one corresponds to a factor of ten.

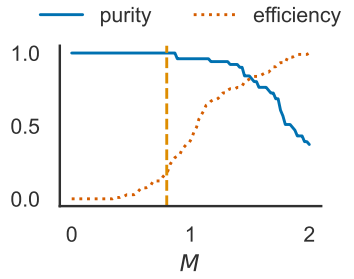

Figure 5.12: Purity (blue solid) and efficiency (orange dotted) of the metric for identfying good resimulations. The orange dashed line indicates the chosen value $M_\mathrm{thresh} = 0.8$.

4: Although the best one available, the definition of purity and efficiency here is pretty crude and only based on two example events. So no *perfect* purity can be claimed.

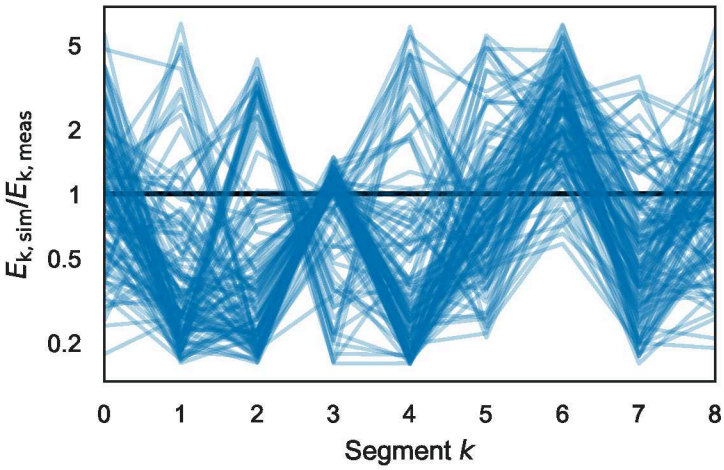

Figure 5.13: Ratio of simulated to measured energy depositions for IC200530A and resimulations accounting for the energy deposition pattern.

Figure 5.13 shows the ratio of simulated to measured energy deposition using the determined threshold $M_{\text{thresh}} = 0.8$ to select viable simulations already after the muon propagation. The difference to the previous results in Figure 5.10 is immediately visible. By construction, the deviation decreased by at least an order of magnitude. But also the spread about the measured value is more random between the individual simulated events. This demonstrates that selecting resimulated events based on energy deposition patterns enables a better definition of similarity to the original event.

5.5.3 Performance Improvement

The improvements introduced in the previous sections not only enable resimulating events with rare energy losses but also potentially consume less computational resources. The changes introduced in these sections are summarized in the following as the new scheme compared to the old scheme from Section 5.4.

Table 5.2 shows the steps of both methods and highlights the changes. Qualitatively, the improvements of the new scheme lie in the more efficient direct sampling of muon tracks, and the selection based on energy before the photon propagation.

To quantify the improvements, IC170922A and IC200530A were simulated with both methods. The simulation chain was executed several times, parallelized on a computing cluster, and the execution time measured each time.
Figure 5.14a shows the median and standard deviations for IC170922A. For this example, the old scheme was run seven times producing 64 events in 52 CPU h, and the new one ten times, producing 168 events in 1.7 CPU h. The bottom panel shows the time difference per final event between both. The earlier energy selection improves the simulation the most, taking only some seconds in the new scheme but around 10^3 s in the old one. The efficiency of the new energy selection and the old charge selection is at the percent level. Although all steps after the energy selection improve per event because they are only performed for the limited number of selected events, this is most visible for the expensive photon propagation. In relative terms,

Table 5.2: Different steps in the old and new scheme for simulating similar events of high-energy neutrino alert events.

Step	Old	New
Generate	ν, its interaction and μ production	Place μ in detector
	μ within 30 m of original track	-
Propagate	μ propagation & energy losses	
Calculate & select energy	-	μ with similar energy depositions
Photons, Detector, L1 & L2	ice systematics, detector response and filtering	
Energy selection	μ within 20% deposited charge	-

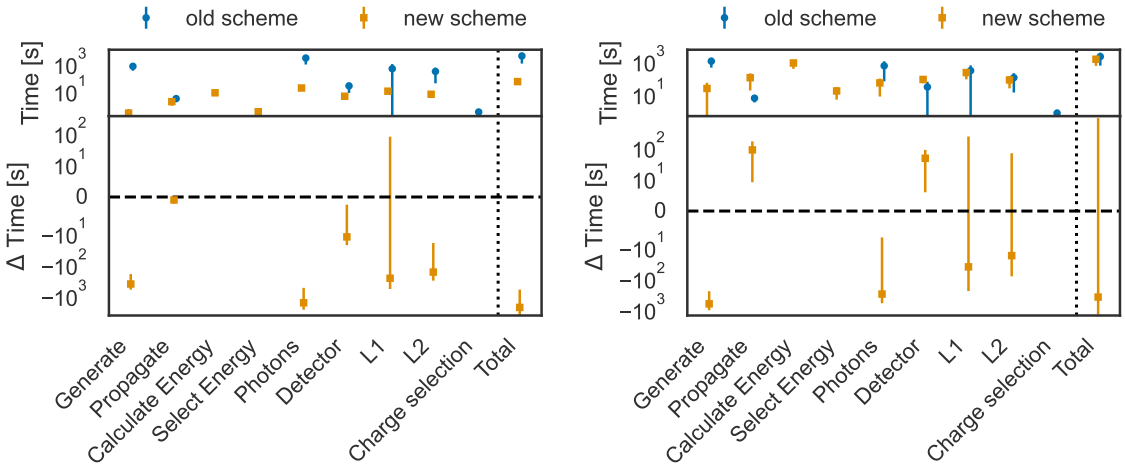

(a) IC170922A

(b) IC200530A

Figure 5.14: Performance improvements of the new resimulation scheme for IC170922A and IC200530A. The respective top panel shows the time per step per resulting event for both schemes. The bottom panel shows the improvement by the new scheme. Circle and square markers indicate the median and the errorbars the standard deviation among several runs.

the improvement of the positional sampling is the same, going from 1×10^2 seconds to 1×10^{-1} s due to the efficiency increase from 10^{-4} to 1 thanks to replacing the simulate-and-select approach with the direct sampling. In total, the old scheme takes 2×10^3 s per simulated event where the new method is 100 times faster, only taking around 40 s. So for 100 simulations, this saves about 50 CPU hours.

For IC200530A, six runs of the old scheme produced 26 events in 10 CPU h and 20 runs of the new one produced five events in 1.4 CPU h. The results are shown in Figure 5.14b. Because of the rare stochastic loss dominating this event the energy selection is very constraining resulting in an efficiency of only 10^{-4}. Of course, this is not taken into account by the old method that only cares about the total charge. That selection efficiency is also at the percent level for this event. Per final simulation, the photon propagation is therefore more expensive than in the case of IC170922A. Note, however, that even though the charge selection of the old method produces some events, they are not representative of the original as explained in the previous section. So although the runtime improvement for this event is less pronounced, the new scheme does produce simulations that are actual representative of the original event.

5.5.4 Summary and Outlook

This section introduced and demonstrated improvements to the resimulation method previously used in IceCube. These improvements exclusively work for though-going muon track events. For those, the runtime was significantly improved and also takes into account the energy deposition pattern. For smooth tracks, that means that hundreds of resimulations can be produced within minutes rather than hours. Events with large stochastic losses become reproducible for the first time. The latter is relevant for this work and will be used in Section 8.2.2.

Beyond that, due to the runtime improvement, it is now in principle possible to produce dedicated simulations of an event in realtime. As mentioned above, this is necessary to derive well-calibrated contours from a likelihood skymap. Of course, this only works in combination with a fast reconstruction of the arrival direction because it has to be run for each simulated event. This is true for *SplineMPE* but not for *Millipede*.

However, *Millipede* could be used to replace *Truncated Energy* as the estimator of the original event's energy deposition. It was mentioned above that the meter scale length of the segments used by *Millipede* is too small and would over constrain the simulations. But several segments could be combined to arrive at the 120 m lengths used in *Truncated Energy*. This way, also the starting cascade of starting tracks could be simulated.

Optical Follow-Up of High-Energy Neutrino Alerts

Constraining Transient Neutrino Source Populations with ASAS-SN

6

The IceCube neutrino alerts are rapidly distributed to the astronomical community, as introduced in the previous chapter. This allows other observatories to probe the sky region where the neutrino originated to try and observe a counterpart in the electromagnetic spectrum. The *All-Sky Automated Survey for SuperNovae* (ASAS-SN) is an optical survey system, consisting of multiple telescopes around the globe, that is daily scanning the sky. As such, it is uniquely suited to conduct follow-up observations of the high-energy neutrino alerts. The summary of this follow-up program and its results will be presented in this chapter. This was already published in Necker et al. [192], and the work presented here is the individual contribution by the author, if not stated otherwise. Section 6.1 introduces the instrument and Section 6.2 its neutrino follow-up performance. The lack of counterparts is discussed in Section 6.3, and limits based on the non-detections are derived in Section 6.4, before some concluding remarks in Section 6.5.

[192]: Necker et al. (2022), *ASAS-SN Follow-up of IceCube High-Energy Neutrino Alerts*

6.1 The All-Sky Automated Survey for Supernovae

ASAS-SN is an instrument composed of five telescope stations around the globe. The first station, Brutus on Haleakala in Hawaii, started observing in late 2013, followd by the second unit in 2014, called Cassius, located at Cerro Tololo International Observatory (CTIO) in Chile. In late 2017, the last three stations, Paczynski, also situated at CTIO in Chile, Leavitt at McDonald Observatory in Texas (USA), and Payne-Gaposchkin at the South African Astrophysical Observatory (SAAO) in Sutherland, South Africa, completed the setup. The two original units used a V-band filter until late-2018, centered at 551 nm. The new units were installed using g-band filters (centered at 475 nm), and the two old units were switched from V to g after roughly a year of V- and g-band overlap (see Appendix A for detailed filter functions). The comissioning of all five stations equipped with g-band filters was finished mid-2019. The stations are hosted by Las Cumbres Observatory [194].

[194]: Brown et al. (2013), *Las Cumbres Observatory Global Telescope Network*

Each station consists of four telescopes, consisting of a 14-cm aperture Nikon telephoto lens, and an FLI ProLine charge-coupled device (CCD) camera with a Fairchild 2k x 2k thinned CCD, resulting in FoV per telescope of $4.47° \times 4.47°$ (around 20 sqd), and a pixel scale of around 8″ [195]. The telescope fields overlap by about 0.5°, so one station's instantaneous FoV is around 70 sqd. The distribution of the five stations around the globe gives the survey a 360° FoV. During normal survey operations, observations typically consist of three dithered[1] 90 s exposures. Including the operations overhead of around 15 s, this amounts to a total time taken per exposure of around 315 s per field [196]. Full coverage of the sky is achieved by

Technical overview

[195]: Shappee et al. (2014), *The Man behind the Curtain: X-Rays Drive the UV through NIR Variability in the 2013 Active Galactic Nucleus Outburst in NGC 2617*

1: Dithering is the process of shifting the piinting direction of the telescope slightly between exposures. The images are re-aligned based on the stars in the frame so that artifacts caused by individual pixels are canceled out.

[196]: de Jaeger et al. (2022), *ASAS-SN Search for Optical Counterparts of Gravitational-Wave Events from the Third Observing Run of Advanced LIGO/Virgo*

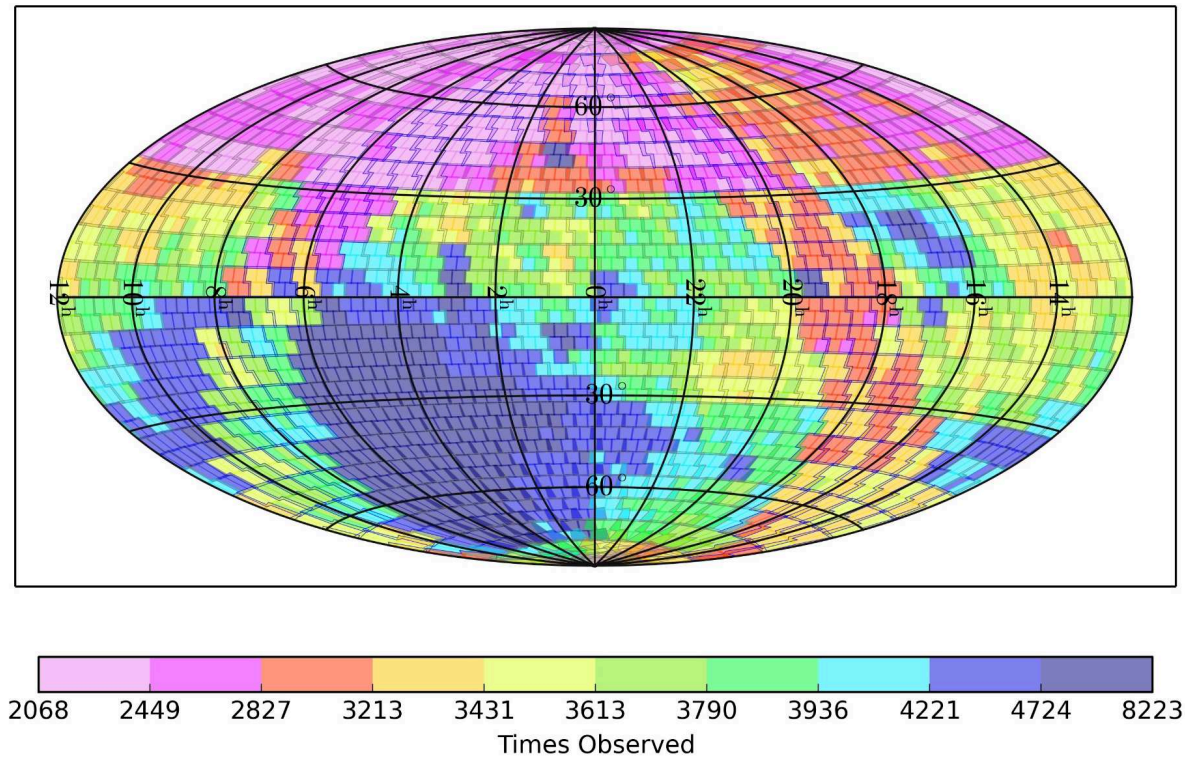

Figure 6.1: ASAS-SN fields and their coverage as of Feb 25, 2023 in equatorial coordinates. Each field consists of four pointings by the individual telescopes. The number of observations is colorcoded. Taken from Hart et al. [193]

dividing the sky into 2824 fields, matching the FoV of an individual telescope, resulting in 706 station pointings across the sky. This is shown in Figure 6.1. Until February 25, 2023, ASAS-SN has observed each part of the sky at least over 2000 times [193].

[193]: Hart et al. (2023), *ASAS-SN Sky Patrol V2.0*

Difference imaging

To get rid of the steady part of the image and extract the transient components, reference images are subtracted from the science exposures, using the ISIS image subtraction package [197, 198]. Sources in these difference images are detected with *SExtractor* [199]. A combination of parameter cuts, a random forest classifier and a convolutional neural network distinguishes real sources from bogus and spurious detections [196].

6.2 Follow-up Performance

Target-of-Opportunity mode

Besides the normal survey mode described above, ASAS-SN also schedules observations in a Target-of-Opportunity (ToO) mode to get rapid imaging follow-up of multi-messenger alerts [196]. If a GCN event is received, a list of 30^2 pointings is generated and observations start immediately if there is a site that can observe the localization region. This is often the case due to the distribution of the stations among four sites. The pointing closest to the center of the search region is observed $\sim 15-20$ times to discover fainter candidate counterparts. After one hour in ToO mode, the standard mode is resumed, but the observations are re-scheduled to increase the cadence of the fields in the GCN event region. Using this strategy, ASAS-SN routinely follows up IceCube neutrino alerts and gravitational-wave events. It is uniquely qualified for this task, as

[196]: de Jaeger et al. (2022), *ASAS-SN Search for Optical Counterparts of Gravitational-Wave Events from the Third Observing Run of Advanced LIGO/Virgo*

2: This number was originally motivated by follow-up observations of gravitational waves [196]. In that case, 30 pointings usually cover more than 70% of the localization area. This holds for neutrinos because they are better localized.

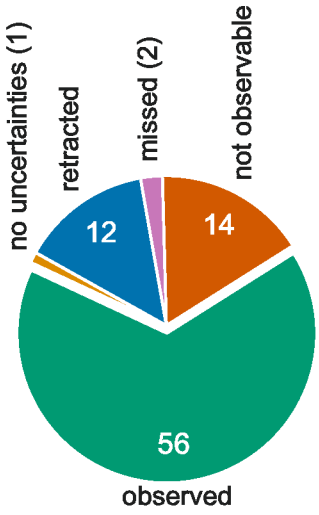

Figure 6.2: Summary of ASAS-SN follow-up observations for the 85 IceCube alerts issued until August 2021. The numbers are the percentages of the respective category.

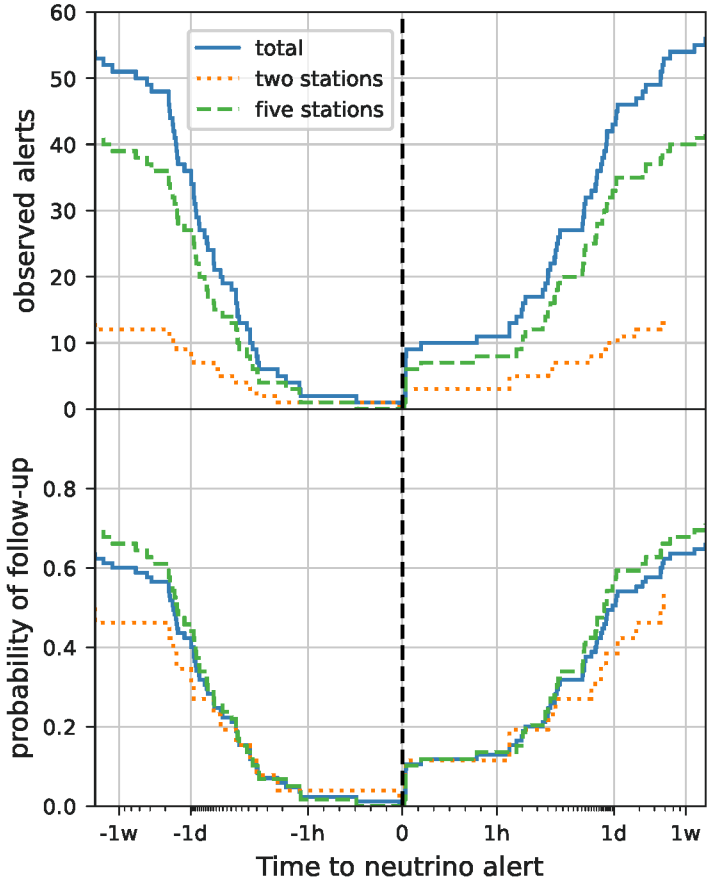

Figure 6.3: Cumulative number (top) and the mean probability (bottom) of observation of IceCube alerts by ASAS-SN. The x-axis is the time to and from the neutrino detection. The total is shown as the blue solid line. The orange dotted and green dashed lines represent the two and five station configurations, respectively.

it is the only ground-based survey that maps the visible sky daily down to a depth of around $g = 18.5$ mag [195, 200].

Up to September 2021, 85 IceCube neutrino alerts (introduced in Chapter 5) were issued. Of these, 12 were subsequently retracted, as they were consistent with atmospheric neutrino background events. For two neutrinos, IC190504A and IC200227A, IceCube was unable to provide the refined *Millipede* contour after the *SplineMPE* localization. Given that the Paraboloid error used for the *SplineMPE* localizations are generally much smaller (see Section 5.3), using them would result in an overestimation of coverage and yield overly restrictive limits (see Section 6.4). As a result, these two alerts have been excluded from further analysis. The remaining 71 neutrino alerts were included as candidates for follow-up.

Figure 6.2 summarizes the follow-up status of these alerts. A full list of IceCube neutrino alerts followed up by ASAS-SN is presented in Table 6.1, while Table 6.2 contains those that could not be observed. The coverages in Table 6.1 were provided to the author by Thomas de Jaeger.

After the ToO mode was implemented in May 2017, all IceCube neutrino alerts were followed up, with images taken as quickly as

[195]: Shappee et al. (2014), *The Man behind the Curtain: X-Rays Drive the UV through NIR Variability in the 2013 Active Galactic Nucleus Outburst in NGC 2617*
[200]: Kochanek et al. (2017), *The All-Sky Automated Survey for Supernovae (ASAS-SN) Light Curve Server v1.0*

possible, in some cases within three minutes of the alert (IC190221A, IC190503A, IC200911A, IC201114A, IC201130A, IC210210A, and IC210811A). In one case (IC161103A), ASAS-SN was already observing the localization region as part of normal survey operations at the time of the neutrino's arrival, resulting in images captured 105 s before and 2.5 s after the alert. Since late 2017, a normal operations image (~18.5 mag) is generally obtained within a day unless hindered by weather, technical issues, or Sun/Moon constraints.

To ensure good image quality, ASAS-SN imposes following observational constraints: the Sun is at least 12 degrees below the horizon, the airmass is no greater than two, the hour angle is within five hours, and the distance to the Moon exceeds 20°. Out of the 71 genuine IceCube alerts, 14 were unable to be observed due to their proximity to the Sun, and one was missed because of a short observing window of less than two hours. This left 56 alerts that were followed up. The top panel in Figure 6.3 shows the cumulative number of events observed by ASAS-SN within approximately two weeks after the neutrino's detection. The right-hand side represents those observed following the neutrino's arrival. Thanks to the implemented strategy, 11 of the 56 followed-up alerts (20%) were imaged within an hour, with nine captured in under five minutes. An additional four alerts (7%) were observed within two hours, and 28 (50%) within a day. This demonstrates that the majority of IceCube alerts were observed promptly, independent of their time or location. Furthermore, 13 additional alerts were observed between 24 hours and two weeks (23%; see Figure 6.3): four within two days, two within three days, four within four days, one within five days, and two within two weeks. The longest delays in observation (IC200107A and IC201221A) were caused by visibility constraints or poor weather conditions. Within at most two weeks, all neutrino alerts were observed, that were not retracted (12), had well-defined search regions, and satisfied the observational constraints.

Serendipituous observations

The cumulative number of events serendipitously captured during routine observations is shown on the left side of the top panel in Figure 6.3. For 36 events, images were obtained within 24 hours before the alert. The localization region of one alert (IC200530A) was imaged approximately 30 minutes before the neutrino's arrival, and another event (IC161103A) was actively being observed at the time of its arrival.

Improvements by five stations

Distributions for the periods before and after mid-2019 are also displayed, marking the commissioning of all five stations, and the transition of the first stations to the g-band filter (shown as *two stations* and *five stations* in Figure 6.3, respectively). The probability of observing any given event is determined by dividing the number of followed-up events by the total number of neutrino alerts. These results are shown in the bottom panel of Figure 6.3. ASAS-SN has approximately a 60% probability of capturing observations for any given neutrino alert. The transition to the five-station configuration boosted the follow-up capabilities within one day by 50%.

Notably, for 12 out of the 71 alerts (around 17%), ASAS-SN observations are the only optical follow-up observation reported to the GCN.

Table 6.1: Summary of the 56 neutrino alerts followed up by ASAS-SN. The first three columns are the name of the alert and its coordinates. Columns four to six include the 90% rectangular localization of the neutrino as reported in the GCN, along with the fraction of this area that ASAS-SN covered within the first 24 hours and 14 days following the neutrino's arrival. Additionally, the signalness of the event and the reference to the original IceCube GCN are listed. For HESE events, no signalness values are available, so they are left out.

Event	R.A. (J2000) [deg]	Dec (J2000) [deg]	90% area [sq. deg.]	1d coverage [%]	14d coverage [%]	Signalness [%]	Refs
IC160427A	240.57	+9.34	1.4	100.0	100.0	-	[201]
IC160731A	214.50	−0.33	2.2	36.2	100.0	85	-
IC160814A	200.30	−32.40	12.0	0.0	100.0	-	-
IC161103A	40.83	+12.56	3.1	79.9	100.0	-	[202]
IC161210A	46.58	+14.98	1.7	0.0	100.0	49	[203]
IC170312A	305.15	−26.61	0.9	0.0	100.0	-	[204]
IC170321A	98.30	−15.02	5.6	4.5	100.0	28	[205]
IC170922A	77.43	+5.72	1.3	100.0	100.0	57	[206]
IC171106A	340.00	+7.40	0.7	100.0	100.0	75	[207]
IC181023A	270.18	−8.57	9.3	70.5	100.0	28	[208]
IC190104A	357.98	−26.65	18.5	14.0	100.0	-	[209]
IC190221A	268.81	−17.04	5.2	78.6	100.0	-	[210]
IC190331A	337.68	−20.70	0.4	0.0	100.0	-	[211]
IC190503A	120.28	+6.35	1.9	100.0	100.0	36	[212]
IC190619A	343.26	+10.73	27.2	100.0	100.0	55	[213]
IC190629A	27.22	+84.33	5.0	0.0	70.6	34	[214]
IC190704A	161.85	+27.11	21.0	100.0	100.0	49	[215]
IC190712A	76.46	+13.06	92.0	0.0	13.1	30	[216]
IC190730A	225.79	+10.47	5.4	100.0	100.0	67	[217]
IC190922B	5.76	−1.57	4.5	100.0	100.0	51	[218]
IC191001A	314.08	+12.94	25.5	100.0	100.0	59	[219]
IC191122A	27.25	−0.04	12.2	100.0	100.0	33	[220]
IC191204A	79.72	+2.80	11.6	98.8	100.0	33	[221]
IC191215A	285.87	+58.92	12.8	0.0	12.4	47	[222]
IC191231A	46.36	+20.42	35.6	100.0	100.0	46	[223]
IC200107A	148.18	+35.46	7.6	0.0	78.2	50*	[224]
IC200109A	164.49	+11.87	22.5	77.7	100.0	77	[225]
IC200117A	116.24	+29.14	2.9	0.0	100.0	38	[226]
IC200410A	242.58	+11.61	377.9	38.0	100.0	31	[227]
IC200425A	100.10	+53.57	18.8	7.2	100.0	48	[228]
IC200512A	295.18	+15.79	9.8	62.5	100.0	32	[229]
IC200523A	338.64	+1.75	90.6	24.5	100.0	25	[230]
IC200530A	255.37	+26.61	25.3	92.4	100.0	59	[231]
IC200614A	33.84	+31.61	47.8	35.2	100.0	42	[232]
IC200615A	142.95	+3.66	5.9	97.9	100.0	83	[233]
IC200620A	162.11	+11.95	1.7	100.0	100.0	32	[234]
IC200911A	51.11	+38.11	52.7	46.5	100.0	41	[235]
IC200916A	109.78	+14.36	4.2	100.0	100.0	32	[236]
IC200926A	96.46	−4.33	1.7	100.0	100.0	44	[237]
IC200929A	29.53	+3.47	1.1	65.1	100.0	47	[238]
IC201007A	265.17	+5.34	0.6	0.0	100.0	88	[239]
IC201021A	260.82	+14.55	6.9	2.6	100.0	30	[240]
IC201114A	105.25	+6.05	4.5	100.0	100.0	56	[241]
IC201115A	195.12	+1.38	6.6	0.0	100.0	46	[242]
IC201120A	307.53	+40.77	64.3	82.5	100.0	50	[243]
IC201130A	30.54	−12.10	5.4	100.0	100.0	15	[244]
IC201209A	6.86	−9.25	4.7	100.0	100.0	19	[245]
IC201221A	261.69	+41.81	8.9	0.0	100.0	56	[246]
IC201222A	206.37	+13.44	1.5	100.0	100.0	53	[247]
IC210210A	206.06	+4.78	2.8	100.0	100.0	65	[248]
IC210503A	143.53	+41.81	102.6	27.1	100.0	41	[249]
IC210510A	268.42	+3.81	4.0	0.0	100.0	28	[250]
IC210608A	337.41	+18.37	109.7	94.8	100.0	31	[251]
IC210629A	340.75	+12.94	6.0	100.0	100.0	35	[252]
IC210717A	46.49	−1.34	30.0	69.2	100.0	50*	[253]
IC210811A	270.79	+25.28	3.2	100.0	100.0	66	[254]

*For offline selected events, no signalness is given. Because they are promising events that were selected by hand, a signalness of 50% is assumed here

Table 6.2: Summary of the 15 neutrino alerts that could not be observed by ASAS-SN. The event name and position are given in the first three columns. The 90% rectangular localization area of the neutrino is listed in column four and the reference to the IceCube GCN in column six.

Event	R.A. (J2000) [deg]	Dec (J2000) [deg]	90% area [sq. deg.]	Reason	Refs
IC160806A	122.81	−0.81	0.0	proximity to sun	[255]
IC171015A	162.86	−15.44	14.9	proximity to sun	[256]
IC180908A	144.58	−2.13	6.3	proximity to sun	[257]
IC181014A	225.15	−34.80	10.5	proximity to sun	[258]
IC190124A	307.4	−32.18	2.0	proximity to sun	[259]
IC190819A	148.8	+1.38	9.3	proximity to sun	[260]
IC190922A	167.43	−22.39	32.2	proximity to sun	[261]
IC191119A	230.1	+3.17	61.2	proximity to sun	[262]
IC200421A	87.93	+8.23	24.4	operation	[263]
IC200806A	157.25	+47.75	1.8	proximity to sun	[264]
IC200921A	195.29	+26.24	12.0	proximity to sun	[265]
IC200926B	184.75	+32.93	9.0	proximity to sun	[237]
IC201014A	221.22	+14.44	1.9	proximity to sun	[266]
IC210516A	91.76	+9.52	2.2	proximity to sun	[267]
IC210730A	105.73	+14.79	6.6	proximity to sun	[268]

6.3 Candidate Counterparts

A full list of all ASAS-SN transients in the footprint of any IceCube alert was provided to the author by Thomas de Jaeger. Table 6.3 lists all of those in the 500 days prior to the neutrino arrival time excluding Type Ia SNe and dwarf novae (cataclysmic variables), and Figure 6.5 shows their light curves. For the motivation of the timescale see Chapter 3. It includes the pair of the TDE AT 2019dsg and IC191001A [269], but not AT 2019fdr [270], which was too faint for the transient detection pipeline (see Figure 6.10). These two coincidences will be discussed in detail in Chapter 7.

[269]: Stein et al. (2021), *A Tidal Disruption Event Coincident with a High-Energy Neutrino*
[270]: Reusch et al. (2022), *Candidate Tidal Disruption Event AT2019fdr Coincident with a High-Energy Neutrino*

Classified supernovae

The supernova SN 2019aah was spatially coincident with IC191119A. It was detected around 300 days before the neutrino alert [271] and classified 30 days after the discovery as a Type II supernovae [272]. Because there are no narrow emission lines in the spectrum, there is no evidence for a strong CSM interaction. In any case, the neutrino emission would be expected near the optical peak [106, 273], so SN 2019aah is unlikely related to the neutrino.
The type II supernova SN 2018coq [274] was spatially coincident with

[106]: Zirakashvili et al. (2016), *Type IIn Supernovae as Sources of High Energy Astrophysical Neutrinos*
[273]: Murase et al. (2019), *High-Energy Emission from Interacting Supernovae: New Constraints on Cosmic-Ray Acceleration in Dense Circumstellar Environments*

Table 6.3: The transients that occur at most 500 days before the corresponding neutrino was detected, excluding spectroscopically-confirmed type Ia supernovae and CVs where neutrino emission is not expected. The name of the transient and the Julian Date of its first ASAS-SN detection are given in the first two columns. Columns three and four list the corresponding IceCube alert, and its arrival time. In the last two column the difference between transient discovery and neutrino arrival time, and the transient type are listed.

Name	Detection time JD	IceCube alert	Alert time JD	Δt days	Type
ZTF18adicfwn (AT 2020rng)	2459089.9	IC210608A	2459373.7	-284	Unknown
ATLAS19ljj (AT 2019fxr)	2458634.9	IC200410A	2458950.5	-316	Unknown
ZTF19aapreis (AT 2019dsg)	2458618.9	IC191001A	2458758.3	-139	TDE
ZTF19aadypig (SN 2019aah)	2458519.6	IC191119A	2458806.5	-287	SN II
ASASSN-18mx (SN 2018coq)	2458286.1	IC190619A	2458654.1	-368	SN II
ASASSN-17ot (AT 2017hzv)	2458070.8	IC180908A	2458370.3	-300	Unknown

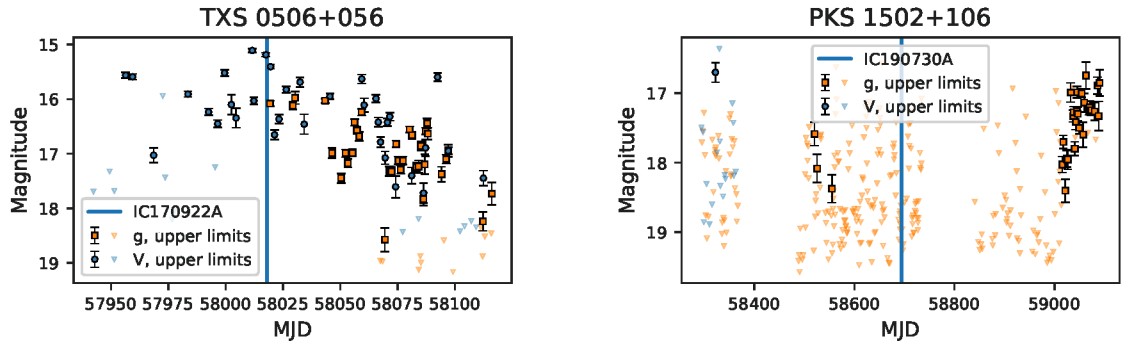

Figure 6.4: The ASAS-SN light curves of the two blazars TXS 0506+056 and PKS 1502+106 observed in spatial coincidence with high-energy neutrino alerts. TXS 0506+056 exhibited a brightening over months prior to the neutrino and reached its peak at the neutrino arrival. Datapoints with errobars are 5σ detections, and the triangles are upper limits. The date of the corresponding neutrino arrival is marked with a vertical line.

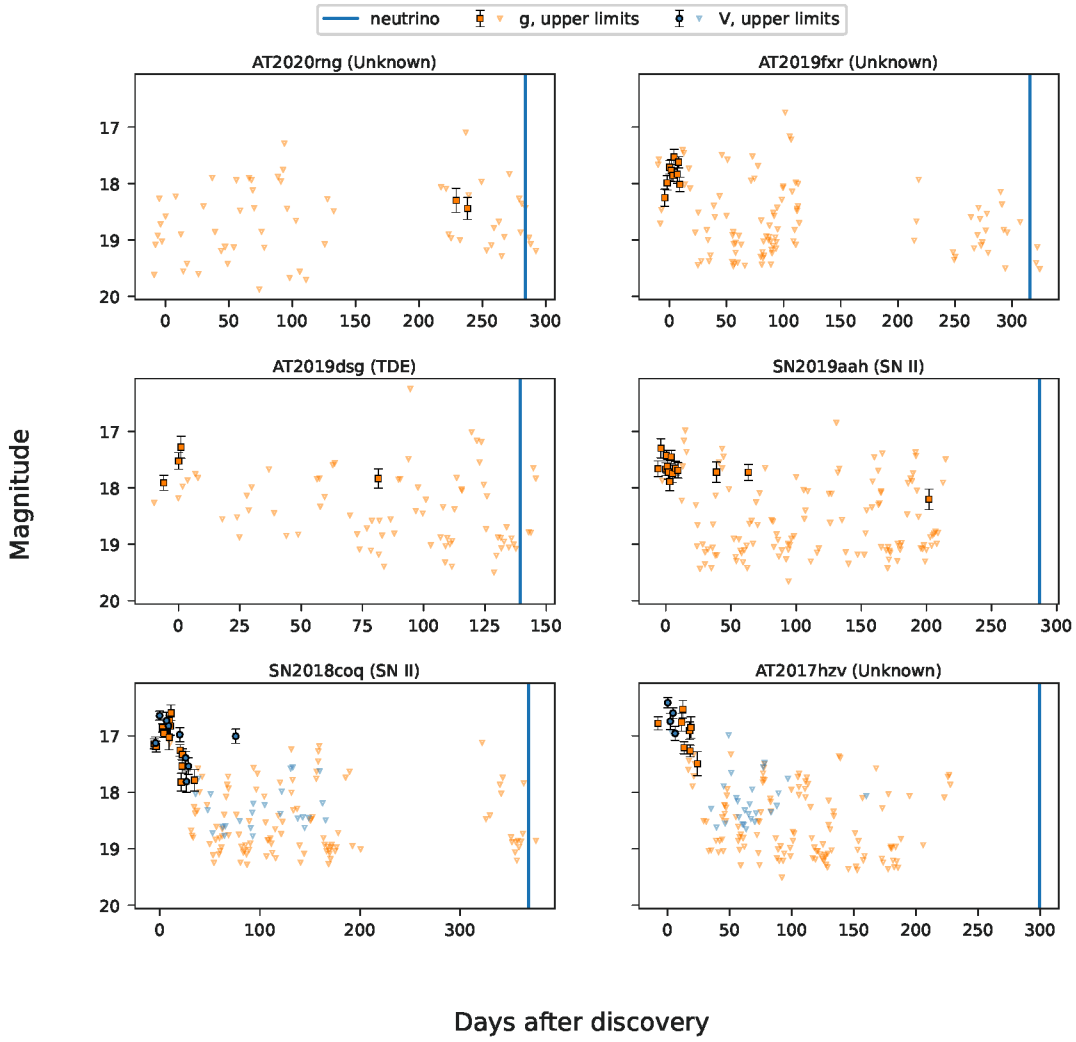

Figure 6.5: The ASAS-SN light curves for the transients found in the footprint of the IceCube neutrinos. The magnitude is shown against days after dicovery by ASAS-SN (Column 2 in Table 6.3). Datapoints with errobars are 5σ detections, and the triangles are upper limits. The time of the corresponding neutrino arrival is marked with a vertical line.

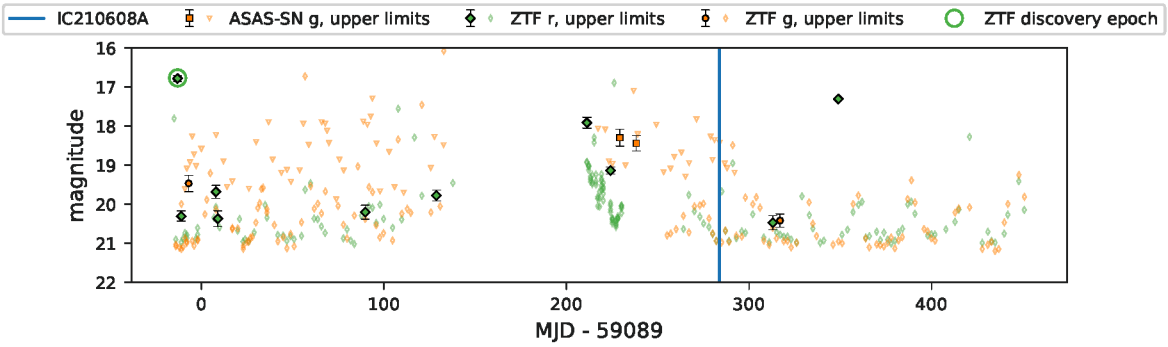

Figure 6.6: Detections and upper limits for AT 2020rng by ASAS-SN and the ZTF forced-photometry service. Datapoints with errobars are 5σ detections, and the triangles are upper limits. The date of the corresponding neutrino arrival is marked with a vertical line.

IC190619A. It was discovered 370 days prior to the neutrino alert [275]. Similar to SN 2019aah, its spectrum 13 days after the discovery does not show prominent narrow lines as a sign of CSM interaction, and because it peaked even earlier relative to the neutrino, it is unlikely related to IC190619A.

Unclassified transients

Four neutrino-coincident events were not classified. All of them were first detected more than 280 days before the corresponding neutrino arrival. AT 2017hzv [276] and AT 2019fxr [277] faded within a few weeks and were not detectable at the time of the neutrino arrival. The rapid fade suggests a supernova or AGN flare, inconsistent with the neutrino arrival time which makes it unlikely they are associated with the corresponding neutrino.
For AT 2020rng, there are only sporadic detections surrounded by upper limits in the forced-photometry data, obtained from the publicly available ZTF service [278] (see Figure 6.6). This, together with the relatively bright host galaxy with a mean g-band magnitude of 15.3 mag suggests that AT 2020rng is a subtraction artifact rather than a physical transient.
There is also no coincident flaring in any of the Fermi 4FGL-DR2 [279, 280] objects within a neutrino alert footprint. The only exception is the previously reported observations of the blazar TXS 0506+056 [47]. This light curve is shown in the top panel of Figure 6.4, with the source exhibiting a month-long brightening prior to the neutrino. It reached its eak brightness at the neutrino arrival.

The Flat Spectrum Radio Quasar (FSRQ) PKS 1502+106 was coincident with IC190730A [217, 281]. The ASAS-SN light curve (Figure 6.4) confirms that the blazar was in a low optical state at the time of the neutrino arrival [282, 283]. Time-dependent modeling found that the detection of a high-energy neutrino from this source is consistent with its multi-wavelength properties [65].

[278]: Masci et al. (2019), *The Zwicky Transient Facility: Data Processing, Products, and Archive*

[279]: Abdollahi et al. (2020), *Fermi Large Area Telescope Fourth Source Catalog*

[280]: Ballet et al. (2020), *Fermi Large Area Telescope Fourth Source Catalog Data Release 2*

[47]: IceCube Collaboration et al. (2018), *Multimessenger Observations of a Flaring Blazar Coincident with High-Energy Neutrino IceCube-170922A*

[217]: Stein (2019), *IceCube-190730A - IceCube Observation of a High-Energy Neutrino Candidate Event*

[281]: Franckowiak et al. (2020), *Patterns in the Multiwavelength Behavior of Candidate Neutrino Blazars*

6.4 Constraining the Optical Luminosity Function of Transient Neutrino Sources

The non-detections of neutrino counterparts by ASAS-SN can be used to derive limits on neutrino source luminosity functions following the method of Stein et al. [284]. Because ASAS-SN did detect

[284]: Stein et al. (2023), *Neutrino Follow-up with the Zwicky Transient Facility: Results from the First 24 Campaigns*

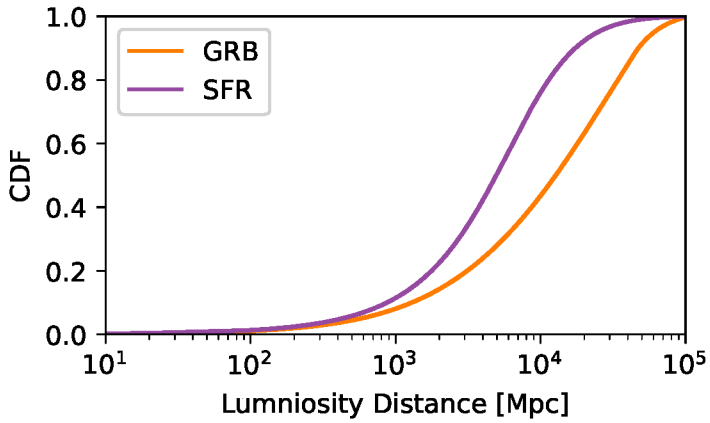

Figure 6.7: The relative cumulative neutrino flux at earth of neutrino source populations with a GRB-like and a SFR-like density evolution.

TXS 0506+056 and AT 2019dsg, these limits do not apply to blazars or TDEs.

6.4.1 Analysis Method

The method derived by Stein et al. [284] to derive upper limits from non-detections on a follow-up program like the one presented in this chapter will be reviewed in the following. The probability that no counterpart is detected is

$$P_{\text{no counterpart}}(M) = \prod_i [1 - P_{\text{find,i}}(M)] \tag{6.1}$$

for an absolute magnitude limit M, where i goes over all neutrino events. The probability of detecting an electromagnetic counterpart to the i-th neutrino is

$$P_{\text{find,i}}(M) = P_{\text{astro}} \cdot P_{\text{obs}} \cdot P_{\text{detectable}}(M) \cdot F_{\text{L}}(M). \tag{6.2}$$

It depends on the probability P_{astro} that the neutrino is of astrophysical origin, the probability P_{obs} that the counterpart was observed, and the probability that it was detected $P_{\text{detectable}}$, as well as the fraction of astrophysical sources $F_{\text{L}}(M)$ brighter than M. The latter is the luminosity function to be constrained. P_{astro} is given by the signalness, and P_{obs} is the observational coverage of the neutrino localization. $P_{\text{detectable}}(M)$ is a combination of the assumed detection efficiency ϵ, and the normalized redshift distribution $P_{\text{dist}}(z)$ of the assumed source population:

Detection probability

$$P_{\text{detectable}}(M) = \int_0^\infty \epsilon[m(M,z)] \cdot P_{\text{dist}}(z)\,\mathrm{d}z. \tag{6.3}$$

The detection efficiency is a function of the apparent magnitude m and is, in general, a continuous function that drops towards dimmer transients. Here, the simplifying assumption is that a transient is detected if it is above a limiting magnitude and not detected if it is below. The limiting magnitudes are 16.5 mag in V-band and 17.5 mag in g-band, respectively [285]. The apparent magnitude as a function of the absolute magnitude and the luminosity distance d_{L}

[285]: Desai et al. (2024), *Supernova Rates and Luminosity Functions from ASAS-SN I: 2014–2017 Type Ia SNe and Their Sub-Types*

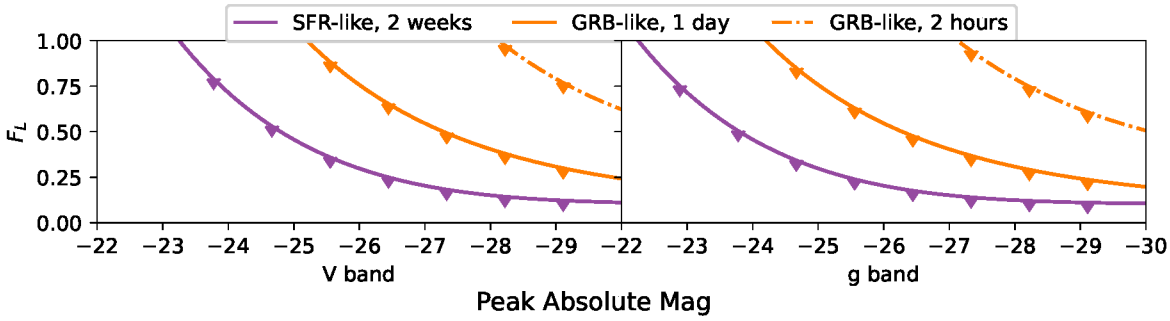

Figure 6.8: Constraints on the fraction F_{L} of a neutrino source population as a function of the intrinsic peak absolute magnitude in V and g-band.

[286]: Ryden (2016), *Introduction to Cosmology*

is [286, Chapter 6]

$$m = 5 \log_{10} \left(\frac{d_{\mathrm{L}}(z)}{1\,\mathrm{Mpc}} \right) + 25 + M. \tag{6.4}$$

The redshift distribution $P_{\mathrm{dist}}(z)$ is derived as Equation 8.24 in Chapter 8. It depends on the rate density evolution $\rho(z)$ of the transient population. The CDF of the neutrino flux at earth of transients following the star formation rate (SFR) and for GRBs is shown in Figure 6.7.

Finally, for each value of M, Equation 6.1 can be numerically inverted to find the value of $F_{\mathrm{L}}(M)$, such that $P_{\text{no counterpart}} > 0.1$. This is then the upper limit at 90% confidence level on the luminosity function.

6.4.2 Results

The area fraction observed of each neutrino localization is listed in Table 6.1 for one and fourteen days after the neutrino arrival, along with the signalness. Using these, the fraction of neutrino sources above the quoted limiting magnitude can be no more than 39.3% and 15.3% for fast transients which reach their peak within two hours and one day, respectively. For transients that peak within fourteen days, the fraction is 10.3%. These are constraints only on the visibility and do not yet include an assumption about the physical origin.

Physical populations can be constrained by considering the GRB-like [287], and SFR-like [288] source evolution models shown in Figure 6.7. Because the optical afterglow of a GRB rapidly fades on the timescale of a few days [289], the coverages for two hours and one day are used. Interacting supernovae typically rise on a timescale of at least two weeks [290], so the for after 14 days is applied. The resulting luminosity function limits are shown in Figure 6.8.

These results are not yet constraining for typical supernovae with absolute magnitudes up to around −21.5. The constraints for a GRB-like source evolution for one day after the neutrino arrival is the first on this timescale, owing to the high observation cadence and rapid follow-up of ASAS-SN. If GRBs are neutrino emitters only for

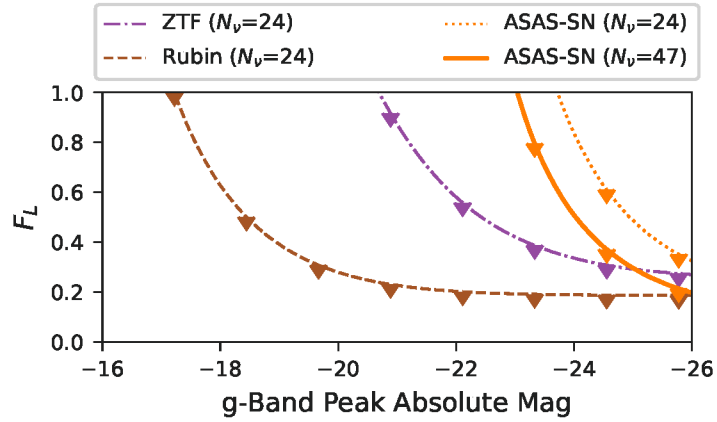

Figure 6.9: Comparison of the ASAS-SN limits to ZTF [284] and the expected performance of the Vera Rubin Observatory. Shown are the ASAS-SN limits based on the same 24 alerts used in the ZTF analysis as well as limits based on all 47 alerts that were observable by ASAS-SN in the ZTF analysis period.

a short time after explosion, for example, only 55% can be brighter than −27 mag in V-band and about 40% in g-band, one day after the neutrino arrival.

Figure 6.9 compares the limits on an SFR-like population from ASAS-SN with those obtained by ZTF [284]. ZTF observed the locations of 24 neutrino alerts between March 20, 2018, and December 31, 2021. Due to higher sensitivity ($g < 21$), the limits are more stringent than those derived from ASAS-SN's follow-up of the same 24 neutrino alerts (orange dotted line in Figure 6.9). The forthcoming *Vera Rubin Observatory* (VRO) [291], with its increased sensitivity[3] ($g < 24$), will start to probe the luminosity space down to typical supernovae brightness (brown dashed line). ASAS-SN's large sky coverage and high cadence allowed the follow-up of 48 alerts during the ZTF analysis period. However, Figure 6.9 illustrates that deeper observations, like those offered by the VRO, will be crucial in probing the luminosity functions of potential candidate populations.

[291]: Ivezić et al. (2019), *LSST: From Science Drivers to Reference Design and Anticipated Data Products*

3: The detailed VRO survey chracteristics are ignored here and it is just assumed it will be able to follow-up all alerts that ZTF can.

6.5 Conclusion

This chapter presented the results of the ASAS-SN neutrino follow-up program. It showed the capabilities of an optical time-domain survey to probe candidate transient neutrino source populations.

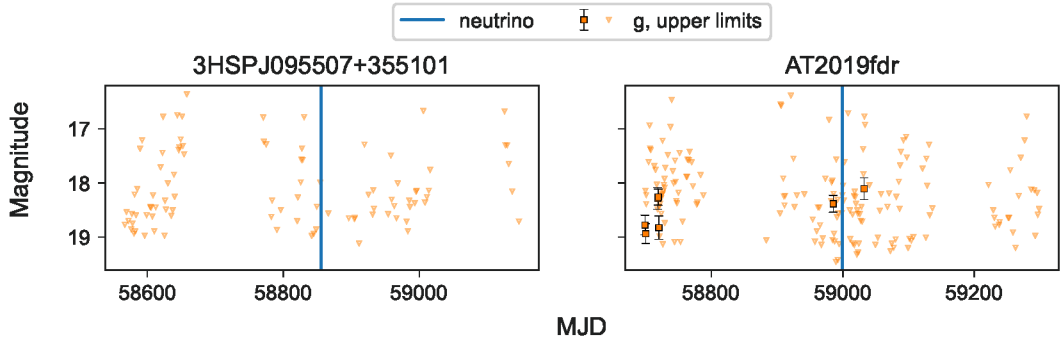

Figure 6.10: ASAS-SN upper limits for AT 2019fdr and 3HSP J095507+355101. Datapoints with errobars are 5σ detections, and the triangles are upper limits. The time of the corresponding neutrino arrival is marked with a vertical line.

The non-detections can be used to at least constrain possible source populations. It turned out that ASAS-SN is not sensitive enough to rule out candidates like supernovae. About 20 neutrino alerts are expected per year if the IceCube stream does not change. With the average ASAS-SN coverage of 18% after two hours and 94% after 14 days, the limits will be twice as strict for GRBs in 3.5 years, and for CCSNe in 3 years, respectively.

Although AT 2019dsg and TXS 0506+056 were the only EM counterparts that ASAS-SN could detect, other candidate counterparts have been reported. As mentioned above, the candidate TDE AT 2019fdr was reported in coincidence with IC200530A [270]. Also, the blazar 3HSP J095507+355101 is in the footprint of IC200107A, and was flaring at neutrino arrival [292, 293]. Both sources were too dim to be detected by the ASAS-SN transient discovery pipeline, although the corresponding sky location was observed within one day of the neutrino event (see Figure 6.10). The limitations of this search are therefore clearly set by the sensitivity rather than the sky coverage or cadence, which is also seen in Figure 6.9.

As already mentioned, ZTF is a sky survey with greater depth that is already in operation, and also conduction neutrino follow-up. The next chapter will introduce this program and discuss the discovery of AT 2019dsg and AT 2019fdr.

[270]: Reusch et al. (2022), *Candidate Tidal Disruption Event AT2019fdr Coincident with a High-Energy Neutrino*

[292]: Giommi et al. (2020), *3HSP J095507.9+355101: A Flaring Extreme Blazar Coincident in Space and Time with IceCube-200107A*

[293]: Paliya et al. (2020), *Multifrequency Observations of the Candidate Neutrino-emitting Blazar BZB J0955+3551*

Follow-Up of High-Energy Neutrino Alerts with ZTF

7

The follow-up program introduced in the previous chapter did not find any new counterparts to high-energy neutrino alerts sent by IceCube, attributed to its limited sensitivity. The *Zwicky Transient Facility* (ZTF) is a survey telescope conducting a similar program. The telescope and related systems are first introduced in Section 7.1, and the neutrino follow-up program in Section 7.2. The detections of TDEs will be reviewed finally in Section 7.3. The author contributed to scheduling observations, as well as the identification and classification of interesting transients. This includes contributions to the software packages *planobs* and *nuztf*, introduced in Section 7.2, as well as conducting spectroscopic observations of which three examples are shown in Section 7.2.2.

7.1 The Zwicky Transient Facility

ZTF is a camera system built into the 48-inch Samuel Oschin Telescope at Palomar Observatory [294]. This is a Schmidt-design telescope [295], where the light is reflected by a 1.2 m mirror at the back of the telescope onto a focal plane inside the tube, resulting in a wide 47 sqd FoV [296]. An overview of the main parts is given in Figure 7.1. The light is collected by the camera, consisting of sixteen 6144×6160 pixel CCDs, covering the whole telescope FoV. They are mounted on a cryostat to keep the assembly at operating temperature. The five CCD controllers (one per CCD mosaic quadrant and one for pixels used for focus) called *Archon* are installed on the exterior of the telescope tube. Because the cryostat window induced aberration, the so-called aspheric trim plate was mounted at the entrance of the telescope tube to counteract this effect [296].
Three filters facilitate observations in the g, r and i-band, illustrated in Figure A.1 in Appendix A. The active filter is mounted in front of the cryostat window, while the others are stored in a closet attached to a pre-existing tube access port. A robotic arm, manufactured by KUKA, is used to exchange the filters [296].
Because a conventional shutter near the focal plane would have obscured too much of the light path and effectively reduced the FoV, a shutter in the pupil plane was developed for ZTF. It is a bi-parting design, attached to the telescope exterior, in front of the corrector plate that can open or close in just 290 ms[296].
To also further mitigate stray light, additional baffles were installed inside the tube [296].
Together with other upgrades to the software, electrical and mechanical infrastructure, this allows the robotic operation of the telescope.

Observing System

[294]: Harrington (1952), *The 48-Inch Schmidt-type Telescope at Palomar Observatory*

[295]: Schmidt (1938), *Ein Lichtstarkes Komafreies Spiegelsystem*

[296]: Dekany et al. (2020), *The Zwicky Transient Facility: Observing System*

Dedicated software handles the robotic scheduling of observations [297]. It maximizes the probed volume per night, or volumetric survey speed [298] while respecting the balance between several observing programs and their cadence. The first phase of ZTF

Surveys and scheduling

[297]: Bellm et al. (2019), *The Zwicky Transient Facility: Surveys and Scheduler*

[298]: Bellm (2016), *Volumetric Survey Speed: A Figure of Merit for Transient Surveys*

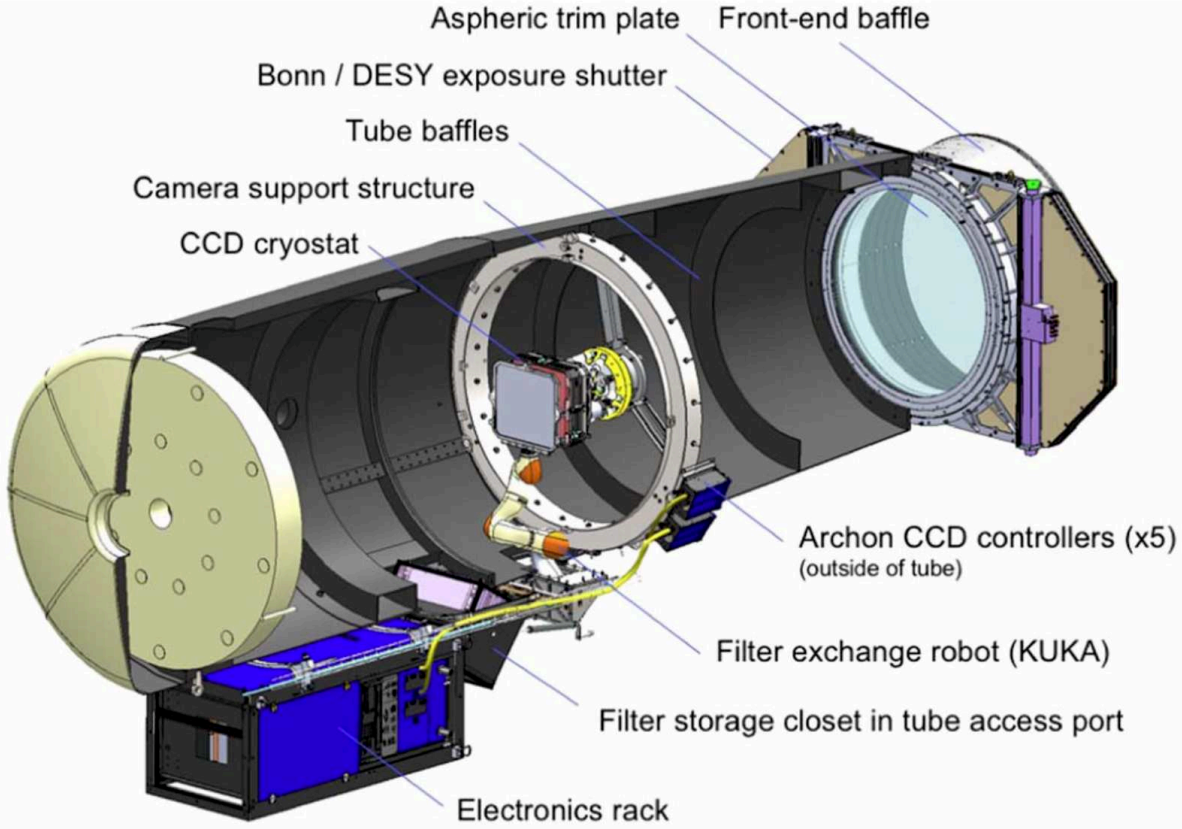

Figure 7.1: ZTF observing system overview. Taken from Dekany et al. [296]

until September 2020, had There are three observing programs: Caltech selected surveys, surveys designed by members of the ZTF collaboration and a public survey. The public survey is again divided into a survey of the northern sky above a declination of $\delta = -31°$ and outside the galactic plane[1] and a galactic plane survey [297]. Since September 2020, the northern sky survey is allocated 50% of the observation time, enabling a cadence of two nights in g and r-band*. Typical observations of 30 s reach a 5σ depth of 21 mag_{AB} in r-band [299]. The ZTF scheduling selects pointing fields based on a fixed grid, with an average overlap of 0.29° in R.A and 0.26° in declination, covering 87.5% of the sky [297].

1: The galactic plane here is defined by the galactic latitude $|b| \leq 7°$

[299]: Bellm et al. (2018), *The Zwicky Transient Facility: System Overview, Performance, and First Results*

Transient Detection

The pipeline for processing ZTF images was developed to provide results in near real-time, within 20 min of the exposure [278]. The instrumental calibration is the first step of this pipeline, using the Gaia catalog [300] as an astrometric reference, and selected sources from *Panoramic Survey Telescope And Rapid Response System* (Pan-STARRS) [301] as photometric reference. The second step is the subtraction of a reference image from the science exposure, based on the *ZOGY* algorithm [302]. Transient detection in the difference images is done with *SExtractor* [199]. Machine learning techniques are used to separate real transients from image subtraction artifacts and identify streaks caused by satellites or near-earth objects [303]. Information on the detected transients is packaged as *Avro*† alerts,

[278]: Masci et al. (2019), *The Zwicky Transient Facility: Data Processing, Products, and Archive*

[303]: Mahabal et al. (2019), *Machine Learning for the Zwicky Transient Facility*

* https://irsa.ipac.caltech.edu/data/ZTF/docs/releases/ztf_release_notes_latest

† https://avro.apache.org

distributed to the science community, and also archived [304].

[304]: Patterson et al. (2018), *The Zwicky Transient Facility Alert Distribution System*

7.2 The ZTF Neutrino Program

Similar to ASAS-SN, ZTF is following up IceCube high-energy neutrino alerts with the aim of detecting optical counterparts [284]. The details of this program and individual contributions by the author to classify candidate counterparts are presented in the following. Section 7.2.1 introduces the scheduling observations, performance, and candidate selection. Then Section 7.2.2 shows three example candidates and the analysis of their spectroscopic counterparts. The program also yielded general limits on transient neutrino source population that were not detected [284], similar to the one derived from ASAS-SN in the previous chapter. The ZTF limits are already shown in Figure 6.9 and will not be discussed here again.

[284]: Stein et al. (2023), *Neutrino Follow-up with the Zwicky Transient Facility: Results from the First 24 Campaigns*

7.2.1 Follow-up Strategy

ZTF follows-up high-quality IceCube neutrino alerts (see Chapter 5), that have a signalness greater than 50%, or a 90% localization region smaller than 10 sqd. To avoid many foreground stars contaminating the exposure, neutrinos at a galactic latitude of $|b| < 10°$ are excluded. A single pointing can typically cover the whole localization region. The corresponding field is observed several times. The first two observations are scheduled in g and r-band for 300 s, reaching a typical limiting magnitude of 21.5. The observations are separated by at least 15 minutes to identify moving objects as explained below. followed by 30 s exposures with a cadence of roughly two days. In practice, planning and scheduling observations is done with *planobs*[305]. Serendipitous coverage as part of the northern sky survey is also expected. On average, the first observation happens within around twelve hours after the neutrino arrival [284]. The observations are processed by the standard ZTF pipeline as described in the previous section. The dedicated software *nuztf*[2] [306] filters the generated alerts to extract candidate counterparts within the neutrino's 90% uncertainty region and reject the following cases:

[305]: Reusch et al. (2023), *Simeonreusch/-Planobs: Release 0.7.3*

2: *nuztf* uses the *Alert Management, Photometry, and Evaluation of Light curves* (AMPEL) software to efficiently filter through candidates.

[306]: Stein et al. (2021), *Desy-Multimessenger/Nuztf: V2.1.0 Release*

Image artifacts can be removed with the machine learning classification provided by the ZTF pipeline.

Moving objects are identified by the ZTF pipeline by a match to known solar system objects. Additionally, the *nuztf* filtering requires multiple detections at least 15 min apart.

Stars are rejected, if the match by the ZTF pipeline to the Gaia catalog has a non-zero parallax measurement with at least 3σ significance. Also, a machine learning classification [307] of the matched Pan-STARRS object is used to identify stars if the stellar probability is greater than 80%.

AGN are identified by the infrared colors [308] listed in the AllWISE Source catalog (introduced in detail in Chapter 9). They are not immediately rejected but flagged.

[307]: Tachibana et al. (2018), *A Morphological Classification Model to Identify Unresolved PanSTARRS1 Sources: Application in the ZTF Real-time Pipeline*

[308]: Stern et al. (2012), *Mid-Infrared Selection of Active Galactic Nuclei with the Wide-Field Infrared Survey Explorer. I. Characterizing WISE-Selected Active Galactic Nuclei in COSMOS*

Promising candidates are selected for follow-up spectroscopy to investigate whether they are part of the candidate neutrino source

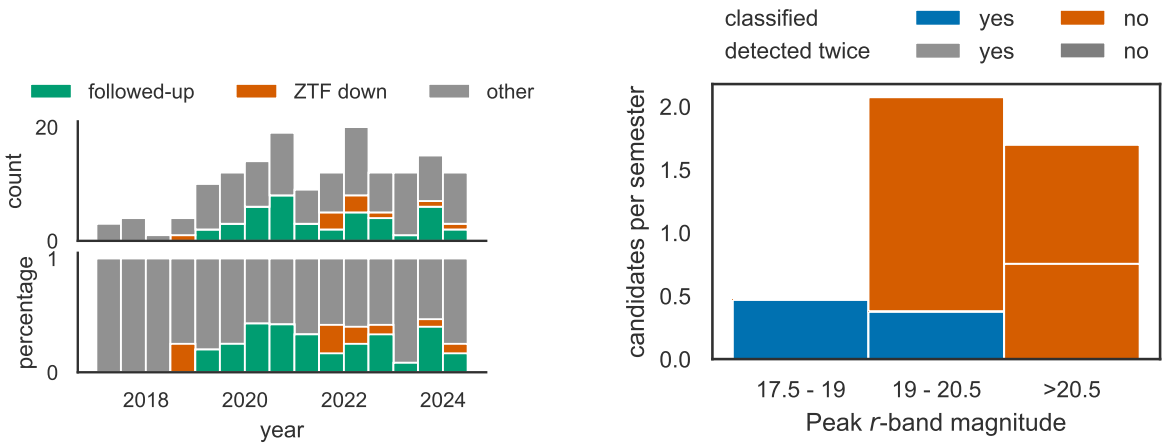

Figure 7.2: Performance plots of the ZTF neutrino follow-up program. Left: Number (top) and percentage (bottom) of high-energy neutrino alerts followed up by ZTF over time. The green histogram is the followed-up alerts, while the red bars are the alerts that ZTF missed due to operations. All others (gray) could not be followed up for non-ZTF related reasons. Right: Brightness of classified and unclassified candidate counterparts found in ZTF neutrino follow-up. The mean number of candidates is shown against their peak brightness in *r*-band.

populations discussed in Chapter 3. The author's contribution to the follow-up program was scheduling the ZTF observations, analyzing the counterparts, conducting follow-up spectroscopy and apply for the spectroscopic resources.

In total, 42 neutrinos were followed up until today[3], amounting to 25% of the 167 alerts issued so far. Only 6% were missed due to ZTF operations while 69% were either not observable or did not meet the quality criteria of the follow-up program. The left plot in Figure 7.2 shows the number and percentage of followed-up neutrinos over time. The increase after 2019 is due to the *V2* update of the IceCube alert stream [309] (see Chapter 5). The large number of missed neutrinos in late 2021 and early 2022 is due to problems with the ZTF camera.

The right plot of Figure 7.2 shows the peak brightness and average number of discovered candidate counterparts per semester. The aim is to classify all candidates brighter than 20.5 $\mathrm{mag_{AB}}$. On average, for 1.5 objects per semester the additional spectroscopic resources are needed for classification. Three examples are presented in the following.

7.2.2 Selected Candidate Counterparts

The following transients were identified as possible neutrino counterparts in the ZTF neutrino follow-up. For those, the author applied for, scheduled and analyzed the spectroscopic observations at the *Nordical Optical Telescope* (NOT) with the *Alhambra Faint Object Spectrograph and Camera* (ALFOSC). Data reduction was performed using *pypeit* [310, 311]

3: 30th September 2024

[309]: Blaufuss et al. (2019), *The Next Generation of IceCube Real-time Neutrino Alerts*

[310]: Prochaska et al. (2020), *Pypeit/PypeIt: Release 1.0.0*

[311]: Prochaska et al. (2020), *PypeIt: The Python Spectroscopic Data Reduction Pipeline*

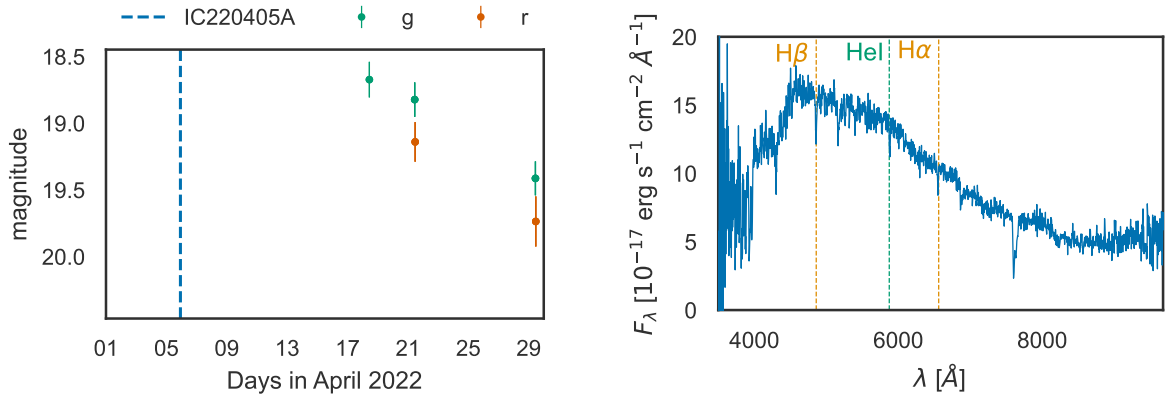

Figure 7.3: Left: The ZTF light curve of ZTF19aavnpjv. The blue-dashed line marks the detection of the corresponding neutrino. Right: The spectrum of ZTF19aavnpjv taken with ALFOSC. The spectral flux is shown against the wavelength. Vertical lines indicate the identified absorption features. Line wavelengths are taken from A. Kramida et al. [35]

ZTF19aavnpjv

ZTF19aavnpjv was identified as a candidate counterpart of IC220405B [312, 313], detected on April 5th, 2022. The transient was detected towards the end of the ToO observations, and faded over the next couple of days (see Figure 7.3 on the left), prompting the possibility of a supernova with an explosion time consistent with the neutrino arrival. The spectroscopic observation took place on May 5th, and the resulting spectrum is shown in Figure 7.3 on the right. It shows absorption features, characteristic for stars. The balmer lines Hα and Hβ and the Helium line at 5876 AA are visible at $z = 0$, confirming that the object is galactic. Together with the variable lightcurve, this object is likely a cataclysmic variable (CV), which is not considered a potential neutrino source [314].

[312]: IceCube Collaboration (2022), *IceCube-220405A - IceCube Observation of a High-Energy Neutrino Candidate Track-like Event*

[313]: Necker et al. (2022), *IceCube-220405B: No Candidate Counterparts from the Zwicky Transient Facility*

[314]: Necker et al. (2022), *IceCube-220405B - ZTF19aavnpjv Unrelated*

ZTF19adgzidh / AT 2021bei

During the follow-up of IC220624A [315], ZTF19adgzidh was identified as a possible candidate counterpart. Its central location in the host galaxy and the brightening of about one magnitude (see Figure 7.4 on the left) could indicate activity connected to the central SMBH, such as a TDE. However, the spectrum, shown in Figure 7.4 on the right, is typical for an AGN, with the broad Balmer, and prominent Oxygen and Magnesium emission lines [316, Chapter 24] at a consistent redshift of $z = 0.4760$. Although the flux increase of around 80% within two months is beyond usual AGN variability (see Section 3.1), this alone is not enough to claim a physical connection. The transient can thus not unambiguously be linked to the neutrino [317].

[315]: IceCube Collaboration (2022), *IceCube-220624A - IceCube Observation of a High-Energy Neutrino Candidate Track-like Event*

[316]: Cox (1999), *Allen's Astrophysical Quantities*

[317]: Stein et al. (2022), *IceCube-220624A: Classification of AT2022nit as a Type Ia Supernova and AT2021bei as an AGN*

ZTF23abidzvf / AT 2023uqf

This transient was identified as a counterpart of IC231004A [123, 318]. It has a sharp rise to maximum of only around two days, and fades again below the ZTF detection threshold in about eight days, as shown in Figure 7.5 on the left. If it is a supernova, the explosion time

[123]: Reusch et al. (2023), *IceCube-231004A: One Candidate Counterpart from the Zwicky Transient Facility*

[318]: IceCube Collaboration (2023), *IceCube-231004A - IceCube Observation of a High-Energy Neutrino Candidate Track-like Event*

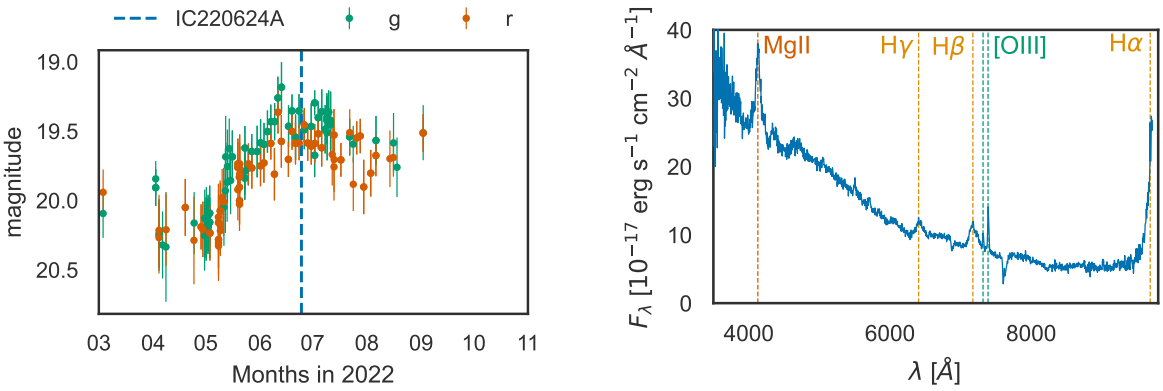

Figure 7.4: Same as Figure 7.3 but for ZTF19adgzidh

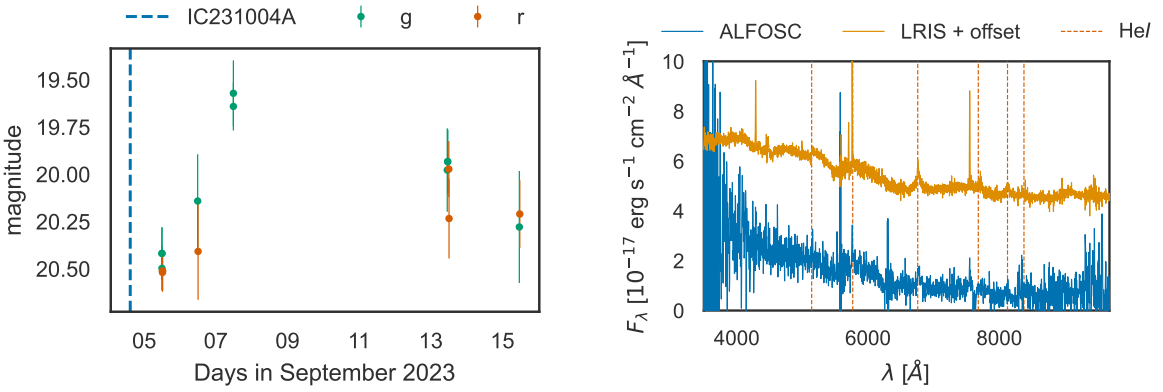

Figure 7.5: Same as Figure 7.3 but for ZTF23abidzvf. The higher-resolution LRIS spectrum shown for comparison was taken by Viraj Karambelkar and Robert Stein.

seems consistent with the neutrino arrival. The right side of Figure 7.5 shows the spectrum taken with ALFOSC, which is noisy because the transient is faint and so no spectral features are visible from this spectrum alone. However, a higher resolution spectrum taken with the *Low-Resolution Imaging Spectrograph* (LRIS) [319] at Keck-I observatory reveals medium width helium lines, likely coming from the interaction of ejecta with helium rich CSM. Because no hydrogen lines are visible, the transient is likely a supernova Ibn [124], the explosion of a star that has lost its outer hydrogen shell prior to explosion. As explained in Chapter 3, the consistency of explosion time and neutrino arrival could indicate neutrino production by a choked jet. Another possibility is neutrino production through the CSM interaction. Thus, ZTF23abidzvf is considered a promising source candidate.

[319]: Oke et al. (1995), *The Keck Low-Resolution Imaging Spectrometer*

[124]: Stein et al. (2023), *IC231004A: Classification of AT2023uqf/ZTF23abidzvf as a Rapidly-Evolving Supernova with CSM Interaction*

7.3 TDEs in Coincidence with High-Energy Neutrinos

The most prominent result of the ZTF neutrino program is the association of two (likely) TDE with high-energy neutrinos. Although the author was not actively involved in these analyses, a review of

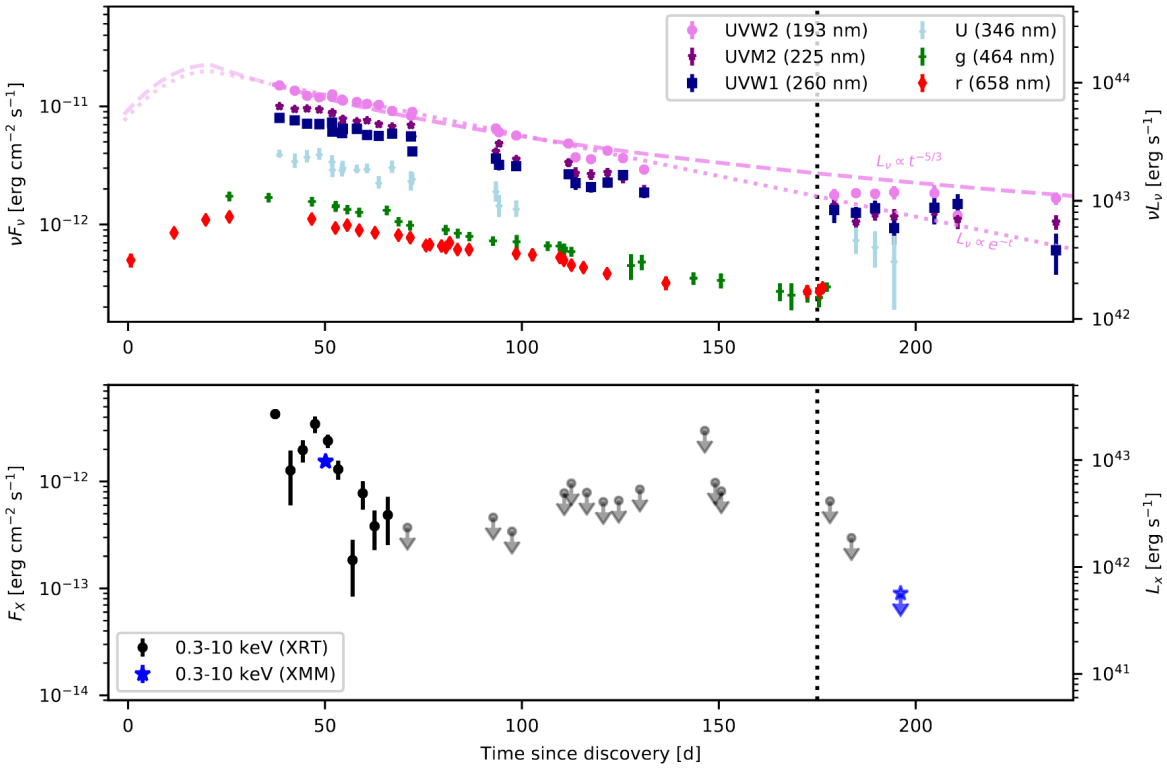

Figure 7.6: Multi-wavelength lightcurve of AT 2019dsg. The top panel shows optical and UV data. *U*-band and UV photometry are from Swift, *g* and *r*-band data from ZTF. Z-ray data from Swift XRT and XMM Newton is shown in the bottom panel. Arrows mark 3σ upper limits from XRT. The vertical dotted line is the arrival of IC191001A. Taken from Stein et al. [269]

these discoveries is important here in the context of the following parts of this thesis.

The observation of the neutrino IC191001A revealed the TDE AT 2019dsg in the footprint [269] which had been classified based on the optical spectrum [320]. The multi-wavelength light curve (Figure 7.6) shows that the neutrino arrives around 150 days after the optical peak. Thermal spectra describe both the OUV and X-ray emissions well with temperatures of around 3.2×10^4 K and 8×10^5 K, respectively [269], and the decline of the UV lightcurve follows approximately $t^{-5/3}$ until around 130 days after discovery. Additionally, radio detections indicate the presence of non-thermal electrons. In particular, the energy injection seems continuous, indicating an energy transfer from the accretion to particle acceleration. The mass of the host SMBH is around $3 \times 10^7 M_\odot$ [269]. All these observations are in line with a TDE origin (see Chapter 3).
The derived magnetic fields are sufficiently high to contain accelerated protons within the source, and the X-ray and/or UV photon densities would enable high-energy neutrino production [269], making the TDE AT 2019dsg the likely source of IC191001A.

AT 2019dsg

[269]: Stein et al. (2021), *A Tidal Disruption Event Coincident with a High-Energy Neutrino*
[320]: Nicholl et al. (2019), *ePESSTO+ Classification of Optical Transients*

The nuclear flare AT 2019fdr was identified as a possible counterpart to IC200530A [270]. It was initially classified as a SLSN-II based on its optical spectrum [321, 322]. However, long-lived OUV emission (see Figure 7.7), the proximity to the host center, late time X-ray detections showing a soft, thermal spectrum, and other spectroscopic characteristics make it more likely a flare connected to the SMBH. It could be a TDE, although an extreme AGN flare cannot be ruled

AT 2019fdr

[270]: Reusch et al. (2022), *Candidate Tidal Disruption Event AT2019fdr Coincident with a High-Energy Neutrino*

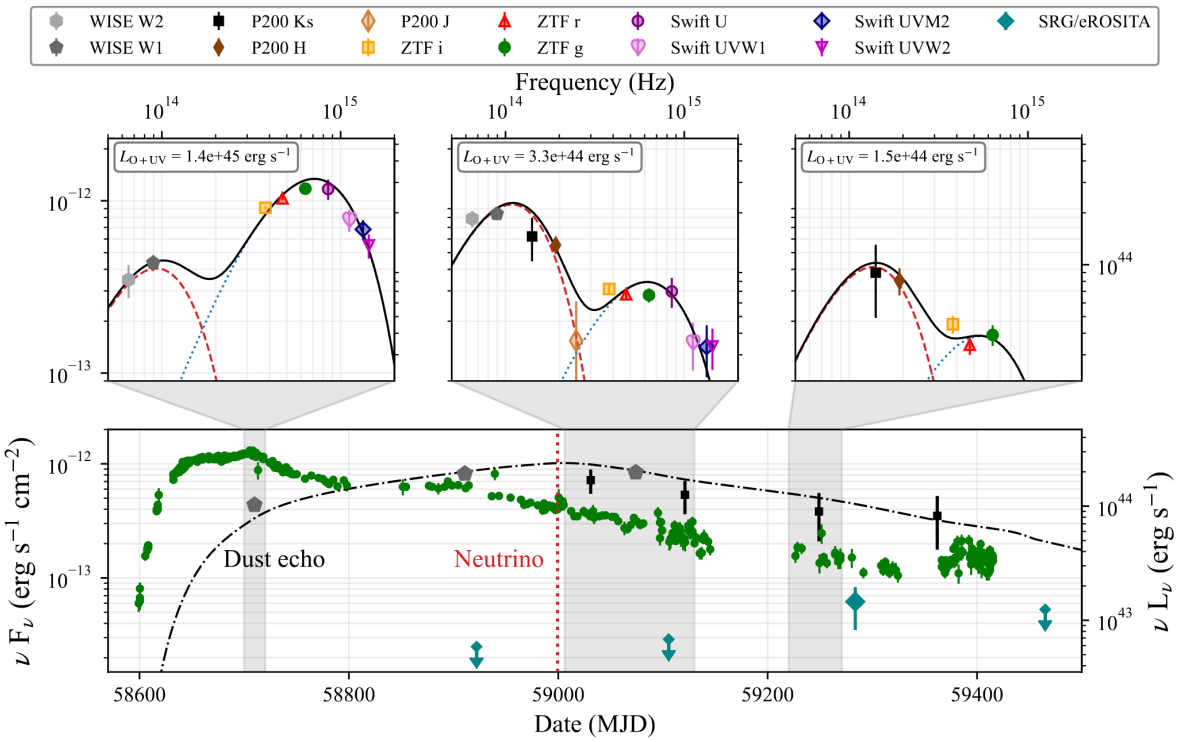

Figure 7.7: Evolution of AT 2019fdr. The bottom panel shows the light curve in the optical (ZTF *g*-band), infrared (WISE W1 and P200 *Ks*), and X-rays. The dash-dotted lines is a model fit of the dust echo infrared light curve, and the dotted vertical line marks the neutrino arrival. The top panel shows the spectral energy distributions (SEDs) of the three epochs indicated in the bottom panel, where the lines indicate the fitted blackbodies. Taken from Reusch et al. [270].

out [270, 323]. The OUV is well described by a blackbody with a temperature of 1.4×10^4 to 1.0×10^4 K, and the X-ray blackbody has a temperature of about 6.5×10^5 K. Its host is a known active galaxy with a SMBH mass of around $10^{7.5} M_\odot$. *Wide-Field Infrared Survey Explorer* (WISE) infrared observations also reveal a delayed flare, interpreted as a dust echo, which will be discussed in detail in the next chapter. The combined model for the infrared and OUV blackbody can be seen in the top row of Figure 7.7, and the modeled dust echo light curve in the bottom panel. This enables the estimation of the total bolometric energy output to be around 3.4×10^{52} erg, making AT 2019fdr one of the most luminous transients ever [270]. Although it is not a clear TDE like AT 2019dsg, it might be a TDE in an AGN. In any case, it is a flare due to enhanced accretion onto the SMBH.

Sufficient proton acceleration and neutrino production are possible in the corona of the accretion disk, sub-relativistic winds or relativistic jets [93, 324], making AT 2019fdr the likely source of IC200530A.

[93]: Murase et al. (2020), *High-Energy Neutrino and Gamma-Ray Emission from Tidal Disruption Events*
[324]: Winter et al. (2021), *A Concordance Scenario for the Observed Neutrino from a Tidal Disruption Event*

Chance coincidence

Taking these two as part of a broader population of TDE-like flares, the probability of the associations happening by chance is only around 3.4×10^{-4} [270]. The implied contribution of TDEs to the diffuse astrophysical neutrino flux is 7.8% [269, 270] which is compatible with the limits from IceCube stacking analyses (see Chapter 3). However, as mentioned above, AT 2019fdr exhibits a strong dust echo. It turns out that the same is true for AT 2019dsg and might be in general important for high-energy neutrino production. The details and implications for the neutrino emitting population will

be discussed in detail in the next chapter.

High-Energy Neutrinos and Infrared Flares

High-Energy Neutrinos and Giant Infrared Flares

8

The previous chapter described the observation of two TDEs in coincidence with high-energy neutrino alerts. It turns out that, in addition to the neutrino association, they have a luminous infrared signal in common, delayed with respect to the optical lightcurve. These are reverberations of a dusty region around the central black hole, called dust echoes. The theory behind these dust echoes will be reviewed in Section 8.1, before discussing further observations of neutrinos and infrared flares and their interpretation in Section 8.2. The author used the re-simulation method developed in Section 5.5 to test the robustness of the reported coincidences in Section 8.2.2. Based on the neutrino coincidences, the author performed a stacking analysis, which is presented in Section 8.3 before concluding in Section 8.4.

8.1 Tidal Disruption Event Dust Echoes

When matter is accreted onto a supermassive black hole (SMBH), it forms a luminous accretion disk, which dissipates gravitational energy across the electromagnetic spectrum [56, 57]. Dust in the vicinity can efficiently absorb the radiation and re-emit it in the mid-infrared [325–329], which is called a dust echo.

Infrared Spectrum

[325]: Rees et al. (1969), *Infrared Radiation from Dust in Seyfert Galaxies*
[327]: Barvainis (1987), *Hot Dust and the Near-Infrared Bump in the Continuum Spectra of Quasars and Active Galactic Nuclei*

The spectrum of a single dust grain with radius a and at a temperature T is given by a modified blackbody spectrum [325, 327]:

$$L_\nu^{\mathrm{gr}} = 4\pi a^2 \, \pi Q_\nu^{\mathrm{IR}} B_\nu(T). \tag{8.1}$$

$B_\nu(T)$ is the blackbody spectrum at frequency ν and temperature T. Q_ν^{IR} describes the dust absorption efficiency in the IR and is generally modeled as a power-law [330]:

$$Q_\nu^{\mathrm{IR}} = \left(\frac{2\pi a}{c}\nu\right)^{\alpha}, \tag{8.2}$$

where the spectral index is $\alpha = 1 - 2$ for typical grain sizes. Note that this modified blackbody spectrum behaves like the standard blackbody under the cosmological redshift: The spectral shape does not change, only the temperature decreases: $T = T_0/(1+z)$.

Sublimation

Close to the SMBH, the irradiation is too intense for the dust to remain stable. Only at greater distances can it persist in thermal equilibrium. This is the case when the emitted energy and absorbed energy are equal. From this condition, one can derive the relation between radius and dust temperature given the luminosity L of the central source [327, 331, 332]:

$$R = C^{-\frac{1}{2}} L^{\frac{1}{2}} T^{-\frac{4+\alpha}{2}}, \tag{8.3}$$

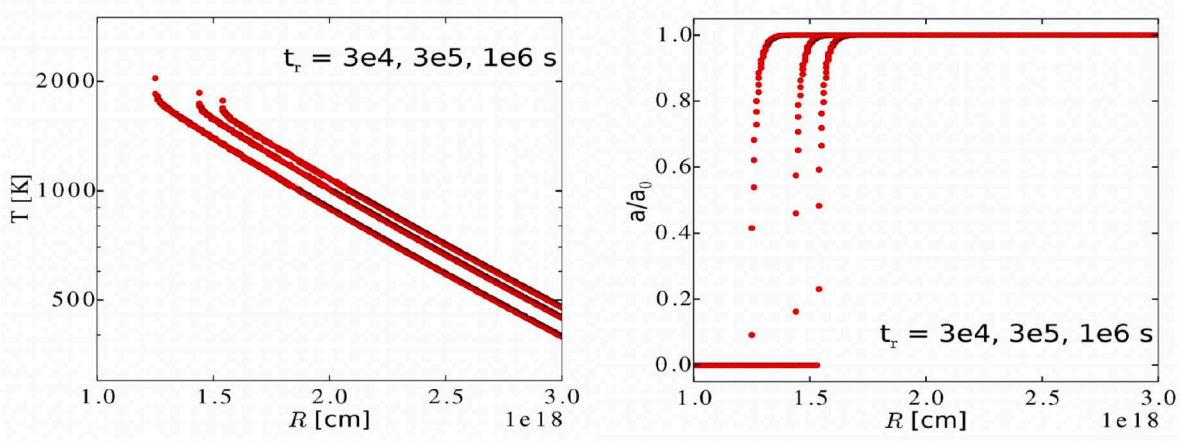

Figure 8.1: Temperature and grain size profile of dust around a TDE based on radiative transfer modeling. The dust grain size a is shown normalized to the innitial grain size a_0. The three curves show the system at three different times, given as the retared time $t_r = t - R/c$ for three values: 3×10^4 s, 3×10^5 s and 1×10^6 s. Taken from Lu, Kumar, and Evans [335]

where C is a constant:

$$C = 32\pi^2 \left(\frac{2\pi a}{c}\right)^{\alpha} \frac{h}{c^2} \left(\frac{k_B}{h}\right)^{\alpha+4} \Gamma(\alpha+4)\,\zeta(\alpha+4). \tag{8.4}$$

Because the dust grains sublimate at a temperature T_c that depends on the dust composition, this gives the minimum radius R_c at which the dust can remain stable. For a source with $L = 10^{46}\,\mathrm{erg\,s^{-1}}$, grains with radius $a = 0.1\,\mu\mathrm{m}$ ($\alpha = 1.8$) composed of graphite ($T_c \approx 1500\,\mathrm{K}$), this gives a radius of about $R_c \approx 0.27\,\mathrm{pc}$.

Thin Shell

Calculating the resulting spectrum of the dusty region is only possible with an assumption about the grain size distribution, and the distribution in space. Both can get arbitrarily complicated from uniform spherical [325], clumpy spherical [327], uniform toroidal [333, 334] and clumpy toroidal [329]. For this work, the fiducial model is a thin, spherical shell with a fixed grain size. The total luminosity is then just the sum of the contribution by the individual grains. If the percentage f_c of the sphere's area is covered in dust, then their total number is

$$N = f_c \frac{4\pi R^2}{4\pi a^2}. \tag{8.5}$$

Covering Factor

f_c is called the covering factor. In principle, it also encodes the absorption efficiency of the OUV radiation Q_{UV} by the dust. However, $Q_{UV} \approx 1$ is a good approximation, which is why f_c is understood as a geometrical factor. The luminosity of the dusty shell is then the grain luminosity times the grain number:

$$\begin{aligned} L_\nu^{IR} &= N \cdot L_\nu^{gr} \\ &= f_c\, 4\pi R^2\, \pi Q_\nu B_\nu(T). \end{aligned} \tag{8.6}$$

If a TDE happens around a quiescent SMBH with dust in the vicinity, the luminous TDE emission starts evaporating the dust, so the dust grain sizes get smaller. It turns out that this only takes a tiny fraction of the flare's energy and that dust at a radius smaller than the sublimation radius R_c does not absorb significant amounts of the

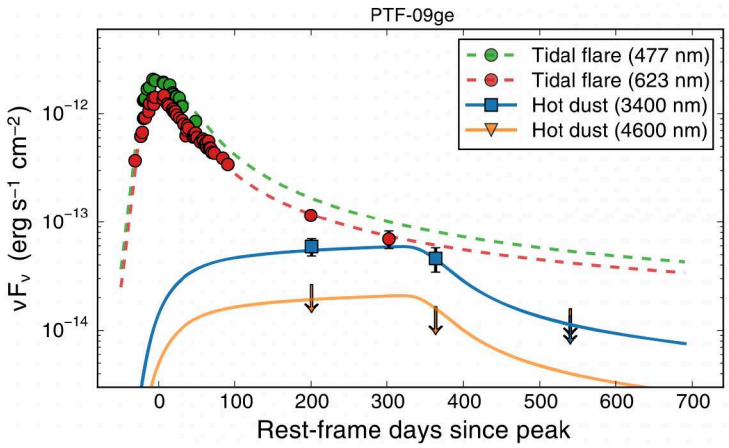

Figure 8.2: Optical and infrared lightcurves of the TDE PTF09ge. The green and red datapoints show observations of the flare in g and r-band. The squares and arrows are WISE difference measurements and 1σ upper limits. The dashed line is the lightcurve of the well-sampled TDE PS1-10jh. The solid line is the dust-echo model. Taken from Velzen et al. [332].

incident radiation before fully sublimating [332, 335]. Figure 8.1 shows the time-dependent profiles of temperature and dust grain sizes obtained from radiative transfer modeling for a 10^6 s long TDEs with $L = 3\times10^{45}$ erg s^{-1} and a dust shell extending from 0.3 to 1.3 pc [335]. The grain size is normalized to the initial grain size a_0. The sublimation can be considered complete for $a/a_0 \lesssim 3\%$. The steep grain size profile shows that the flare burns a cavity into the dust that expands outwards. The peak temperature is at its inner edge and cools with time. Because the integrated infrared luminosity relates to the temperature like $L^{\rm IR} \propto T^{4+\alpha}$ [325–327], the major contribution comes from the inner edge. The fiducial model of a thin shell for the total IR luminosity is therefore a good approximation.

Due to the light travel time, the infrared signal is related to the radius of the dust sphere R_c and has a width of $2\,R_c/c$. This signal has been observed in optically detected TDEs [332, 336, 337], of which an example is shown in Figure 8.2. The typical luminosity is around 10^{42} to 10^{43} erg s^{-1} and the derived covering factor is $f_c \lesssim 10^{-2}$ [338]. This is much lower than for AGN which have $f_c = 0.5$ to 0.8 [339–341].

[338]: Jiang et al. (2021), *Infrared Echoes of Optical Tidal Disruption Events: ~1% Dust-covering Factor or Less at Subparsec Scale*

This difference could, however, be an observational bias. For systems with a lot of dust, the EM emission is absorbed and re-radiated by the dust so that the optical or X-ray signal is weak or absent. Indeed, infrared flares without optical counterparts have been observed that are probably the dust echoes of TDEs in dusty environments [345–347], which motivated samples of purely infrared-selected candidate TDEs, mostly using data from WISE, introduced in Section 9.1.

MIRONG

Jiang et al. [348] created infrared lightcurves from WISE data for a sample of galaxies to search for flares. These are around 10^6 objects, spectroscopically identified by the *Sloan Digital Sky Survey* (SDSS) as galaxies with a redshift of $z < 0.35$. The lightcurves contain AllWISE and NEOWISE-R (see Section 9.1) photometry stacked per visit. Variable lightcurves are selected based on the difference between the brightest and dimmest measurements in any of the two WISE bands of at least 0.5 mag with a significance of at least 5σ. In addition, a brightening of at least 0.5 mag compared to a visually identified baseline is required. This results in 137 flares, dubbed the *Mid-infrared Outbursts in Nearby Galaxies* (MIRONG). The host galaxies differ in their properties from optically selected TDEs. In particular, they do not show the green-valley preference in contrast to optical and X-ray TDEs (see Figure 8.3). Spectroscopic follow-up

[348]: Jiang et al. (2021), *Mid-Infrared Outbursts in Nearby Galaxies (MIRONG). I. Sample Selection and Characterization*

Green valley

The *green valley* is a region in the mass-color diagram of galaxies, separating star-forming and passive galaxies as shown in Figure 8.3 [349]. There are indications that TDEs happen mostly in green valley galaxies which could be explained by a temporal enhancement of the TDE rate by a galaxy merger [350].

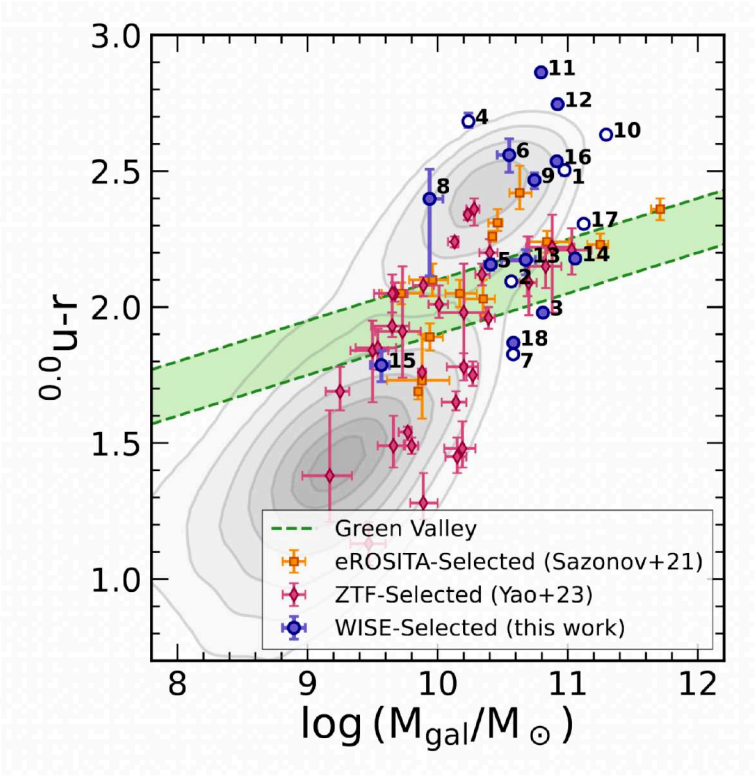

Figure 8.3: Distribution of the magnitude difference in the u and r-band against the stellar mass of galaxies. The gray contours are a volume-limited galaxy sample from SDSS, and the green-shaded region indicates the so-called green valey. Hosts of optically [342] and X-ray [343] detected TDEs are indicated with pink diamonds and orange squares, respectively. The hosts of IR selected TDE candidates from Masterson et al. [344] are the blue circels. Taken from Masterson et al. [344].

TDEs in ULRIGS

[352]: Reynolds et al. (2022), *Energetic Nuclear Transients in Luminous and Ultraluminous Infrared Galaxies*

WTP TDEs

[344]: Masterson et al. (2024), *A New Population of Mid-infrared-selected Tidal Disruption Events: Implications for Tidal Disruption Event Rates and Host Galaxy Properties*

revealed the emergence of coronal lines, and the fading of Balmer lines, suggesting that most of these flares are likely dust echoes of TDEs or instances of extreme transient AGN accretion [351].

Reynolds et al. [352] studied the variability of 215 Ultra Luminous Infrared Galaxies (ULIRGs). The infrared lightcurves were created in the same way as for the MIRONG sample. The selection of transients is based on a luminosity increase between minimum and maximum in the NEOWISE-R period of at least $10^{43}\,\mathrm{erg\,s^{-1}}$. Further investigation of the individual lightcurves resulted in a sample of five transients. If those are indeed TDEs, it implies a rate increase in galaxy mergers by a factor of around $\mathcal{O}(10^2)$.

In contrast to these samples, Masterson et al. [344] identified IR TDE candidates with the *WISE Transient Pipeline* (WTP). It makes use of co-added images instead of single-exposure photometry [353, 354], and transients were detected in difference images [355]. A crossmatch to local galaxies closer than 200 Mpc [356] identified those in the nucleus of the hosts. To reject stochastic AGN variability, the flares had to meet several requirements: a luminosity in W2 of at least $10^{42}\,\mathrm{erg\,s^{-1}}$, detection over at least 2.5 yr with a fast rise, and a slow, monotonic decay, no significant prior variability and pre-flare colors of $m_{W1} - m_{W2} > 0.8$ to exclude AGN hosts [308]. Finally, this yielded 18 sources, of which 12 are promising TDE candidates. Figure 8.3 shows the color-mass distribution of galaxies with hosts of these IR selected TDEs, and in addition, optical and X-ray selected ones. Similar to the MIRONG sample, the infrared selected TDEs occupy a different part in this parameter space, and do not show a preference for the green valley.

It should be noted that the flares in these samples are not uniquely identified as TDEs. That is because the classification is usually based on the optical and X-ray properties (see Chapter 3) that are not

accessible due to the high obscuration by the dust.

Summarizing, these searches indicate that selecting TDEs in the infrared is possible and reveals events in systematically different host galaxy environments. They demonstrate that this is an important detection channel that gives access to a TDE subpopulation that stays hidden at other frequencies.

8.2 Coincidences with High-Energy Neutrino Alerts

Although TDE dust echoes can shed light on an otherwise obscured part of the population, a connection with high-energy neutrino production has not been considered until recently. This was motivated by observed coincidence with IceCube high-energy neutrino alerts. These observations will be introduced in this section, as well as a probe of their robustness, before modeling attempts to connect the dust echo to neutrino production will be discussed.

8.2.1 Observations

The ZTF observed two (candidate) TDEs in coincidence with high-energy neutrino alerts (see Section 7.3): AT 2019dsg and AT 2019fdr. The most notable unifying feature of these two flares is a strong dust echo. As discussed in the previous section, this is not a common feature among optically detected TDEs and consequently prompted follow-up studies.

ZTF Accretion Flares

[80]: van Velzen et al. (2024), *Establishing Accretion Flares from Supermassive Black Holes as a Source of High-Energy Neutrinos*

van Velzen et al. [80] compiled a sample of flares, similar to AT 2019dsg and AT 2019fdr: nuclear optical flares with a strong dust echo. The optical flares are selected based on a fast e-fold rise and fade of no more than 150 d and 500 d, respectively, and a minimum amplitude of $\Delta m < -1$. The infrared lightcurves were again built from NEOWISE-R data, stacking the observations per visit for each object. In contrast to the samples introduced in the previous section, the optical lightcurve provides prior knowledge of the dust echo onset. Consequently, the baseline was calculated using all observations up to six months before the optical peak. The selection of strong dust echoes is then based on the echo strength $\Delta F_{\rm IR}/F_{\rm rms}$. Here, $\Delta F_{\rm IR}$ is the difference between baseline and the mean flux within one year after the optical peak, and $F_{\rm rms}$ is the root-mean-squared variability of the baseline. The significance of the pre-flare variability is defined as $F_{\rm rms}/\sigma_{\rm F}$, where $\sigma_{\rm F}$ is the baseline uncertainty. Strong echoes are then identified by an echo strength exceeding the pre-flare variability:

Dust echo strength

$$\frac{\Delta F_{\rm IR}}{F_{\rm rms}} > \frac{F_{\rm rms}}{\sigma_{\rm F}}. \tag{8.7}$$

This results in a sample of 63 flares.
Similar to the previously introduced samples, the exact nature of these outbursts is not clear. Although there is an optical signal, only a few were observed spectroscopically. The infrared flare is

agnostic to the incident radiation, because the dust efficiently absorbs throughout a wide wavelength range, so it is only sensitive to the total energy. However, all events are likely due to extreme accretion onto the SMBH and are consequently dubbed accretion flares. This sample will be referred to as the *Zwicky Transient Facility Accretion Flares* (ZTF AF).

AT 2019aalc

A crossmatch of the ZTF AFs with the 43 IceCube alerts in the ZTF footprint and during the ZTF observation period uncovered a third coincident event: AT 2019aalc (see the bottom panel in Figure 8.4). Next to the strong dust echo, it also shares a soft, thermal X-ray spectrum and low-luminosity radio emission with AT 2019dsg and AT 2019fdr. Similar to AT 2019fdr but in contrast to AT 2019dsg, the host is an active galaxy. It was classified as a Seyfert 1 [357] and shows prior activity in radio emission and infrared. Meanwhile, a second optical flare was reported [358]. This could indicate a repeating TDE in an AGN [359] or extreme accretion connected to the existing disk. The three flares and the coincident neutrinos are shown in Figure 8.4. The luminous dust echo is clearly visible. In all three cases, the neutrino arrives after the optical peak. In the case of AT 2019fdr, the delay is 289 d.

[358]: Veres et al. (2023), *Significant Re-Brightening of the Candidate Tidal Disruption Event AT2019aalc*

[359]: Veres et al. (2024), *Back from the Dead: AT2019aalc as a Candidate Repeating TDE in an AGN*

Neutrino correlation

These coincidences lead to a correlation of the ZTF AFs, and the IceCube high-energy neutrino alerts at the level of 3.6σ [80]. The assumptions included in the underlying likelihood have important implications and will be reviewed here briefly.

An accretion flare is considered spatially coincident with a neutrino event if it is within the publicly available 90% rectangular uncertainty contour of the event, derived with *Millipede*. As explained in Section 5.3, these contours may not have the correct coverage, which could lead to mis-associations. Additionally, although included in the *Millipede* uncertainty region, all three flares are relatively far away from the best-fit neutrino arrival direction: 1.3 to 1.9° (see Figure 8.8). The robustness of the uncertainty region thus is crucial for the correlation result and will be analyzed in more detail in Section 8.2.2. The temporal coincidence is established if the neutrino arrives within one year after the optical peak.

The likelihood incorporates a probability of each flare being a neutrino source or not. The assumption is that these are the single strong outbursts in contrast to regular AGN variability. Therefore, the strength $\Delta F_{\mathrm{IR}}/F_{\mathrm{rms}}$ is used to construct the corresponding PDF. In particular, for $\Delta F_{\mathrm{IR}}/F_{\mathrm{rms}} > 10$ the sample is dominated by TDE-like flares.

The last assumption is that the neutrino luminosity scales with the total electromagnetic output. Because, as mentioned above, the dust absorbs efficiently across the electromagnetic spectrum, and almost acts as a bolometer, the infrared lightcurve is taken as a tracer for the bolometric luminosity and thus for the neutrino luminosity.

[360]: Jiang et al. (2023), *Two Candidate Obscured Tidal Disruption Events Coincident with High-energy Neutrinos*

Jiang et al. [360] found two neutrino alerts coincident with two flares from the MIRONG sample. Based on their high luminosity and total energy output, these two flares are also likely extreme transient accretion flares, supposedly raising the number of neutrino-TDE coincidences to five.

In this case, the positional coincidence is based on the circularized mean of the rectangular 90% uncertainty contour[1]. The neutrinos are

1: In the second GCN Notice that IceCube sends out, the circularized mean is provided as *SRC_ERROR*

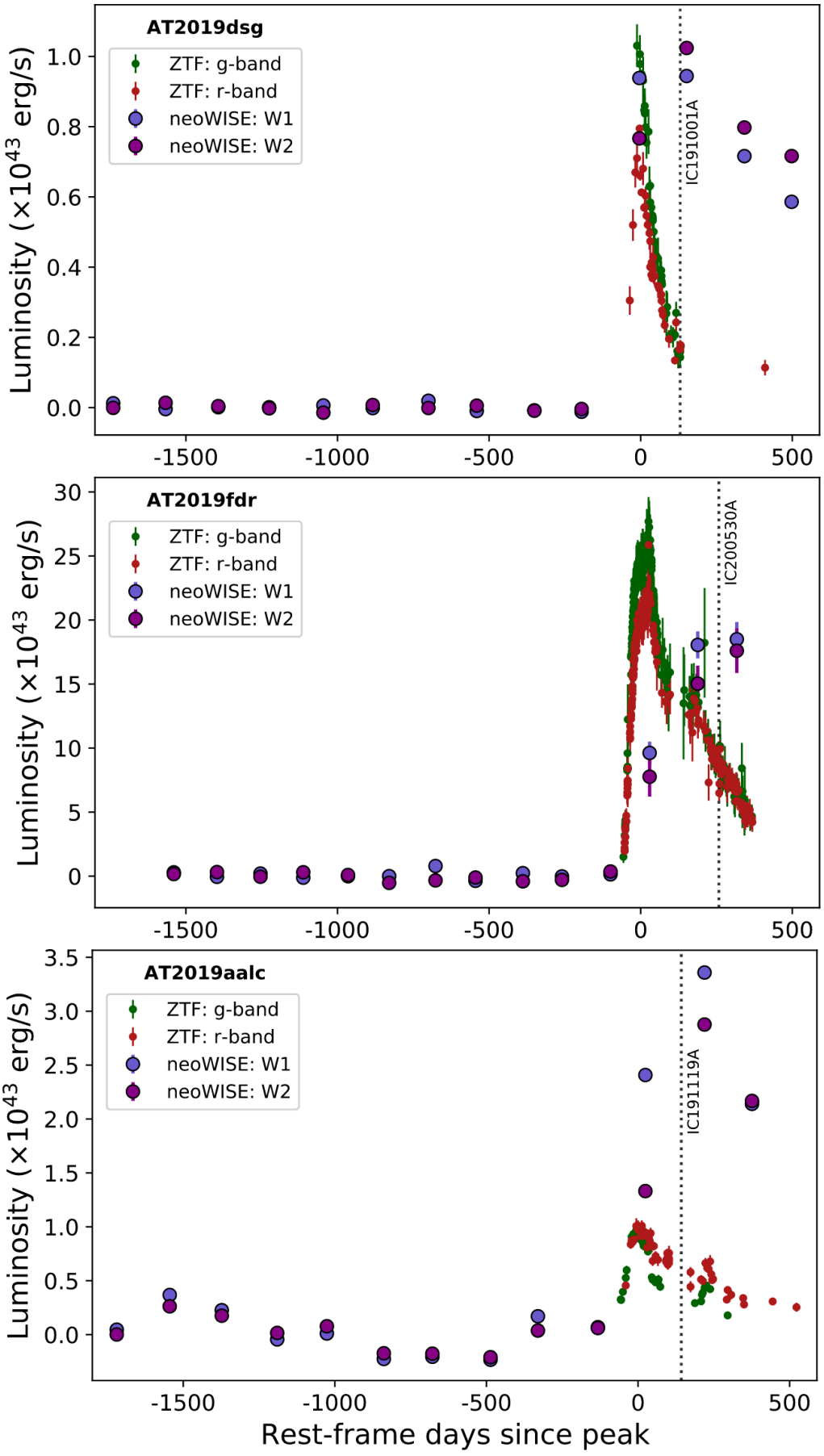

Figure 8.4: The optical and infrared lightcurves of three accretion flares coincident with high-energy neutrino alerts. The purple datapoints are infrared detections in WISE data, and the green and red ones are optical detections by ZTF. The vertical dotted line indicates the arrival time of the associated alert neutrino. Taken From van Velzen et al. [80]

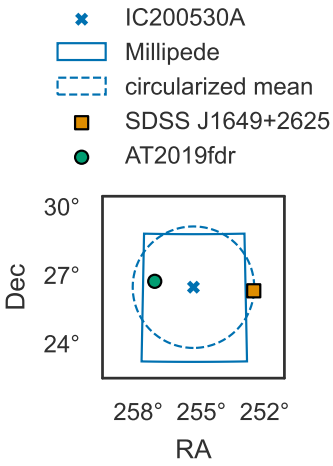

Figure 8.5: The uncertainty contour of IC200530A and the positions of the claimed counterparts AT 2019fdr [80], and the flare in SDSS J1649+2625 [360]. The rectangular alert uncertainty contour from *Millipede* is shown as the solid line, and the averaged, circularized error as the dashed line.

required to arrive within six months of the infrared peak. By simply considering the number of flares in the footprint of the relevant gold neutrino alerts, the authors estimate a chance-coincidence of 6.9% based on Poisson statistics.
Although these two further coincidences are alluring, the author's claim to raise the total number of coincidences to five is wrong. The flare in the galaxy SDSS J1649+2625 is found in coincidence with IC200530A, the same neutrino claimed to be associated with AT 2019fdr [80, 270]. The neutrino uncertainty area, both the rectangle based on the *Millipede* results that was used to associate AT 2019fdr, and the averaged circular area used for the MIRONG analysis, are shown in Figure 8.5. Although SDSS J1649+2625 is inside the averaged circular region, it is outside the *Millipede* rectangle. This makes AT 2019fdr the more likely counterpart.

There are no coincidences between the WTP TDEs and gold neutrino alerts. However, due to the low number of both transients and gold alerts, no constraining conclusion was drawn [344].

8.2.2 Resimulations of Alert Neutrinos

As mentioned in the previous section, the size of the neutrino alert uncertainty area plays a large role in the likelihood analysis leading to the correlation with the accretion flares. This section uses the re-simulation method introduced in Section 5.5 to evaluate their robustness. Re-simulations of IC191001A with the old scheme as introduced below were performed by Cristina Lagunas Gualda.

The events reported to be coincident with ZTF AFs are shown in Figure 8.6. Before going into detail about investigating the reconstruction of the arrival direction, it is worth reviewing their individual properties.

IC191001A is a HESE event, produced by a muon neutrino interaction inside the detector with an outgoing muon track. The interaction happens inside the dust layer around halfway through the detector. As already discussed in Section 5.5, IC200530A is a through-going muon track event that traverses the full length of IceCube. The event is dominated by a large stochastic energy deposition shortly after entering the detector. The second half is going through the dust layer with a lot less detected photoelectrons. Nevertheless, these detections form a long lever arm with the early light depositions and potentially influence the directional reconstruction a lot. IC191119A is a smooth through-going track event that traverses the detector close to the edge, leading to a short lever arm.

Old and New Scheme

These properties have important implications for producing resimulations. In the following, the scheme that existed already within IceCube introduced in Section 5.4 will be referred to as the *old* scheme while the one proposed in this work in Section 5.5 will be dubbed the *new* scheme. Because IC191001A is a starting event, it cannot be resimulated with the new scheme. It explicitly assumes a through-going track which will produce light also along the first half of the track in the detector and does not include the starting cascade. The results shown in the following for this event thus use the already existing simulations using the old scheme. Because of the peculiar

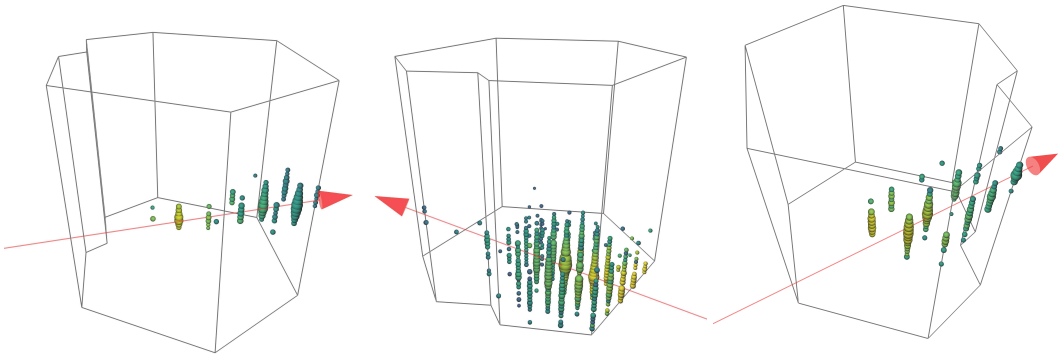

(a) IC191001A **(b)** IC200530A **(c)** IC191119A

Figure 8.6: Event views of the three neutrino alert events that were reported to be coincident with an accretion flare.

Event	Resimulations	Consistent with GCN [%]
IC170922A	346	100
IC191001A	100 (old scheme)	98
IC191119A	773	99
IC200530A	121	100

Table 8.1: Resimulation results for the three neutrinos coincient with accretion flares and IC170922A. The first column is the event name, the second one the number of resimulations and the third one the number of simulations consistent with the 90% bounding rectangle reported in the GCN Circular.

light pattern of IC200530A, the new scheme is essential to capture the characteristics of this event. The old one produced too much light towards the exit of the track in the dust layer (see Figure 5.9) which produces events with a better reconstructed arrival direction than the original. The new scheme does by construction include the energy deposition pattern in the selection of viable resimulations and is thus vital for reproducing IC200530A[2]. IC191119A can in principle be reproduced by both methods. However, the new scheme does improve performance, which is why it is used in the following also for this event. Because the energy deposition pattern is easily reproducible, the value of M_{tresh} can be lowered from $M_{\text{thresh}} = 0.8$ to $M_{\text{thresh}} = 0.6$, corresponding to an allowed ratio between simulated and measured energy deposition of 4 instead of 6 in any segment (see Chapter 5 for the explanation of M_{thresh} and the derivation of the values quoted here).

2: Indeed, IC200530A was the event that motivated the development of the new scheme in the first place. See Section 5.5 for more details.

Figure 8.7 shows the results of these resimulations in terms of charge and number of DOMs that detected a signal. IC191001A and IC191119A are well reproduced by the majority of the resimulations. IC200530A is within the boundaries of the events with the most extreme energy deposition. This highlights that its energy deposition pattern makes it a very rarely occurring event. Most notably, the resimulations do not produce more light inside and around the dust layer than the original event. This is the biggest difference to the resimulations produced with the old scheme (see Figure 5.9). As a reference, the well-reconstructed event IC170922A is also shown. It is well reproduced by the new scheme as expected for a smooth through-going track.

Reconstructing the arrival direction of the resimulations and comparing to the true, simulated direction, one can make a statement about the consistency of the original reconstructed arrival direction and the position of the EM counterpart. Indeed, this is the first step towards a likelihood contour, calibrated with dedicated simulations. Using

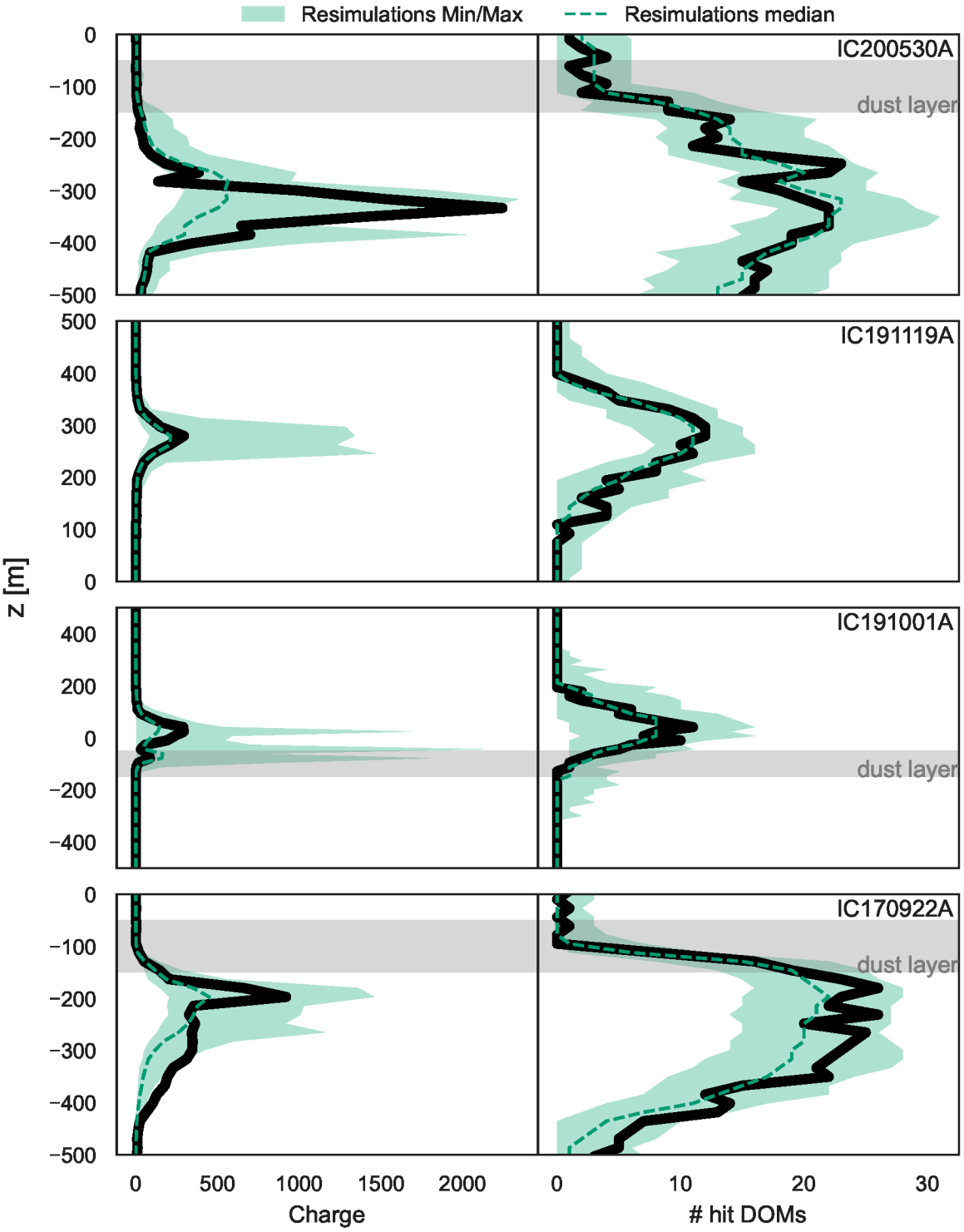

Figure 8.7: Charge distribution and number of DOMs that detected a signal for the neutrino alerts coincident with TDEs, IC170922A and their resimulations as a function of height in the detector. The black solid line is the original event, the green dashed line the median of the resimulations, and the green-shaded area their minimum and maximum per height bin. The y-axis indicates the height in the detector measured in IceCube coordinates. The gray shaded area indicates the position of the dust layer.

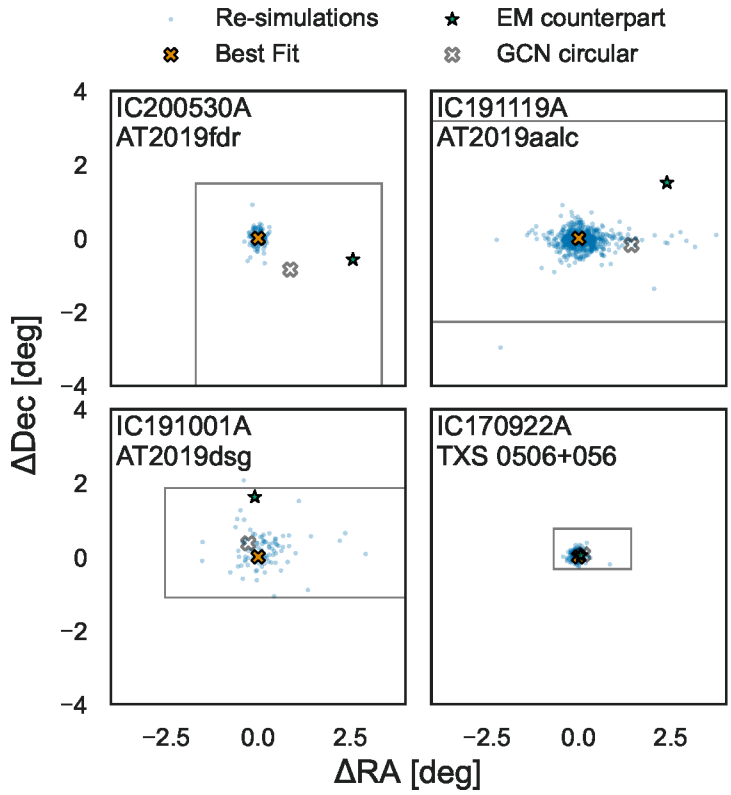

Figure 8.8: Reconstructed arrival directions for the neutrinos coincident with TDEs, IC170922A and their resimulations. The center (orange cross) marks the reconstruction with *SplineMPE*. The blue dots show the offset of the reconstructed simulations to their true direction. For comparison, the gray line and cross show the 90% bounding rectangle and best fit by *Millipede* as sent out in the GCN Circular. The green star shows the position of the (claimed) EM counterpart.

SplineMPE, the results are shown in Figure 8.8. The third column in Table 8.1 shows the percentage of reconstructed resimulations that fall within the 90% bounding rectangle reported in the GCN Circular. For fully compatible results, this value is expected to also be 90%. As a crosscheck, the results are also included for IC170922A, and the associated blazar TXS 0506+056 [47]. For this neutrino and counterpart pair, the resimulation offsets are fully consistent both with the *SplineMPE* and the *Millipede* best fit. Because the resimulations are clustered around the best fit position even closer than the *Millipede* bounding rectangle would suggest, it seems that the resolution using *SplineMPE* in this case would be even better.
For the neutrino and TDE pairs, this is less clear. Because the potential counterparts are relatively far from the best fit position (more than 1°), the corresponding uncertainty region would have to have a similar extent. However, almost all resimulated events have an offset smaller than the 90% bounding rectangle. This suggests that the 90% uncertainty regions should be smaller than the bounding rectangle. In the case of IC200530A, the furthest offset to the best fit position is only about 1°, suggesting that the contour should be much smaller.

In summary, these findings challenge the association of the three accretion flares with high-energy neutrino alerts. However, they are not conclusive yet. The framework to perform a robust sky-scan and produce contours with *SplineMPE* is currently under development [177]. Using the resimulations from this work, these contours would most likely not include the position of the respective accretion flare. If this is the case, the reason for the large *Millipede* uncertainty areas has to be understood.

[47]: IceCube Collaboration et al. (2018), *Multimessenger Observations of a Flaring Blazar Coincident with High-Energy Neutrino IceCube-170922A*

[177]: Sommani et al. (2023), *Towards a More Robust Reconstruction Method for IceCube's Real-Time Program*

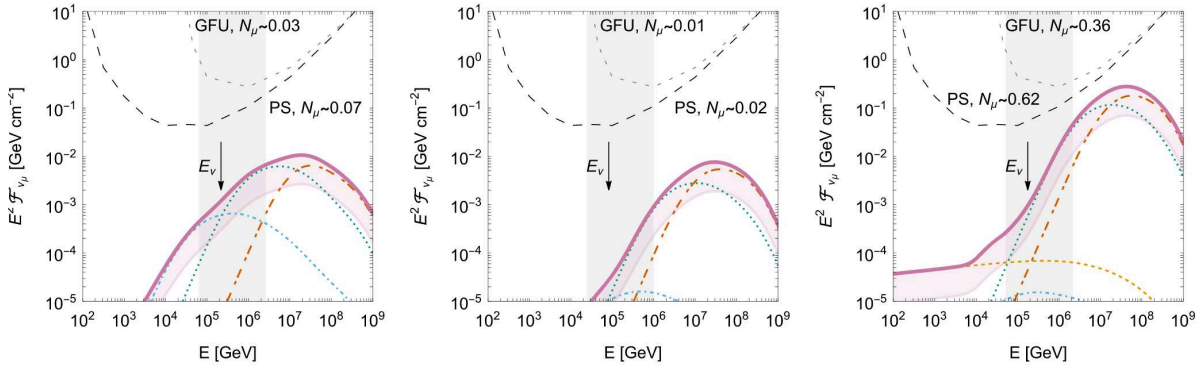

Figure 8.9: Neutrino spectra resulting from proton interaction with the dust echo IR photons for AT 2019dsg (left), AT 2019fdr (center) and AT 2019aalc (right). The fluence is shown against neutrino energy. The blue dash-dotted, green dotted and red dash-dotted lines show the contribution by interactions with the X-tay, OUV and IR targets. The yellow dahed line is the contribution by pp interactions. The red line shows the combined neutrino spectrum. The black arrow indicated the energy of the associated alert neutrino. The neutrino alert (GFU) and point source (PS) limits are shown together with the integrated event number. Taken from Winter and Lunardini [361].

8.2.3 Theoretical Modelling

This chapter so far has presented the dust echos in TDEs, correlations of (likely) TDEs dust echos with high-energy neutrinos, and closer investigation of the respective high-energy neutrino events. Another important consideration is whether high-energy neutrino production in these TDEs fits into one consistent picture. Neutrino production in TDEs was already in general discussed in Chapter 3. However, the models introduced there do not incorporate the dust echoes. The observations presented in Section 8.2.1 do not necessarily entail a direct connection of the infrared and neutrino signal. But the fact that the flares with neutrino association have the brightest dust echoes [338], although dust echoes are in general rare among optically detected TDEs [80], makes it an interesting possibility.

[338]: Jiang et al. (2021), *Infrared Echoes of Optical Tidal Disruption Events: ~1% Dust-covering Factor or Less at Subparsec Scale*

[80]: van Velzen et al. (2024), *Establishing Accretion Flares from Supermassive Black Holes as a Source of High-Energy Neutrinos*

[361]: Winter et al. (2023), *Interpretation of the Observed Neutrino Emission from Three Tidal Disruption Events*

Winter and Lunardini [361] model neutrino production in AT 2019dsg, AT 2019fdr and AT 2019aalc, in an attempt to reproduce the observed neutrino energy and arrival time delay with respect to the optical peak. Because it is the only work also exploring the possibility of a direct neutrino-dust-echo connection, this will be reviewed in the following.

Proton acceleration

The initial acceleration of protons is not investigated in detail but rather described by the maximum achieved proton energy $E_{\mathrm{p,max}}$, following a power-law spectrum with an exponential cutoff:

$$J_{\mathrm{p}}(E_{\mathrm{p}}) \propto E_{\mathrm{p}}^{-2} \exp\left(-\frac{E_{\mathrm{p}}}{E_{\mathrm{p,max}}}\right), \tag{8.8}$$

where E_{p} is the proton energy. The injection is assumed to be isotropic, evolving in time like the mass accretion rate, where the dissipation efficiency ϵ_{diss} describes the energy transfer from the accretion to non-thermal protons:

Dissipation efficiency

$$L_{\mathrm{p}} = \epsilon_{\mathrm{diss}}\,\dot{M}c^2. \tag{8.9}$$

To produce neutrinos, interactions of the accelerated protons with other protons (pp) and photons ($p\gamma$) are necessary. Assuming all

photon fields are blackbodies with a temperature T, the preferred photon target temperature depends on $E_{\mathrm{p,\,max}}$:

$$T \approx 160\,\mathrm{eV}\left(\frac{E_{\mathrm{p,max}}}{1\,\mathrm{PeV}}\right)^{-1}. \tag{8.10}$$

pp interaction is assumed with a mildly relativistic outflow, and plays a role for low photon densities or at energies below the $p\gamma$ threshold.

X-ray, OUV and IR targets

With this in mind, the authors chose three values for $E_{\mathrm{p,\,max}}$: 5 PeV, 100 PeV and 5 EeV. This results in target photon field temperature of 1×10^7 K, 2×10^4 K and 1×10^3 K, respectively, corresponding to the X-ray, OUV and dust-echo IR photons. The corresponding model realizations will be referred to as the X-ray, OUV and IR models, respectively.
The radiation zone, where the interaction with the target happens, is parameterized by the radius R which also depends on the model. In the X-ray case, this is within 5×10^{15} cm (1.6×10^{-3} pc). For the OUV case, this is 5×10^{14} to 1×10^{16} cm (1.6×10^{-4} to 3.2×10^{-3} pc). The radius of the dusty torus, producing the dust echo determines the radiation zone for the IR model and consequently is about a magnitude larger with 5×10^{16} to 2.5×10^{17} cm (0.06 to 0.08 pc).

In the OUV model, the neutrinos arrive around the optical peak which does not match the reported coincidences, where the neutrino arrived up to 289 d later. In the X-ray model, the moderate-energy protons are confined and accumulate, so that the neutrino production gets more efficient over time, which might explain the observed neutrino arrival delay. However, it is best explained in the IR model. Due to the light travel time to the dust torus, the IR target photon field only exists at later times, so neutrino production is naturally delayed in the same way, so that it approximately follows the dust echo lightcurve.

It should be noted that while the IR model explains the delay, it does require a high dissipation efficiency of about $\epsilon_{\mathrm{diss}} \gtrsim 0.1$. The high proton energy leads to high neutrino energies, as shown in Figure 8.9. The peak of the neutrino spectra is between 10 PeV and 100 PeV with the main contribution by the IR interactions. However, the OVU interactions also contribute a lot at slightly lower energies. This means that also TDEs without dust echoes would produce high-energy neutrinos, albeit with lower energies and less fluence.

Diffuse Flux

The resulting neutrino numbers are integrated over redshift and blackhole mass M, assuming a neutrino rate $\dot{\rho}(z, M)$[3]. Per model, the spectra of AT 2019dsg, AT 2019fdr and AT 2019aalc are assumed to contribute equally. The percentage of neutrino emitting TDEs η was tuned to fit the diffuse flux measurements. Because the diffuse flux depends only on the product of ϵ_{diss} and η, the product is constrained to $\epsilon_{\mathrm{diss}}\eta \leq 2\times10^{-3}$. For the IR model, in the pessimistic case of $\epsilon_{\mathrm{diss}} = 0.05$, this means that around $\eta \approx 4\%$ of TDEs have to emmit neutrinos. In the optimistic case $\epsilon_{\mathrm{diss}} = 0.2$ this has to go down to $\eta \approx 1\%$.
The diffuse fluxes are shown in Figure 8.10. The IR model can be approximated well by a power-law with $\gamma \approx 1$ up to around 10 PeV. The OUV models follows $\gamma \approx 1.5$ in the IceCube energy range. The

3: The integration over redshift is similar to the approach taken in Section 8.3.6

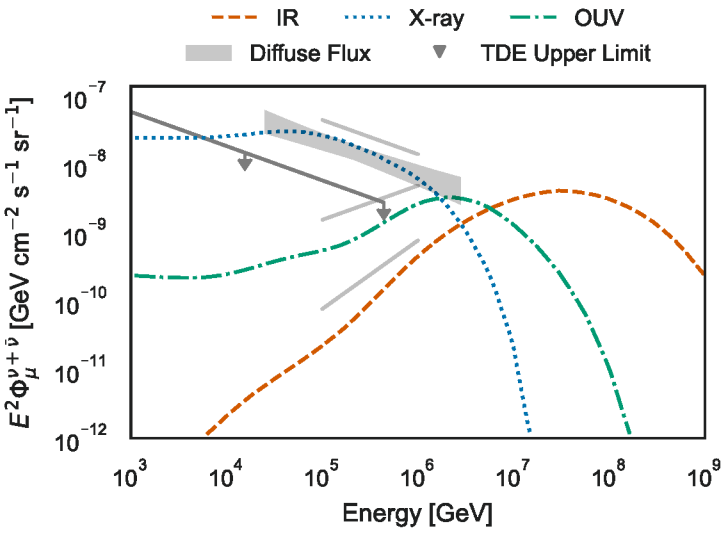

Figure 8.10: Contribution to the diffuse neutrino flux from accretion flares for three different models from Winter and Lunardini [361]. The energy scaled muon neutrino flux (ν and $\bar{\nu}$) is shown against the neutrino energy. The colored lines show the X-ray, OUV and MIR model, respectively. The straight, gray lines show the power-law approximations with spectral indices of 2.5, 1.5, and 1 from top to bottom. The gray butterfly and line are the measurement of the diffuse flux [43] and upper limits on the contribution by TDEs [92] by IceCube, respectively.

X-ray model follows $\gamma \approx 2$ up to around 300 TeV. Also shown in the same Figure is the 90% upper limits from the previous TDE IceCube stacking analysis (see Chapter 3). These already exclude the X-ray model for the chosen value of η and ϵ_{diss}, but are not sensitive enough to probe the parameter space predicted by the OUV and IR model. An analysis to do so will be presented in the next section.

8.3 Looking for High-Energy Neutrinos from Accretion Flares with IceCube

So far, this chapter introduced dust echoes in TDEs and reviewed the claimed correlation with high-energy neutrino alerts. Although the robustness of the correlation still has to be verified, modeling of proton interaction with the dust echo photons can produce neutrinos with the observed time delay. It is natural to expand the correlation analysis from the limited sample of high-energy neutrino alerts to the full sample of IceCube neutrinos. This uses the point-source stacking method, generally introduced in Section 4.4. The main ingredients, the source catalog and neutrino dataset, will be discussed, before detailing the likelihood analysis and presenting results.

8.3.1 Catalog Selection

To test the correlation between accretion flares and high-energy neutrinos reported by van Velzen et al. [80], an obvious choice of source catalog is to use the ZTF accretion flares. However, as outlined in Section 8.2.1, the likelihood used to by van Velzen et al. [80] incorporates a probability of the flares being neutrino sources based on their dust echo strength. An equivalent term does not exist in the standard stacking likelihood described by Equation 4.17. Instead, a simple cut was applied to compile the most promising sources from the accretion flare catalog. As mentioned in Section 8.2.1, for a strength of $\Delta F_{\mathrm{IR}}/F_{\mathrm{rms}} > 10$, the flares are dominated by

Table 8.2: Accretion flare catalog used in the stacking analysis, ordered by their infrared flux. The position, peak time, redshift and dust echo flux are taken from van Velzen et al. [80]. The peak time referes to the optical peak. The weight is the normalised dust echo flux.

Name	z	Peak time [MJD]	RA [deg]	Dec [deg]	ΔF_{IR} [mJy]	weight
AT2019aalc	0.04	58658.2	231.069435	4.855293	11.13	0.352773
AT2013kp	0.01	58753.1	71.657817	-10.226320	2.14	0.067829
AT2019meh	0.09	58713.1	321.822708	64.416439	1.99	0.063074
AT2019avd	0.03	58534.3	125.903198	4.384017	1.87	0.059271
AT2019dqv	0.08	58628.2	160.875250	51.358050	1.77	0.056101
AT2019thh	0.05	58851.1	336.993542	18.322069	1.75	0.055468
AT2019dsg	0.05	58620.2	314.262393	14.204406	1.58	0.050079
AT2018dyk	0.04	58261.4	233.283395	44.535612	1.41	0.044691
AT2021aetz	0.09	58390.3	327.732241	-1.115063	0.81	0.025674
AT2019fdr	0.27	58672.5	257.278579	26.855695	0.71	0.022504
AT2020atq	-	58903.2	102.323538	62.513401	0.66	0.020919
AT2019cyq	0.26	58637.2	149.025250	19.549039	0.54	0.017116
AT2018iql	-	58449.4	74.579667	-7.767961	0.48	0.015214
AT2020iq	0.10	58878.1	43.832167	-11.413511	0.45	0.014263
AT2019idm	0.05	58682.2	208.195250	20.412181	0.41	0.012995
AT2019aami	-	58717.4	8.931108	47.259255	0.41	0.012995
AT2019mss	-	58811.6	207.102417	8.528700	0.38	0.012044
AT2019nna	-	58717.4	357.160287	19.262802	0.36	0.011410
AT2018lhv	-	58513.5	196.353800	21.954463	0.35	0.011094
AT2019gur	-	58607.5	343.703265	77.352967	0.34	0.010777
AT2020hle	0.10	58978.3	166.928627	74.633932	0.33	0.010460
AT2018ige	-	58432.5	118.638051	9.494126	0.31	0.009826
AT2019cle	-	58568.4	267.754637	14.918397	0.25	0.007924
AT2019qpt	0.24	58798.3	120.357375	24.929439	0.24	0.007607
AT2021aeuj	0.69	58974.2	137.107204	42.894802	0.20	0.006339
AT2019aame	-	58363.2	215.051819	31.894183	0.18	0.005705
AT2021aeuf	-	58556.4	191.028451	47.445135	0.18	0.005705
AT2020afac	-	58758.3	268.417394	55.857536	0.16	0.005071
AT2018lcp	0.06	58547.2	117.708416	1.358350	0.16	0.005071

TDEs in contrast to regular AGN variability, which leaves a sample of 29 flares listed in the Table 8.2.

8.3.2 Neutrino Dataset

Because the selected sources extend into the southern sky to a declination of about $\delta \approx -11°$, an all-sky neutrino dataset is necessary. As mentioned in Section 4.2.4, muon tracks provide the best angular resolution and are best suited for astronomy purposes. Thus, the dataset used in this work is an all-sky sample of muon neutrinos, called *Point-Source Tracks v4.0*, based on a selection of 10 yr of IceCube data [165]. Specifically, all data starting on May 23rd, 2018 is used which is the earliest peak of any transient in the catalog. The dataset extends until May 29th, 2020. Both IC191001A and IC191119A are included, the neutrino events associated with AT 2019fdr and AT 2019dsg. However, as mentioned in Section 8.2.1, the flares are far from the best-fit *Millipede* position of the corresponding neutrino but inside the 90% uncertainty region. The position in this dataset, however, is reconstructed using *SplineMPE*

[165]: Aartsen et al. (2020), *Time-Integrated Neutrino Source Searches with 10 Years of IceCube Data*

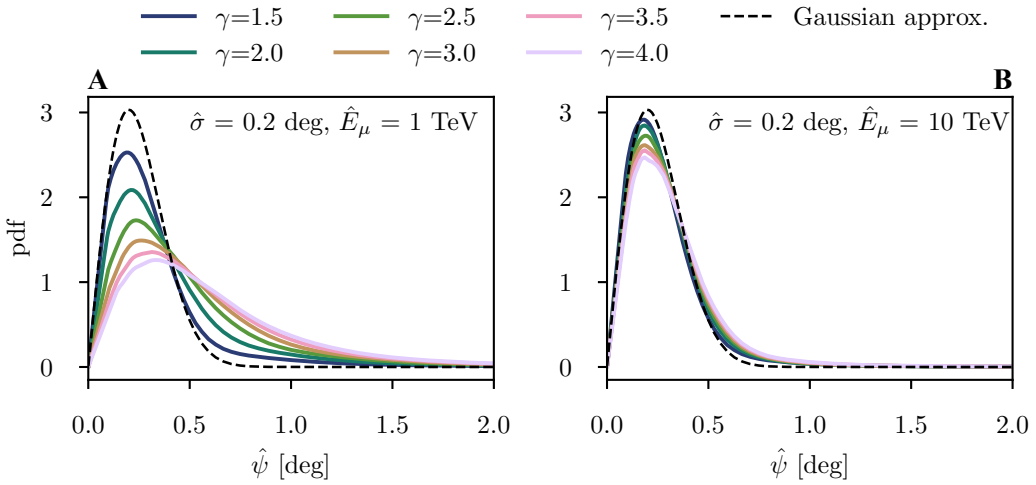

Figure 8.11: The distribution of the angular distance Ψ between the reconstructed and true neutrino arrival direction for an angular uncertainty of $\sigma = 0.2$ deg. The gaussian assumption used in this work is shown as the dashed line, the colored, solid lines are the distributions obtained from Monte-Carlo simulations for two different muon energies: $E_\mu = 1$ TeV (A) and $E_\mu = 10$ TeV (B). Taken from IceCube Collaboration et al. [48].

with the *Paraboloid* error (see Section 4.3.2). The best-fit does usually not change significantly between *SplineMPE* and *Millipede*, but the *Paraboloid* error is significantly smaller than the uncertainty region derived from the *Millipede* sky-scan. Therefore, the alert neutrinos are not expected to contribute much in this analysis.
IC200530A is not included in the dataset as it arrived one day after the dataset ends.
The distribution in energy and declination of the neutrino events is shown in the middle panel of Figure 8.13. The distribution is different in the northern and southern sky. The earth shields high-energy neutrinos in the north, while low energy neutrinos are suppressed by the event selection in the south to get rid of the atmospheric muon background. Because most of the flares are in the northern sky, the bulk of events are around 1 TeV. Thus, it is expected that the analysis will be less constraining for hard spectra.

8.3.3 Likelihood Analysis

The relative distribution, or weighting, of the neutrino signal between the sources in the selected catalog is uncertain. To take this into account, a stacking analysis with floating weights was performed, introduced in Section 4.4.3. The missing ingredients for this analysis are the PDFs.

Signal spatial PDF

The signal is assumed to follow a two-dimensional gaussian around the source position. This is the best available choice for the chosen neutrino dataset, and a good approximation at higher energies around 10 TeV. This degrades towards lower energies, especially for soft spectral indices, as shown in Figure 8.11, resulting in sensitivity loss. An improved description of the spatial signal PDF has since been developed [48] but was not readily available at the time of this analysis.

[48]: IceCube Collaboration et al. (2022), *Evidence for Neutrino Emission from the Nearby Active Galaxy NGC 1068*

Signal energy PDF

Because the signal energy PDF depends on the detector acceptance, it can not be described analytically. Instead, it is obtained using

Monte-Carlo simulations. The simulated events are weighted based on a specific spectral assumption, which in this case is a power-law with varying spectral index. As an example, the PDF for a spectral index of $\gamma = 2$ is shown in the left panel of Figure 8.13.

Signal time PDF

The neutrino emission is not expected to be steady but correlated with the EM emission of the flares. The models discussed in Section 8.2.3 predict the peak of the neutrino emission either at the peak of the optical lightcurve (X-ray and OUV model), or following the infrared lightcurve (IR model). To incorporate these models, a box-shaped signal time PDF was chosen, fixed to the optical peak time t_{ref}:

$$\mathcal{T}_{\text{sig}} = \begin{cases} T^{-1}, & t_{\text{ref}} < t < t_{\text{ref}} + 1\,\text{yr} \\ 0, & \text{else} \end{cases}, \tag{8.11}$$

where T^{-1} is the integrated *livetime* from t_{ref} to $t_{\text{ref}} + 1$ yr and takes care of the normalization of the PDF. With this, the analysis is sensitive to a neutrino signal within the chosen time window while not making detailed assumptions about the temporal evolution.

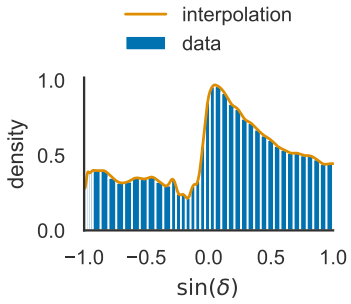

Figure 8.12: The spatial background PDF, obtained from the data. The declination-dependent distribution is shown as the histogram. The solid line is the interpolation used as the PDF.

Background spatial PDF

As discussed in detail in Section 4.1.4, the background is dominated by atmospheric muons in the Southern Hemisphere and atmospheric neutrinos in the north. The muons cannot be accurately simulated, so it is not possible to get the spatial background expectation that way. Although the domination of the atmospheric background makes the search for the astrophysical signal tough in the first place, it at least enables the data to be directly used as the background PDF. Because IceCube is located at the South Pole, the data is declination-dependent but uniform in right ascension. The declination is put in a histogram, and the interpolation used as the PDF, as shown in Figure 8.12.

Background energy PDF

The same is true for the background energy PDF. It is built from the data, assuming the signal contribution is negligible. The corresponding histogram is shown in the middle panel in Figure 8.13.

Background time PDF

In contrast to the signal, the background is assumed to be steady. The seasonal variation of the stratosphere temperature leads to a long-established variation in atmospheric muons [144] that has been measured also with IceCube [362]. Even the atmospheric neutrino flux is undergoing the same variation [363]. However, it is only on the level of a few percent and is usually neglected when looking for astrophysical signals.

Because the energy PDF of the signal does not depend on the source, it can be factored out. The remaining relevant term for the calculation of the test statistic in Equation 4.19 is the ratio between the signal and background energy PDF. This is shown in the right panel in Figure 8.13, illustrating the declination dependence of the energy PDF.

8.3.4 Energy Range

The sensitive energy range of the analysis depends on the assumed neutrino spectrum. The softer the spectrum, the more relatively low energetic events will contribute to the signal, shifting the sensitive range towards lower energies. The neutrino events in the sample are between 10^2 to 10^7 GeV, so the sensitive range will lie between those

[144]: Barrett et al. (1952), *Interpretation of Cosmic-Ray Measurements Far Underground*

[362]: Gaisser et al. (2021), *Seasonal Variation of Atmospheric Muons in IceCube*

[363]: Abbasi et al. (2023), *Observation of Seasonal Variations of the Flux of High-Energy Atmospheric Neutrinos with IceCube*

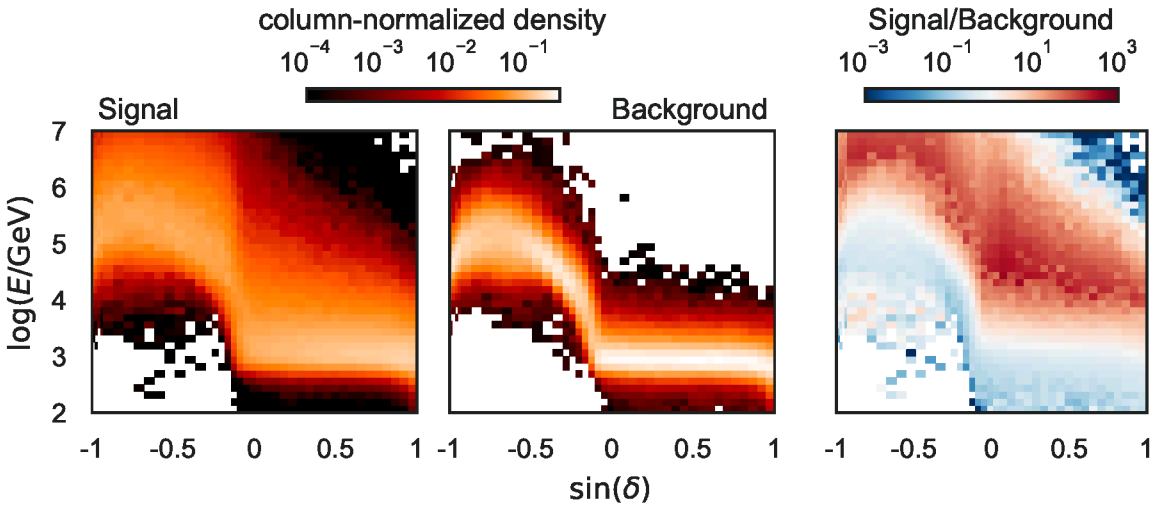

Figure 8.13: Energy PDFs for a power-law with a spectral index of $\gamma = 2$. The energy is shown against the declination. The left 2d-histogram shows the weighted signal Monte-Carlo event count in each bin. The middle panel shows the equivalent background distribution, and the right panel the ratio between the two.

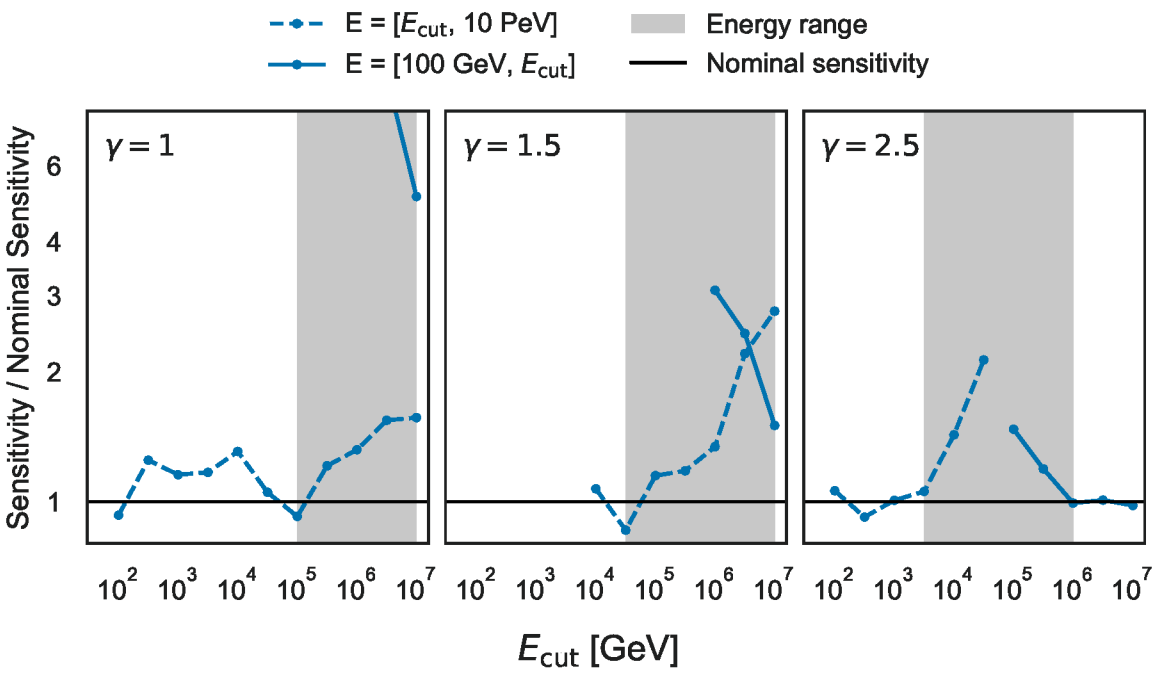

Figure 8.14: The calculation of the sensitive energy range for a power-law neutrino spectrum with $\gamma = 1$ (left), $\gamma = 1.5$ (center) and $\gamma = 2.5$ (right). The sensitivity flux is shown against the energy bound. Dashed and solid lines correspond to the lower and upper energy range, respectively. The gray shaded are is the determined sensitive energy range, and the solid black line is the nominal sensitivity from the unbounded calculation.

values. For the calculation of the lower (upper) energy limit, the signal injection is restricted to events above (below) a threshold E_{cut} and the sensitivity determined following Section 4.4.4. The point at which the sensitivity degrades significantly marks the respective limit.

The results are shown in Figure 8.14 for $\gamma = 1$, $\gamma = 1.5$, and $\gamma = 2$, which correspond roughly to the models in Section 8.2.3. For all spectral indices, the analysis is sensitive to the upper bound 10 PeV. For $\gamma = 1$, the sensitive energy range only extends down to 100 TeV, while for $\gamma = 1.5$ and $\gamma = 2.5$ it goes down to 30 TeV and 30 TeV, respectively.

8.3.5 Catalog Constraints

The test statistic distribution expected from background is shown in Figure 8.15. The median value is $\lambda_{\text{bkg}} \approx 11.7$. The observed value $\lambda_{\text{obs}} \approx 12.2$ is only slightly higher, and consequently the p-value is $p \approx 0.46$ which is compatible with the background expectation.
The 90% upper limit flux is calculated following Section 4.4.4, under the assumption that the neutrino flux is proportional to the infrared flux. The corresponding weights are shown in the last column of Table 8.2. The results are given in Table 8.3. Because the observed test statistic value was slightly higher than the background median, the limits are about 8% worse than the sensitivity.

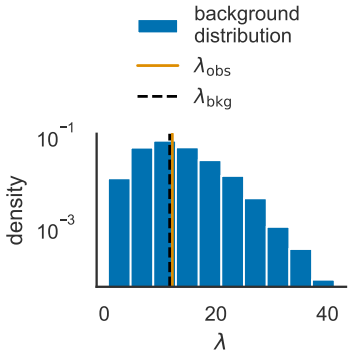

Figure 8.15: Background test staistic distribution and observed value for the IceCube stacking of accretion flares. The histogram depicts the density of test statistic values λ. The vertical black-dashed line is the background median, and the vertical orange line is the observed one.

It is interesting to look for the parameter space where the correlation with the neutrino alerts [80] and this non-detection are compatible. This is possible because for hard spectra, the main contribution of the signal is at higher energies where the neutrino data runs out of statistics (see Figure 8.13). To estimate the number of alert events corresponding to the limits in Table 8.3, the number of events above 100 TeV is calculated from the signal Monte-Carlo simulations, which approximates the neutrino alert event selection.
The resulting alert number limits are shown in Figure 8.16. Note that this only applies to the catalog of accretion flares in Table 8.2 and not to the full population.
The IR, OUV and X-ray models can be approximated with power-laws with spectral indices of 1, 1.5 and 2.5, respectively, in the relevant energy range (see Figure 8.10). These are indicated as vertical lines in Figure 8.16. The 90% limit on the alert event number for $\gamma = 2.5$ is $N_{\nu,\,\gamma=2.5} \approx 1.3$, disfavoring the X-ray model, while the OUV and IR models still seem compatible. This illustrates the fact that for hard spectral indices, the contribution at lower energies is so small

[80]: van Velzen et al. (2024), *Establishing Accretion Flares from Supermassive Black Holes as a Source of High-Energy Neutrinos*

γ	ϕ_{sens}	ϕ_{lim}
1.0	1.27×10^{-15}	1.37×10^{-15}
1.5	4.99×10^{-12}	5.35×10^{-12}
2.0	4.76×10^{-9}	5.10×10^{-9}
2.5	1.43×10^{-6}	1.55×10^{-6}
3.0	1.52×10^{-4}	1.64×10^{-4}
3.5	7.72×10^{-3}	8.35×10^{-3}

Table 8.3: Sensitivities ϕ_{sens} 90% upper limits ϕ_{lim} on the neutrino flux from the accretion flare catalog. All values are given at 1 GeV in $\text{GeV}^{-1}\ \text{s}^{-1}\ \text{cm}^{-2}$

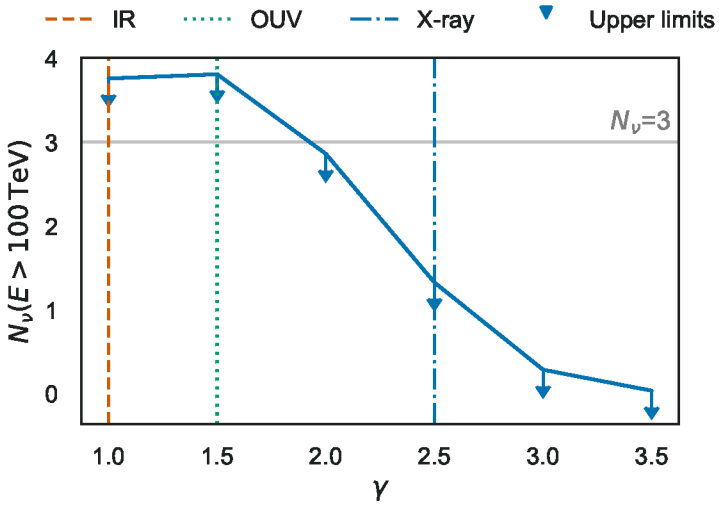

Figure 8.16: Constraints in the number of alerts from the analyzed catalog of accretion flares. The number of neutrinos above an energy of 100 TeV is shown against the spectral index of an assumed neutrino power-law spectrum. The vertical lines show the approximate spectral index predicted by interaction with the X-ray, OUV or IR photons shown in Figure 8.10.

compared to the atmospheric background that the analysis is not sensitive enough to probe the correlation seen with the high-energy alert events[4].

4: IceCube performed a search for additional neutrinos from the high-energy alerts using the same point source tracks dataset as in this work. No additional signal was found. A possible explanation is a neutrino source population with a power-law with a spectral index $\gamma \lesssim 1$ [364]

8.3.6 Population Constraints

Extrapolating these catalog limits to a whole population starts with the directly constrained quantity, which is the energy flux per area and time:

$$S = \frac{\mathrm{d}}{\mathrm{d}A\mathrm{d}t} \int E \frac{\mathrm{d}N}{\mathrm{d}E}\,\mathrm{d}E. \tag{8.12}$$

Luminosity distance

[286]: Ryden (2016), *Introduction to Cosmology*

This flux directly relates to the intrinsic luminosity L' through the *luminosity distance* d_L [286, Chapter 6]

$$S = \frac{L'}{4\pi d_\mathrm{L}^2}. \tag{8.13}$$

Redshift

The cosmological expansion, measured as the redshift z, leads to time dilation [286]:

$$\mathrm{d}t' = (1+z)\,\mathrm{d}t. \tag{8.16}$$

In addition, relativistic particles, like photons and neutrinos, loose energy:

$$\mathrm{d}E' = (1+z)\,\mathrm{d}E. \tag{8.17}$$

This is the reason for K corrections, which also play a role in Chapter 9.

The intrinsic luminosity is defined as the emitted energy per time:

$$L' = \frac{\mathrm{d}}{\mathrm{d}t'} \int E' \frac{\mathrm{d}N'}{\mathrm{d}E'}\,\mathrm{d}E'. \tag{8.14}$$

Because the sensitivity is determined based on a spectral assumption, it is convenient to define the spectral flux:

$$\begin{aligned} \frac{\mathrm{d}S}{\mathrm{d}E} &= \frac{1}{4\pi d_\mathrm{L}^2} \frac{\mathrm{d}L'}{\mathrm{d}E'} \frac{\mathrm{d}E'}{\mathrm{d}E} \\ &= (1+z) \frac{1}{4\pi d_\mathrm{L}^2} \frac{\mathrm{d}L'}{\mathrm{d}E'} \\ &= (1+z) \frac{E'}{4\pi d_\mathrm{L}^2} \frac{\mathrm{d}N'}{\mathrm{d}t'\mathrm{d}E'}. \end{aligned} \tag{8.15}$$

With the definition of the flux in Equation 8.12, this gives the relation between the sensitivity result and the intrinsic spectrum:

$$\frac{\mathrm{d}N}{\mathrm{d}A\mathrm{d}t\mathrm{d}E} = \frac{(1+z)^2}{4\pi d_\mathrm{L}^2}\frac{\mathrm{d}N'}{\mathrm{d}t'\mathrm{d}E'}. \tag{8.18}$$

Power-law spectrum

In this work, the spectrum is explicitly assumed to follow a power-law with the time-dependent normalization $\phi(t')$, anchored at energy E_0:

$$\frac{\mathrm{d}N'}{\mathrm{d}t'\mathrm{d}E'} = \phi(t')\left(\frac{E'}{E_0}\right)^{-\gamma}. \tag{8.19}$$

Inserting Equation 8.19 into Equation 8.18 finally gives the flux from a single source:

$$\frac{\mathrm{d}N}{\mathrm{d}A\mathrm{d}t\mathrm{d}E} = (1+z)^{2-\gamma}\frac{\phi(t')}{4\pi d_\mathrm{L}^2}\left(\frac{E}{E_0}\right)^{-\gamma}. \tag{8.20}$$

For a time window as defined in Section 8.3.3, integration over the transient time is trivial:

$$\begin{aligned}\int \phi(t')\,\mathrm{d}t &= (1+z)\int \phi(t')\,\mathrm{d}t' \\ &= (1+z)\,\phi_0\,T',\end{aligned} \tag{8.21}$$

where T' is the length of the time window. Therefore, the time integrated flux per area is

$$\frac{\mathrm{d}N}{\mathrm{d}A\mathrm{d}E} = (1+z)^{3-\gamma}\frac{\phi_0\,T'}{4\pi d_\mathrm{L}^2}\left(\frac{E}{E_0}\right)^{-\gamma}. \tag{8.22}$$

To calculate the contribution of an astrophysical transient population to the diffuse neutrino flux, the redshift dependent rate per comoving volume V_c and time in the source frame $\rho'(z)$ has to be considered:

$$\frac{\mathrm{d}N}{\mathrm{d}A\mathrm{d}t\mathrm{d}E} = \int \frac{\mathrm{d}N}{\mathrm{d}A\mathrm{d}E}\rho'(z)\mathrm{d}V_\mathrm{c}. \tag{8.23}$$

Population diffuse flux

Time dilation due to redshift makes the rate appear slower at higher redshift such that $\rho'(z) = (1+z)\rho(z)$. Substituting for integration over redshift using the differential comoving volume $\mathrm{d}V_\mathrm{c}/\mathrm{d}z$ gives the flux from an astrophysical transient population:

$$\frac{\mathrm{d}N}{\mathrm{d}A\mathrm{d}t\mathrm{d}E} = \int (1+z)^{2-\gamma}\frac{\phi_0\,T'\,\rho(z)}{4\pi d_\mathrm{L}^2}\left(\frac{E}{E_0}\right)^{-\gamma}\frac{\mathrm{d}V_\mathrm{c}}{\mathrm{d}z}\,\mathrm{d}z. \tag{8.24}$$

Note that it is implicitly assumed here that all transients have the same intrinsic neutrino luminosity[5]. In a more common notation, this is the flux ϕ. More specifically, what the analysis is sensitive to is the muon neutrino and anti-neutrino flux $\phi_\mu^{\nu+\bar{\nu}}$, owing to the muon track dataset used.

5: The upper limits were calculated assuming that the neutrino flux is proportional to the IR dust echo flux. Using this same relation instead of assuming equal nqureino luminosity for extrapolation to the whole TDE population would require a measurement of the distribution of IR luminosities over cosmic time, the so-called luminosity function Such a measurement is not yet, but Chapter 9 provides first steps in this direction.

Closest source

From the 90% limiting fluxes in Table 8.3, the flux from the closest source AT 2013kp is obtained by multiplying by the respective

weight ω_0 (Column 7 in Table 8.2). Inverting Equation 8.22 then gets the spectral normalization per source:

$$\phi_0 \, T' = (1+z_0)^{\gamma-3} \, 4\pi [d_L(z_0)]^2 \omega_0 \, T \frac{\mathrm{d}N}{\mathrm{d}A\mathrm{d}t\mathrm{d}E} \, , \tag{8.25}$$

where $T = 365\,\mathrm{d}$, corresponding to the analysis time window, and $z_0 = 0.01$ is the redshift of AT 2013kp.

TDE rate

With this, the last missing piece is the rate $\rho(z)$. As pointed out by van Velzen et al. [80], most of the flares are not unambiguous TDEs. However, for this novel, general population of accretion flares, there is no local rate or redshift evolution measurement available, although a first attempt will be presented in Chapter 9. Instead, because Wang et al. [351] showed that a sizable fraction of the MIRONG are TDEs, corresponding rate and evolution measurements are used here, namely the local rate from Velzen [365] and evolution from Sun, Zhang, and Li [366]

[80]: van Velzen et al. (2024), *Establishing Accretion Flares from Supermassive Black Holes as a Source of High-Energy Neutrinos*

[351]: Wang et al. (2022), *Mid-Infrared Outbursts in Nearby Galaxies (MIRONG). II. Optical Spectroscopic Follow-up*

[365]: Velzen (2018), *On the Mass and Luminosity Functions of Tidal Disruption Flares: Rate Suppression Due to Black Hole Event Horizons*

[366]: Sun et al. (2015), *Extragalactic High-Energy Transients: Event Rate Densities and Luminosity Functions*

Plugging these into Equation 8.24 gives the limits on the contributions to the diffuse flux. The normalizations are listed in Table 8.4. Compared to the previous IceCube results for TDEs and $\gamma = 2.5$ [92], this is an improvement by a factor of four, primarily owed to a larger catalog.

Table 8.4: 90% upper limits on the flux from a TDE population using Equation 8.24, the local TDE rate from Velzen [365] and the evolution from Sun, Zhang, and Li [366].

γ	ϕ_0 at 1 GeV $[\mathrm{GeV}^{-1}\,\mathrm{s}^{-1}\,\mathrm{cm}^{-2}]$
1	6.6×10^{-16}
1.5	2.2×10^{-12}
2.5	5.0×10^{-7}

The comparison with the measured diffuse flux and the models introduced in Section 8.2.3 is shown in Figure 8.17. The mid and high-energy proton injection models, where the protons prefer the X-ray and OUV photon field target, respectively, are inconsistent with the limits. The very high energy proton injection model, where the interaction happens with the dust-echo IR photons, is just below the reach of this analysis. This is consistent with the catalog limits in the previous section. In general, the contribution by TDEs to the diffuse high-energy neutrino flux [43] is constrained to be less than about 7.1% for $\gamma = 2.5$, which is about the best-fit spectral index of the diffuse flux. For $\gamma = 1$, the contribution must be less than about 0.3% at 100 TeV.

Dissipation efficiency limits

So far, it was assumed that all TDEs emit neutrinos. If this is instead only true for a fraction η, then the resulting flux is just $\eta\,\phi$. As mentioned in Section 8.2.3, the theoretical neutrino flux is proportional to the product of η and the dissipation efficiency ϵ_{diss}. Comparing the limit and the model prediction can therefore constrain ϵ_{diss}. Because the model prediction approximately follows a power-law with $\gamma \approx 1$ over the sensitive energy range, this can be done at any energy:

$$\phi_{\mathrm{model}} \, \eta \, \epsilon_{\mathrm{diss}} < \phi_0 \, \eta \tag{8.26}$$

$$\epsilon_{\mathrm{diss}} < \frac{\phi_0}{\phi_{\mathrm{model}}} . \tag{8.27}$$

With the limit for $\gamma = 1$ from Table 8.4, and the prediction of $\phi_{\mathrm{model}} = 1.1 \times 10^{-18}\,\mathrm{GeV}^{-1}\,\mathrm{cm}^{-2}\,\mathrm{s}^{-1}$ at 100 TeV for $\eta\epsilon_{\mathrm{diss}} = 1$, this constrains the dissipation efficiency to $\epsilon_{\mathrm{diss}} < 6 \times 10^{-3}$. This is an order of magnitude lower than the pessimistic case $\epsilon_{\mathrm{diss}} = 0.05$ assumed by Winter and Lunardini [361] and 20 times smaller than the value required to approximately reproduce the three associations observed with the high-energy alerts. However, it should be noted

[361]: Winter et al. (2023), *Interpretation of the Observed Neutrino Emission from Three Tidal Disruption Events*

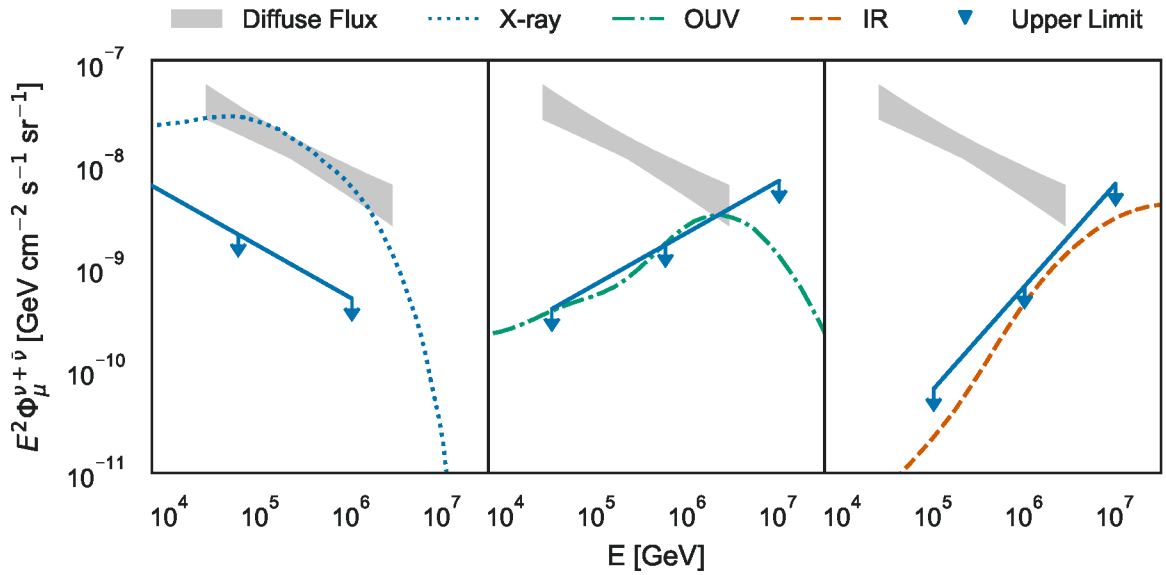

Figure 8.17: 90% upper limits on the contribution to the diffuse flux by a TDE population using Equation 8.24, the local TDE rate from Velzen [365] and the evolution from Sun, Zhang, and Li [366]. The energy scaled muon neutrino flux (ν and $\bar{\nu}$) is shown against the neutrino energy. The models for contributions by TDEs introduced in Section 8.2.3 are shown in dotted blue (interaction with X-rays), dash-dotted green (interaction with OUV photons) and dashed red (interaction with dust echo IR photons).

that there are some more degenerate parameters in the model: The lowest energy of the proton spectrum was chosen conservatively, and a more optimistic value can relax the requirement by a factor of 5. This is especially true for TDEs in AGN, that might benefit from the material in an already existing accretion disk [361]. This might be relevant for many sources in the analyzed sample that have AGN hosts, but also for accretion flares with large dust echoes in general because there is typically a lot of dust in the vicinity of AGN. Also, lowering the minimal blackhole mass for which TDEs occur can relax the required value of ϵ_{diss} by an order of magnitude [361, 367].

8.4 Conclusions

This chapter presented the possibility of neutrino production connected to the dust echo of TDEs. The claimed association of three TDEs with large dust echoes with high-energy neutrinos was investigated by re-simulating the respective alert events with a newly developed method. Although no firm conclusion can be drawn yet, it shows that a refined treatment of the alert uncertainty contours is necessary to confirm the claimed association. Under the premise that the TDEs are in fact the sources of the neutrinos, a stacking analysis was performed, harnessing the full power of the IceCube muon tracks dataset. The limits derived from the non-detection cannot rule out neutrino production by proton interaction with the dust echo IR photons, although the efficiency with which mass accretion is converted into non-thermal protons is constrained. It should be noted that this constraint does rely on the assumed TDE rate evolution which is a theoretical prediction and has yet to be measured.

While this does constrain model parameters, it does not rule out neutrino production in TDE dust echoes. The sensitivity could be increased by analyzing a larger flare catalog that has covered more of the IceCube data-taking period since 2010. This will be addressed in the next chapter.

A Comprehensive Catalogue of Infrared Flares

9

In the previous chapter, evidence was reviewed that connects accretion flares with large dust echoes to high-energy neutrino emission. However, the follow-up study could not support that claim [368], but the accretion flare sample was small and restricted to those flares with an optical counterpart. A full-sky sample that spans the full IceCube data-taking period since 2010, and is independent of optical detections, could utilize more of the neutrino data and increase sensitivity. Additionally, because neutrinos travel the universe unattenuated, this sample should be as deep as possible. This chapter describes the assembly of such a sample. The instrument that is used is described in Section 9.1. The author developed a pipeline to compile the necessary data, which is described in Section 9.2. The dust-echo origin of the infrared emission and the nature of the initial transient are evaluated in Section 9.3 before discussing the sample completeness in Section 9.4. The unique sample size allows for a first look at the rate at which these events occur in Section 9.5 before a summary and conclusion in Section 9.6. This chapter is based on the manuscript of an already submitted paper [369].

[369]: Necker et al. (2024), *Flaires: A Comprehensive Catalog of Dust-Echo-like Infrared Flares*

9.1 The Wide Field Infrared Survey Explorer

The *Wide-Field Infrared Survey Explorer* (WISE) was a satellite surveying the sky in four MIR bands from 2010 to 2024.

Observing system

The optical system is shown in Figure 9.1. The light collection happens with an afocal optics system with a 40 cm primary mirror, providing 8x magnification. The imaging optics consist of a scanning mirror, a beam splitter assembly, and four focal planes with the detectors. The scanning mirror stabilizes the FoV over the integration time while the telescope continuously rotates. It can then return to its original position within 1.1 s. The beam splitter separates the light into four different bands W1, W2, W3, and W4. The detailed filter functions are shown in Figure A.1. The central wavelengths are 3.4 µm, 4.6 µm, 12 µm and 22 µm. The nominal operating temperature of the W1 and W2 detectors is 32 K while the W3 and W4 detectors have to be cooled down to 7.8 K. These temperatures are achieved by a solid hydrogen fueled cryostat. This system enables simultaneous observation of a 47′ FoV in all four bands [370].

[370]: Larsen et al. (2005), *Wide-Field Infrared Survey Explorer Science Payload Overview*

Sky scan pattern

WISE scanned the sky in great circles from the north to the south pole of the ecliptic. As mentioned above, this was achieved with the scanning mirror stabilizing the FoV over the integration time of around 8.8 s while the telescope is rotating at a constant rate. The overlap between consecutive exposures is around 10% and the scan circle advances around 4′ per orbit, as shown in Figure 9.2. Around 12 of the 15 orbits per day were on top of any given source. This resulted in a full sky scan every half year [371].

[371]: Wright et al. (2010), *The Wide-Field Infrared Survey Explorer (WISE): Mission Description and Initial On-Orbit Performance*

Nominal mission

The satellite was launched in 2009 and began routine operations in

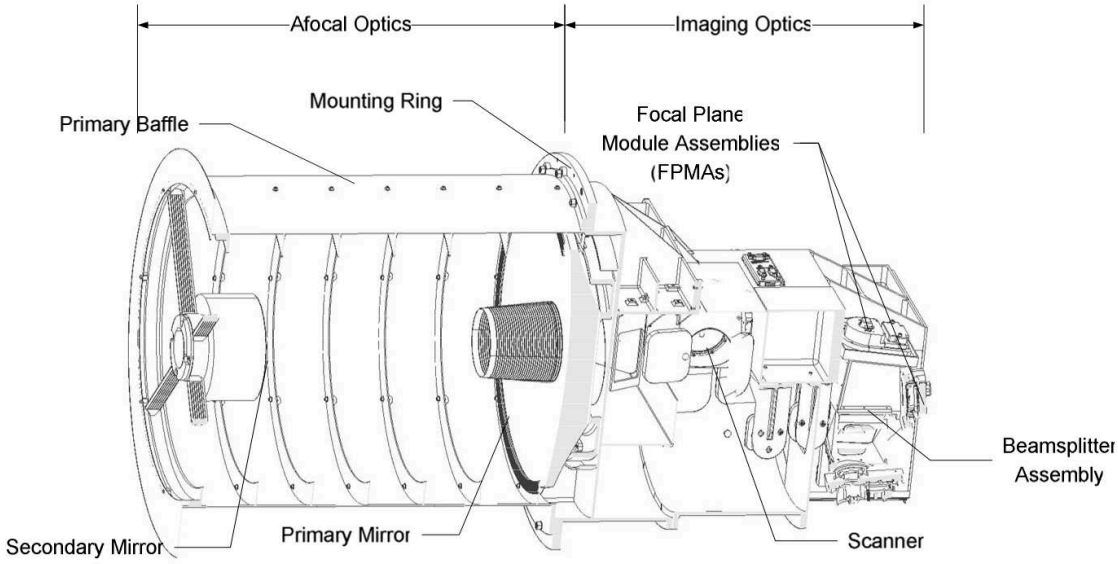

Figure 9.1: The WISE optical system. Taken from Larsen and Schick [370]

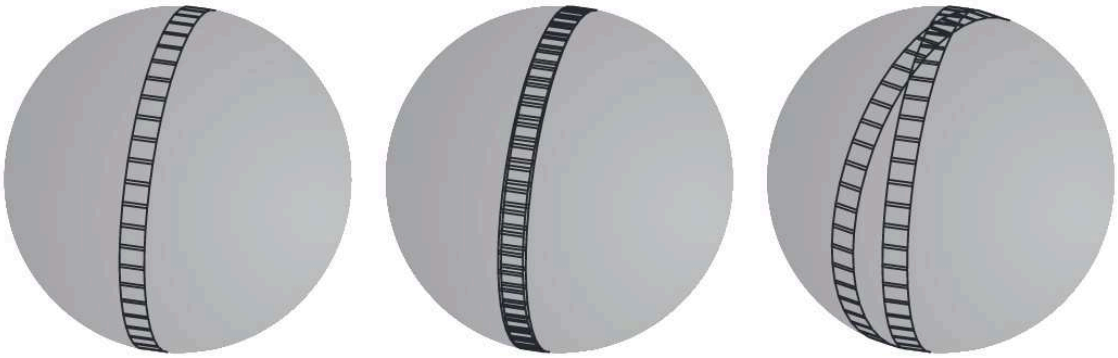

Figure 9.2: WISE Sky scanning pattern. Coverage on the sphere for one orbit, for two consecutive orbits and for two orbits 20 days apart. Taken from Wright et al. [371]

Post-cryo phase

NEOWISE reactivation

1: The *R* stand for *reactivation*. It is a distinction to the post-cryo phase, which is sometimes also called NEOWISE phase.

[372]: Mainzer et al. (2014), *Initial Performance of the NEOWISE Reactivation Mission*

Mission end

2010. Until September 2010 it had surveyed the sky 1.2 times before the solid hydrogen reserves ran out. The W3 and W4 band channels could not be operated without the coolant but the temperature of around 73.5 K achievable by passive cooling was low enough to continue observations in W1 and W2. The mission was extended for a post-cryogenic phase of four months before being put into hibernation in February 2011. In late 2013 the telescope was reactivated and resumed survey operations in December 2013, again only in the W1 and W2 band. Because the primary goal in this phase was to discover Near Earth Objects (NEOs), the mission was dubbed NEOWISE-R[1] from then on [372]. Although only expected to last until 2017, observations continued for more than ten years until the end of July 2024, providing around 10 observations of each point in the sky within a day, about once every six months. The satellite had not been equipped with maneuvering capabilities, so its orbit had been decaying due to residual atmospheric drag, and it finally re-entered into Earth's atmosphere during writing of this thesis on November 2nd 2024[373].

All-Sky data release

There are three major WISE data releases. The first was the *WISE*

All-Sky[*] data release, containing data from the first nine months of fully cryogenic, four-band observations. It contains a catalog of detected sources including their photometry, derived from stacked images to extend the sensitivity beyond that of the single exposure. This was superseded by the *AllWISE*[†] release, which includes also the W1 and W2 exposures of the post-cryo phase. As a result the sensitivity improved compared to the All-Sky data release. In addition, it also provides multi-epoch photometry, obtained from the single exposures, measured at the position of the sources detected in the stacked images.

AllWISE data release

The *NEOWISE-R*[‡] data was released for the first time in March 2015, including the data until the preceding December. It contains point spread function (PSF) fit photometry performed on the single exposures instead of stacked images. As a result, faint sources that are detected in the stacked images and reported in the AllWISE source catalog might not have a corresponding entry in the NEOWISE-R single exposure photometry data. Sources near the detection threshold of a single exposure can also appear too bright as a result of Eddington bias [372, 374].

NEOWISE-R data release

[372]: Mainzer et al. (2014), *Initial Performance of the NEOWISE Reactivation Mission*
[374]: Eddington (1913), *On a Formula for Correcting Statistics for the Effects of a Known Probable Error of Observation*

9.2 Agnostic Infrared Flare Selection

The wavelengths of the WISE bands are perfect for the study of dust echoes of extreme transients. Because the dust typically radiates at a temperature of around 1800 K (see Section 8.1), the W1 and W2 bands are close to the maximum of the corresponding spectrum (see Figure 9.3). This is even more the case if the dust is cooler ($T \sim 1200$ K) or the temperature of the spectrum is shifted down due to the expansion of the universe.

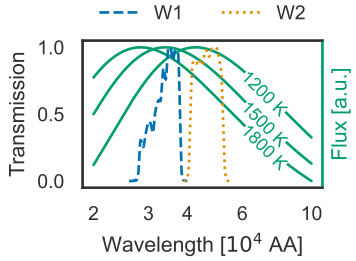

Figure 9.3: The transmission of the WISE bandpasses compared to the shape of a blackbody spectrum with different temperatures.

Furthermore, the sampling rate of one visit every six months is sufficient to detect and characterise the dust echo of a luminous transient in a dusty shell which happens on the timescale of one year (see Section 8.1). Thanks to the long observation time of around ten years, the WISE dataset can facilitate the observation of many such transients.

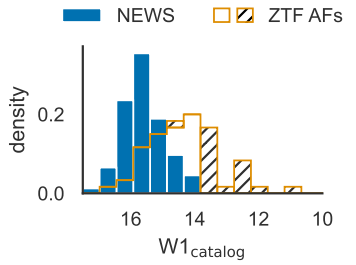

Figure 9.4: Apparent W1 magnitude distrbution of the NEWS objects and the hosts of the ZTF accretion flares. The ZTF flare hosts that er not included in NEWS are indicated with stripes.

9.2.1 Parent Galaxy Sample

Because the final sample of infrared flares should be as complete as possible, the underlying galaxy sample should cover the whole sky and go as deep as possible.

The largest available catalog[2] is the *The Northern Extragalactic WISE × Pan-STARRS catalogue* (NEWS) [375], a list of around 4×10^7 extragalactic objects, identified by machine learning techniques. It is itself based on the data of the AllWISE source catalog supplemented by PSF optical to infrared photometry measurements by Pan-STARRS (g, r, i, z and y bands) by a crossmatch in a 1.5″ circular window. To avoid foreground stars, bright objects were excluded ($m_{W1} <$

NEWS catalog

2: The NEWS catalog was the largest catalog at the start of the analysis in early 2022. The WISE-PS1-STRM, introduced below, was only published in late 2022.

[375]: Khramtsov et al. (2020), *The Northern Extragalactic WISE × Pan-STARRS (NEWS) Catalogue - Machine-learning Identification of 40 Million Extragalactic Objects*

[*] https://wise2.ipac.caltech.edu/docs/release/allsky
[†] https://wise2.ipac.caltech.edu/docs/release/allwise
[‡] https://wise2.ipac.caltech.edu/docs/release/neowise

13.8 $\mathrm{mag}_{\mathrm{Vega}}$, $m_g < 14\,\mathrm{mag}_{\mathrm{AB}}$ and $m_r < 14\,\mathrm{mag}_{\mathrm{AB}}$). This initial sample contained around 2×10^8 sources. Five abstract features were constructed from the 21 color indices using a neural network autoencoder [376]. The separation between galactic and extragalactic sources in the feature space was constructed with a support vector machine [377]. In the relevant magnitude range $18\,\mathrm{mag}_{\mathrm{AB}} < m_g < 22\,\mathrm{mag}_{\mathrm{AB}}$, the purity of the selection is good[3], and the completeness compared to other sky surveys is at least 95% [375].

Because the flare sample should ultimately expand on the sample of ZTF accretion flares introduced in Section 8.2, it is desirable that most of that sample's host galaxies are included in the parent galaxy sample. The distribution of apparent W1 magnitudes is shown in Figure 9.4. Around 30% of ZTF accretion flare hosts are missing from the NEWS catalog, almost all of which are brighter than the NEWS cutoff of $W1_{\mathrm{NEWS}} = 13.8\,\mathrm{mag}_{\mathrm{Vega}}$.

The WISE-PS1-STRM sample [379] can facilitate the inclusion of brighter hosts. It used data from the WISE All-Sky release (see Section 9.1) and Pan-STARRS photometry to infer object classifications and photometric redshifts without selection cuts based on the brightness of sources. For the resulting crossmatch of around 4×10^8 objects, classification probabilities for the classes star, galaxy and quasar were derived as well as a redshift. This was done by two separate dense neural networks based on 98 photometric parameters (40 from Pan-STARRS and 56 from WISE). Objects outside the parameters of the training set were flagged as extrapolated.
The subsample of objects supplementing NEWS are probable galaxies with a g-band magnitude brighter than 20 mag, contained within the training dataset parameter space. The detailed parameters and ranges are listed in Table 9.1. The resulting 3.2×10^6 objects were crossmatched to the NEWS sample based on the Pan-STARRS object identifier which resulted in 9.6×10^5 non-overlapping sources.

To ensure that the galaxy sample is as complete as possible in the local universe, the *Local Volume Sample from the NASA Extragalactic Database* (NED-LVS) [380] is also included. It contains around 1.8×10^6 sources with a redshift up to $z = 0.2$. Because for these objects high-quality photometric data and distance measurements are available, the completeness was calculated by Cook et al. [380] based on galaxy luminosity functions from the literature. Concerning the total luminosity it is 70% complete up to $z \approx 0.06$ while the number of galaxies above a certain magnitude is complete up to $z \approx 0.08$ (see Section B.1). We include 6.7×10^5 sources from NED-LVS that have no counterpart in our sample within a radius of 1″.

The resulting parent galaxy sample has 4.2×10^7 sources with the majority located in the northern part of the sky above $\delta \gtrsim -30°$ (see Figure 9.6). This reflects the FoV of Pan-STARRS which both NEWS and WISE-PS1-STRM are based on. All sources with $\delta \lesssim -30°$ come from the NED-LVS.
For around 1.9×10^6 sources redshift estimates are available through NED-LVS, and for another 3.2×10^7 sources there is an inferred photometric redshift from WISE-PS1-STRM. There is at least a photometric redshift estimate for 3.4×10^7 sources, around 80% of the sample.

[376]: Rumelhart et al. (1986), *Learning Internal Representations by Error Propagation*

[377]: Vapnik (1995), *The Nature of Statistical Learning Theory*

3: The purity of more than 99% given in the appendix of Khramtsov, Akhmetov, and Fedorov [375] is not a good metric for the unbalanced sample as explained in the same paper. The Matthews correlation coefficient [378] takes this into account. The determined value near unity also indicates high purity, but the interpetation of the exact value is less clear, which is why no numerical value is quoted here.

WISE-PS1-STRM

[379]: Beck et al. (2022), *WISE-PS1-STRM: Neural Network Source Classification and Photometric Redshifts for WISE×PS1*

Table 9.1: Parameters to select supplementary objects from WISE-PS1-STRM [379]

Parameter	Range
`prob_Galaxy`	> 0.5
`gFPSFMag`	≤ 20
`extrapolation_Class`	$= 0$

NED-LVS

[380]: Cook et al. (2023), *Completeness of the NASA/IPAC Extragalactic Database (NED) Local Volume Sample*

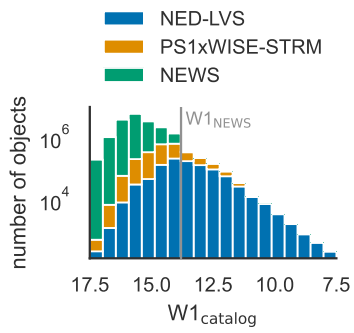

Figure 9.5: Distribution of the apparent magnitude in W1 of the parent galaxy samples. The grey line indicates the cutoff of the NEWS sample.

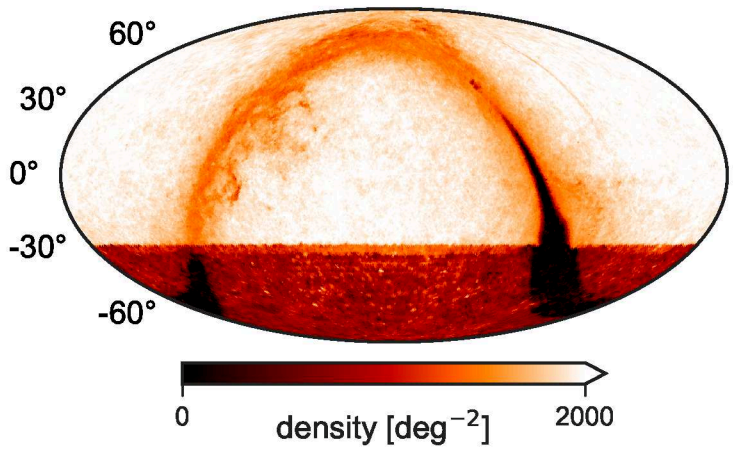

Figure 9.6: Skymap of the parent galaxy sample. The color scale shows the density of galaxies per square degree.

For galaxies brighter than $M_{W1} = -24\,\mathrm{mag}_{\mathrm{Vega}}$, the parent sample is complete up to a redshift of about $z = 0.2$ (see Section B.1), almost doubling the redshift range compared to NED-LVS. However, for dimmer galaxies or larger distances, the exact completeness is hard to estimate which is why eventual resulting rates in Section 9.5 of transients can only be given per galaxy and not in absolute volumetric densities.

9.2.2 Infrared Light Curves

To produce light curves in the infrared, the time-resolved data from WISE was used[4]. WISE visits each point in the sky roughly every six months, producing around a dozen single exposures. Photometric measurements are extracted by fitting the PSF. These are available for both the AllWISE[§] as multi-epoch photometry and NEOWISE-R[¶] single exposures.

4: This is in contrast to the AllWISE source catalog, for example, where all exposure over a long time were stacked to extract a single photometric measurement.

Data Quality Criteria

Photometric measurements based on single exposure are prone to many sources of errors: image artifacts, cosmic rays, blending of close sources or stray moonlight. Following the WISE data release documentation[‖], the detections have to meet the following requirements: good image quality, no de-blending, no contamination by image artifacts, a separation to the Southern Atlantic Anomaly of more than 5°, and a position outside the moon mask.

The selection of data from the WISE database depends on which sample the galaxy is included in.

Selection by Identifier

All source in the NEWS sample come with the corresponding AllWISE source catalog identifier, so all related AllWISE multi-epoch photometry and all associated NEOWISE-R detections can be downloaded.

Selection by Position

The sources from the WISE-PS1-STRM and NED-LVS samples lack associated entries in the AllWISE database. Therefore, the data selection was based on positional coordinates. Given that the full width at half maximum (FWHM) of the WISE PSF is approximately 6″, all

§ https://wise2.ipac.caltech.edu/docs/release/allwise/
¶ https://wise2.ipac.caltech.edu/docs/release/neowise/
‖ https://wise2.ipac.caltech.edu/docs/release/neowise/expsup/sec2_3.html#reliable

single exposure photometry data for both AllWISE and NEOWISE-R within this radius was downloaded. This approach encompasses all data for extended or faint objects, for which there may be significant scatter in the best-fit position. However, it also introduces the risk of incorporating data points from neighboring objects. The AllWISE data, in particular, is susceptible to this error because it includes single epoch measurements or upper limits of faint objects only detected in the AllWISE source catalog. The NEOWISE-R images are analysed before any association with AllWISE sources so the position of the PSF is a free parameter. Only if an excess is detected in any of the two bands, it is reported in the data release where it is associated to the closest source from the AllWISE catalog within 3″. The AllWISE multi-epoch photometry is calculated for all sources from the AllWISE source catalog with its fixed position. That means that there exist entries in the AllWISE multi-epoch photometry database for fainter sources, even if the single exposure only resulted in upper limits.
In such instances, blending can compromise the quality of the AllWISE photometry, rendering it insufficient to simply select the closest AllWISE photometry. To mitigate this issue, clusters of data points were identified, and the closest cluster was associated with the corresponding source in the parent sample.

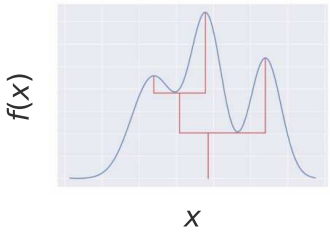

Figure 9.7: Illustration of the HDBSCAN clustering algorithm. Adapted from McInnes and Healy [381]

Accelerated Density Based Clustering

[381]: McInnes et al. (2017), *Accelerated Hierarchical Density Based Clustering*

[382]: Pedregosa et al. (2011), *Scikit-Learn: Machine Learning in Python*

To do the clustering, the Accelerated Density Based Clustering algorithm [381] was used, implemented as HDBSCAN in `scikit-learn` [382]. Assuming a density function $f(x)$, clusters are a connected subset with $f(x) \geq \lambda$ (see Figure 9.7). For varying $\lambda \geq 0$, a hierarchical cluster structure can be constructed, referred to as the cluster tree, where each cluster is a branch of that tree. HDBSCAN estimates this cluster tree, converging to the true density function as the sample size goes to infinity.
The clustering was used to find clusters of datapoints in the downloaded 6″ region around the parent sample source position. Because the algorithm performs best in cartesian coordinates, the position angle P and angular offset α were calculated and the clustering performed on $\Delta x = \alpha \cos(P)$ and $\Delta y = \alpha \sin(P)$.
All points belonging to the nearest cluster were selected if that cluster was within a radius of 1″. Additionally, all data points within 1″ were included, irrespective of whether they belonged to a different cluster or no cluster at all. This method facilitates the selection of corresponding single epoch photometry, particularly in cases of significant positional scatter, while minimizing the inclusion of unrelated data points.

Stacked Photometry

Combining the measured instrument level counts for each visit yields more robust stacked photometry. The photometric zero-point $ZP_{\nu,i,j}$ for each single exposure measurement i of visit j per band with frequency ν describes the relationship between physical magnitude in the vega system $V_{\nu,i,j}$ and measured instrument counts $C_{\nu,i,j}$:

$$ZP_{\nu,i,j} = V_{\nu,i,j} + 2.5 \log_{10}(C_{\nu,i,j}). \tag{9.1}$$

For each visit and band, the median of the zero-point $ZP_{\nu,\mathrm{med},j}$ can then be used to calculate the constant relating the instrument counts

to flux densities:

$$c_{\nu,\mathrm{j}} = F_{\nu,0} \cdot \log_{10}(ZP_{\nu,\mathrm{med},j}/2.5), \tag{9.2}$$

where $F_{\nu,0}$ is the zero magnitude flux density [383]. The spectral flux densities for each exposure are then:

[383]: Jarrett et al. (2011), *The Spitzer–WISE Survey of the Ecliptic Poles*

$$F_{\nu,i,j} = C_{\nu,i,j} \cdot c_{\nu,\mathrm{j}}. \tag{9.3}$$

Finally, the stacked flux density is calculated as the median of the spectral flux densities for each visit and band:

$$F_{\nu,j} = \mathrm{med}_i(F_{\nu,i,j}). \tag{9.4}$$

The uncertainty is determined as the maximum of the standard deviation from the median and the Pythagorean sum of the individual measurement uncertainties:

$$\sigma_{F_{\nu,j}} = \sqrt{\frac{1}{N}\sum_i^N (F_{\nu,i,j} - F_{\nu,j})^2} \tag{9.5}$$

$$u_{F_{\nu,j}} = \max\left[\sigma_{F_{\nu,j}}, \sqrt{\sum_i^N u_{F_{\nu,i,j}}^2}\right]. \tag{9.6}$$

These error-bars were validated based on the expected distributions of the deviation from the median and the coverage by the errors (see Section B.2). Outliers with unreasonably high fluxes, likely caused by cosmic rays, spurious detections escaping WISE flagging, or asteroids passing through the line of sight, were noted. These outliers were rejected if their deviation from the median exceeded 20 times the 70th percentile.

χ^2_{red} Variability Measure

For each light curve and band, the reduced chi-square χ^2_{red} was calculated relative to the median, serving as an initial measure of the light curve's variability. This metric enables the early identification of quiescent light curves based on a low χ^2_{red} value. To establish a significant threshold, the flare search algorithm, as described in the subsequent section, was applied to a subset of 2×10^6 light curves. It was determined that all light curves exhibiting flaring had a value greater than $\chi^2_{\mathrm{red}} = 1$ in both bands. Approximately half of the 4.2×10^7 sources did not meet this threshold and were thus excluded from further analysis (refer to Figure 9.8).

The pipeline described in this section was implemented by the author and made publicly available as the python package `timewise` [384].

9.2.3 Flare Selection

Bayesian Blocks

To find any potential excess in the light curves, they have to be analyzed in an agnostic fashion, since no prior information about the onset of a potential flare is available. The Bayesian Blocks algorithm [385] is an algorithm that is widely used in the astronomical community for this task. Here, the implementation in `astropy` [386] is used. The algorithm divides the light curve into intervals of constant

[385]: Scargle et al. (2013), *Studies in Astronomical Time Series Analysis. VI. Bayesian Block Representations*

flux, with a preference for fewer intervals depending on a prior. The empirically motivated prior for point measures for the number of change points is given by

$$N_{\mathrm{cp,\,prior}} = 1.32 + 0.577\ \log_{10}(N_{\mathrm{visit}}) \tag{9.7}$$

where N_{visit} represents the number of visits [385]. The quiescent state, or baseline, is defined as the lowest flux measured across the light curve. This baseline does not need to be a continuous interval but can be interrupted by excesses. To consolidate all baseline intervals into one measurement, the blocks with the lowest spectral flux density are successively combined with the baseline. The updated baseline is calculated as the mean of all data points in the baseline blocks, with its uncertainty represented by the standard deviation. The combination process stops when no additional block falls within 5σ of the baseline. Blocks not within the baseline are considered excess blocks. Adjacent excess blocks are combined into a single excess, with its start and end defined by the time of the first and last data points within the excess, respectively.

To efficiently analyze the $\mathcal{O}(10^6)$ light curves, the procedure is implemented within the AMPEL framework [387], which supports high-throughput streaming of data and allows for the integration of user-contributed code in the form of units. The AMPEL pipelines are divided into four stages, or tiers. The Bayesian Blocks analysis is implemented in tier two as the unit, `T2BayesianBlocks` (see Figure 9.8).

[387]: Nordin et al. (2019), *Transient Processing and Analysis Using AMPEL: Alert Management, Photometry, and Evaluation of Light Curves*

Selection Cuts

The significance of the flaring behavior identified by the Bayesian Blocks result are quantified to select significant dust-echo-like flares. The following cuts were implemented as another tier two unit `T2DustEchoEval`:

1. *Flare Region*: an excess in at least one of the two WISE filters
2. *Flares coincident in both filters*: a coincident excess in the other band
3. $\Delta F/F_{\mathrm{rms}} > F_{\mathrm{rms}}/\sigma_{\mathrm{F}}$: dust echo strength $\Delta F/F_{\mathrm{rms}}$ higher than the significance of variability in the extraneous part of the light curve $F_{\mathrm{rms}}/\sigma_{\mathrm{F}}$ to make the distinction to stochastic AGN variability [80]. ΔF is the difference between baseline and peak flux, F_{rms} the root-mean-square of the extraneous light curve and σ_{F} the standard deviation of the baseline.
4. *Baseline before excess*: at least one baseline datapoint before the excess
5. *Gap*: a baseline datapoint not more than 500 d before the first detection of the excess. This criterion excludes flares that rise during the *AllWISE* period.
6. *State transition*: a segmentation of the excess into at least two blocks to reject state transitions or a difference in time between the first and last datapoint in the excess of no more than 3 yr
7. $N_{\mathrm{E}} > 1$: more than one datapoint in the excess
8. $\Delta F/\sigma_{\mathrm{F}} > 5$: a detection significance of the excess of at least 5σ with respect to the baseline.
9. *Just started*: at least two blocks if the excess is at the end of the light curve.

[80]: van Velzen et al. (2024), *Establishing Accretion Flares from Supermassive Black Holes as a Source of High-Energy Neutrinos*

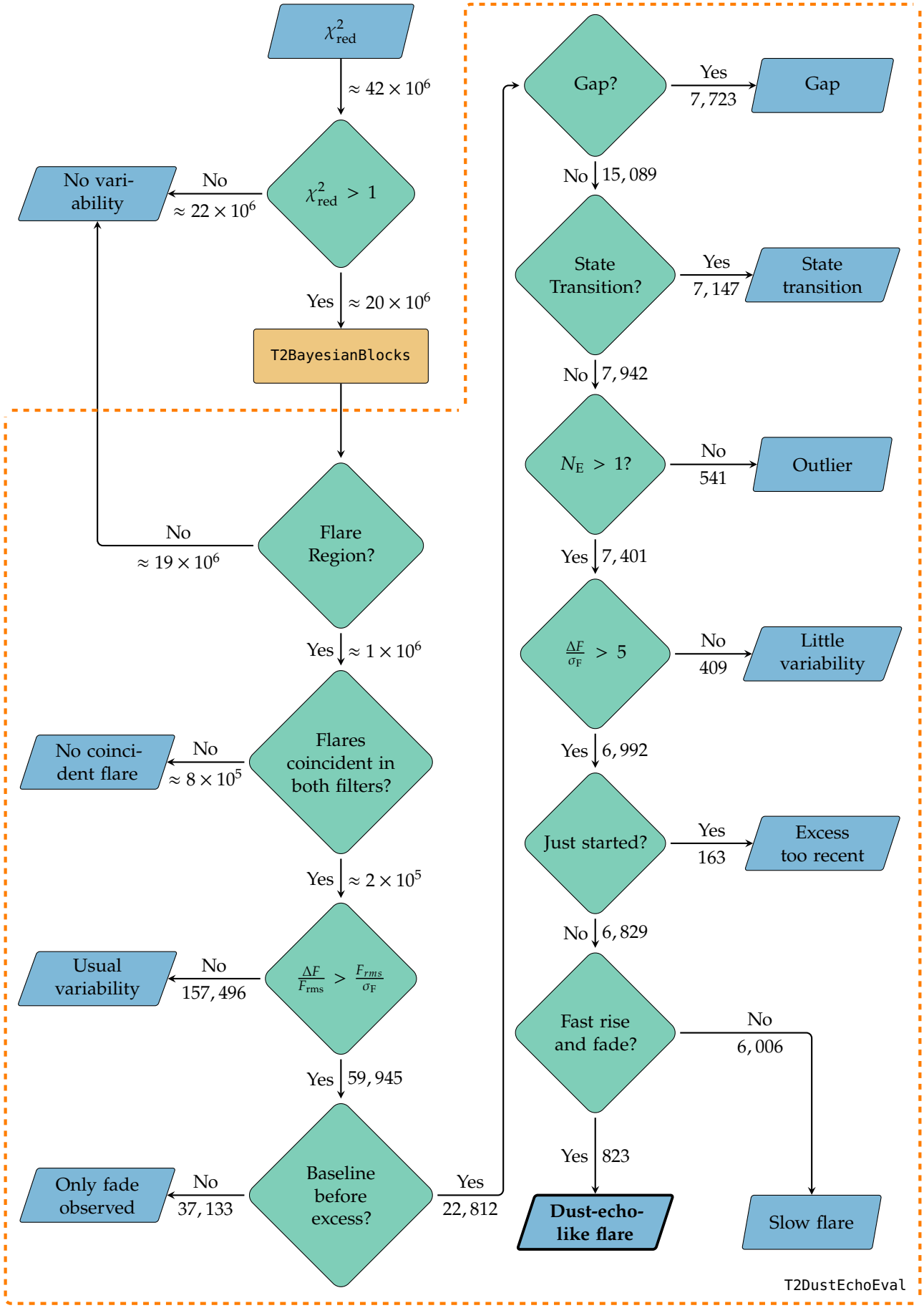

Figure 9.8: Flowchart of the flare selection process. See Section 9.2.3 for a detailed explanation of the selection steps.

At this stage, the e-folding rise and fade times were calculated:

$$\tau = \frac{\Delta t}{\log(F_2/F_1)}. \tag{9.8}$$

For the rise time, Δt represents the interval between the last baseline datapoint and the peak of the light curve, where F_1 denotes the baseline spectral flux density and F_2 denotes the peak spectral flux density. For the fade time, Δt is the duration from the peak to the last datapoint in the excess, with F_1 representing the peak spectral flux density and F_2 representing the final measurement of the excess. The distinction between dust echo-like flares and those occurring over longer timescales is made using these e-folding times:

10. *Fast rise and fade*: $\tau_{\text{rise}} < 1000\,\text{d}$ and $400\,\text{d} < \tau_{\text{fade}} < 5000\,\text{d}$.

After these cuts, 823 flares are left that meet the criteria for dust-echo-like infrared flares. Figure 9.8 summarizes the pipeline as a flowchart and lists the number of flares accepted and rejected at each step.

This flare selection pipeline is publicly available as the *`timewise` Subtraction Pipeline* python package, `timewise-sup` [388].

[388]: Necker (2024), *Timewise-Sup: The Timewise Subtraction Pipeline v0.5.0*

9.2.4 Difference Light Curves

To analyze the flare properties, it is necessary to isolate the flare contribution from the light curve baseline. To obtain this difference photometry, the baseline, as measured in Section 9.2.2, was subtracted from the data. The uncertainty in the difference photometry is calculated as the Pythagorean sum of the baseline uncertainty and the uncertainty of the stacked data. The spectral flux νF_ν is then determined by multiplying the difference spectral flux density F_ν by the frequency ν corresponding to the central wavelength of the WISE bandpass.

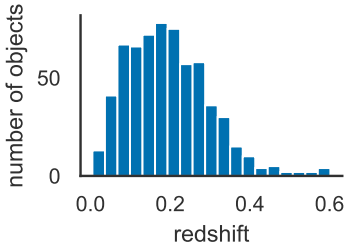

Figure 9.9: Redshift distribution of the non-quasar flares.

Well-curated redshifts from the NED-LVS are available for 135 sources. For 411, photometric redshifts from WISE-PS1-STRM were utilized, covering 411 sources. For 139 sources, redshifts were also found in other catalogs (see Table 9.2). In cases where multiple redshifts were identified, they were categorized based on whether they were spectroscopic or photometric, as well as the match distance, and the mean of the best category was taken. This is done by the unit `T2DigestRedshifts`**. Luminosities per bandpass in the rest frame were calculated based on the luminosity distance d_L [389, Chapter 3]:

$$\nu_\text{e} L_{\nu_\text{e}} = \nu F_\nu \cdot 4\pi d_\text{L}^2(z), \tag{9.9}$$

where the subscript e indicates the rest frame quantities.

[389]: Weedman (1986), *Quasar Astronomy*

Eddington Bias

Because the measurement of the baseline directly affects the difference photometry and is by construction a lot dimmer than the flare, it is worth reviewing the so-called Eddington bias, connected to the measurement of dim fluxes [374].
Using the single exposure photometry can introduce a bias for dim

[374]: Eddington (1913), *On a Formula for Correcting Statistics for the Effects of a Known Probable Error of Observation*

** https://github.com/AmpelAstro/Ampel-HU-astro/blob/main/ampel/contrib/hu/t2/T2DigestRedshifts.py

Catalog	matches	Reference
WISE x SuperCOSMOS	66	[390]
SDSS DR10	5	[391]
GLADE	7	[392]
LS DR8	75	[393]
NEDz	29	[a]

Table 9.2: Number of matches in redshift catalogs

[a] https://ned.ipac.caltech.edu/

sources near or below the limiting magnitude of $m_{W1} \approx 16.0$ and $m_{W2} \approx 14.9$. Scatter due to instrument noise can still produce detections above these limits. Because the corresponding down-scattered data is below the detection limit, the measurement is skewed toward brighter values. This has been identified as an effect already for the Infrared Astronomical Satellite [394] as well as for NEOWISE-R [372]. As the bias intensifies with dimmer sources, the baseline measurements are primarily affected as opposed to the flare data. Figure 9.10 shows the change in apparent magnitude and color as a function of the magnitude in the AllWISE source catalog. The photometry in the AllWISE source catalog is obtained from stacked images and therefore unbiased down to fainter magnitudes. In this comparison, it is taken as the true value. The results are consistent for $W1_{\mathrm{catalog}} < 15\,\mathrm{mag}_{\mathrm{Vega}}$. Beyond that, the W2 band surpasses its single-exposure sensitivity and the Eddington bias starts to take effect. This is also clearly visible in the color difference where the measurements appear redder.
As a test, replacing the measurement of the baseline from Section 9.2.2 with the deep AllWISE source catalog measurements, the results of the further analysis remain consistent, demonstrating the robustness against Eddington bias. The measured values for the difference photometry were retained to ensure that the lowest state was detected, even if there was some excess during the AllWISE period.

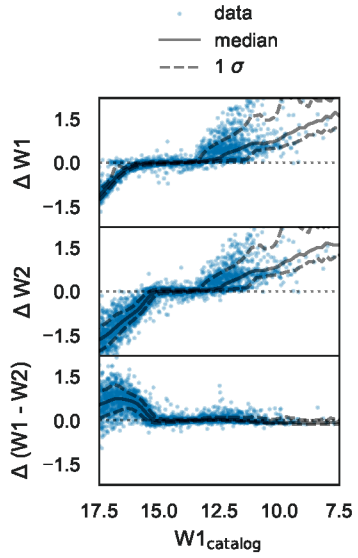

Figure 9.10: Changes in baseline magnitude measurement to AllWISE stacked images. The median and 1σ are calculated in 0.1 mag bins. 100 randomly sampled sources are shown per bin.

9.3 Physical Origin

This section explores the possible origin of the flare sample selected in the previous section. The selection so far already implicitly assumed that the infrared excess is due to a dust echo of an activating function. This assumption will be explicitly tested before exploring the nature of the initial transient.

9.3.1 Dust Echo Fit

Assuming that the infrared flares are due to reprocessed emission by dust distributed in a thin, spherical shell around the central engine, the spectrum of the emission can be modeled using a blackbody (see Section 8.1). Although the dust emission is expected to follow a modified blackbody spectrum [395], the resulting bolometric luminosity is almost unaffected, and the temperature is only slightly lower [348].

[395]: Draine et al. (1984), *Optical Properties of Interstellar Graphite and Silicate Grains*

Blackbody Fit

Fitting the rest frame luminosity in each band to the corresponding value predicted by the blackbody emission, one can obtain the

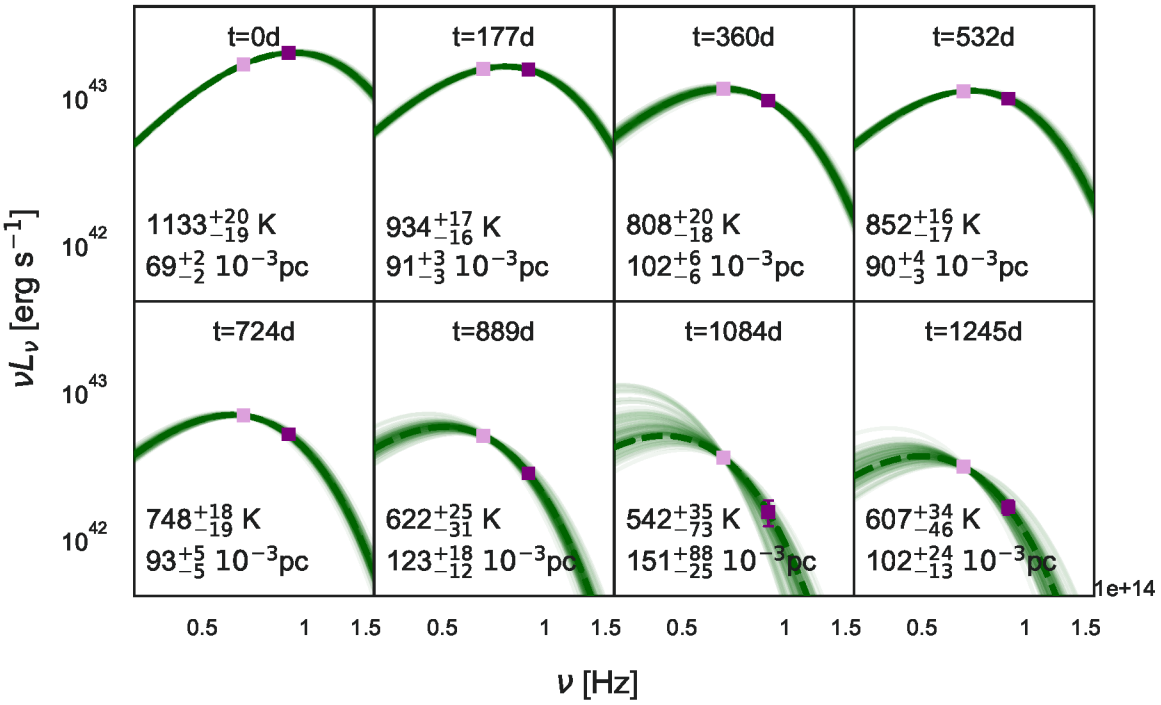

Figure 9.11: Blackbody fits for NGC 7392 for all epochs of the flare where the Markov-Chain Monte-Carlo (MCMC) sampling resulted in meaningful constraints on the fit parameters. The dashed green line shows the best fit and the transparent lines the results from the MCMC sampling. The best fit and 68th percentile temperature and effective radius values are shown in the bottom left corner. The frequency ν is given in the source frame.

temperature T and the effective radius R_{eff} for each visit [29, Chapter 6]:

$$\nu L_{\nu,\text{BB}} = \pi \cdot \nu B_\nu(T) \cdot 4\pi R_{\text{eff}}^2 \tag{9.10}$$

[29]: Bradt (2008), *Astrophysics Processes: The Physics of Astronomical Phenomena*

Taking the ratio between the two WISE bands yields an expression for the temperature:

$$\frac{\nu_1 L_{\nu_1,\text{BB}}}{\nu_2 L_{\nu_2,\text{BB}}} = \frac{\nu_1 B_{\nu_1}(T)}{\nu_2 B_{\nu_2}(T)} \tag{9.11}$$

The numerical solution of Equation 9.11 was used as seed for a ML fit to obtain the best-fit values for T and R_{eff}. This was done for each visit independently.

MCMC sampling

To investigate how well the parameter space is constrained by the data and to derive uncertainties and posterior distributions, MCMC sampling was performed using `emcee` [396]. Because the fit is performed in the rest frame, it directly leads to the rest frame temperature. For each pair of fit parameters, the bolometric luminosity was also calculated:

$$L_{\text{bol}} = \sigma_{\text{B}} T^4 \cdot 4\pi R_{\text{eff}}^2. \tag{9.12}$$

[396]: Foreman-Mackey et al. (2013), *Emcee: The MCMC Hammer*

where σ_{B} is the Stefan-Boltzmann constant.

Fit quality constraints

To ensure a sufficient signal-to-noise ratio, some quality criteria were applied. Firstly, the ratio of the luminosities in both bands was required to be greater than its uncertainty because that directly relates to the temperature through Equation 9.11. To investigate convergence, the auto-correlation time τ of the MCMC ensemble [397] provides a good metric, because it gives an estimate of the number of independent samples in the MCMC chain. To obtain at

[397]: Sokal (1997), *Monte Carlo Methods in Statistical Mechanics: Foundations and New Algorithms*

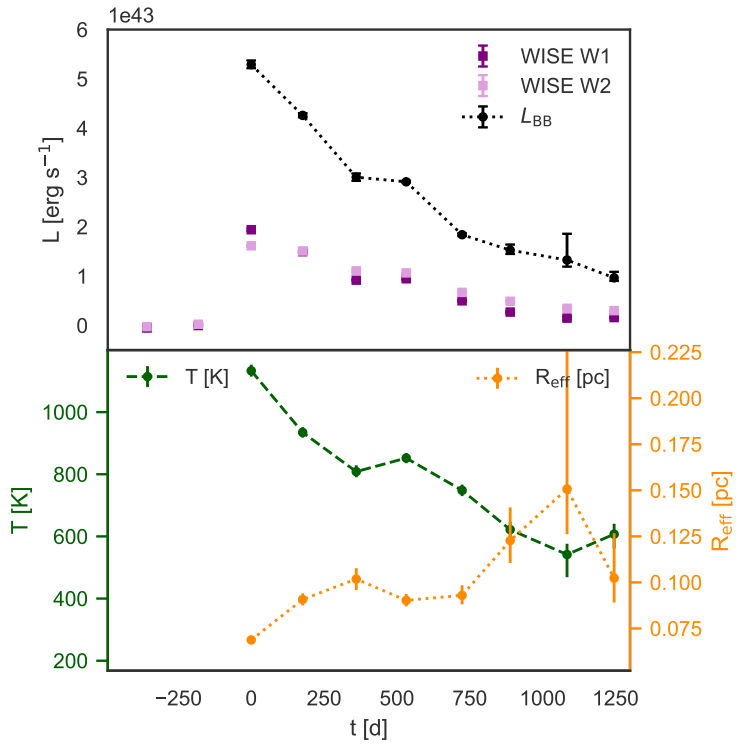

Figure 9.12: Light curve and evolution of R_{eff} and T for NGC 7392. The crosses mark the best-fit values of the visit where the MCMC sampling did not result in a meaningful constraint of L_{bol}. The results are consistent with [398].

least 100 independent points, the sampling was stopped after N iterations if $N > 100\tau$. If this condition was not reached after 1×10^5 iterations, the fit has not converged and the visit was excluded from further analysis. Lastly, the constraints on the bolometric luminosity should be meaningful. Thus, if the 69th percentile for the bolometric luminosity is larger than the best-fit value, we do not consider the sampling successful.
For 568 sources, we find at least two epochs with good constraints on the fit parameters.

As an example, Figure 9.11 depicts the blackbody spectra and the fits for the flare with the highest fluence in the sample, situated in the nearby galaxy NGC 7392. The parameters derived are shown in Figure 9.12 and align with previous measurements [398]. Figure 9.13 shows the evolution of L_{bol}, T, and R_{eff} for all 568 sources with at least two epochs with strong constraints, as well as the bolometric flux $L_{\text{bol}}/4\pi d_{\text{L}}^2$.

[398]: Panagiotou et al. (2023), *A Luminous Dust-obscured Tidal Disruption Event Candidate in a Star-forming Galaxy at 42 Mpc*

Total Energy

To calculate the total emitted energy by a flare, L_{bol} was integrated over the total duration of the flare in the source frame by linearly interpolating between measurements:

$$E_{\text{bol}} = \int L_{\text{bol}}(t)\,\mathrm{d}t = \sum_{k=1}^{N} \frac{L_{\text{bol}}(t_{k-1}) + L_{\text{bol}}(t_k)}{2}(t_k - t_{k-1}) \quad (9.13)$$

where the sum runs over all good fit epochs. The distribution is shown in Figure 9.14. The range of values goes from 10^{50} to 10^{55} erg. However, the majority of flares seems to be consistently distributed between 10^{51} to 10^{52} erg.

Quasar contribution

The population with $E_{\text{bol}} > 10^{53}$ erg is likely not due to hot dust. Instead, infrared emission from relativistic electrons inside jets can

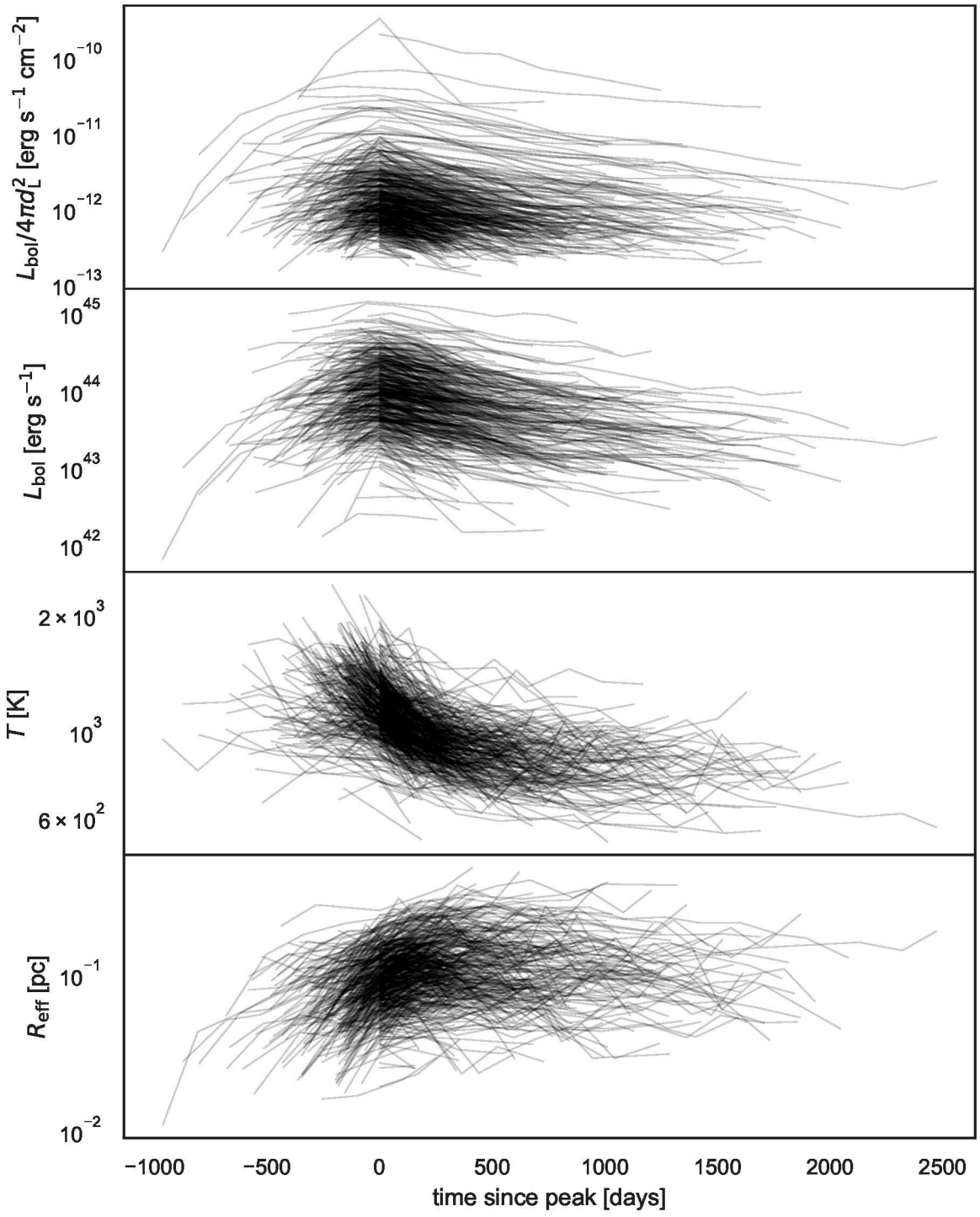

Figure 9.13: Parameters from the blackbody fits for the 449 non-quasar sources where at least two epochs have a good fit. The time is given in the source frame. *First panel*: Bolometric flux based on the bolometric luminosity and the luminosity distance. *Second panel*: Bolometric luminosity (see Equation 9.12). *Third and fourth panel*: Temperature and effective radius as defined in Equation 9.10.

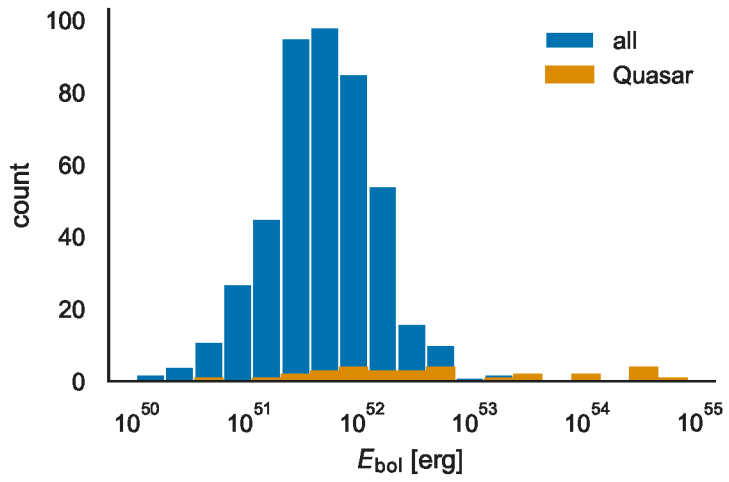

Figure 9.14: The distribution of the total emitted energy, assuming hot dust (Equation 9.13). The Quasars are identified by a match to Milliquas (see Section 9.3.1).

contribute to the variability of the MIR light curves [399, 400]. The same population of electrons typically also produces synchrotron emission in the radio band. To identify potential candidates for this emission, the sample was matched to the Million Quasars Catalog [Milliquas: 401], the largest compilation of type-I Quasars and AGN. A total of 86 matches were found within a search radius of 5″, with the maximum distance of 1.4″ of any match. Seventy objects are identified as core-dominated Quasars, BL Lacs, or narrow-line AGN. The infrared emission of most of these high-redshift objects presumably originates from synchrotron emission. In Figure 9.14, they are indicated as Quasars. Almost all objects at $E_{\mathrm{bol}} > 10^{53}$ erg are quasars, which does not mean that they emit this energy. Because the emission does not come from hot dust, the blackbody model does not apply and the derived energy and luminosity are wrong.

[399]: Jiang et al. (2012), *Rapid Infrared Variability of Three Radio-Loud Narrow-Line Seyfert 1 Galaxies: A View from the Wide-Field Infrared Survey Explorer*

[400]: Liao et al. (2019), *Multi-Wavelength Variability Properties of CGRaBS J0733+0456: Identifying a Distant Gamma-Ray Blazar at z = 3.01*

[401]: Flesch (2023), *The Million Quasars (Milliquas) Catalogue, V8*

9.3.2 Parameter Consistency

To validate the fit results, it is worth comparing the inferred parameters with other estimates if possible. The infrared light curve shape provides an independent estimate of the radius of the dust sphere. The dust echo light curve is the result of convolving the initial transient's light curve with a tophat function. The width of the tophat function τ is determined by the radius of the dust shell $\tau = 2 \cdot R/c$, where c is the speed of light [332]. It relates to the bolometric light curve by dividing the integral by the peak:

$$\tau = \frac{1}{L_{\mathrm{bol,\,max}}} \int L_{\mathrm{bol}}(t)\,\mathrm{d}t. \tag{9.14}$$

[332]: Velzen et al. (2016), *Discovery of Transient Infrared Emission from Dust Heated by Stellar Tidal Disruption Flares*

For a tophat function, this is a good approximation. With the definition of the bolometric energy in Equation 9.13, the radius of the dusty region can be calculated based on the bolometric luminosity and energy:

$$R_{\mathrm{LC}} = \frac{c\,E_{\mathrm{bol}}}{2\,L_{\mathrm{bol,\,max}}} \tag{9.15}$$

Before comparing this with the radius obtained from the blackbody fits, it is important to consider that at any given time, only a spatial slice of the dusty region is visible due to the light travel time. This is

illustrated in Figure 9.15. The value of R_{eff} was derived in Equation 9.10 assuming a blackbody with an area of $A_{\text{BB, eff}} = 4\pi R_{\text{eff}}^2$. However, due to the extension of the sphere, the observable surface area of the sphere is $A_{\text{BB}} \approx 2\pi R_{\text{BB}} \cdot c\Delta T_{\text{opt}}$, where ΔT_{opt} represents the width of the activating flare. The relation between the effective and the actual radius is then dependent on ΔT_{opt}:

$$R_{\text{BB}} = \frac{2}{c\Delta T_{\text{opt}}} R_{\text{eff}}^2. \tag{9.16}$$

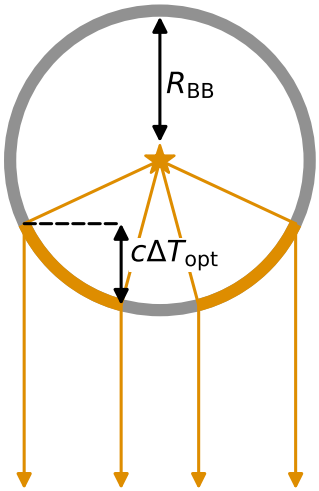

Figure 9.15: An illustration of the illumination of a dust sphere by a central transient.

[83]: Gezari (2021), *Tidal Disruption Events*
[402]: Komossa (2015), *Tidal Disruption of Stars by Supermassive Black Holes: Status of Observations*
[332]: Velzen et al. (2016), *Discovery of Transient Infrared Emission from Dust Heated by Stellar Tidal Disruption Flares*

The comparison between R_{LC} and the peak effective radius at peak $R_{\text{eff, peak}}$ is presented in Figure 9.16, with different values for ΔT_{opt}. For typical durations of TDEs [83, 402], the model remains self-consistent, allowing R_{LC} to be considered a reasonable estimate for R_{BB}.

Furthermore, the relationship between the dust radius and the total bolometric energy is expected to be $R_{\text{LC}} \sim E_{\text{bol}}^{1/2}$ [332]. According to Equation 9.15, this suggests that $R_{\text{LC}} \sim L_{\text{bol,peak}}$. Under the assumption of perfect blackbody emission, the relationship between radius and temperature is $R_{\text{LC}} \sim T^{-2}$. Figure 9.17 illustrates these expected relations as the grey dotted line, alongside the measured values. Although there is significant scatter in all cases, the scaling of E_{bol} with the dust radius aligns reasonably well with the data. While no definitive conclusion can be drawn for the temperature and the peak bolometric luminosity, these findings further support the dust echo model.

Also, the temperature evolution in Figure 9.13 is consistent with cooling dust. Most of the flares begin at a temperature of $T < 2000\,\text{K}$, which broadly aligns with the sublimation temperature for the relevant dust grains [332], before cooling to lower temperatures of 600 to 800 K.

As mentioned above, the total emitted energy falls in the range between a few times 10^{50} to 10^{53} erg with most of the events between 10^{51} to 10^{52} erg (see Figure 9.14). The next section will discuss this in more detail.

9.3.3 Possible Nature of the Initial Transient

The previous section conclusively showed that the physical origin of the infrared emission is dust, heated by an initial transient. It also identified the cases where this is probably not applicable. Determining the nature of the initial transient is harder because of the wide wavelength range over which the dust efficiently absorbs radiation. The resulting dust echo is therefore agnostic to the spectral energy distribution of the incident radiation and only sensitive to the total energy. Conclusions for single objects are still possible based on auxiliary information such as transient emission observed at other wavelengths or host features.

The main possibilities are AGN variability, supernovae and extreme transient accretion events such as TDEs. These possibilities will be investigated in the following in this order.

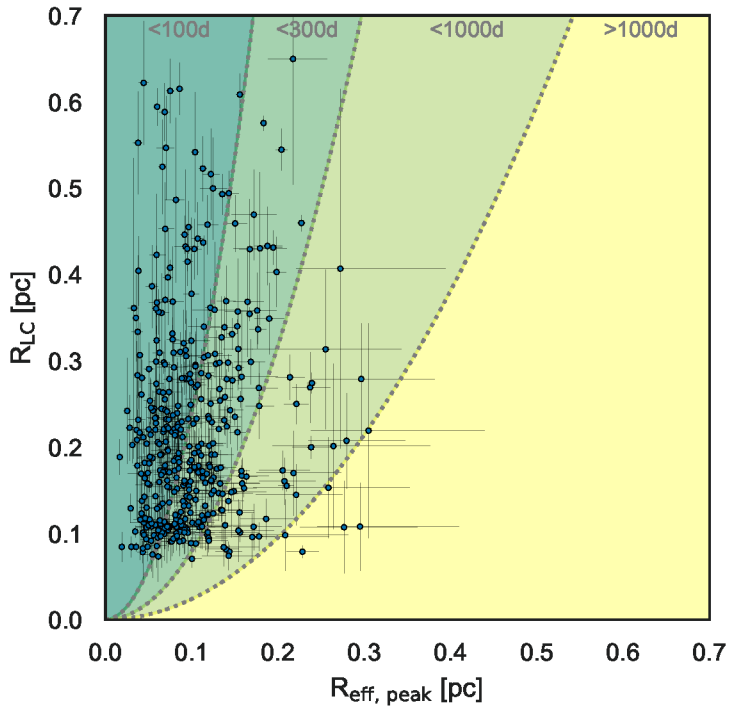

Figure 9.16: The dust radius estimated from the IR lighturve R_{LC} against the radius at peak $R_{\text{eff, peak}}$ obtained from the blackbody fits. The colored contours represent the actual blackbody radius for a finite width of the initial OUV transient (see Equation 9.16).

Contribution by Active Galactic Nuclei

Variability in active galaxies is well-known, as is delayed IR emission due to dust reprocessing [59]. Although unusually bright IR flares compared to the extraneous part of the light curve were selected, hosts exhibiting AGN activity before the flare were not explicitly excluded. Therefore, it is expected that a certain percentage of the flares are related to the typical accretion onto the SMBH, and their contribution to the sample was estimated.

[59]: Ulrich et al. (1997), *Variability of Active Galactic Nuclei*

The classification based on Baldwin–Phillips–Terlevich (BPT) diagrams [403], derived from SDSS spectroscopic observations [391], was used to obtain a robust classification of the host galaxies. A total of 61 matches were identified, comprising 22 star-forming galaxies, 19 composite objects, 11 AGN, and 9 LINER galaxies. Therefore, at least one third of the spectroscopically classified hosts do not exhibit signs of AGN activity before the flare. However, this small subsample is not entirely representative. It is, on average, one magnitude brighter, and the W1-W2 color is approximately 0.16 mag_{Vega} bluer.

Host Spectra

[403]: Baldwin et al. (1981), *Classification Parameters for the Emission-Line Spectra of Extragalactic Objects*

[391]: Brescia et al. (2015), *Automated Physical Classification in the SDSS DR10. A Catalogue of Candidate Quasars*

Looking for possibly classified optical counterparts, the TNS[††] provides 68 matches within 5″. 54 are unclassified, but 6 objects are classified as AGN flares. However, at least five of them are unlikely regular statistical AGN variability.
While a regular TDE origin was ruled out for AT 2017bgt, it was attributed to enhanced accretion onto the SMBH, marking a re-ignition of the active nucleus, and used to define a new flare class [79].
AT 2018bcb is similar to both regular TDEs and the AT 2017bgt-like flares [404].

Optical Counterparts

[79]: Trakhtenbrot et al. (2019), *A New Class of Flares from Accreting Supermassive Black Holes*

[404]: Neustadt et al. (2020), *To TDE or Not to TDE: The Luminous Transient ASASSN-18jd with TDE-like and AGN-like Qualities*

[††] https://www.wis-tns.org

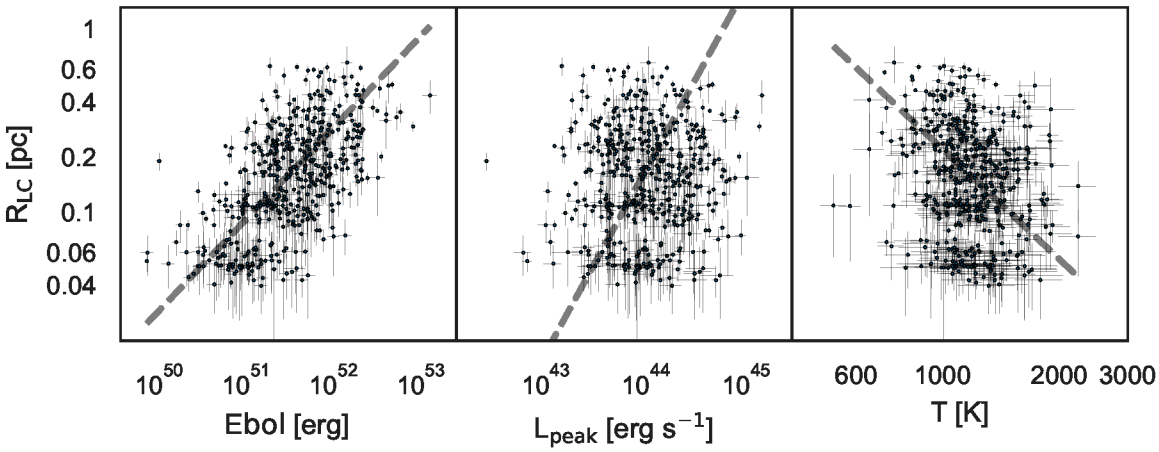

Figure 9.17: Correlation of the total emitted bolometric energy E_{bol}, the peak bolometric luminosity $L_{bol,peak}$ and the dust temperature T with the dust radius infered from the light curve R_{LC}. The dashed lines represent the theoretically expected relations.

[405]: Ochmann et al. (2024), *The Transient Event in NGC 1566 from 2017 to 2019. I. An Eccentric Accretion Disk and a Turbulent, Disk-Dominated Broad-Line Region Unveiled by Double-Peaked Ca II and O I Lines*

[270]: Reusch et al. (2022), *Candidate Tidal Disruption Event AT2019fdr Coincident with a High-Energy Neutrino*

[323]: Frederick et al. (2021), *A Family Tree of Optical Transients from Narrow-line Seyfert 1 Galaxies*

[409]: Holoien et al. (2022), *Investigating the Nature of the Luminous Ambiguous Nuclear Transient ASASSN-17jz*

[410]: Malyali et al. (2021), *AT 2019avd: A Novel Addition to the Diverse Population of Nuclear Transients*

[411]: Chen et al. (2022), *AT 2019avd: A Tidal Disruption Event with a Two-phase Evolution*

[412]: Wang et al. (2023), *The Radio Detection and Accretion Properties of the Peculiar Nuclear Transient AT 2019avd*

[414]: Frederick et al. (2019), *A New Class of Changing-look LINERs*

The same is true for the flare in the nearby AGN NGC 1566 [405], the brightest transient in our sample.
The spectrum of AT 2017fro was initially identified as a supernova type II [406], but subsequently found to align more closely with an AGN [407]. Further analysis highlighted similarities with other nuclear transients of uncertain classification, such as CSS100217 [408] and AT 2019fdr [270, 323]. It appears most consistent with a supernova type IIn in an AGN that triggered increased accretion activity, although a TDE origin can not be excluded [409].
AT 2019avd is a well-studied nuclear flare in a previously inactive galaxy, exhibiting X-ray properties consistent with a TDE scenario, though its OUV emissions are less characteristic of TDEs [410]. It has also been proposed as a turn-on AGN event [323], similar to AT 2017fro, as a partial TDE [411], or as a particular type of jetted TDE [412].
AT 2018dyk was classified as a TDE [413] which was later challenged to favor an AGN turn-on [414].
AT 2022sxl was classified as an AGN flare [415] but is unrelated to the corresponding infrared flare because it happened roughly six years after its peak.
In summary, all the reported optical AGN flares in our sample are not a result of typical statistical AGN variability but are isolated events linked to enhanced accretion onto the SMBH.

AGN Hosts

To investigate the overall contribution of flares occurring in AGN hosts, the galaxies were classified based on their red infrared color. The measured baseline magnitudes were not used due to biases affecting dim sources. The redder band W2 is less sensitive, and the bias is more pronounced, reddening the measured color, particularly for blue sources. Therefore, using the measured baseline can lead to an overestimation of the percentage of AGN hosts. Instead, magnitudes derived from stacked WISE images from the parent sample catalogs were utilized (see Figure 9.10 in Section 9.2.3). The distribution is shown in Figure 9.18 for both the flare sample and the complete parent galaxy sample. The distribution of the flare sample extends to redder infrared colors. With the selection cut on the magnitude difference between the W1 and W2 bands,

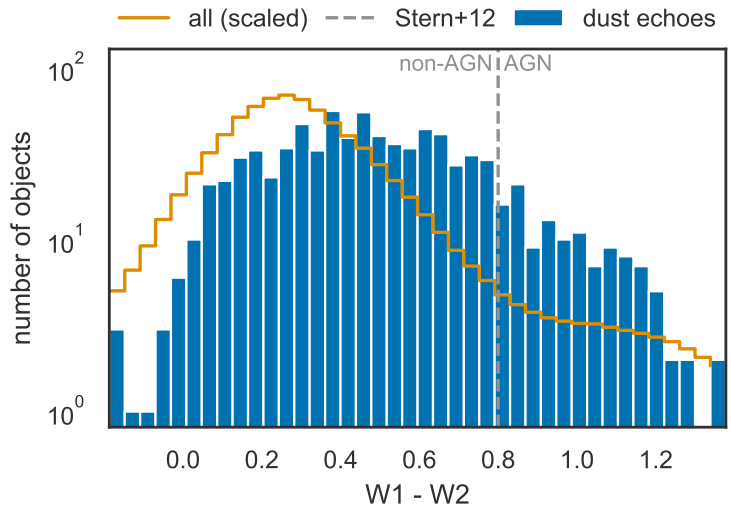

Figure 9.18: Distribution of W1-W2 colors of the flares and the parent galaxy sample. The histogram of all source is scaled so that the density matches the one of the flares.

$m_{W1} - m_{W2} > 0.8$ [308], the percentage of hosts with signs of AGN activity in the flare sample is 14%. It increases from 6% in the parent sample, but still shows that most of the hosts do not have strong AGN contributions.

[308]: Stern et al. (2012), *Mid-Infrared Selection of Active Galactic Nuclei with the Wide-Field Infrared Survey Explorer. I. Characterizing WISE-Selected Active Galactic Nuclei in COSMOS*

Contribution by Supernovae

Infrared emission from hot dust following a supernova explosion has been studied previously, with some supernovae remaining detectable in the infrared even decades after explosion [416]. Therefore, it is worth investigating the presence of supernovae within our sample. Six matches were found with transients classified as supernovae on TNS. However, at least two of them could instead be flares associated with accretion onto the SMBH.

[416]: Tinyanont et al. (2016), *A Systematic Study of Mid-infrared Emission from Core-collapse Supernovae with SPIRITS*

SN 2018gn was first classified as a type II supernova [417] but recently interpreted as a dusty TDE based on the large dust echo and the emergence of coronal lines [418, 419] and is part of the sample of infrared detected TDEs by the WISE Transient Pipeline [344].

[418]: Thévenot et al. (2021), *Mid-Infrared Detections of Type I Supernovae and Unclassified Possible Supernovae with NEOWISE*
[419]: Wang et al. (2024), *ASASSN-18ap: A Dusty Tidal Disruption Event Candidate with an Early Bump in the Light Curve*
[344]: Masterson et al. (2024), *A New Population of Mid-infrared-selected Tidal Disruption Events: Implications for Tidal Disruption Event Rates and Host Galaxy Properties*

SN 2020edi was classified as a superluminous supernova of type II at the center of an AGN [420]. Its very luminous dust echo was previously reported [421], and the inferred bolometric energy of almost 10^{52} erg aligns with that of the other nuclear transients in the sample created in this work. Spectroscopic follow-up observations could determine the emergence of coronal lines, similar to SN 2018gn.

[420]: Tucker (2021), *SCAT Transient Classification Report for 2021-02-11*

There is no evidence that would suggest that the remaining four flares classified as supernovae are instead linked to SMBH accretion. Three of them show spectral features interpreted as signs of interaction with the circumstellar medium and are classified as type IIn: SN 2020iq [422], SN 2018ctj [423], and 2018hfm [424]. Notably, SN 2020iq has a high inferred bolometric energy [421] of approximately 2×10^{51} erg, nearly a magnitude higher than the other supernovae. However, the distance to the nearest source detected with Pan-STARRS is about 0.4″, placing it at an angular diameter distance of roughly 700 pc from the host center, which is too far to be related to the SMBH. SN 2018ktv was classified as a type IIL [425].

[424]: Zhang et al. (2022), *SN 2018hfm: A Low-Energy Type II Supernova with Prominent Signatures of Circumstellar Interaction and Dust Formation*

To also check for supernova detections before the introduction of TNS in 2016, a crossmatch was performed with a list of supernovae detected by ASAS-SN[‡‡], operating since 2013 [195]. Besides ASASSN-18xl/AT 2018hfm, ASASSN-18ap/AT 2018gn, and ASASSN-17jz/AT 2017fro described above, no additional matches were found.

Offset from Host

To confirm that the infrared flares occur at the center of the host galaxies, the median position of the single-exposure photometry data points was calculated for both baseline and flare data. 39 flares have a separation from the host exceeding 0.5″ among which are the three supernovae mentioned above. These are shown in the top row of Figure 9.19. For only three of the remaining 36 sources the offset appears genuine, making them promising supernova candidates (second row in Figure 9.19), bringing the total number of classified supernovae in the flare sample up to six, which suggests a contamination rate of merely around 1%.
The remainder of offset transients likely suffers from inaccurate photometry or confusion regarding the host galaxies. The first two panels of the last row display flares with an offset, the origin of which is unclear. In the Pan-STARRS images, there is no visible host galaxy at the flare's location. J183948+674334 is surrounded by three other sources, which could explain the offset, although the flare lies between the parent sample galaxy and two of its neighbors. The remaining objects are affected by host galaxy confusion. The third row of Figure 9.19 presents the three objects where the baseline data aligns with the parent sample's specified position, but the flare might be related to a neighboring galaxy. Conversely, for the 28 other offset flares, the flare data aligns better with the parent sample position, while the baseline data is shifted towards a neighboring galaxy, as illustrated in the last panel. This confusion likely arises from a host too dim in the infrared to produce single-exposure photometry detections. Consequently, the baseline associated with the brighter neighbor appears overly bright, leading to an underestimation of the flare's luminosity.

In summary, the contribution of supernovae to the flare sample is minimal.

Transient Accretion Events

As discussed above, neither regular AGN activity nor supernovae account for the observed flares. However, they occur at the centers of their host galaxies, and the derived physical parameters are consistent with dust echoes from an initial flare in a dust shell with $R \approx \mathcal{O}(10^{-1}\,\mathrm{pc})$. This suggests that the flares are likely dust echoes resulting from extreme accretion events onto the SMBH. The inferred bolometric energy ranges from 10^{51} to 10^{52} erg, which is approximately an order of magnitude greater than estimates for most (candidate) supernovae. This energy output aligns with that of a TDE, assuming a covering factor of $f_c \gtrsim 0.1$, the disruption of a solar mass star, subsequent accretion of half its mass, and a

[‡‡] www.astronomy.ohio-state.edu/asassn/sn_list.html

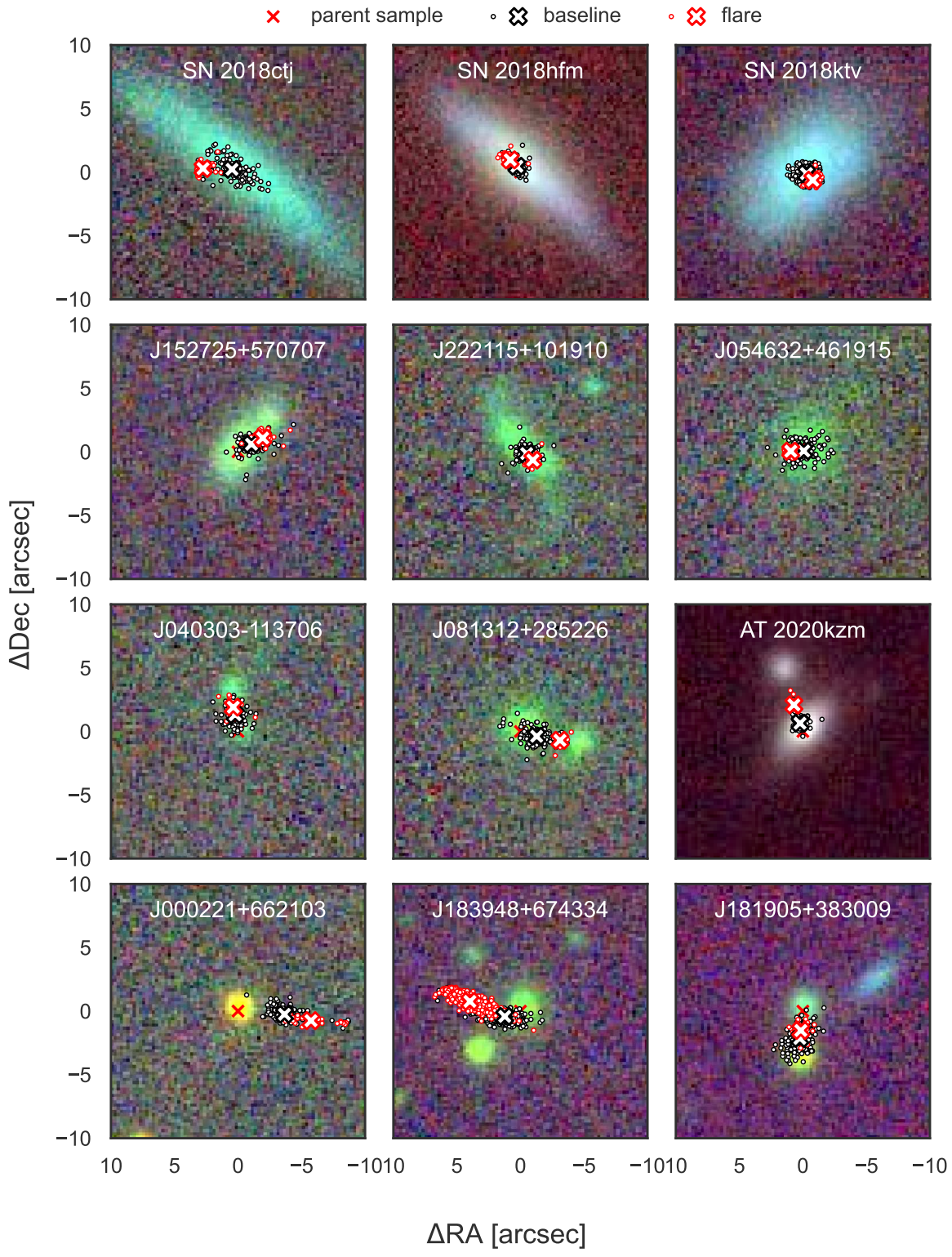

Figure 9.19: Pan-STARRS images of the objects that show a significant offset to their host galaxy. The images are centered on the position of the parent sample galaxy, indiacated by a simple red cross. The single exposure data is shown as circles, encircled red for the flare data and black for the baseline data. The white crosses with the corespondingly colored edges mark the center of the flare and basleine data, respectively.

dissipation efficiency of $\epsilon \approx 0.1$:

$$E_{\mathrm{IR,\,TDE}} \approx 0.5\,M_\odot \cdot f_c \cdot \epsilon \cdot c^2 \approx 9 \times 10^{51}\ \mathrm{erg}.$$

Indeed, approximately half of the 39 brightest flares have been classified as either candidates for tidal disruption events (TDEs) or as peculiar AGN flaring activity (see Table B.2). As mentioned in Section 9.3.3, similarities with both TDEs and peculiar AGN flares are shared by the brightest flare in the nearby AGN NGC 1566 [405]. This is similar to AT 2017gbt [79], ranking fourth brightest. Also the second and third brightest are considered promising candidates for TDEs detected in the infrared [344, 398], along with seven other flares. Additionally, five of the 39 brightest flares are included in the MIRONG sample, introduced in Section 8.1. Notably, the 14th brightest flare, AT 2019avd, is identified as a potential TDE [410].

[405]: Ochmann et al. (2024), *The Transient Event in NGC 1566 from 2017 to 2019. I. An Eccentric Accretion Disk and a Turbulent, Disk-Dominated Broad-Line Region Unveiled by Double-Peaked Ca II and O I Lines*

[79]: Trakhtenbrot et al. (2019), *A New Class of Flares from Accreting Supermassive Black Holes*

[344]: Masterson et al. (2024), *A New Population of Mid-infrared-selected Tidal Disruption Events: Implications for Tidal Disruption Event Rates and Host Galaxy Properties*

[398]: Panagiotou et al. (2023), *A Luminous Dust-obscured Tidal Disruption Event Candidate in a Star-forming Galaxy at 42 Mpc*

[410]: Malyali et al. (2021), *AT 2019avd: A Novel Addition to the Diverse Population of Nuclear Transients*

9.4 Completeness

In order to make statements about a population of astrophysical sources, it is crucial to assess the fraction of sources that are missing from the underlying catalog. The loss can generally be attributed to three distinct factors: incompleteness of the survey area, depth limitations, or detection deficiency within the survey volume. For this study, incompleteness of the survey area is primarily associated with the selection of the parent galaxy sample, while detection deficiency is determined by the Bayesian Blocks analysis and subsequent criteria. Depth limitations are influenced by both factors: the completeness of the parent galaxy sample decreases at higher redshifts, and detection efficiency is worse for fainter signals. The discussion will concentrate on detection efficiency before addressing the issues related to the parent galaxy sample and depth.

Detection Efficiency

The detection efficiency is influenced by both the detection capabilities of WISE and the selection efficiency of the pipeline developed in this work. To evaluate the efficiency in detail, each step would necessitate its own dedicated simulations, which are beyond the scope of this work. The efficiency is instead estimated by comparing the sample to results documented in the literature. Results for each object are provided in Table B.1. The samples themselves are only briefly introduced here because a thorough review is given in Section 8.1.

WTP TDEs

[344]: Masterson et al. (2024), *A New Population of Mid-infrared-selected Tidal Disruption Events: Implications for Tidal Disruption Event Rates and Host Galaxy Properties*

Masterson et al. [344] identified 18 candidates for infrared-selected TDEs using the *WISE Transient Pipeline* (WTP). The selection was based on criteria including high peak luminosity, rapid rise, and a monotonic decline, with the absence of an underlying AGN host or prior variability. Table 9.3 summarizes the results of this work's pipeline for this sample. Half of the WTP TDEs are classified as dust-echo-like, while four candidates are categorized as long flares. Four candidates are rejected due to insufficient strength compared to the variability observed in the rest of the light curve. One flare lacks a baseline detection prior to the excess. Given that the WTP TDE

selection relies on a crossmatch against a galaxy catalog extending up to approximately 200 Mpc [356], the sample does not include candidates beyond a redshift of $z \lesssim 0.045$. Among the 40 brightest flares in this work's sample, only 13 are below this redshift. Of these, six are not present in the WTP TDE sample (see Table B.2).

[356]: Cook et al. (2019), *Census of the Local Universe (CLU) Narrowband Survey. I. Galaxy Catalogs from Preliminary Fields*

MIRONG sample

The MIRONG sample [348] followed an approach similar to the one taken in this work: collecting WISE photometry for a parent galaxy sample. The selection is based on the difference between the maximum and minimum brightness, resulting in a sample of 137 flares. Only 33 (24%) of those are selected as dust-echo-like by the pipeline from this work (see Table 9.3) while 40 are long flares and 35 show signs of extraneous activity (55%). Three of the galaxies, all at a high redshift between 0.2 and 0.3, are missing from our parent galaxy sample. The remaining 26 flares (19%) have poor data quality, either because the excess is due to an outlier, the peak is during a longer gap in the data, or there is no baseline detection before the flare. In two instances, the rejection is attributed to the initial selection of photometry data points detailed in Section 9.2.2. Namely for SDSS J010320+140149, the coordinates are significantly offset from its nucleus and the WISE photometry position, leading to the photometry being discarded as unrelated. The same is true for SDSS J153151+372445. Consequently, the light curve does not meet the initial variability criterion of $\chi^2_{\text{red}} < 1$.
Looking at the results by the analysis in this work for all MIRONG parent galaxies (SDSS spectroscopic galaxies with a redshift of $z \leq 0.35$), it was found that only four flares were not selected by the MIRONG analysis. Among these are AT 2018dyk and SN2018ctj, a probable TDE and a supernova which were already discussed in Section 9.3.3. Although the other two flares, in WISE J170944.87+445042.2 and WISEA J085808.47+082116.1, are faint ($\nu_{\text{W1}} F_{\nu_{\text{W1}},\,\text{peak}} \approx 10^{-13}\,\text{erg}\,\text{s}^{-1}\,\text{cm}^{-2}$), they were detectable over at least three visits. In terms of sky coverage, this work's sample thus appears to be an extension of the MIRONG dataset.

[348]: Jiang et al. (2021), *Mid-Infrared Outbursts in Nearby Galaxies (MIRONG). I. Sample Selection and Characterization*

ZTF accretion flares

So far, the reference samples relied on cataloged host galaxies. Because galaxies must be bright enough to facilitate observations adequate for classification, intrinsically dim and distant hosts are likely absent from such catalogs. One way to decouple the infrared flare search from host parameters is to utilize a different tracer for potential flare locations. Using nuclear flares detected in the optical by ZTF, van Velzen et al. [80] searched for infrared flares at the same position using WISE data, resulting in a sample of 63 optical transients with large dust echoes that are likely TDEs or exceptional AGN flares. It was already introduced in Section 8.2 as the *Zwicky Transient Facility Accretion Flares* (ZTF AF). 22 of these flares are classified by the analysis in this work as dust-echo-like (35%, see Table 9.3). Most of the rejected events (around 27%) do not pass the cut on extraneous activity, while 14% are classified as long flares.
For AT 2019pev, only one datapoint is found in one band in the single exposure photometry while all others are excluded because of de-blending (see Section 9.2). An excess is detected in only one band for AT 2018jut and AT 2019dll, and no excess at all for AT 2020aezy. This is because the significance of the excess is not high enough to be recognized by the Bayesian Blocks but is sufficient to pass

[80]: van Velzen et al. (2024), *Establishing Accretion Flares from Supermassive Black Holes as a Source of High-Energy Neutrinos*

the significance threshold when using the expected flare start time based on the optical flare like in van Velzen et al. [80]. This highlights the advantage of prior knowledge about the infrared excess time. For AT 2021aeuh and AT 2019msq, the flux in the AllWISE single epoch photometry is systematically lower than in the NEOWISE-R photometry, leading to a false identification of the entire NEOWISE-R period as a flare. They are then rejected because the peak of that supposed flare would fall in the gap between 2011 and 2014. The hosts of another 14% are not included in the parent galaxy sample of this work. These galaxies are, on average, one magnitude dimmer in the WISE bands and also redder, indicating they are further away, although redshift measurements are necessary for confirmation.

The results for these samples combined suggest a completeness of the selection procedure of roughly $25 - 50\%$, where the main losses are attributed to our definition of long flares and extraneous activity. However, we remind the reader that these cuts are necessary to exclude AGN variability as the source of the IR flares as described in Section 9.3.3.

As previously mentioned, the completeness in absolute numbers per volume also depends on the completeness of the parent sample since it provides the positional information. Assessing its completeness is complicated, especially because it is not derived from a homogenous survey sample but from three different catalogs (see Section 9.2.1). If these catalogs were homogenous over the whole sky, one could in principle obtain the completeness by comparing to a small and deep observation and extrapolate that to the rest of the sky. However, because two of the three parent sub-samples make use of Pan-STARRS data, the sky below a declination of around $-30°$ is sampled significantly worse. Another possibility is to compare the cumulative luminosity included in our sample to a measured luminosity function. However, there exists no such measurement based on the WISE filters[5]. Therefore, no detailed calculation of the parent sample completeness is possible at this point.
Because the NED-LVS sample is included, a lower estimate of this work's parent sample completeness is given by the completeness of the NED-LVS, which is complete in the very nearby universe up to 30 Mpc, around 70% complete to 200 Mpc and drops to a completeness of about 1% at 1 Gpc [380]. Because, in addition, many more faint sources wer included, this is expected to improve. Indeed, a simple analysis based on the scaling with the co-moving volume suggests completeness of the parent sample up to $z = 0.2$ at least for brighter hosts at $M_{\mathrm{W1}} < -24\,\mathrm{mag}_{\mathrm{Vega}}$ (see Section B.1).

5: Luminosity functions were derived from observations of the Spitzer Space Telescope, but only for AGN [426]

[380]: Cook et al. (2023), *Completeness of the NASA/IPAC Extragalactic Database (NED) Local Volume Sample*

Table 9.3: Results of the pipeline presented in this work for three reference samples: MIRONG [348], TDE candidates found by the WTP [344] and accretion flares from ZTF (*Zwicky Transient Facility Accretion Flares* (ZTF AFs); [80]). The first column describes which category our analysis assigned the flares. The numbers refer to the selection steps described in Section 9.2.3.

Sample	MIRONG		WTP TDEs		ZTF AFs	
	#	[%]	#	[%]	#	[%]
Result						
dust echo like	33	**24**	9	**50**	22	**35**
long flare	40	29	4	22	9	14
3: extraneous activity	35	26	4	22	17	27
2: no coincident excess region	-	-	-	-	2	3
1: no excess	-	-	-	-	1	2
4: no prior baseline	2	1	1	6	-	-
7: outlier in the lightcurve	2	1	-	-	-	-
5: gap in the lightcurve	20	15	-	-	2	3
no data	1	<1	-	-	-	-
not in parent sample	3	2	-	-	9	14
$\chi^2_{\mathrm{red}} < 1$	1	<1	-	-	1	2

9.5 Implications for the Rate and its Evolution

Section 9.3.3 established that the flares are likely TDEs or at least enhanced accretion states. It is worth exploring the resulting rate of the events and comparing them with results from other samples. If the rate aligns with other TDE rate measurements, it would indicate a significant contribution of TDEs in the sample. Moreover, due to the large size of the sample, the evolution of this rate with redshift can be investigated. Analyzing this per volume and time would require a better understanding of the completeness of the parent sample which is not available (see Section 9.4). Thus, the focus is on the rate of events per galaxy.

If the mass of the SMBH is larger than $m_{\mathrm{BH}} \approx 10^8 m_\odot$, the so-called Hills Mass [81], the tidal disruption of a solar mass star happens inside the event horizon so no emission can escape (see Chapter 3). Therefore, TDEs should only occur around SMBHs with smaller masses. Examining the rate as a function of black hole mass can therefore provide additional insight into the TDE nature of the transients. Sophisticated measurements of the black hole mass are based on spectroscopic observations which are not available. Instead, the host's absolute magnitude in W1, M_{W1}, was used as a proxy.

Hills Mass

[81]: Hills (1975), *Possible Power Source of Seyfert Galaxies and QSOs*

This is possible, because the total stellar mass of a galaxy $M_\star$ is linked to its brightness through the so-called mass-to-light ratio. It turns out that the mid-infrared is optimal for estimating this ratio [428, 429] and it was found consistent with expectations from stellar population synthesis models [427, 430–432]:

$$\frac{m_\star}{m_\odot}\frac{L_{\mathrm{W1},\odot}}{L_{\mathrm{W1},\star}} \approx 0.6. \tag{9.17}$$

The stellar mass in turn is correlated with the SMBH mass [433–437]:

$$\log_{10}\left(\frac{m_{\mathrm{BH}}}{m_\odot}\right) = \alpha + \beta \log_{10}\left(\frac{m_\star}{10^{11} m_\odot}\right). \tag{9.18}$$

Table 9.4: Parameters of Equation 9.18 for the SMBH mass and total stellar mass relation for elliptical galaxies and AGN from Kettley et al. [427]

Class	α	β
Ellipticals	8.95	1.40
AGN	7.45	1.05

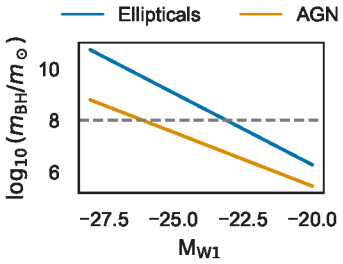

Figure 9.20: Empirical relation between host absolute magnitude M_{W1} and SMBH mass m_{BH}.

Kettlety et al. [427] find that there are distinct parameters for AGN and elliptical galaxies. They are used here and are listed in Table 9.4. Inserting Equation 9.17 into Equation 9.18 and using absolute magnitudes M_{W1} instead of luminosities gives the relation between absolute magnitude and SMBH mass:

$$\log_{10}\left(\frac{m_{BH}}{m_\odot}\right) = \alpha - \beta\left[0.24 \cdot (M_{W1} - M_{W1,\odot}) + 11\right], \tag{9.19}$$

where the absolute magnitude of the sun in W1 is $M_{W1,\odot} = 3.26$ [438]. This relation is shown in Figure 9.20. For elliptical galaxies, the Hills Mass corresponds to $M_{W1} \approx -23\,\mathrm{mag_{Vega}}$, whereas for AGN, it corresponds to $M_{W1} \approx -26\,\mathrm{mag_{Vega}}$.

[438]: Willmer (2018), *The Absolute Magnitude of the Sun in Several Filters*

K correction

To use this relation on the flare sample, the absolute magnitude has to be calculated from the measured apparent magnitude m_{W1}, the distance modulus $\mu = 5\,\log_{10}(d_L(z)/10\,\mathrm{pc})$ and the K correction [439, 440]:

$$M = m - \mu - K. \tag{9.20}$$

The K term corrects for the fact that the observer frame observation wavelength range is redshifted. Therefore the observed part of the spectrum is not around $\lambda_{W1} = 3.4\,\mu\mathrm{m}$ but at $(1+z)^{-1}\lambda_{W1}$. For a source with spectrum L, the K correction can be calculated [439]:

$$K = -2.5\,\log\left[(1+z)\frac{L\left(\frac{\lambda}{(1+z)}\right)}{L(\lambda)}\right]. \tag{9.21}$$

[439]: Oke et al. (1968), *Energy Distributions, K Corrections, and the Stebbins-Whitford Effect for Giant Elliptical Galaxies*
[440]: Hogg et al. (2002), *The Luminosity Density of Red Galaxies*

For a power-law spectrum $L(\lambda) \propto C\,\lambda^\alpha$ with a constant C, the term can be simplified [389, Chapter 3]:

$$K = 2.5 \cdot (1+\alpha) \cdot \log(1+z). \tag{9.22}$$

[389]: Weedman (1986), *Quasar Astronomy*

The power-law index can be obtained from galaxy spectral templates. Blanton and Roweis [441] derived a basis of five templates from observations by fitting star formation history models. This basis is a good representation of the spectral space in which galaxy spectra exist. They are shown in Figure 9.21 in units of spectral flux density, normalized to their maximum. When fitting the infrared range from 1 to 10 µm (10^4 to 10^5 AA) with a power-law (dashed lines in Figure 9.21), the spectral indices are between −2.7 and −3.8, so −3 was selected as a good approximation. Because the luminosity scales with the flux like $L \propto \lambda F$, the spectral index for the luminosity is then $\alpha = -2$.

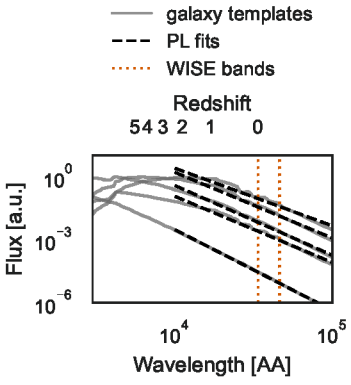

Figure 9.21: Galaxy spectral templates from Blanton and Roweis [441] and power-law fits in the infrared.

The histograms in Figure 9.23 depict the absolute number of flares and parent galaxies as a function of redshift and M_{W1}, using the determined α for the correction in Equation 9.22. Flares are found in galaxies with M_{W1} ranging from −20.5 to $-27.5\,\mathrm{mag_{Vega}}$, with the majority between −23 to $-25\,\mathrm{mag_{Vega}}$. This suggests that most flares can not be attributed to TDEs, as the SMBH mass exceeds the Hills Mass based on the elliptical galaxy relation. In this case, they would be AGN flares, necessitating the corresponding relation, yielding an SMBH mass below the Hills Mass. Due to this ambiguity, conclusions can not be drawn from the hosts' absolute magnitudes

alone. Instead, the evolution of the rate in each magnitude bin was analyzed.

The rate of flares per galaxy for magnitude bin i and redshift bin j is

$$\mathcal{R}_{i,j} = \frac{(1+\bar{z}_j)}{T} \frac{N_{\text{flare},i,j}}{N_{\text{gal},i,j}}. \tag{9.23}$$

where T is the sampling time, $N_{\text{flare},i,j}$ is the number of flares and $N_{\text{gal},i,j}$ the number of parent galaxies in the respective bin. $\bar{z}_j$ is the median redshift value of bin j and accounts for the time dilation of the observed rate with the cosmic expansion. The uncertainty is the 95th-percentile Poisson confidence interval based on $N_{\text{flare},i,j}$.

Sampling Time

The missing ingredient to calculate the rate is the sampling time. One could expect it to be around 11 yr because data was included from AllWISE until the last release of NEWOWISE-R data in December 2021. However, due to WISE being inactive between February 2011 and December 2013, there is approximately a 1.5 yr gap in the data. Additionally, a baseline detection before the flare and at least two detections of the flare were required (see steps 4 and 9 in Section 9.2.3). Given that there is, on average, a visit every six months, each of these two requirements reduces the sampling time by about 0.5 yr. Therefore, the naively estimated sampling time would be approximately 8 yr.

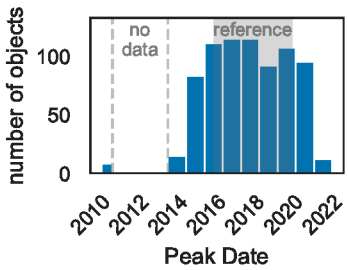

Figure 9.22: The distribution of peak dates over time. The reference time window from around May 2016 to June 2020 is indicated as the grey-shaded region. The break of WISE data taking is indicated with grey dashed lines.

The actual effective sampling time is shorter due to edge effects near the start, end, and break of the dataset. To account for this effect, the average rate of flares per time $\mathcal{R}_{\text{ref}}$ within a reference window can be compared to the overall observed rate $\mathcal{R}_{\text{obs}}$. Assuming the true astrophysical flare rate is roughly constant over time, the effective sampling time is calculated by taking the total duration from the start of WISE observations to the last datapoint and scaling it by the ratio of the observed flare rate to the expected rate:

$$T_{\text{eff}} = T_{\text{ref}} \frac{N_{\text{obs}}}{N_{\text{ref}}}. \tag{9.24}$$

Figure 9.22 shows the distribution of flare peak dates. There are $N_{\text{ref}} = 507$ flares in the reference region from around May 2016 to June 2020 and $N_{\text{obs}} = 753$ flares in total, resulting in an effective sampling time $T_{\text{eff}} = (6.1 \pm 0.3)\,\text{yr}$.

The resulting rates are shown in Figure 9.23. The highest measured value is $\mathcal{R}_{[-26,-24],<0.05} \approx 3.7^{+2.6}_{-1.7} \times 10^{-5}\,\text{galaxy}^{-1}\,\text{yr}^{-1}$ at $M_{\text{W1}} = [-26,-24]\,\text{mag}_{\text{Vega}}$ and $z < 0.05$. This aligns with the lower limit on the TDE rate using the WTP TDEs [344]: $\mathcal{R}_{\text{ref}} \approx (2.0 \pm 0.3) \times 10^{-5}\,\text{galaxy}^{-1}\,\text{yr}^{-1}$. The rate shows a rapid decrease towards brighter galaxies but falls shallower towards the fainter end.

Luminosity Function

To understand how the rate changes with redshift, one has to account for sensitivity loss. Figure 9.24 depicts the luminosity function, the distribution of bolometric luminosity at peak, across different redshifts, normalized by the number of galaxies in each redshift bin. To start simple, it is assumed that the luminosity function does not change with redshift, so the intrinsic distribution of luminosities is the same. Implications of a deviation from that will be discussed in Section 9.6. As expected, the loss of sensitivity is visible at low

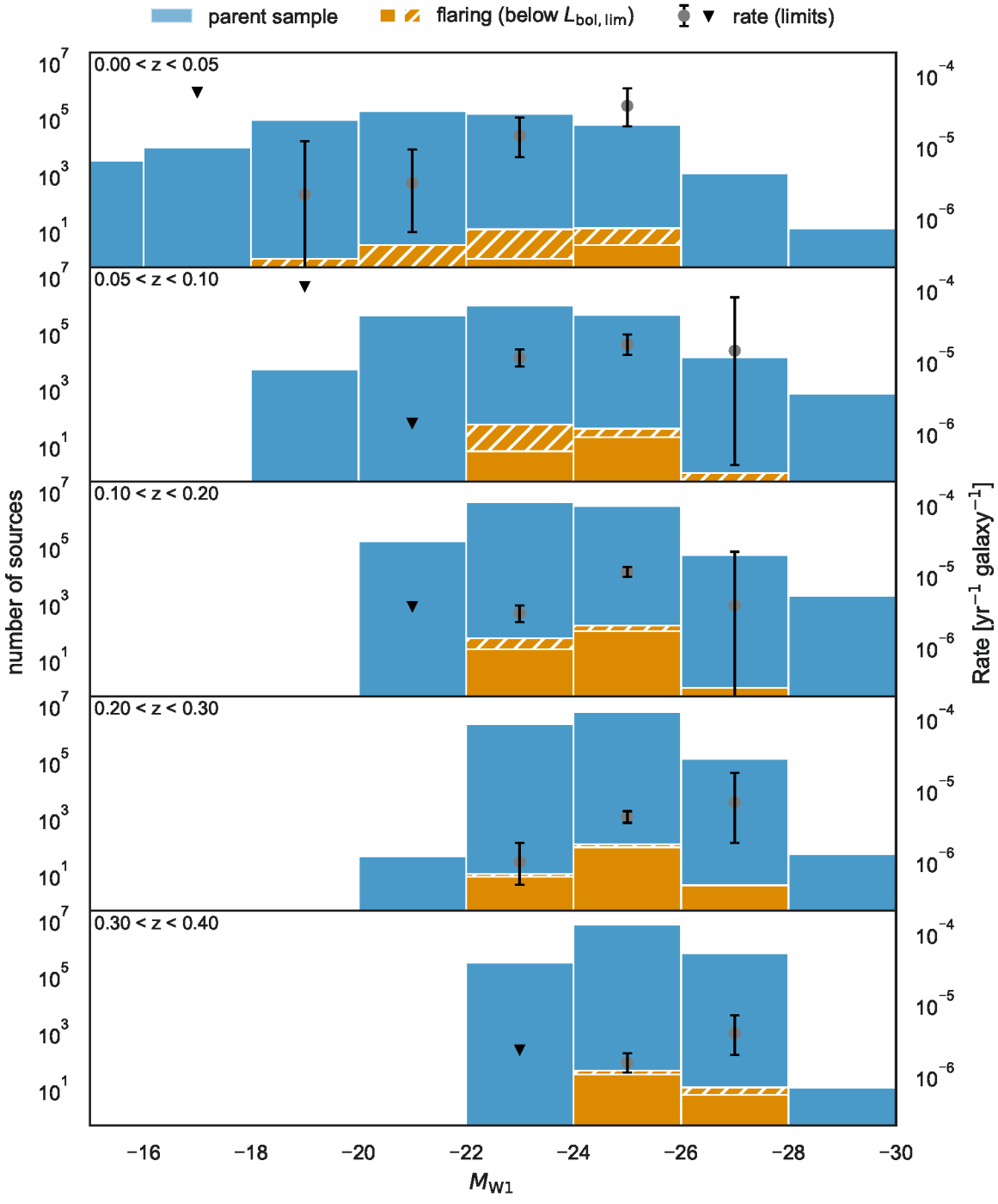

Figure 9.23: The rate as a function of the absolute magnitude in W1 and redshift. Light blue is all parent sample galaxies and orange the ones hosting a flare. The hatched bars represent hosts with flares with $L_{\mathrm{bol,peak}} < 6 \times 10^{43}$ erg. The grey data points and black errors show the rate using Equation 9.23, and black triangles indicate the corresponding 90% upper limit where no flare was observed. The errors are statistical only.

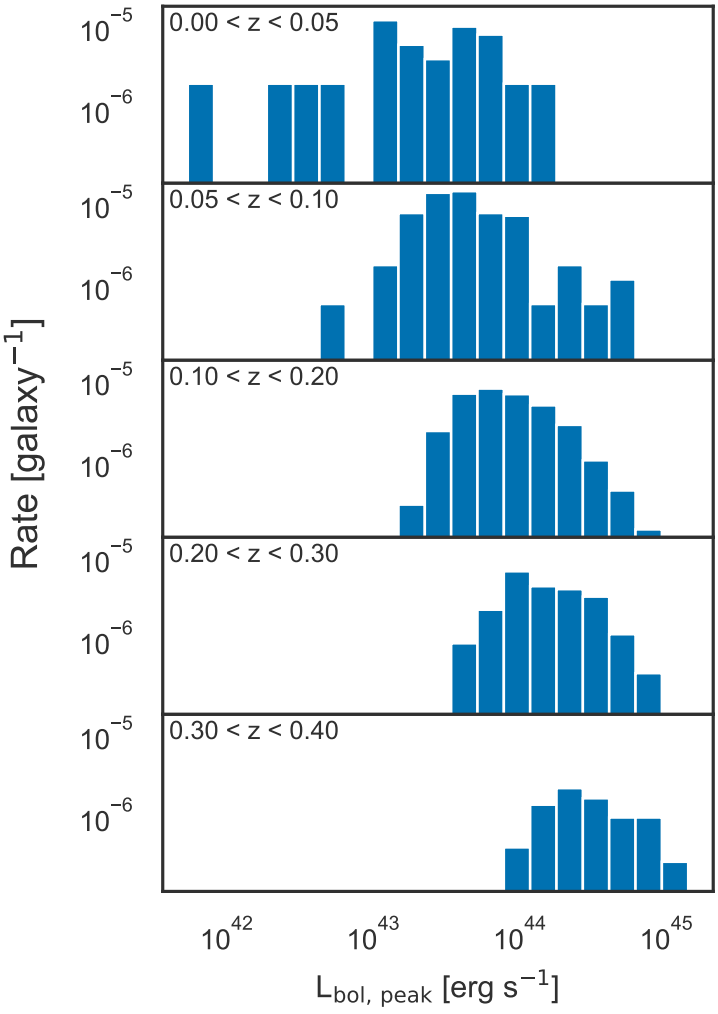

Figure 9.24: The distribution of the maximum bolometric luminosity as a function of redshift of the non- flares with

luminosities, as dimmer flares become harder to detect at higher redshifts. However, since flares with $L_{\mathrm{bol,\,lim}} \approx 6 \times 10^{43}\,\mathrm{erg\,s^{-1}}$ are detected in all redshift bins, a simple assumption is that the analysis is effective at detecting flares with $L_{\mathrm{bol,\,lim}}$ up to the highest redshift bin. The flares with $L_{\mathrm{bol}} < L_{\mathrm{bol,\,lim}}$ are indicated as the hatched portion of the bars in Figure 9.24.

Redshift Evolution

The rate of flares above the limiting luminosity should then not be influenced by loss of sensitivity towards higher redshifts:

$$\mathscr{R}_{i,j}^{\mathrm{lim}} = \frac{(1+\bar{z}_j)}{T} \frac{N_{\mathrm{lim},i,j}}{N_{\mathrm{gal},i,j}}, \tag{9.25}$$

where $N_{\mathrm{lim},i,j}$ is the number of flares with $L_{\mathrm{bol}} > L_{\mathrm{bol,\,lim}}$ in the respective magnitude and redshift bin. The relative rate evolution is then just the rate in a redshift bin divided by the corresponding rate in the first redshift bin:

$$r_{i,j}^{\mathrm{lim}} = \frac{\mathscr{R}_{i,j}^{\mathrm{lim}}}{\mathscr{R}_{i,0}^{\mathrm{lim}}}. \tag{9.26}$$

To also investigate the redshift evolution summed over the magni-

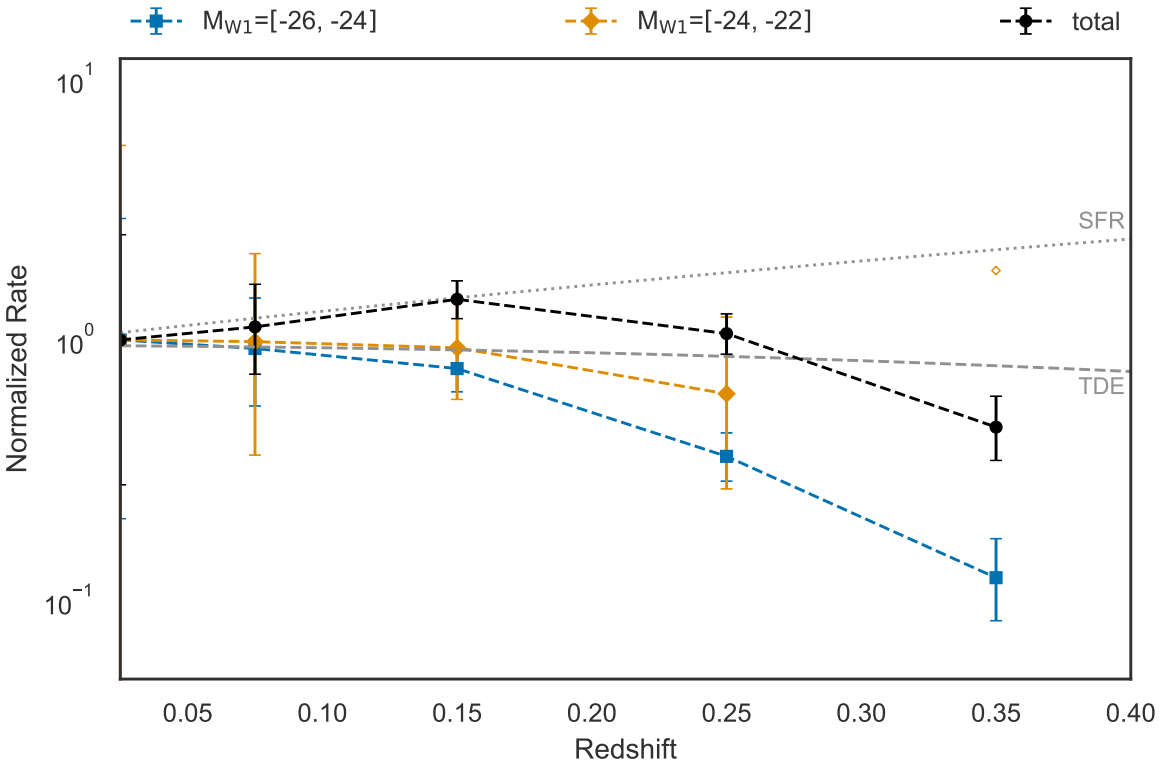

Figure 9.25: Evolution of the rate with redshift for the two M_{W1} bins (blue and orange) where there are flares in the first and at least one other redshift bin, normalized to the first redshift bin. The black line is the redshift evolution over all bins. Open symbols represent upper limits. The redshift evolution of the star formation rate (SFR) [442] and for TDEs [366] is shown for comparison.

tude bins, the total rate per redshift bin is calculated:

$$\mathcal{R}_j^{\lim} = \frac{(1+\bar{z}_j)}{T} \frac{\sum_{i\in\mathbb{M}} N_{\lim,i,j}}{\sum_{i\in\mathbb{M}} N_{\mathrm{gal},i,j}}, \tag{9.27}$$

where the sum goes over the three redshift bins $\mathbb{M}$ that contain at least one flare with $L_{\mathrm{bol}} > L_{\mathrm{bol,lim}}$ in any redshift bin: $M_{W1} = [-24, -22]\,\mathrm{mag_{Vega}}$, $M_{W1} = [-26, -24]\,\mathrm{mag_{Vega}}$ and $M_{W1} = [-28, -26]\,\mathrm{mag_{Vega}}$. Consequently, the summed relative rate evolution is can then be calculated:

$$r_j^{\lim} = \frac{\mathcal{R}_j^{\lim}}{\mathcal{R}_0^{\lim}}. \tag{9.28}$$

The results for $r_j^{\lim}$ are shown in Figure 9.25 along with the relative rate $r_{i,j}^{\lim}$ for the two magnitude bins with a flare in the first and at least one other redshift bin. The results for these two magnitude bins ($M_{W1} = [-26, -24]\,\mathrm{mag_{Vega}}$ and $M_{W1} = [-24, -22]\,\mathrm{mag_{Vega}}$) suggest a strictly negative evolution with a decreasing rate towards higher redshifts.

Theoretical TDE Rate

The evolution of the rate of TDEs, when based solely on the density of SMBHs, forecasts a more gradual decline [366, 443]. There are, however, indications, that TDEs prefer post-starburst galaxies [350, 444, 445] which are more abundant at higher redshifts [446]. The resulting TDE rate could even increase although the exact evolution

is unclear.

As previously noted, even for AGN, the Hills Mass corresponds to a host absolute magnitude of $M_{W1} \approx -26\,\mathrm{mag_{Vega}}$, suggesting that flares in the highest host magnitude bin, $M_{W1} = [-26, -28]\mathrm{mag_{Vega}}$, are more likely AGN activity than TDEs. It would therefore be interesting to determine whether the evolution of that bin aligns with the lower magnitude ones. Unfortunately, no flares above $L_{\mathrm{bol,\,lim}}$ are observed in the first two redshift bins.

In summary, the rate aligns with previous findings from infrared-detected TDEs, and the evolution, measured for the first time, appears consistently negative. This leads to the conclusion that the majority of flares in the sample are likely TDEs.

9.6 Summary, Discussion and Outlook

This chapter presented a pipeline for building infrared light curves based on data from WISE spanning about a decade, filtering them and extracting promising dust echo flares for millions of objects. Fed with a large parent galaxy sample, the pipeline produced the largest catalog of nuclear infrared flares available. Compared to previous studies, this at least doubles the sky area [MIRONG: 348] or greatly expands the probed volume [WTP TDEs: 344]. The around 800 outbursts last for thousands of days with a peak luminosity of 10^{43} to $10^{45}\,\mathrm{erg\,s^{-1}}$ and a peak dust temperature of 1000 to 2000 K. The incident transient has a width of 100 to 1000 d, which is consistent with dust echoes from TDEs or extreme accretion events in AGN, subsumed under the term accretion flares. The rate per galaxy is consistent with measurements of infrared detected TDEs in the local universe [344]. Because of the large sample size, there is enough statistics to probe the redshift evolution of accretion flares for the first time. It is consistent with negative evolution for dimmer hosts with SMBHs probably below the Hills Mass and capable of producing TDEs of a solar mass star. Including brighter galaxies with higher mass black holes, the evolution follows the star formation rate before dropping of at higher redshifts. This could indicate that the flares from lower mass black holes are indeed TDEs while the ones from higher mass black holes are not.
In summary, this sample is the largest and most complete list of accretion flares available which makes it unique for looking for high-energy neutrinos.
However, there are some caveats and it is worth discussing how each of them could influence the results. Some of them are already discussed above but will be revisited again here.

[344]: Masterson et al. (2024), *A New Population of Mid-infrared-selected Tidal Disruption Events: Implications for Tidal Disruption Event Rates and Host Galaxy Properties*

AGN contribution

The most significant is the potential contribution of regular AGN activity. Given that the selection accounts for pre-flare variability, regular AGN variability is unlikely to be a significant factor (see Section 9.3.3). However, despite selecting for dust echoes by obscured TDEs or extreme accretion events, distinguishing between these scenarios solely on infrared data is not possible. A reliable indicator would be the mass of the black hole, which can be determined most accurately through spectroscopy. Observations of the host galaxies

could refine the rough estimate provided in Section 9.5 and clarify whether a population of flares exists in hosts above the Hills Mass: $m_{\mathrm{BH}} > 10^8 m_\odot$. For such cases, a TDE origin would be improbable.

Selection Efficiency

Furthermore, the results for the rate and its evolution are not a conclusive measurement but rather evaluate the consistency with TDEs. The selection efficiency is particularly impacted by the stringent cuts required to distinguish regular AGN variability (refer to step 3 in Section 9.2.3). These cuts are sensitive to the baseline measurement uncertainty, σ_{F}, which is small for bright flares, making the selection threshold very restrictive. As a result, the selection efficiency is likely reduced for bright, nearby flares which would make the rate evolution artificially steep. To mitigate this issue, defining selection cuts independently of the baseline measurement uncertainty could be beneficial, though a comprehensive study is required to fine-tune these new parameters.

To preliminarily study relaxing the cut on extraneous variability, the dust echo strength was required to be greater than the significance of extraneous variability but at least five. This effectively introduces a cap on the significance of extraneous variability. An additional 329 flares pass the selection, many of which seem to be due to non-thermal emission by quasars based on their rapidly varying lightcurve but are not listed in Milliquas. The brightest one is AT 2019aalc, a nuclear transient claimed to be coincident with a high-energy neutrino [80], introduced in Section 8.2. Also AT 2017gbl passes, a candidate obscured TDE [347]. However, the rate and evolution do not change significantly. So while the sample would be more complete and the resulting rate and evolution more robust, this potential bias against bright sources would not alter the conclusions.

In contrast to the potential artificial steepening, flares at higher redshift appear stretched and might be harder to select against brightness changes on longer timescales due to time dilation. This would have lead to an artificial flattening of the rate evolution. Quantifying this bias is possible through detailed simulation of the selection efficiency.

[80]: van Velzen et al. (2024), *Establishing Accretion Flares from Supermassive Black Holes as a Source of High-Energy Neutrinos*

[347]: Kool et al. (2020), *AT 2017gbl: A Dust Obscured TDE Candidate in a Luminous Infrared Galaxy*

Eddington bias

Another caveat is the Eddington bias, affecting measurements near the detection limit of the single-exposure photometry (see Section 9.2.3 and 9.3.3). Although the robustness of the rate was verified, the exact values for the luminosities of dim sources should still be taken with care. The flare luminosities at higher redshifts could be systematically too high. If this is the case, the detection threshold $L_{\mathrm{bol,\,lim}}$ would be smaller. More flares would be included at lower redshift which would make the rate fall even steeper at higher redshift. To overcome this bias, photometry based on stacked images is necessary to make sure that also epochs are included where the source brightness is below the single-epoch limit.

To derive the rate evolution, the luminosity function was implicitly assumed to not vary with redshift. However, the distribution of bolometric luminosities in Figure 9.24 could suggest that the luminosities of the dust echoes are higher at higher redshifts. Figure 9.26 shows the scaling due to the fitted temperature and radius with redshift where the scaling is determined by Equation 9.12. The driving factor for an evolving luminosity is the fitted effective radius. In this analysis, it captures the normalisation of the bolometric light curve which relates to the radius if the dusty shell like Equation 9.16 but also to the *covering factor*. That the fitted effective radius increases with redshift could indicate more dust in the SMBH systems at higher redshifts. To make a more robust rate evolution measurement, this would have to be studied and taken into account.

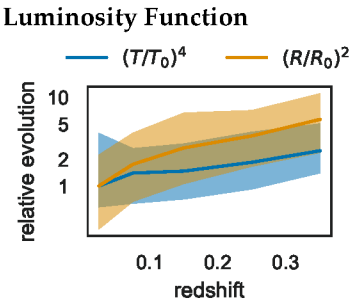

Figure 9.26: The evolution of infered blackbody luminosity with redshift due to the fitted temperature and radius. The solid line and shaded region show the median and the 68% quantile.

Finally, the selection effects presented in Section 9.2.3 are only characterized relative to three reference samples. The first step to make a refined statement about the completeness of the sample is a robust estimate of the parent galaxy sample completeness. Although the number evolution with redshift indicates a relative complete sample up to $z \approx 0.2$ (see Section B.1), this does not take into account the relative brightnesses of the hosts. A comparison of the total included luminosity with a luminosity function would be more robust. Either an independent measurement of the galaxy luminosity functions in the WISE bands would be necessary for that or photometric observations in bands where luminosity functions have been determined. Additionally, as previously mentioned, an absolute calibration of the completeness would entail detailed simulations.

Parent Sample completeness

As of writing this thesis, WISE is spending its last days in orbit: It was shut down on July 31st, 2024 [447] and re-entered the atmosphere on November 2nd [373]. There are 2.5 yr of WISE data that can supplement this analysis. And although the sample presented here is the largest and most complete, it is not exhausting the potential of the WISE dataset as the caveats listed above demonstrate. More detailed analysis of selection efficiencies and stacked photometry could help a future analysis identify even more accretion flares.
In the near future, the *Nancy Roman Space Telescope* (formerly WFIRST) will observe the sky in the near infrared from 0.5 to 2.3 µm [448]. Its planned survey to find supernovae Ia will also enable an efficient search for transient dust echoes [449]. It will primarily enable detection and characterisation of nearby sources since further away ones are redshifted so that they are undetectable in the Roman bands.

[448]: Akeson et al. (2019), *The Wide Field Infrared Survey Telescope: 100 Hubbles for the 2020s*

[449]: Foley et al. (2019), *WFIRST: Enhancing Transient Science and Multi-Messenger Astronomy*

Conclusion

Summary and Outlook 10

With the discovery of astrophysical neutrinos by IceCube in 2013 [2], multimessenger astronomy opened a window that promised to reveal the sources of CRs. With the detection of the flaring blazar TXS 0506+056 and the active galaxy NGC 1068, IceCube showed that high-energy neutrino astronomy is indeed possible, although the sources of the majority of neutrinos have yet to be identified. This thesis advances the search for these sources and presents constraints on high-energy neutrino emission from transients using modern time-domain astronomy.

[2]: IceCube Collaboration (2013), *Evidence for High-Energy Extraterrestrial Neutrinos at the IceCube Detector*

IceCube's real-time alert program is an important system to enable prompt follow-up observations by other observatories. It is the only way that a timely, rich multimessenger dataset can be generated for interesting transients. To associate potential counterparts to the alert neutrino, the spatial uncertainty contours are crucial. An improved re-simulation method of through-going muon tracks to calibrate these contours is introduced in this thesis. For the first time, it respects the energy loss pattern of the muon in the detector volume. Besides speeding up the algorithm, this enables the calibration of events that were inaccessible with previous techniques.

The follow-up of IceCube's high-energy neutrino alerts by the optical sky survey ASAS-SN is summarized and all candidates are evaluated. No new counterparts are found, and corresponding upper limits on the luminosity function of neutrino source populations are derived. Due to ASAS-SN's distributed stations, the follow-up happens so fast that constraints on the timescale of hours are possible. However, they do not yet reach the depth of typical candidate neutrino source populations like interacting supernovae or gamma-ray burst afterglows. For the relevant physical range, the comparison with other current and future facilities highlights the benefit of deep observations compared with fast and wide ones.

ZTF is a more sensitive telescope that identified three TDE-like flares in the footprint of IceCube's high-energy neutrino alerts. Bright *dust echo*s are common to all of them, and a corresponding sample is correlated above the 3σ level with the IceCube alerts. In this work, the uncertainty region's robustness of the respective neutrino events is probed with the improved re-simulation mentioned above. The results suggest that the flares lie outside the uncertainty contour, although further studies inside IceCube are ongoing to reach a firm conclusion. The correlation is also probed with a stacking analysis, treating the flare catalog as a single effective source and leveraging the statistical power of the full IceCube energy range. The result is consistent with background expectations. The easiest reconciliation with the observed three coincidences is if the neutrinos are produced in the interaction of highly energetic protons with the OUV or MIR dust echo photons, while interaction with X-ray photons is excluded. Assuming that the flares in the sample are all TDEs and further making an assumption about the rate of TDEs across cosmic time,

the result was extrapolated to get a limit on the contribution of the full TDEs population to the diffuse high-energy neutrino flux. Compared to a previous result, this limit is around four times more constraining. For a spectral index $\gamma = 2.5$, it is below around 7.1%. For neutrino production through interaction with the dust echo, the contribution must even be below about 0.3% at 100 TeV. Although this scenario is still possible, model parameters like the energy conversion efficiency from accretion to proton acceleration are constrained to below optimistic values. The main uncertainty when extrapolating to the full TDE population is the evolution of the rate.

A large sample of similar MIR flares is compiled from millions of lightcurves. The dust-echo nature of the transients is consistent within the model, and the most likely origin are transient accretion events around SMBHs. The rate of these events declines with increasing redshift which follows the TDEs rate expectation if it is only influenced by the number of SMBHs in the universe. This is the widest and deepest such sample, expanding on the accretion flare sample used in the IceCube stacking analysis by a factor of ten, which will allow further neutrino correlation studies with improved sensitivity.

Ultimately, this work probes high-energy neutrino emission from optical and IR transients at the sensitivity boundary set by the current generation of telescopes. These capabilities will be expanded soon. The VRO [291] is set to start science operations in 2025 [450] and will observe the sky in six bands. Follow-up observations of IceCube alerts are planned, and the projected sensitivity will finally be able to probe the full parameter space of potential neutrino source populations (see Figure 6.9). Although the WISE mission has ended, the IR sky will also be observed in the future by the *Nancy Grace Roman Space Telescope* [448], expected to launch in 2027 [451]. Its mirror area is more than 30 times the size of WISE making it a lot more sensitive. However, with a 0.28 sqd FoV it is not built as a survey instrument and its filters only extend up to a wavelength of about 2.3 µm. No other mission is currently planned that matches WISE's capabilities when it comes to learning about hot dust emission. However, at shorter wavelengths, the wide field satellite *ULTRASAT* [452], also expected to launch in 2027 [453], will map the sky in the UV. It will discover many SNe very early, constraining their explosion time extremely well, and the expected rate of TDEs discoveries ranges from hundreds to thousands per year.

Significant efforts are also put into the further exploration of the high-energy universe. The *Cherenkov Telescope Array* (CTA) [454] will significantly improve the ground-based observation of highly energetic gamma-rays. It is an array of telescopes observing Cherenkov radiation of air-showers induced by gamma-rays hitting the atmosphere, split in a southern site in Chile and a northern site on La Palma. Combining the observations with IceCube data can greatly improve the particle acceleration models for extragalactic sources like GRBs but also remnants of SNe in the Milky Way [455]. CTA will be composed of telescopes of three different sizes. The first *Large*

[291]: Ivezić et al. (2019), *LSST: From Science Drivers to Reference Design and Anticipated Data Products*

[448]: Akeson et al. (2019), *The Wide Field Infrared Survey Telescope: 100 Hubbles for the 2020s*

[452]: Shvartzvald et al. (2024), *ULTRASAT: A Wide-field Time-domain UV Space Telescope*

[454]: Actis et al. (2011), *Design Concepts for the Cherenkov Telescope Array CTA: An Advanced Facility for Ground-Based High-Energy Gamma-Ray Astronomy*

[455]: Halzen (2013), *Pionic Photons and Neutrinos from Cosmic Ray Accelerators*

Size Telescope (LST) is already observing on La Palma and three more are expected to be operational by 2026 [456].

Both the sensitivity and energy range of neutrino observatories will increase in the future. The next km^3 scale detectors, *KM3NeT* [457] and *Baikal GVD* [458], are close to independent measurements of the diffuse astrophysical neutrino flux [459, 460]. These are Cherenkov detectors similar to IceCube but operating in deep seawater. Because there is less scattering, and the modules themselves record directional information, the angular resolution of KM3NeT is expected to improve compared to IceCube. Consequently, the sensitivity for the same data collection period is expected to improve by around 60% [460]. The particle shower induced by neutrino interactions in ice also produces radio emission. Because this radio emission can be measured over large distances, a single radio antenna station can monitor 1 to 100 km^3 for neutrino energies above the Cherenkov detector range at 100 PeV to 1 EeV. The *Radio Neutrino Observatory in Greenland* (RNO-G) [461] has already built 7 out of 35 antenna stations for neutrino detection. In the coming years it will be able to probe ultra high-energy astrophysical neutrinos as well as the expected cosmogenic neutrino flux related to the GZK cutoff (see Chapter 2). This radio detection of high energy neutrinos is also part of the concept for the next generation of IceCube, *IceCube Gen2* [462]. Planned to begin deployment in 2027, it extends the instrumented volume of the in-ice array by a factor of eight. Together with other improvements, this leads to an effective area for neutrino detection ten times larger than IceCube. A radio component similar to RNO-G is also planned, extending the sensitive range to higher energies. With this instrument, neutrino astrophysics will fully mature to an integral part of astronomy. Together with the future EM facilities, it will uncover the sources of neutrinos and cosmic rays.

[456]: Abe et al. (2023), *First Science Results from CTA LST-1 Telescope and Status of LST-2-4*

[457]: Adrián-Martínez et al. (2016), *Letter of Intent for KM3NeT 2.0*

[458]: Avrorin et al. (2016), *Status of the Early Construction Phase of Baikal-GVD*

[459]: Dvornicky (2023), *Large Neutrino Telescope Baikal-GVD: Recent Status*

[460]: van Eeden et al. (2023), *Astronomy Potential of KM3NeT/ARCA230*

[461]: Aguilar et al. (2024), *Design and Sensitivity of the Radio Neutrino Observatory in Greenland (RNO-G)*

Appendix

Bandpasses A

Figure A.1 shows the bandpasses of the optical and infrared instruments used in this work: the *All-Sky Automated Survey for SuperNovae* (ASAS-SN), introduced in Chapter 6, the *Zwicky Transient Facility* (ZTF), introduced in Chapter 7, and the *Wide-Field Infrared Survey Explorer* (WISE), introduced in Chapter 9).

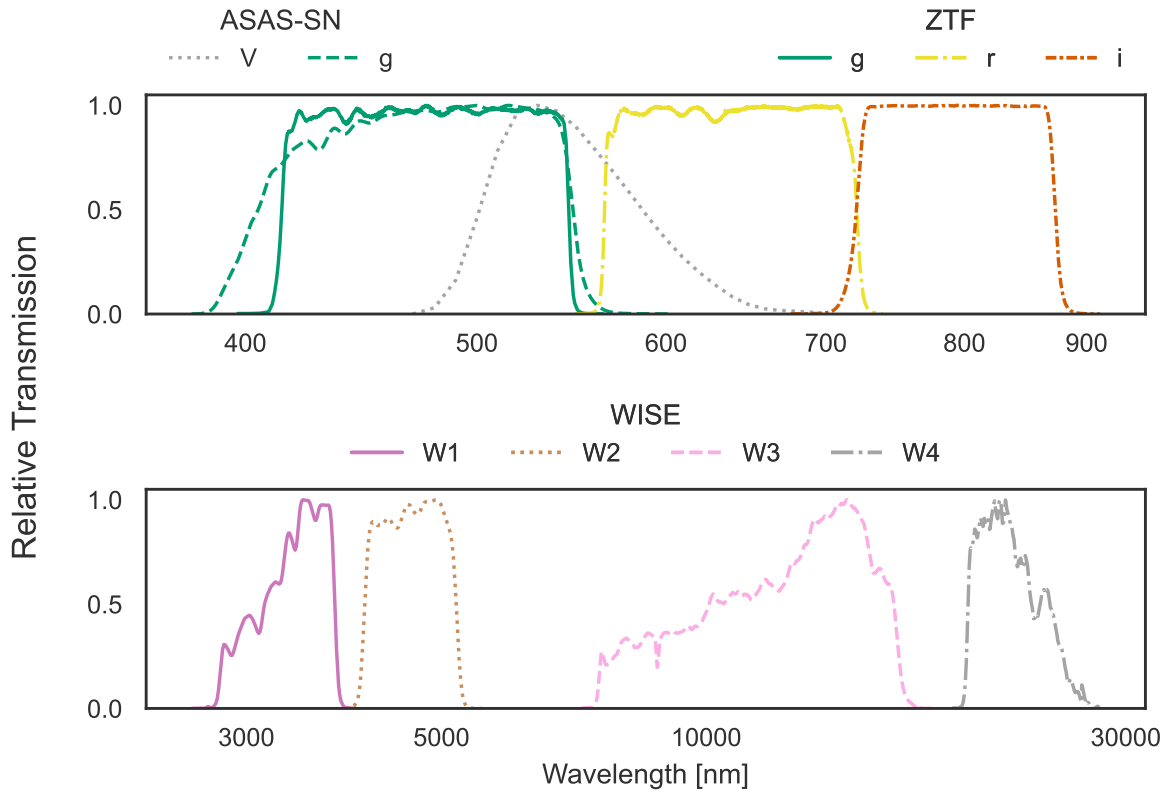

Figure A.1: The filter curves of ZTF, ASAS-SN and WISE. The relative transmission is the absolute transmission, normalized to one at the maximum. The ASAS-SN filter functions are not available but match the SDSS g-band and Bessell V-band, which are shown here. Obtained using the Filter Profile Service by the Spanish Virtual Observatory [463, 464].

Infrared Flare Sample: Systematic Checks

B

B.1 Parent Sample Completeness

Cook et al. [380] calculate the completeness of NED-LVS by comparing the luminosity contained in distance shells to the expectation from galaxy luminosity functions. This is done in the infrared using the K_s band where there exists a luminosity function estimate in the literature. Concerning the total luminosity, NED-LVS is complete up to 30 Mpc and around 70% complete until 300 Mpc ($z \approx 0.06$). Unfortunately, such a measurement does not exist yet for the WISE bands, so an equivalent .

[380]: Cook et al. (2023), *Completeness of the NASA/IPAC Extragalactic Database (NED) Local Volume Sample*

Instead, a simpler estimate of the completeness is to look for the redshift until which the scaling of number of objects N agrees with the expected scaling with distance. The number in a spherical shell relates to the volume element via the density:

$$\mathrm{d}N = \rho \, \mathrm{d}V. \tag{B.1}$$

For a Euclidean space, this is just

$$\mathrm{d}N = \rho \frac{4}{3} \pi D^2 \, \mathrm{d}r, \tag{B.2}$$

giving the relation between number and distance $N \propto D^2$. The fully relativistic volume element form considering the expansion of the universe is [465]

[465]: Hogg (2000), *Distance Measures in Cosmology*

$$\mathrm{d}V = \frac{c}{H_0} \frac{d_\mathrm{L}^2(z)}{(1+z)^2 \, E(z)} \mathrm{d}\Omega \mathrm{d}z, \tag{B.3}$$

assuming a flat universe. $E(z)$ is a function of redshift and the dimensionless cosmological density parameters Ω_x:

$$E(z) = \sqrt{\Omega_m (1+z)^3 + \Omega_k (1+z)^2 + \Omega_\Lambda}, \tag{B.4}$$

where Ω_m is the contribution by matter, Ω_k the contribution by curvature and Ω_Λ describes the cosmological constant.

Figure B.1 shows the redshift distribution of the galaxy sample. To compare the distribution with the expectation, the scaled luminosity distance,

$$D^2(z) \equiv \frac{d_\mathrm{L}^2(z)}{(1+z)^2 E(z)}, \tag{B.5}$$

was fitted to the histogram. The redshift until which the scaling is consistent gives an estimate of the completeness limit. The result is shown as the solid blue line in Figure B.1. The exponent is not two as expected but close to unity, indicating that galaxies are missing from subsequently further redshift shells. These are likely galaxies too dim to be detected.

Characteristic Magnitude

The characteristic magnitude $M^\star$ (or the equivalent characterstic luminosity $L^\star$) is a parameter of the Schechter function, commonly used to describe the galaxy luminosity function [466]. It marks the point at which the slope flattens towards fainter luminosities. The value by [467] used in [380] is given as $M^\star_{\mathrm{K_s}} - 5 \log_{10}(h) = -23.83$ where h is the numerical value of the Hubble constant such that $H_0 = 100 \, h \, \mathrm{km \, s^{-1} \, Mpc^{-1}}$. Here $h = 0.7$ is assumed.

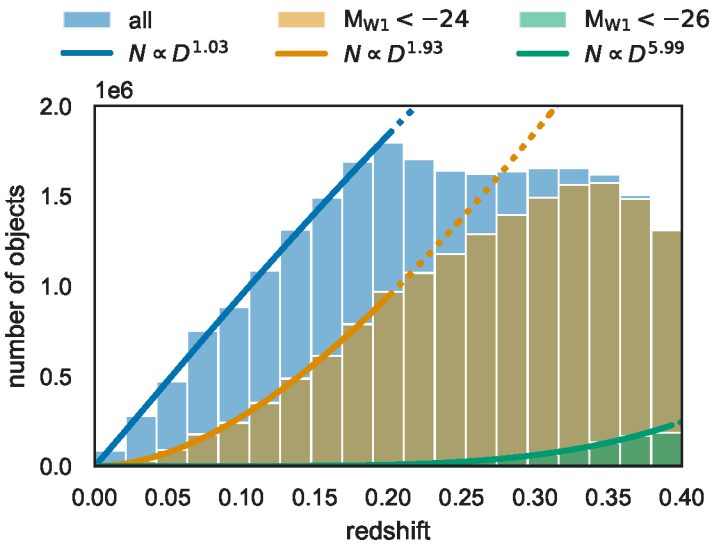

Figure B.1: The redshift distribution of the parent galaxy sample with fitted scalings of the number with distance.

Following [380], the completeness above a characteristic luminosity $L^\star$ or magnitude $M^\star$ can be probed to confirm this. Concerning the number of galaxies above $M^\star_{K_s} = -23.06$, NED-LVS is complete until 400 Mpc ($z \approx 0.08$). As mentioned above, no measurement of the luminosity function exists for the WISE bands and thus no $M^\star_{W1}$. However, assuming a power-law spectrum, the values for the K_s band can be extrapolated. For any two bands, the relation between luminosity and absolute magnitude is

$$\frac{L^\star_1}{L^\star_2} = 10^{\frac{M^\star_2 - M^\star_1}{2.5}}. \tag{B.6}$$

As shown in Section 9.6 (Figure 9.21), the flux spectrum can be approximated with a power-law $F \propto \lambda^{-3}$. The luminosity then scales with the wavelength as $L \propto \lambda F \propto \lambda^{-2}$. Inserting this into Equation B.6 and solving for the magnitude gives the characteristic absolute magnitude in band two:

$$M^\star_1 = M^\star_2 + 5 \log_{10} \frac{\lambda_1}{\lambda_2}. \tag{B.7}$$

The K_s band has a central wavelength of around $\lambda_{K_s} = 2.2\,\mu m$ [468]. The W1-band at the wavelength $\lambda_{W1} = 3.4\,\mu m$ then has a charachteristic magnitude $M^\star_{W1} = -23.7$.

[468]: Skrutskie et al. (2006), *The Two Micron All Sky Survey (2MASS)*

The orange and green histogram in Figure B.1 show the distributions of objects with $M < -24$ and $M < -26$. For the first case, the scaling with D is close to the expected one and indicates completeness down to about $z = 0.2$, almost doubling the redshift range compared to NED-LVS. For the latter case, the scaling is a lot steeper than expected from a constant number density which could indicate more luminous galaxies at higher redshift.

B.2 Stacked Photometry Errors

In Section 9.2.2, the procedure to stack single-exposure datapoints was already explained in detail, including the calculation of the error bars. These indicate the 1σ uncertainty of the nominal value, assuming a normal distribution. A useful metric to confirm this is the reduced χ^2 with respect to the median:

$$\chi^2_{\mathrm{red}} = \frac{1}{N-1} \sum_{\mathrm{i}}^{N-1} \frac{(f_\mathrm{i} - \tilde{\mu})^2}{\sigma_\mathrm{i}^2}, \tag{B.8}$$

where the sum goes over all stacked datapoints i that have a flux f_i and an error σ_i. $\tilde{\mu}$ is the estimated median of all stacked datapoints in a light curve. If the datapoints f_i are indeed distributed according to a normal distribution around the true median μ, χ^2_{red} follows a χ^2-distribution with $N-1$[1] degrees-of-freedom [183]. This is not the case for variable sources where the flux changes over time. However, most sources are expected to be steady, so the majority of light curves should still follow the χ^2-distribution.

1: The estimation of the median from the data leaves only $N-1$ independent points, not N.

[183]: Wilks (1938), *The Large-Sample Distribution of the Likelihood Ratio for Testing Composite Hypotheses*

Figure B.3 and Figure B.4 show the distributions pf χ^2_{red} for both WISE bands. Differences are visible between the two bands and between light curves with more and fewer datapoints. In general, there is a larger tail towards higher χ^2 values than expected. If all light curves were from steady sources, this would entail that the computed error-bars are too small. As mentioned above, however, not all sources are expected to be steady, and so the variable population will therefore show up at large χ^2 values and can be responsible for the large tails. At least in the W1 band, the distributions line up with the expected χ^2-distribution for number of datapoints between about 4 and 16 at $\chi^2_{\mathrm{red}} \lesssim 0.5$.

The histograms of the W2-band for light curves with four to 19 datapoints show a bump at small χ^2_{red} values that is not consistent with the χ^2-distribution. This is not unexpected when considering dim sources where only a small number of single-exposures per visit yield a detection. In that case, the nominal value of the stacked datapoint is no longer distributed according to a normal distribution but the Student's t-distribution. Its parameter ν describes the number of single detections and approaches the normal distribution for $\nu \to \infty$ [469, Chapter 42]. For a light curve with N datapoints where each datapoint is the mean of ν single detections, the χ^2_{red} from Equation B.8 is then distributed like

$$\chi^2_{\mathrm{red}} \sim \frac{1}{N-1} \sum_{i}^{N-1} t^2_{\nu_i} \tag{B.9}$$

instead of $\chi^2_{\mathrm{red}} \sim \sum_i^{N-1} \mathcal{N}(0,1)^2$, where $\mathcal{N}(0,1)$ is a normal distribution with mean $\mu = 0$ and standard deviation $\sigma = 1$. The equivalent of the χ^2 distribution for the t-distribution is the F-distribution [469, Chapter 20]:

$$F(\omega, \nu) \sim \frac{\chi^2_\omega / \omega}{\chi^2_\nu / \nu}, \tag{B.10}$$

so that $t^2_\nu \sim F(1, \nu)$. With that, χ^2_{red} follows the sum of several

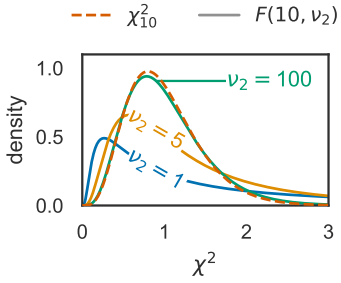

Figure B.2: Illustration of the F-distribution and hwo it approaches the χ^2-distribution for an example degree-of-freedom of 10.

[469]: Forbes et al. (2011), *Statistical Distributions*

F-distribution

F-distributions:

$$\chi^2_{\text{red}} \sim \frac{1}{N-1} \sum_i^{N-1} F(1, \nu_i). \tag{B.11}$$

Assuming all datapoints in a light curve are the result of stacking the same number of single-exposures, so that all $\nu_i = \nu$, then the sum can be expressed as a single F-distribution:

$$\begin{aligned} \chi^2_{\text{red}} &\sim \frac{1}{N-1} \sum_i^{N-1} F(1, \nu) \\ &\sim \frac{1}{N-1} \sum_i^{N-1} \frac{\chi^2_1}{\chi^2_\nu/\nu} \\ &\sim \frac{1}{N-1} \frac{\chi^2_{N-1}}{\chi^2_\nu/\nu} \\ &\sim F(N-1, \nu). \end{aligned} \tag{B.12}$$

To get from line two to three, $\sum^N \chi^2_1 = \chi^2_N$ was used [469, Chapter 11]. This approaches a χ^2 distribution for $\nu \to \infty$.

The green lines in Figure B.3 and Figure B.4 show this distribution for $\nu = 1$. It captures the bump at low χ^2_{red} values in the W2-band, which means that this feature is a result of some light curves having stacked datapoints that are based on only very few single-exposures. Because the W1 band is more sensitive, the same light curves that have few detections in W2 can have more in W1. and has more single-exposure detections, thus following the χ^2 more closely.

Although the bump feature can be understood this way, the whole χ^2_{red} distribution still is not explained, including the excess at higher values. It likely follows a complex superposition of F-distributions with different ν_2. What can be used instead to validate the error-bars is the coverage of the median: the percentage of datapoints where the error-bar includes the median. For the 1σ errors, this is expected to be around 68%. Figure B.5 shows the coverage distribution for all light curves and both WISE bands. The median value and 68% confidence interval for W1 is $0.68^{+0.11}_{-0.13}$ which matches the expectation. The value for W2 is $0.76^{+0.12}_{-0.16}$ which is slightly too high which means that more error-bars include the median than expected. This is equivalent to the bump in the χ^2_{red}-distributions at low χ^2_{red} values which is already understood. Therefore, this allows the conclusion that the error-bars do, in fact, represent the 1σ uncertainties.

Coverage

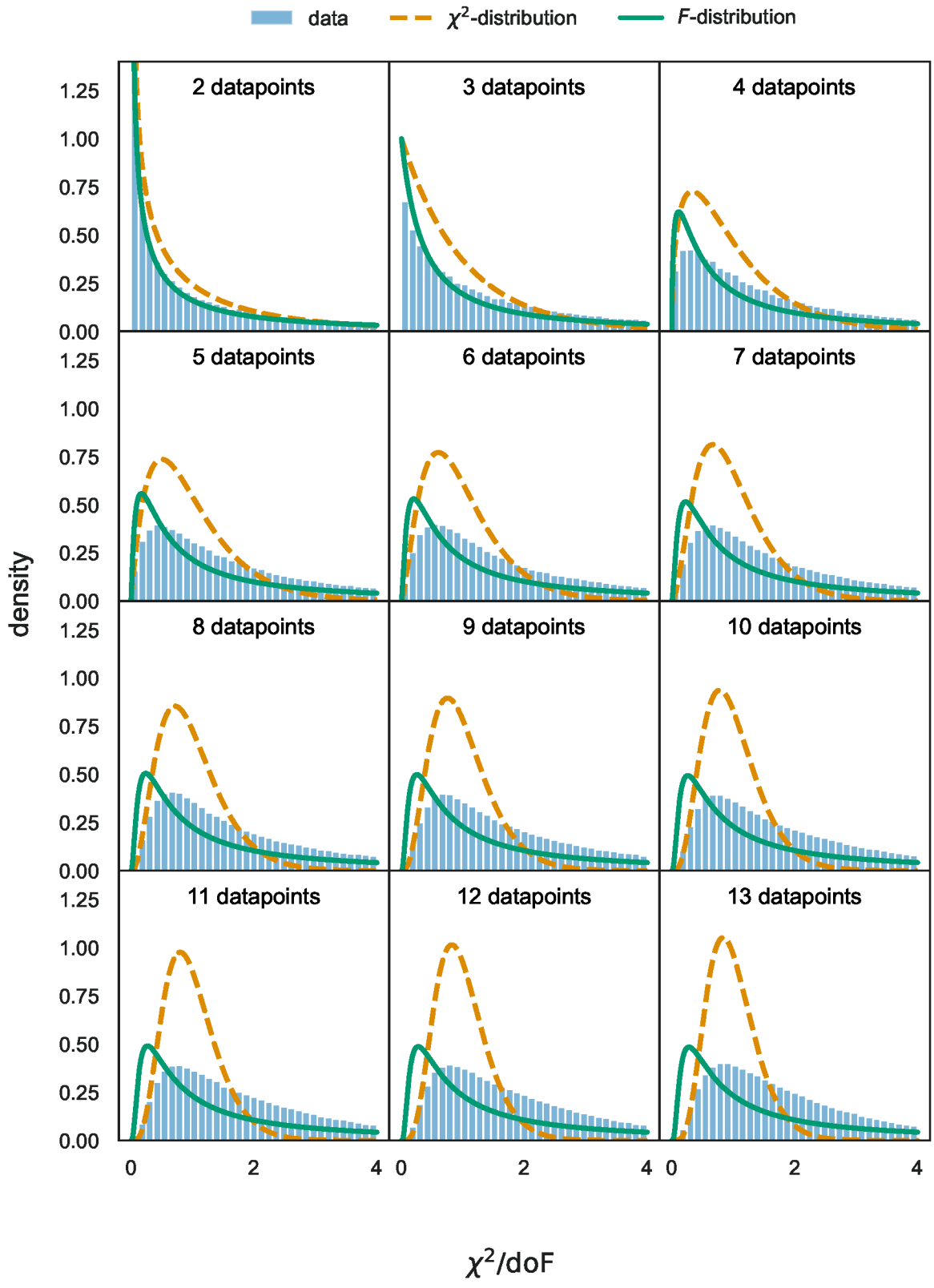

Figure B.3a: χ^2_{red}-distributions in the W1-band for all WISE light curves and theoretically expected distributions. N denotes the number of datapoints in each light curve. The χ^2-distributions have $N-1$ degrees of freedom and the F-distributions have parameters $N-1$ and 1.

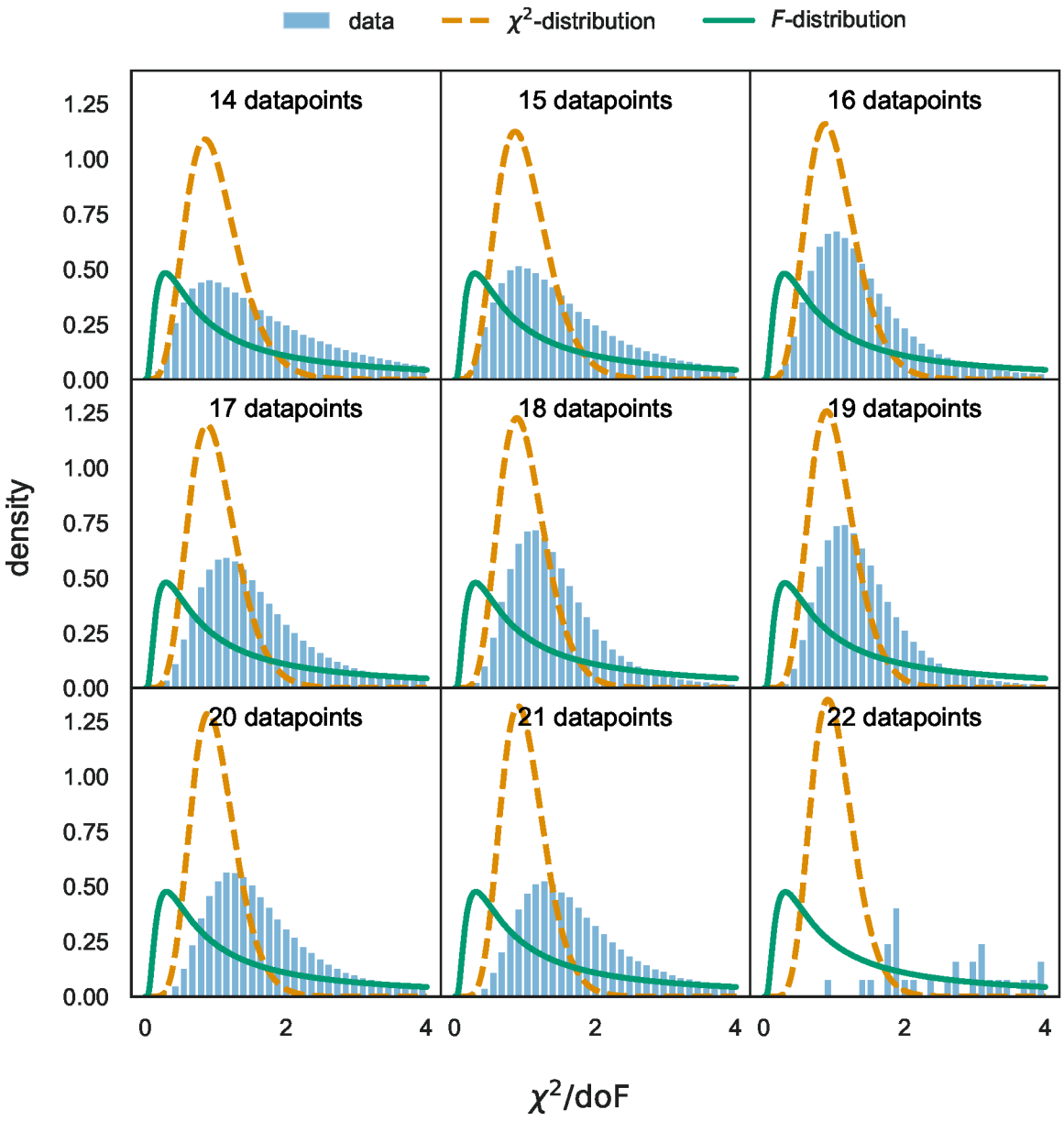

Figure B.3b: Continued from Figure B.3

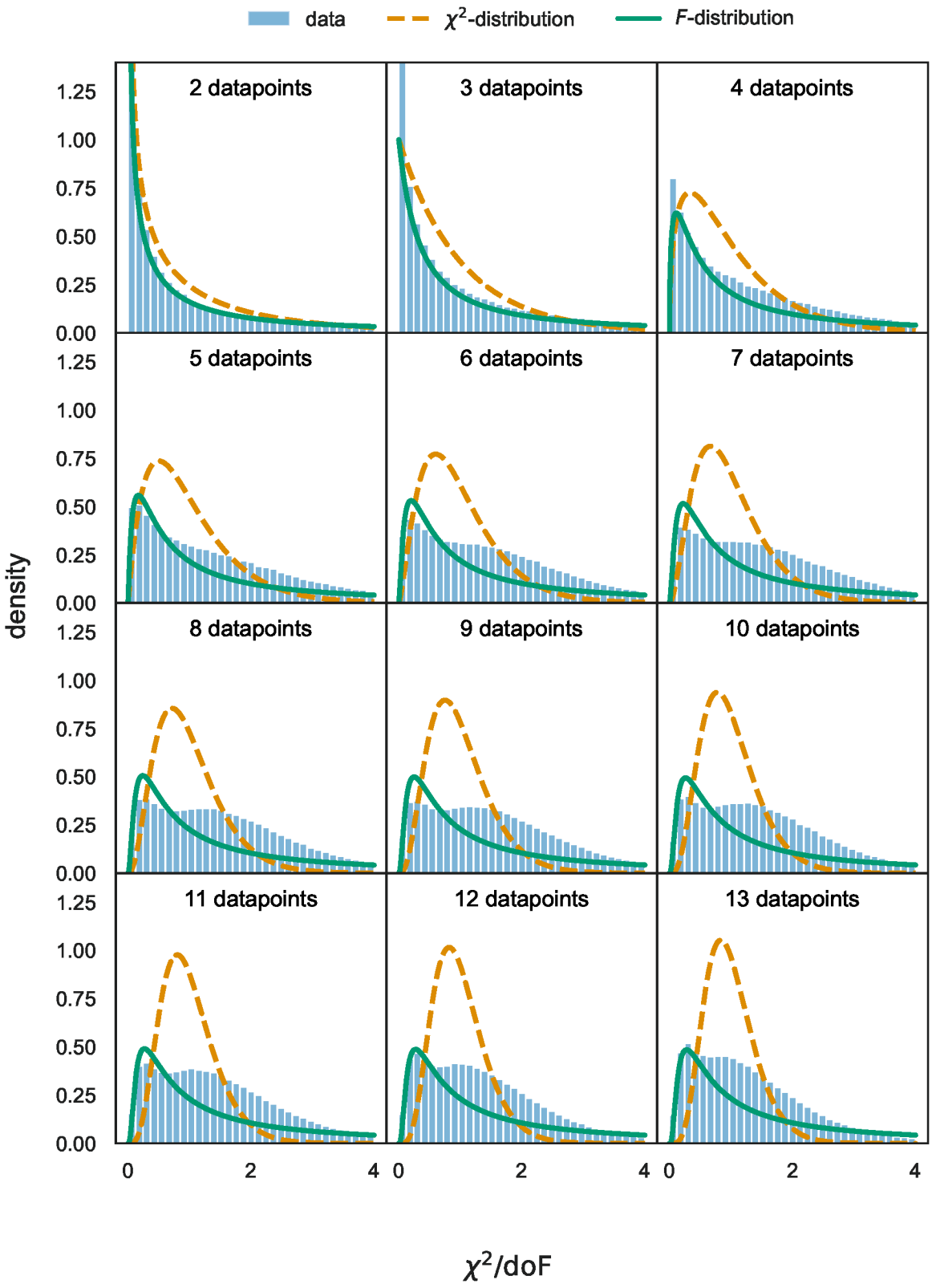

Figure B.4a: Same as Figure B.3 but for W2.

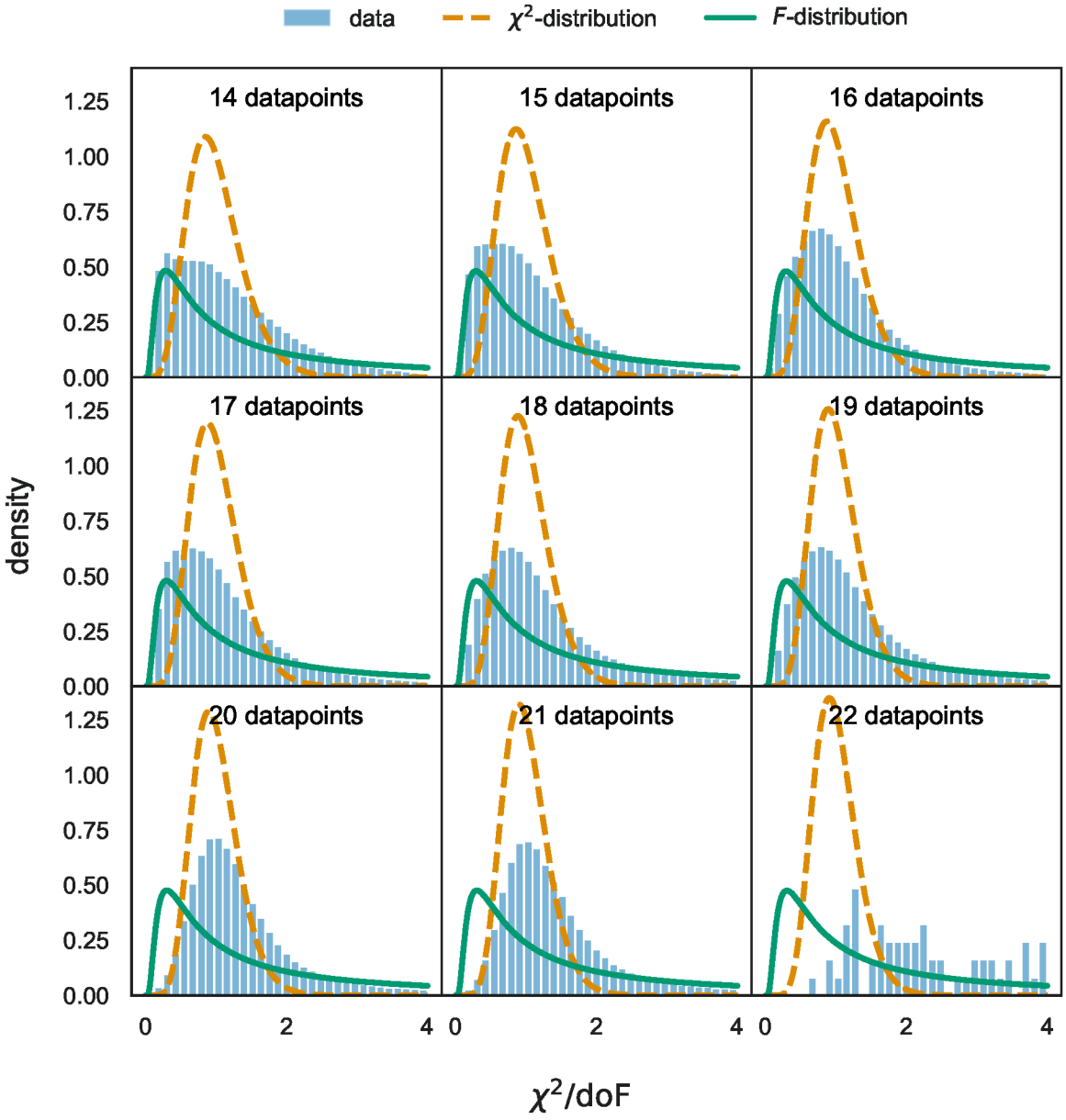

Figure B.4b: Continued from Figure B.4

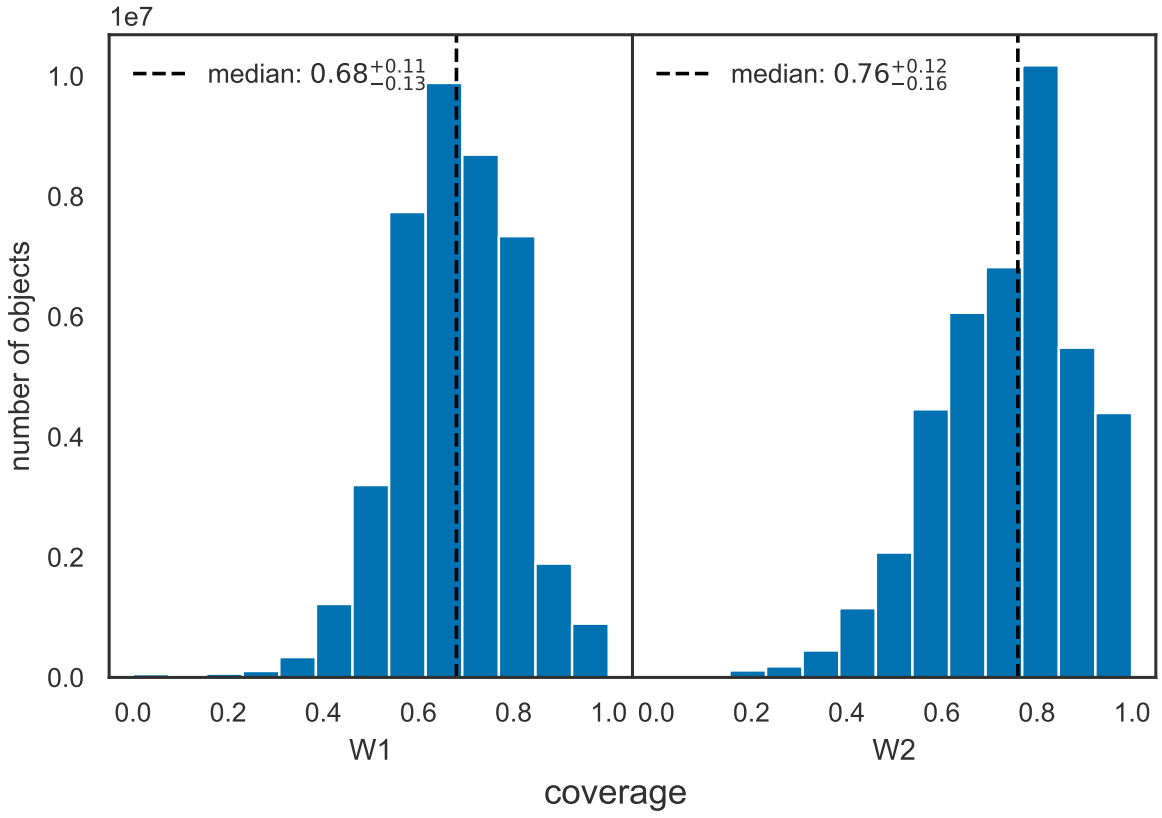

Figure B.5: Covergae of the median per light curve by the error-bars of the stacked photometry datapoints. The histogram shows the distribution for all around 40 million light curves. The black dashed line shows the median per band.

B.3 Additional Tables

Table B.1 shows the results of the infrared lightcurve analysis presented in Chapter 9 for the three reference samples introduced in Section 9.4. Table B.2 lists the 39 brightest objects in the final infrared flare catalog.

Table B.1: Results for reference sample flares. The first column is the name of the host or flare given in the reference sample. The other columns are the dust echo strength, the significance of the extraneaous activity, the χ^2_{red}, and the final result determined by the analysis pipeline as described in Chapter 9.

Name	$\Delta F/F_{\mathrm{rms}}$	$F_{\mathrm{rms}}/\sigma_{\mathrm{F}}$	χ^2_{red}	Result
		MIRONG		
SDSSJ000046.47+143813.0	7.235460	6.176324	51.499871	long flare
SDSSJ002701.04+071357.6	9.416179	5.010366	25.979449	long flare
SDSSJ004500.49-004723.0	4.987654	5.604017	19.852376	3: extraneous activity
SDSSJ010320.42+140149.8	-	-	-	no data
SDSSJ012048.00-082918.4	5.290421	12.039740	253.113113	3: extraneous activity
SDSSJ012100.68+140517.3	5.647730	7.327357	20.514548	3: extraneous activity
SDSSJ015804.75-005221.9	55.093009	5.044866	536.118395	long flare
SDSSJ020552.15+000411.7	39.568772	6.698829	506.233210	**dust echo like**
SDSSJ074547.87+265538.0	6.065738	6.103610	241.904915	3: extraneous activity
SDSSJ075709.70+190842.8	10.424613	3.903862	51.304172	long flare
SDSSJ081121.40+405451.8	15.843710	7.293818	666.367277	long flare
SDSSJ081403.78+261144.3	10.676061	5.313606	55.389235	5: gap in the lightcurve
SDSSJ081451.88+533732.6	34.289755	1.296370	50.196344	5: gap in the lightcurve
SDSSJ083536.49+493542.7	17.811010	5.238040	171.993866	long flare
SDSSJ083721.86+414342.1	12.243468	7.497678	52.028684	long flare
SDSSJ084157.99+052605.8	8.819825	7.603010	70.854667	long flare
SDSSJ084232.88+235719.7	6.412621	9.477398	24.187445	3: extraneous activity
SDSSJ084752.78+514236.2	5.395527	5.175775	11.194459	long flare
SDSSJ085434.66+111334.8	13.042479	7.318329	125.188190	long flare
SDSSJ085835.91+412113.9	4.259047	5.779492	9.223576	3: extraneous activity
SDSSJ085959.47+092225.7	32.584427	3.778876	539.141133	**dust echo like**
SDSSJ090924.55+192004.8	9.701734	5.078224	119.042151	**dust echo like**
SDSSJ091531.04+481407.7	11.704594	4.957337	97.747321	long flare
SDSSJ093135.48+662652.2	6.264897	4.142224	31.024734	long flare
SDSSJ093608.59+061525.4	16.196292	2.815029	17.307738	**dust echo like**
SDSSJ094303.26+595809.5	5.408209	5.323915	12.650494	long flare
SDSSJ094456.57+310552.2	5.220873	9.704360	34.462898	3: extraneous activity
SDSSJ095754.77+020711.2	6.273216	4.991772	52.640732	5: gap in the lightcurve
SDSSJ100120.37+182926.7	4.170072	8.954458	7.178640	3: extraneous activity
SDSSJ100256.90+442457.8	9.133122	4.655360	10.924204	long flare
SDSSJ100350.98+020227.7	14.319672	3.776481	78.438508	**dust echo like**
SDSSJ100809.03+154951.4	19.496603	3.069665	105.320703	5: gap in the lightcurve
SDSSJ100931.71+343604.8	5.840619	7.921774	21.541772	3: extraneous activity
SDSSJ100955.71+220949.3	9.839760	9.975518	57.164248	5: gap in the lightcurve
SDSSJ101157.64+534857.9	-	-	-	not in parent sample
SDSSJ101708.95+122412.2	3.524767	16.669487	47.759490	3: extraneous activity
SDSSJ102017.72+251554.4	7.700326	5.184621	12.675709	**dust echo like**

Continued on next page

Table B.1: Reasons for rejection of reference sample objects

Name	$\Delta F/F_{\rm rms}$	$F_{\rm rms}/\sigma_{\rm F}$	$\chi^2_{\rm red}$	Result
SDSSJ102934.89+252635.8	13.488708	5.564740	28.956184	4: no prior baseline
SDSSJ102959.96+482937.9	6.251344	13.197655	99.358152	3: extraneous activity
SDSSJ103753.69+391249.7	11.407591	4.859846	45.388561	long flare
SDSSJ104138.80+341253.6	7.691065	5.175065	39.831729	**dust echo like**
SDSSJ104306.57+271602.2	7.525025	6.519724	98.379477	**dust echo like**
SDSSJ104609.62+165511.5	-	-	-	not in parent sample
SDSSJ105145.48+210132.2	5.666400	9.385510	23.403331	3: extraneous activity
SDSSJ105344.14+552405.7	2.848154	8.681730	16.270909	3: extraneous activity
SDSSJ105801.53+544437.0	7.568631	4.630113	36.149122	long flare
SDSSJ110501.98+594103.6	39.665225	6.202336	1511.553381	**dust echo like**
SDSSJ110958.35+370809.7	44.304717	2.219532	183.171075	5: gap in the lightcurve
SDSSJ111122.44+592334.3	22.176583	2.429040	60.373333	**dust echo like**
SDSSJ111431.84+405613.8	44.444486	1.256672	160.798730	5: gap in the lightcurve
SDSSJ111536.57+054449.7	18.460730	5.601628	346.176550	**dust echo like**
SDSSJ112018.32+193345.8	13.902317	7.711235	171.920453	**dust echo like**
SDSSJ112238.85+143348.4	4.805302	19.970664	82.419412	3: extraneous activity
SDSSJ112446.22+045525.4	24.807607	2.549719	123.793682	long flare
SDSSJ112916.13+513123.5	7.890306	6.872648	34.293054	long flare
SDSSJ113355.94+670107.1	18.300889	6.037712	507.653610	5: gap in the lightcurve
SDSSJ113901.27+613408.7	11.103334	5.650358	70.008886	long flare
SDSSJ114922.03+544151.4	4.504857	5.856587	142.418867	3: extraneous activity
SDSSJ115205.33+485050.0	50.118754	2.486997	442.994482	5: gap in the lightcurve
SDSSJ115326.76+403719.2	16.255859	5.822790	95.590271	**dust echo like**
SDSSJ120057.93+064823.1	8.561520	17.287579	246.516277	3: extraneous activity
SDSSJ120145.97+352522.5	42.640895	1.865613	173.707928	5: gap in the lightcurve
SDSSJ120338.30+585911.9	11.833001	2.732505	72.328231	**dust echo like**
SDSSJ120842.70+330523.1	2.691464	8.594059	10.803171	3: extraneous activity
SDSSJ120942.23+320258.8	23.750284	9.475727	379.246307	4: no prior baseline
SDSSJ121130.31+404743.2	6.307153	5.388289	73.887041	5: gap in the lightcurve
SDSSJ121457.42+101418.2	14.902525	5.708388	51.276918	5: gap in the lightcurve
SDSSJ121825.51+295154.9	41.000503	1.865143	278.278463	**dust echo like**
SDSSJ121907.89+051645.7	15.330164	5.671076	89.094686	**dust echo like**
SDSSJ122823.87+361729.1	20.547117	5.483538	142.763904	**dust echo like**
SDSSJ123852.88+081512.1	6.069469	4.707630	125.426539	5: gap in the lightcurve
SDSSJ124255.37+253728.0	13.175970	4.156801	45.506969	**dust echo like**
SDSSJ124521.42-014735.5	4.776322	5.924130	13.054067	long flare
SDSSJ130355.94+220338.7	7.525088	12.523780	24.659995	3: extraneous activity
SDSSJ130532.91+395337.9	23.287563	3.012912	120.724890	**dust echo like**
SDSSJ130815.58+042909.6	15.568442	4.941736	114.815733	long flare
SDSSJ131022.78+251809.3	11.829497	5.084214	38.121376	long flare
SDSSJ131509.34+072737.7	15.796398	8.519733	110.744750	**dust echo like**
SDSSJ132259.95+330121.9	9.922793	5.485206	38.644442	long flare
SDSSJ132848.46+275227.8	3.899487	20.167541	134.132646	3: extraneous activity
SDSSJ132902.05+234108.4	13.974117	5.057244	163.485784	long flare
SDSSJ133212.63+203638.0	309.273783	0.626732	438.228317	**dust echo like**
SDSSJ133731.36+003529.0	-	-	-	not in parent sample
SDSSJ134032.49+184218.6	3.992887	5.683695	16.722340	3: extraneous activity
SDSSJ134105.98-004902.6	14.053779	5.164794	135.278992	5: gap in the lightcurve

Continued on next page

Table B.1: Reasons for rejection of reference sample objects

Name	$\Delta F/F_{\rm rms}$	$F_{\rm rms}/\sigma_{\rm F}$	$\chi^2_{\rm red}$	Result
SDSSJ134123.21+151650.5	7.636517	6.827178	56.799892	long flare
SDSSJ134849.39+155902.1	26.355265	2.360722	63.378168	long flare
SDSSJ135241.37+000925.8	9.652395	2.819655	20.870745	5: gap in the lightcurve
SDSSJ140221.27+392212.4	101.749204	4.832630	952.400900	**dust echo like**
SDSSJ140648.44+062834.8	6.613004	9.104817	40.956218	3: extraneous activity
SDSSJ140950.27+105740.3	4.571289	9.851900	40.481812	3: extraneous activity
SDSSJ141235.90+411458.6	5.822121	7.487867	29.179248	3: extraneous activity
SDSSJ142254.12+060953.4	13.936775	7.827294	321.202300	**dust echo like**
SDSSJ142420.78+624916.6	3.236530	38.492208	275.307065	3: extraneous activity
SDSSJ142808.89-023124.9	5.854497	6.932831	12.347123	3: extraneous activity
SDSSJ143016.06+230344.5	25.783246	4.861648	369.158601	long flare
SDSSJ144024.32+175852.7	5.403224	4.179069	16.210109	long flare
SDSSJ144227.59+555846.4	183.048216	3.653513	13421.909636	long flare
SDSSJ144758.41+402335.9	15.614246	11.811118	394.460979	**dust echo like**
SDSSJ144829.01+113732.2	4.316780	7.214739	78.442872	3: extraneous activity
SDSSJ150440.38+010735.8	37.343165	4.253255	1456.140895	5: gap in the lightcurve
SDSSJ150844.23+260249.1	5.758626	4.968898	30.026187	long flare
SDSSJ151117.94+221428.2	7.311309	8.573347	91.304618	3: extraneous activity
SDSSJ151257.19+280937.5	5.724501	5.885187	27.818087	long flare
SDSSJ151345.77+311125.1	47.166524	2.948985	244.165767	**dust echo like**
SDSSJ152438.15+531458.6	19.154969	8.903445	127.762977	**dust echo like**
SDSSJ153151.42+372445.8	-	-	0.719872	$\chi^2_{\rm red} < 1$
SDSSJ153310.03+272920.3	8.679626	19.731642	531.791620	3: extraneous activity
SDSSJ153711.31+581420.3	12.550327	16.313233	999.639717	3: extraneous activity
SDSSJ154029.29+005437.3	5.384957	3.442214	5.424775	7: outlier in the lightcurve
SDSSJ154158.64+071836.4	8.508220	4.139101	23.421340	long flare
SDSSJ154843.07+220812.6	659.673932	3.514871	12702.736785	**dust echo like**
SDSSJ154955.20+332751.9	30.868220	5.776725	379.537908	**dust echo like**
SDSSJ155437.26+525526.4	1271.279330	0.143139	657.535016	long flare
SDSSJ155438.40+163637.7	14.749947	6.228978	29.971927	7: outlier in the lightcurve
SDSSJ155440.26+362952.1	16.760530	5.629148	290.076472	5: gap in the lightcurve
SDSSJ155539.96+212005.7	41.948255	2.775905	258.965049	long flare
SDSSJ155640.32+451338.4	18.968964	4.807138	230.319451	5: gap in the lightcurve
SDSSJ155743.53+272753.0	2.588124	5.552205	10.200410	3: extraneous activity
SDSSJ160052.27+461243.0	11.793526	6.265247	75.773865	long flare
SDSSJ161258.17+141617.5	17.550276	5.854813	105.504794	long flare
SDSSJ162034.99+240726.6	61.299406	3.576756	639.213949	**dust echo like**
SDSSJ162810.05+481047.7	6.826520	3.609516	26.329869	long flare
SDSSJ163246.85+441618.6	24.381124	4.926145	419.247326	long flare
SDSSJ164754.38+384341.9	74.538679	3.283795	594.017860	**dust echo like**
SDSSJ165726.81+234528.1	237.869626	4.502757	14781.705683	**dust echo like**
SDSSJ165922.66+204947.5	3.924276	11.771531	34.284158	3: extraneous activity
SDSSJ211529.89-001107.0	6.509595	7.194816	11.941335	3: extraneous activity
SDSSJ214142.91-085702.4	10.083664	5.490241	66.055054	5: gap in the lightcurve
SDSSJ214603.88+104128.7	16.339630	5.191079	39.573875	**dust echo like**
SDSSJ215055.73-010654.2	33.545180	4.658560	175.679014	**dust echo like**
SDSSJ215648.47+004110.7	4.685745	10.900456	16.319207	3: extraneous activity
SDSSJ220349.24+112433.0	17.582776	5.065091	368.421979	long flare

Continued on next page

Table B.1: Reasons for rejection of reference sample objects

Name	$\Delta F/F_{\rm rms}$	$F_{\rm rms}/\sigma_{\rm F}$	$\chi^2_{\rm red}$	Result
SDSSJ221541.61-010721.1	3.371077	6.499031	29.575881	3: extraneous activity
SDSSJ231055.38+222008.6	5.167343	10.500322	22.236243	3: extraneous activity
SDSSJ231222.78+133538.8	5.958648	5.588821	22.233304	long flare
SDSSJ232452.26+154251.1	14.606632	5.909944	46.370852	5: gap in the lightcurve
		WTP TDEs		
WTP14abnpgk	4.971051	6.232620	91.249217	3: extraneous activity
WTP14acnjbu	8.174150	14.032765	236.938983	3: extraneous activity
WTP14adbjsh	59.113039	6.146779	1283.181653	**dust echo like**
WTP14adbwvs	12.525113	3.867966	104.866597	long flare
WTP14adeqka	51.673148	12.767377	5867.342130	**dust echo like**
WTP15abymdq	73.177181	5.642893	2594.497185	**dust echo like**
WTP15acbgpn	39.665225	6.202336	1511.553381	**dust echo like**
WTP15acbuuv	44.479987	5.618758	1666.751397	4: no prior baseline
WTP16aaqrcr	15.088180	6.358838	55.112767	long flare
WTP16aatsnw	3.924276	11.771531	34.284158	3: extraneous activity
WTP17aaldjb	15.568442	4.941736	114.815733	long flare
WTP17aalzpx	10.001899	7.965015	95.018065	long flare
WTP17aamoxe	44.621840	10.767805	915.644330	**dust echo like**
WTP17aamzew	5.220873	9.704360	34.462898	3: extraneous activity
WTP17aanbso	11.833001	2.732505	72.328231	**dust echo like**
WTP18aajkmk	83.110764	6.096719	1775.218803	**dust echo like**
WTP18aamced	14.931887	9.411465	167.557396	**dust echo like**
WTP18aampwj	73.452458	7.503002	1792.968383	**dust echo like**
		ZTF AF		
AT2013kp	78.258921	4.135601	1103.236541	long flare
AT2016eix	8.998844	6.760484	33.569221	long flare
AT2018dyk	14.931887	9.411465	167.557396	**dust echo like**
AT2018ige	12.981374	4.641984	76.570456	**dust echo like**
AT2018iql	30.078050	2.446704	33.652369	**dust echo like**
AT2018jut	1.844687	2.869888	1.779824	2: no coincident excess region
AT2018kox	6.687261	8.802474	19.021367	3: extraneous activity
AT2018lcp	5.924980	5.038824	15.961950	long flare
AT2018lhv	17.236311	3.967455	59.900819	**dust echo like**
AT2018lof	3.212749	9.202141	10.283567	3: extraneous activity
AT2018lzs	3.424038	5.607693	3.797937	3: extraneous activity
AT2019aalc	16.178021	29.512714	2039.271256	3: extraneous activity
AT2019aame	4.145465	7.868080	7.681842	3: extraneous activity
AT2019aamf	6.150682	8.161504	28.706692	3: extraneous activity
AT2019aamg	7.893936	8.338644	12.922134	**dust echo like**
AT2019aamh	-	-	-	not in parent sample
AT2019aami	28.339675	4.180189	92.996992	long flare
AT2019avd	115.478889	3.324406	694.058150	**dust echo like**
AT2019brs	21.896789	6.646403	140.781792	**dust echo like**
AT2019cle	28.265672	4.428900	111.836658	**dust echo like**

Continued on next page

Table B.1: Reasons for rejection of reference sample objects

Name	$\Delta F/F_{\mathrm{rms}}$	$F_{\mathrm{rms}}/\sigma_{\mathrm{F}}$	χ^2_{red}	Result
AT2019cyq	17.336724	4.953578	42.660725	**dust echo like**
AT2019dll	2.699543	6.309565	1.825533	2: no coincident excess region
AT2019dqv	69.361343	6.047845	1469.749062	**dust echo like**
AT2019dsg	74.945459	3.992322	449.400951	**dust echo like**
AT2019dzh	5.708300	7.620262	20.090393	3: extraneous activity
AT2019fdr	-	-	-	not in parent sample
AT2019gur	20.219231	8.223698	78.136849	**dust echo like**
AT2019hbh	9.181261	5.758469	296.091001	**dust echo like**
AT2019hdy	-	-	-	not in parent sample
AT2019idm	36.587385	2.950314	166.409069	**dust echo like**
AT2019ihu	-	-	-	not in parent sample
AT2019ihv	3.485036	16.348000	22.663403	3: extraneous activity
AT2019kqu	6.596225	9.466918	66.630822	3: extraneous activity
AT2019meh	43.997366	5.994053	543.008547	long flare
AT2019msq	10.998912	3.649930	23.684240	5: gap in the lightcurve
AT2019mss	17.014102	5.788265	43.704722	**dust echo like**
AT2019nna	8.644302	8.329182	30.209895	**dust echo like**
AT2019nni	6.253971	8.709367	27.787737	3: extraneous activity
AT2019pev	-	-	-	$\chi^2_{\mathrm{red}} < 1$
AT2019qpt	6.206294	7.391323	43.749811	3: extraneous activity
AT2019thh	82.094303	5.167433	753.972348	**dust echo like**
AT2019wrd	15.061761	4.644523	29.172083	long flare
AT2019xgg	4.882445	6.480683	10.520460	3: extraneous activity
AT2020aezy	1.973578	4.987611	2.407830	1: no excess
AT2020aezz	8.076402	10.318643	73.891077	3: extraneous activity
AT2020afaa	4.546167	3.065439	5.057972	**dust echo like**
AT2020afab	-	-	-	not in parent sample
AT2020afac	9.259604	9.365964	21.928723	3: extraneous activity
AT2020afad	-	-	-	not in parent sample
AT2020afae	8.423922	10.185686	42.966593	3: extraneous activity
AT2020atq	35.855980	6.917691	242.942820	**dust echo like**
AT2020hle	22.608236	6.985780	70.301757	long flare
AT2020iq	38.331778	4.271493	122.568764	**dust echo like**
AT2020mw	-	-	-	not in parent sample
AT2021aetz	33.545180	4.658560	175.679014	**dust echo like**
AT2021aeud	5.584794	4.331697	7.296335	long flare
AT2021aeue	2.398531	10.688374	6.055754	3: extraneous activity
AT2021aeuf	7.269850	5.060153	32.370354	**dust echo like**
AT2021aeug	4.039072	13.195234	68.342928	3: extraneous activity
AT2021aeuh	16.924663	3.375365	89.581822	5: gap in the lightcurve
AT2021aeui	-	-	-	not in parent sample
AT2021aeuj	9.010752	3.961792	47.369657	long flare
AT2021aeuk	-	-	-	not in parent sample

Table B.2: The 39 brightest mid-IR flares in the catalog, sorted by the maximum flux density in W1 $\max(\nu_{W1}F_{\nu_{W1}})$ listed in the first column. The second column shows the bolometric luminosity at peak. The third column is the total emitted bolometric energy, defined as a trapezoidal intergal of L_{bol} in Equation 9.13. The last columns contain the redshift from the literature and references that discuss the respective object. (1) [405] (2) [398] (3) [344] (4) [79] (5) [348] (6) [410]

Host	RA [deg]	Dec [deg]	Peak Time [MJD]	$\max(\nu_{W1}F_{\nu_{W1}})$ [10^{-12} ergs^{-1}cm^{-2}]	$L_{bol,\,peak}$ [10^{43} erg s^{-1}]	E_{bol} [10^{51} erg]	z	Ref.
NGC 1566	65.001750	-54.937810	58324	117.40	1.90	0.56	0.00500	1
NGC 7392	342.953080	-20.608080	57170	72.42	5.29	2.78	0.01060	2, 3
UGC 11487	297.353630	63.509080	57825	17.94	5.75	6.81	0.01900	3
WISEA J161105.71+023400.3	242.773700	2.566750	58351	14.84	41.45	30.22	0.06300	4
WISEA J010320.39+140152.5	15.835000	14.031260	58313	10.81	13.77	9.63	0.04230	
WISEA J034144.49-534221.4	55.435250	-53.705830	57749	9.51	31.86	17.98	0.06660	
WISEA J130916.33-444647.2	197.318040	-44.779780	58406	9.27	3.22	2.50	0.02490	
WISEA J154843.06+220812.6	237.179440	22.136860	59151	9.22	6.43	5.78	0.03130	5
WISEA J210858.16-562831.1	317.242370	-56.475330	58229	7.44	10.03	4.36	0.04310	3
KUG 0143+322	26.676760	32.508030	58774	7.24	6.88	4.69	0.03750	3
MCG -01-07-028 NED02	40.098950	-2.728240	58408	7.00	4.59	3.30	0.02890	3
WISEA J165726.80+234528.1	254.361710	23.757820	57979	6.32	18.40	17.40	0.05910	5
SBS 1102+599A	166.258250	59.684310	57964	6.01	4.60	5.63	0.03370	5, 3
WISEA J082336.76+042302.4	125.903200	4.384020	59152	5.37	3.39	2.25	0.03070	6
J023427.78-045431.0	38.615890	-4.908670	57042	5.30	-	-	-	
WISEA J083812.21-584836.5	129.550750	-58.810220	56646	4.32	8.72	4.18	0.05280	
ESO 156- G 016	57.220000	-55.426360	57749	4.16	4.01	3.36	0.03740	3
WISEA J003908.77-235916.4	9.786580	-23.987940	57281	3.83	11.15	12.44	0.06440	
CGCG 047-028	215.725510	6.164820	57858	3.51	7.87	8.50	0.05640	5
WISEA J074352.55-245057.8	115.968970	-24.849410	57690	3.47	2.48	2.16	0.03240	
WISEA J115405.00-054959.9	178.520860	-5.833350	58634	3.21	20.86	18.51	0.09040	
2MASX J14022128+3922122	210.588630	39.370110	57556	3.20	9.13	2.28	0.06370	5
WISEA J154419.65-064915.3	236.081890	-6.820940	58327	3.15	29.34	12.33	0.11110	
WISEA J034438.85+044346.2	56.161850	4.729520	57419	2.91	23.55	19.52	0.10060	
WISEA J104601.57-361808.4	161.506630	-36.302310	57907	2.88	20.44	7.24	0.09700	
WISEA J113737.65-431947.3	174.406960	-43.329670	58023	2.78	7.43	6.57	0.06140	

Continued on next page

Table B.2: The 39 brightest mid-IR flares in the catalog, sorted by the maximum flux density in W1 max($\nu_{W1}F_{\nu_{W1}}$).The last column contains references that discuss the respective object. All other columns are described above. (1) [405] (2) [398] (3) [344] (4) [79] (5) [348] (6) [410]

Host	RA [deg]	Dec [deg]	Peak Time [MJD]	max($\nu_{W1}F_{\nu_{W1}}$) [10^{-12} ergs^{-1}cm^{-2}]	$L_{\mathrm{bol,\,peak}}$ [10^{43} erg s^{-1}]	E_{bol} [10^{51} erg]	z	Ref.
WISEA J082030.24-050448.5	125.125970	-5.080460	57132	2.73	10.47	3.98	0.07340	
J205002.28+361952.6	312.509520	36.331250	58788	2.59	-	-	-	
2MASX J14024483+0726493	210.686620	7.447200	59595	2.50	9.50	4.75	0.07230	
WISEA J224342.87-165908.5	340.928650	-16.985700	58265	2.47	45.24	12.27	0.14850	
WISEA J100036.44+511653.0	150.151860	51.281370	57960	2.37	24.89	13.81	0.11670	
J070309.40+505944.8	105.789210	50.995760	58552	2.37	28.38	16.28	0.12550	
WISEA J180932.24+044515.8	272.384170	4.754420	57194	2.29	13.67	15.32	0.08290	
WISEA J201133.97-415732.0	302.891580	-41.959060	57306	2.29	3.82	0.92	0.04860	
J020252.75-322516.9	30.719800	-32.421360	57385	2.26	-	-	-	
WISEA J222758.44+181918.5	336.993570	18.322070	59006	2.16	3.81	1.91	0.05060	
WISEA J104330.05+512129.0	160.875250	51.358050	58957	2.14	10.30	5.57	0.08160	
WISEA J215925.29+114306.7	329.855360	11.718480	57901	2.09	23.44	5.46	0.12100	5
J231703.06+261401.2	349.262760	26.233710	58820	2.08	54.71	17.45	0.17860	

Bibliography

Here are the references in citation order.

[1] Victor F. Hess. 'Über Beobachtungen Der Durchdringenden Strahlung Bei Sieben Freiballonfahrten'. In: *Phys. Z.* 13 (1912), pp. 1084–1091 (cited on pages 1, 7).

[2] IceCube Collaboration. 'Evidence for High-Energy Extraterrestrial Neutrinos at the IceCube Detector'. In: *Science* 342.6161 (Nov. 2013), p. 1242856. DOI: 10.1126/science.1242856. (Visited on 05/15/2023) (cited on pages 1, 7, 14, 149).

[3] F. Reines. 'The Neutrino: From Poltergeist to Particle'. In: *Reviews of Modern Physics* 68.2 (Apr. 1996), pp. 317–327. DOI: 10.1103/RevModPhys.68.317. (Visited on 11/09/2024) (cited on page 1).

[4] *Structure et propriétés des noyaux atomiques: rapports et discussions du septième Conseil de physique tenu à Bruxelles du 22 du 29 octobre 1933, sous les auspices de l'Institut international de physique Solvay*. Paris: Gauthier-Villars, 1934 (cited on page 1).

[5] Raymond Davis, Don S. Harmer, and Kenneth C. Hoffman. 'Search for Neutrinos from the Sun'. In: *Physical Review Letters* 20.21 (May 1968), pp. 1205–1209. DOI: 10.1103/PhysRevLett.20.1205. (Visited on 10/30/2024) (cited on pages 7, 13).

[6] LIGO Scientific Collaboration and Virgo Collaboration et al. 'Observation of Gravitational Waves from a Binary Black Hole Merger'. In: *Physical Review Letters* 116.6 (Feb. 2016), p. 061102. DOI: 10.1103/PhysRevLett.116.061102. (Visited on 06/07/2024) (cited on pages 7, 16).

[7] Telescope Array Collaboration. 'An Extremely Energetic Cosmic Ray Observed by a Surface Detector Array'. In: *Science* 382.6673 (Nov. 2023), pp. 903–907. DOI: 10.1126/science.abo5095. (Visited on 10/28/2024) (cited on page 7).

[8] D. J. Bird et al. 'Detection of a Cosmic Ray with Measured Energy Well beyond the Expected Spectral Cutoff Due to Cosmic Microwave Radiation'. In: *The Astrophysical Journal* 441 (Mar. 1995), p. 144. DOI: 10.1086/175344. (Visited on 10/29/2024) (cited on page 7).

[9] Maurizio Spurio. 'Probes of Multimessenger Astrophysics : Charged Cosmic Rays, Neutrinos, γ-Rays and Gravitational Waves / Maurizio Spurio'. In: *Probes of Multimessenger Astrophysics : Charged Cosmic Rays, Neutrinos, γ-Rays and Gravitational Waves*. Second edition. Astronomy and Astrophysics Library. Cham, 2018 (cited on pages 7–12, 14–16).

[10] Particle Data Group et al. 'Review of Particle Physics'. In: *Progress of Theoretical and Experimental Physics* 2022.8 (Aug. 2022), p. 083C01. DOI: 10.1093/ptep/ptac097. (Visited on 06/19/2024) (cited on pages 7, 8, 10, 13, 30, 31).

[11] G. Giacinti, M. Kachelrieß, and D. V. Semikoz. 'Explaining the Spectra of Cosmic Ray Groups above the Knee by Escape from the Galaxy'. In: *Physical Review D* 90.4 (Aug. 2014), p. 041302. DOI: 10.1103/PhysRevD.90.041302. (Visited on 10/28/2024) (cited on page 8).

[12] Carmelo Evoli. *The Cosmic-Ray Energy Spectrum*. Dec. 2020. DOI: 10.5281/zenodo.4396125 (cited on page 8).

[13] Kenneth Greisen. 'End to the Cosmic-Ray Spectrum?' In: *Physical Review Letters* 16.17 (Apr. 1966), pp. 748–750. DOI: 10.1103/PhysRevLett.16.748. (Visited on 10/28/2024) (cited on page 8).

[14] G. T. Zatsepin and V. A. Kuz'min. 'Upper Limit of the Spectrum of Cosmic Rays'. In: *Soviet Journal of Experimental and Theoretical Physics Letters* 4 (Aug. 1966), p. 78. (Visited on 10/28/2024) (cited on page 8).

[15] T. Abu-Zayyad et al. 'The Surface Detector Array of the Telescope Array Experiment'. In: *Nuclear Instruments and Methods in Physics Research Section A: Accelerators, Spectrometers, Detectors and Associated Equipment* 689 (Oct. 2012), pp. 87–97. DOI: 10.1016/j.nima.2012.05.079. (Visited on 11/10/2024) (cited on page 8).

[16] 'The Pierre Auger Cosmic Ray Observatory'. In: *Nuclear Instruments and Methods in Physics Research Section A: Accelerators, Spectrometers, Detectors and Associated Equipment* 798 (Oct. 2015), pp. 172–213. DOI: 10.1016/j.nima.2015.06.058. (Visited on 11/10/2024) (cited on page 8).

[17] Dmitri Ivanov. 'Energy Spectrum Measured by the Telescope Array'. In: *Proceedings of 36th International Cosmic Ray Conference — PoS(ICRC2019)*. Vol. 358. 2019, p. 298. DOI: 10.22323/1.358.0298 (cited on page 8).

[18] The Pierre Auger Collaboration et al. 'Measurement of the Cosmic-Ray Energy Spectrum above 2.5×10^{18}eV Using the Pierre Auger Observatory'. In: *Physical Review D* 102.6 (Sept. 2020), p. 062005. DOI: 10.1103/PhysRevD.102.062005. (Visited on 10/28/2024) (cited on page 8).

[19] E. Fermi. 'Galactic Magnetic Fields and the Origin of Cosmic Radiation.' In: *The Astrophysical Journal* 119 (Jan. 1954), p. 1. DOI: 10.1086/145789. (Visited on 10/28/2024) (cited on page 9).

[20] A. M. Hillas. 'The Origin of Ultra-High-Energy Cosmic Rays'. In: *Annual Review of Astronomy and Astrophysics* 22.Volume 22, 1984 (Sept. 1984), pp. 425–444. DOI: 10.1146/annurev.aa.22.090184.002233. (Visited on 10/28/2024) (cited on page 9).

[21] Rafael Alves Batista et al. 'Open Questions in Cosmic-Ray Research at Ultrahigh Energies'. In: *Frontiers in Astronomy and Space Sciences* 6 (June 2019). DOI: 10.3389/fspas.2019.00023. (Visited on 10/28/2024) (cited on page 9).

[22] THE PIERRE AUGER COLLABORATION et al. 'Observation of a Large-Scale Anisotropy in the Arrival Directions of Cosmic Rays above 8×10^{18} eV'. In: *Science* 357.6357 (Sept. 2017), pp. 1266–1270. DOI: 10.1126/science.aan4338. (Visited on 10/29/2024) (cited on page 10).

[23] Adila Abdul Halim et al. 'An Update on the Arrival Direction Studies Made with Data from the Pierre Auger Observatory'. In: *Proceedings of 38th International Cosmic Ray Conference — PoS(ICRC2023)*. Vol. 444. 2023, p. 252. DOI: 10.22323/1.444.0252 (cited on page 10).

[24] R. U. Abbasi et al. 'Indications of Intermediate-Scale Anisotropy of Cosmic Rays with Energy Greater than 57 EeV in the Northern Sky Measured with the Surface Detector of the Telescope Array Experiment'. In: *The Astrophysical Journal Letters* 790.2 (July 2014), p. L21. DOI: 10.1088/2041-8205/790/2/L21. (Visited on 10/29/2024) (cited on page 10).

[25] Jihyun Kim et al. 'Anisotropies in the Arrival Direction Distribution of Ultra-High Energy Cosmic Rays Measured by the Telescope Array Surface Detector'. In: *Proceedings of 38th International Cosmic Ray Conference — PoS(ICRC2023)*. Vol. 444. 2023, p. 244. DOI: 10.22323/1.444.0244 (cited on page 10).

[26] J. Abraham et al. 'Correlation of the Highest-Energy Cosmic Rays with Nearby Extragalactic Objects'. In: *Science* 318.5852 (Nov. 2007), pp. 938–943. DOI: 10.1126/science.1151124. (Visited on 10/29/2024) (cited on page 10).

[27] P. Abreu et al. 'Arrival Directions of Cosmic Rays above 32 EeV from Phase One of the Pierre Auger Observatory'. In: *The Astrophysical Journal* 935.2 (Aug. 2022), p. 170. DOI: 10.3847/1538-4357/ac7d4e. (Visited on 10/29/2024) (cited on page 10).

[28] Igor Tkachev et al. 'Telescope Array Anisotropy Summary'. In: *Proceedings of 37th International Cosmic Ray Conference — PoS(ICRC2021)*. Vol. 395. 2021, p. 392. DOI: 10.22323/1.395.0392 (cited on page 10).

[29] Hale Bradt. *Astrophysics Processes: The Physics of Astronomical Phenomena*. 1st ed. Cambridge: Cambridge University Press, 2008 (cited on pages 11, 124).

[30] Andrii Neronov. 'Introduction to Multi-Messenger Astronomy'. In: *Journal of Physics: Conference Series* 1263.1 (June 2019), p. 012001. DOI: 10.1088/1742-6596/1263/1/012001. (Visited on 11/01/2024) (cited on pages 11, 12).

[31] H.E.S.S. Collaboration et al. 'Time-Resolved Hadronic Particle Acceleration in the Recurrent Nova RS Ophiuchi'. In: *Science* 376.6588 (Apr. 2022), pp. 77–80. DOI: 10.1126/science.abn0567. (Visited on 11/01/2024) (cited on page 11).

[32] M. Ackermann et al. 'Fermi-LAT Observations of the Diffuse Gamma-Ray Emission: Implications for Cosmic Rays and the Interstellar Medium'. In: *The Astrophysical Journal* 750.1 (Apr. 2012), p. 3. DOI: 10.1088/0004-637X/750/1/3. (Visited on 11/01/2024) (cited on page 12).

[33] M. Ackermann et al. 'The Spectrum of Isotropic Diffuse Gamma-Ray Emission Between 100 MeV and 820 GeV'. In: *The Astrophysical Journal* 799.1 (Jan. 2015), p. 86. DOI: 10.1088/0004-637X/799/1/86. (Visited on 11/01/2024) (cited on page 12).

[34] H Karttunen et al. *Fundamental Astronomy*. Fifth Edition. Berlin/Heidelberg: Springer Berlin / Heidelberg, 2007 (cited on pages 12, 22, 23).

[35] A. Kramida et al. *NIST Atomic Spectra Database (Ver. 5.11)*. https://physics.nist.gov/asd. 2023. (Visited on 11/01/2024) (cited on pages 12, 81).

[36] Christian Spiering. 'Towards High-Energy Neutrino Astronomy'. In: *The European Physical Journal H* 37.3 (Aug. 2012), pp. 515–565. DOI: 10.1140/epjh/e2012-30014-2. (Visited on 10/30/2024) (cited on pages 13, 14).

[37] Joseph A. Formaggio, André Luiz C. de Gouvêa, and R. G. Hamish Robertson. 'Direct Measurements of Neutrino Mass'. In: *Physics Reports*. Direct Measurements of Neutrino Mass 914 (June 2021), pp. 1–54. DOI: 10.1016/j.physrep.2021.02.002. (Visited on 11/10/2024) (cited on page 13).

[38] M. Aker et al. 'Direct Neutrino-Mass Measurement with Sub-Electronvolt Sensitivity'. In: *Nature Physics* 18.2 (Feb. 2022), pp. 160–166. DOI: 10.1038/s41567-021-01463-1. (Visited on 11/01/2024) (cited on page 13).

[39] Anna M. Suliga. 'Diffuse Supernova Neutrino Background'. In: *Handbook of Nuclear Physics*. Ed. by Isao Tanihata, Hiroshi Toki, and Toshitaka Kajino. Singapore: Springer Nature, 2023, pp. 3789–3806. DOI: 10.1007/978-981-19-6345-2_129. (Visited on 10/30/2024) (cited on page 13).

[40] C. L. Cowan et al. 'Detection of the Free Neutrino: A Confirmation'. In: *Science* 124.3212 (1956), pp. 103–104. (Visited on 10/30/2024) (cited on page 13).

[41] G. Bellini et al. 'Observation of Geo-Neutrinos'. In: *Physics Letters B* 687.4 (Apr. 2010), pp. 299–304. DOI: 10.1016/j.physletb.2010.03.051. (Visited on 10/30/2024) (cited on page 13).

[42] J. A. Aguilar et al. *The Next-Generation Radio Neutrino Observatory – Multi-Messenger Neutrino Astrophysics at Extreme Energies*. Sept. 2019. DOI: 10.48550/arXiv.1907.12526. (Visited on 11/02/2024) (cited on page 14).

[43] M. G. Aartsen et al. 'A Combined Maximum-likelihood Analysis of the High-energy Astrophysical Neutrino Flux Measured with IceCube'. In: *The Astrophysical Journal* 809 (Aug. 2015), p. 98. DOI: 10.1088/0004-637X/809/1/98. (Visited on 02/08/2023) (cited on pages 14, 15, 102, 110).

[44] Richard Naab et al. 'Measurement of the Astrophysical Diffuse Neutrino Flux in a Combined Fit of IceCube's High Energy Neutrino Data'. In: *Proceedings of 38th International Cosmic Ray Conference — PoS(ICRC2023)*. Vol. 444. SISSA Medialab, Aug. 2023, p. 1064. DOI: 10.22323/1.444.1064. (Visited on 01/05/2024) (cited on pages 14, 15).

[45] R. Abbasi et al. 'Improved Characterization of the Astrophysical Muon–Neutrino Flux with 9.5 Years of IceCube Data'. In: *The Astrophysical Journal* 928.1 (Mar. 2022), p. 50. DOI: 10.3847/1538-4357/ac4d29. (Visited on 03/25/2024) (cited on pages 14, 15).

[46] R. Abbasi et al. 'Detection of Astrophysical Tau Neutrino Candidates in IceCube'. In: *The European Physical Journal C* 82.11 (Nov. 2022), p. 1031. DOI: 10.1140/epjc/s10052-022-10795-y. (Visited on 10/03/2024) (cited on pages 15, 37).

[47] IceCube Collaboration et al. 'Multimessenger Observations of a Flaring Blazar Coincident with High-Energy Neutrino IceCube-170922A'. In: *Science* 361.6398 (July 2018), eaat1378. DOI: 10.1126/science.aat1378. (Visited on 05/15/2023) (cited on pages 15, 17, 18, 72, 99).

[48] IceCube Collaboration et al. 'Evidence for Neutrino Emission from the Nearby Active Galaxy NGC 1068'. In: *Science* 378.6619 (Nov. 2022), pp. 538–543. DOI: 10.1126/science.abg3395. (Visited on 01/19/2023) (cited on pages 15, 17, 19, 36, 104).

[49] IceCube Collaboration et al. 'Observation of High-Energy Neutrinos from the Galactic Plane'. In: *Science* (June 2023). DOI: 10.1126/science.adc9818. (Visited on 01/05/2024) (cited on pages 15, 17, 37).

[50] R. Abbasi et al. 'Search for Neutrino Emission from Cores of Active Galactic Nuclei'. In: *Physical Review D* 106 (July 2022), p. 022005. DOI: 10.1103/PhysRevD.106.022005. (Visited on 01/13/2023) (cited on pages 15, 17, 19).

[51] R. A. Hulse and J. H. Taylor. 'Discovery of a Pulsar in a Binary System.' In: *The Astrophysical Journal* 195 (Jan. 1975), pp. L51–L53. DOI: 10.1086/181708. (Visited on 04/08/2025) (cited on page 15).

[52] J. H. Taylor and J. M. Weisberg. 'A New Test of General Relativity - Gravitational Radiation and the Binary Pulsar PSR 1913+16'. In: *The Astrophysical Journal* 253 (Feb. 1982), pp. 908–920. DOI: 10.1086/159690. (Visited on 04/08/2025) (cited on page 15).

[53] B. P. Abbott et al. 'Multi-Messenger Observations of a Binary Neutron Star Merger'. In: *The Astrophysical Journal Letters* 848.2 (Oct. 2017), p. L12. DOI: 10.3847/2041-8213/aa91c9 (cited on pages 16, 26).

[54] Gabriella Agazie et al. 'The NANOGrav 15 Yr Data Set: Evidence for a Gravitational-wave Background'. In: *The Astrophysical Journal Letters* 951.1 (June 2023), p. L8. DOI: 10.3847/2041-8213/acdac6. (Visited on 10/24/2024) (cited on page 16).

[55] John Magorrian et al. 'The Demography of Massive Dark Objects in GalaxyCenters'. In: *The Astronomical Journal* 115.6 (June 1998), p. 2285. DOI: 10.1086/300353. (Visited on 05/02/2024) (cited on page 17).

[56] D. Lynden-Bell. 'Galactic Nuclei as Collapsed Old Quasars'. In: *Nature* 223.5207 (Aug. 1969), pp. 690–694. DOI: 10.1038/223690a0. (Visited on 04/24/2024) (cited on pages 17, 89).

[57] Martin J. Rees. 'Black Hole Models for Active Galactic Nuclei'. In: *Annual Review of Astronomy and Astrophysics* 22.Volume 22, 1984 (Sept. 1984), pp. 471–506. DOI: 10.1146/annurev.aa.22.090184.002351. (Visited on 04/24/2024) (cited on pages 17, 89).

[58] C. Megan Urry and Paolo Padovani. 'Unified Schemes for Radio-Loud Active Galactic Nuclei'. In: *Publications of the Astronomical Society of the Pacific* 107.715 (Sept. 1995), p. 803. DOI: 10.1086/133630. (Visited on 10/20/2024) (cited on page 17).

[59] Marie-Helene Ulrich, Laura Maraschi, and C. Megan Urry. 'Variability of Active Galactic Nuclei'. In: *Annual Review of Astronomy and Astrophysics* 35.Volume 35, 1997 (Sept. 1997), pp. 445–502. DOI: 10.1146/annurev.astro.35.1.445. (Visited on 04/29/2024) (cited on pages 18, 19, 129).

[60] Volker Beckmann. 'Active Galactic Nuclei'. In: *Active Galactic Nuclei*. Weinheim : Chichester: Wiley-VCH ; John Wiley [distributor], 2012 (cited on page 18).

[61] K. Mannheim. 'The Proton Blazar.' In: *Astronomy and Astrophysics* 269 (Mar. 1993), pp. 67–76. DOI: 10.48550/arXiv.astro-ph/9302006. (Visited on 10/22/2024) (cited on page 18).

[62] Karl Mannheim. 'High-Energy Neutrinos from Extragalactic Jets'. In: *Astroparticle Physics* 3.3 (May 1995), pp. 295–302. DOI: 10.1016/0927-6505(94)00044-4. (Visited on 10/22/2024) (cited on page 18).

[63] IceCube Collaboration et al. 'Neutrino Emission from the Direction of the Blazar TXS 0506+056 Prior to the IceCube-170922A Alert'. In: *Science* 361.6398 (July 2018), pp. 147–151. DOI: 10.1126/science.aat2890. (Visited on 06/19/2023) (cited on page 19).

[64] Francis Halzen et al. 'On the Neutrino Flares from the Direction of TXS 0506+056'. In: *The Astrophysical Journal Letters* 874.1 (Mar. 2019), p. L9. DOI: 10.3847/2041-8213/ab0d27. (Visited on 10/23/2024) (cited on pages 19, 27).

[65] Xavier Rodrigues et al. 'Multiwavelength and Neutrino Emission from Blazar PKS 1502 + 106'. In: *The Astrophysical Journal* 912.1 (May 2021), p. 54. DOI: 10.3847/1538-4357/abe87b. (Visited on 10/22/2024) (cited on pages 19, 72).

[66] Kenji Yoshida et al. 'Flare Duty Cycle of Gamma-Ray Blazars and Implications for High-energy Neutrino Emission'. In: *The Astrophysical Journal* 954.2 (Sept. 2023), p. 194. DOI: 10.3847/1538-4357/acea74. (Visited on 10/20/2024) (cited on page 19).

[67] M. G. Aartsen et al. 'The Contribution of Fermi-2LAC Blazars to Diffuse TeV–PeV Neutrino Flux'. In: *The Astrophysical Journal* 835.1 (Jan. 2017), p. 45. DOI: 10.3847/1538-4357/835/1/45. (Visited on 04/24/2023) (cited on pages 19, 44).

[68] Sara Buson et al. 'Beginning a Journey Across the Universe: The Discovery of Extragalactic Neutrino Factories'. In: *Astrophys. J. Lett.* 933.2 (2022), p. L43. DOI: 10.3847/2041-8213/ac7d5b (cited on page 19).

[69] Chiara Bellenghi et al. 'Correlating High-energy IceCube Neutrinos with 5BZCAT Blazars and RFC Sources'. In: *The Astrophysical Journal Letters* 955.2 (Sept. 2023), p. L32. DOI: 10.3847/2041-8213/acf711. (Visited on 10/22/2024) (cited on page 19).

[70] F. W. Stecker et al. 'High-Energy Neutrinos from Active Galactic Nuclei'. In: *Phys. Rev. Lett.* 66.21 (May 1991), pp. 2697–2700. DOI: 10.1103/PhysRevLett.66.2697 (cited on page 19).

[71] Kohta Murase and Floyd W. Stecker. 'High-Energy Neutrinos from Active Galactic Nuclei'. In: *The Encyclopedia of Cosmology*. World Scientific Series in Astrophysics. WORLD SCIENTIFIC, July 2023, pp. 483–540. DOI: 10.1142/9789811282645_0010. (Visited on 10/21/2024) (cited on page 19).

[72] R. Abbasi et al. *Search for Neutrino Emission from Hard X-ray AGN with IceCube*. June 2024. DOI: 10.48550/arXiv.2406.06684. (Visited on 10/20/2024) (cited on page 19).

[73] R. Abbasi et al. *IceCube Search for Neutrino Emission from X-ray Bright Seyfert Galaxies*. June 2024. DOI: 10.48550/arXiv.2406.07601. (Visited on 10/20/2024) (cited on page 19).

[74] Glennys R. Farrar and Andrei Gruzinov. 'Giant AGN Flares and Cosmic Ray Bursts'. In: *The Astrophysical Journal* 693.1 (Mar. 2009), p. 329. DOI: 10.1088/0004-637X/693/1/329. (Visited on 05/02/2024) (cited on pages 19, 21).

[75] W. Bednarek and R. J. Protheroe. 'Gamma-Ray and Neutrino Flares Produced by Protons Accelerated on an Accretion Disc Surface in Active Galactic Nuclei'. In: *Monthly Notices of the Royal Astronomical Society* 302.2 (Jan. 1999), pp. 373–380. DOI: 10.1046/j.1365-8711.1999.02132.x. (Visited on 10/21/2024) (cited on page 19).

[76] Daniel E. Vanden Berk et al. 'The Ensemble Photometric Variability of ~25,000 Quasars in the Sloan Digital Sky Survey'. In: *The Astrophysical Journal* 601.2 (Feb. 2004), p. 692. DOI: 10.1086/380563. (Visited on 05/02/2024) (cited on page 19).

[77] Claudio Ricci and Benny Trakhtenbrot. 'Changing-Look Active Galactic Nuclei'. In: *Nature Astronomy* 7.11 (Nov. 2023), pp. 1282–1294. DOI: 10.1038/s41550-023-02108-4. (Visited on 05/02/2024) (cited on page 20).

[78] Zhenfeng Sheng et al. 'Mid-Infrared Variability of Changing-look AGNs'. In: *The Astrophysical Journal Letters* 846.1 (Aug. 2017), p. L7. DOI: 10.3847/2041-8213/aa85de. (Visited on 10/21/2024) (cited on page 20).

[79] Benny Trakhtenbrot et al. 'A New Class of Flares from Accreting Supermassive Black Holes'. In: *Nature Astronomy* 3.3 (Mar. 2019), pp. 242–250. DOI: 10.1038/s41550-018-0661-3. (Visited on 03/12/2024) (cited on pages 20, 129, 134, 171, 172).

[80] Sjoert van Velzen et al. 'Establishing Accretion Flares from Supermassive Black Holes as a Source of High-Energy Neutrinos'. In: *Monthly Notices of the Royal Astronomical Society* 529.3 (Apr. 2024), pp. 2559–2576. DOI: 10.1093/mnras/stae610. (Visited on 03/21/2024) (cited on pages 20, 22, 93–96, 100, 102, 103, 107, 110, 120, 135–137, 144).

[81] J. G. Hills. 'Possible Power Source of Seyfert Galaxies and QSOs'. In: *Nature* 254.5498 (Mar. 1975), pp. 295–298. DOI: 10.1038/254295a0. (Visited on 04/25/2024) (cited on pages 20, 137).

[82] Martin J. Rees. 'Tidal Disruption of Stars by Black Holes of 106–108 Solar Masses in Nearby Galaxies'. In: *Nature* 333.6173 (June 1988), pp. 523–528. DOI: 10.1038/333523a0. (Visited on 01/05/2024) (cited on page 20).

[83] Suvi Gezari. 'Tidal Disruption Events'. In: *Annual Review of Astronomy and Astrophysics* 59 (Sept. 2021), pp. 21–58. DOI: 10.1146/annurev-astro-111720-030029. (Visited on 02/21/2024) (cited on pages 20, 21, 128).

[84] Stefanie Komossa and Norbert Bade. 'The Giant X-ray Outbursts in NGC 5905 and IC 3599: Follow-up Observations and Outburst Scenarios'. In: *Astronomy & Astrophysics* 343 (Mar. 1999), p. 775. DOI: 10.48550/arXiv.astro-ph/9901141. (Visited on 10/14/2024) (cited on page 20).

[85] Sjoert van Velzen et al. 'Optical-Ultraviolet Tidal Disruption Events'. In: *Space Science Reviews* 216.8 (Oct. 2020), p. 124. DOI: 10.1007/s11214-020-00753-z. (Visited on 11/10/2024) (cited on page 20).

[86] Kimitake Hayasaki. 'Neutrinos from Tidal Disruption Events'. In: *Nature Astronomy* 5.5 (2021), pp. 436–437. DOI: 10.1038/s41550-021-01309-z (cited on page 21).

[87] Joshua S. Bloom et al. 'A Possible Relativistic Jetted Outburst from a Massive Black Hole Fed by a Tidally Disrupted Star'. In: *Science* 333.6039 (July 2011), pp. 203–206. DOI: 10.1126/science.1207150. (Visited on 10/14/2024) (cited on page 20).

[88] Kate D. Alexander et al. 'Radio Properties of Tidal Disruption Events'. In: *Space Science Reviews* 216.5 (June 2020), p. 81. DOI: 10.1007/s11214-020-00702-w. (Visited on 11/10/2024) (cited on page 21).

[89] Lixin Dai et al. 'A Unified Model for Tidal Disruption Events'. In: *The Astrophysical Journal Letters* 859.2 (May 2018), p. L20. DOI: 10.3847/2041-8213/aab429. (Visited on 09/07/2024) (cited on page 21).

[90] Elad Steinberg and Nicholas C. Stone. 'Stream–Disk Shocks as the Origins of Peak Light in Tidal Disruption Events'. In: *Nature* 625.7995 (Jan. 2024), pp. 463–467. DOI: 10.1038/s41586-023-06875-y. (Visited on 09/07/2024) (cited on page 21).

[91] Daniel Biehl et al. 'Tidally Disrupted Stars as a Possible Origin of Both Cosmic Rays and Neutrinos at the Highest Energies'. In: *Scientific Reports* 8.1 (July 2018), p. 10828. DOI: 10.1038/s41598-018-29022-4. (Visited on 10/14/2024) (cited on page 21).

[92] R. Stein. 'Search for High-Energy Neutrinos from Populations of Optical Transients'. In: *36th International Cosmic Ray Conference (ICRC2019)*. Vol. 36. International Cosmic Ray Conference. July 2019, p. 1016. DOI: 10.22323/1.358.1016 (cited on pages 21, 22, 102, 110).

[93] Kohta Murase et al. 'High-Energy Neutrino and Gamma-Ray Emission from Tidal Disruption Events'. In: *The Astrophysical Journal* 902.2 (Oct. 2020), p. 108. DOI: 10.3847/1538-4357/abb3c0. (Visited on 10/01/2024) (cited on pages 21, 84).

[94] Kimitake Hayasaki and Ryo Yamazaki. 'Neutrino Emissions from Tidal Disruption Remnants'. In: *The Astrophysical Journal* 886.2 (Nov. 2019), p. 114. DOI: 10.3847/1538-4357/ab44ca. (Visited on 10/25/2024) (cited on page 21).

[95] Massimo Turatto. 'Classification of Supernovae'. In: *Supernovae and Gamma-Ray Bursters*. Lecture Notes in Physics. Berlin, Heidelberg: Springer Berlin Heidelberg, 2003, pp. 21–36 (cited on pages 22, 23).

[96] Daniel A. Perley et al. 'The Zwicky Transient Facility Bright Transient Survey. II. A Public Statistical Sample for Exploring Supernova Demographics*'. In: *The Astrophysical Journal* 904.1 (Nov. 2020), p. 35. DOI: 10.3847/1538-4357/abbd98. (Visited on 05/22/2023) (cited on page 22).

[97] S. Chandrasekhar. 'The Maximum Mass of Ideal White Dwarfs'. In: *Astrophysical Journal* (1931) (cited on page 22).

[98] Weidong Li, Jesse Leaman, et al. 'Nearby Supernova Rates from the Lick Observatory Supernova Search – II. The Observed Luminosity Functions and Fractions of Supernovae in a Complete Sample'. In: *Monthly Notices of the Royal Astronomical Society* 412.3 (Apr. 2011), pp. 1441–1472. DOI: 10.1111/j.1365-2966.2011.18160.x (cited on page 22).

[99] S. E. Woosley, A. Heger, and T. A. Weaver. 'The Evolution and Explosion of Massive Stars'. In: 74.4 (Nov. 2002), pp. 1015–1071. DOI: 10.1103/RevModPhys.74.1015 (cited on page 23).

[100] R. M. Bionta et al. 'Observation of a Neutrino Burst in Coincidence with Supernova 1987A in the Large Magellanic Cloud'. In: *Phys. Rev. Lett.* 58.14 (Apr. 1987), pp. 1494–1496. DOI: 10.1103/PhysRevLett.58.1494 (cited on page 23).

[101] K. Hirata et al. 'Observation of a Neutrino Burst from the Supernova SN1987A'. In: *Phys. Rev. Lett.* 58.14 (Apr. 1987), pp. 1490–1493. DOI: 10.1103/PhysRevLett.58.1490 (cited on page 23).

[102] Takashi J. Moriya, Elena I. Sorokina, and Roger A. Chevalier. 'Superluminous Supernovae'. In: *Space Science Reviews* 214.2 (Mar. 2018), p. 59. DOI: 10.1007/s11214-018-0493-6. (Visited on 10/26/2024) (cited on page 24).

[103] M. R. Drout et al. 'Rapidly Evolving and Luminous Transients from Pan-STARRS1'. In: *The Astrophysical Journal* 794.1 (Sept. 2014), p. 23. DOI: 10.1088/0004-637X/794/1/23. (Visited on 10/26/2024) (cited on page 24).

[104] Anna Y. Q. Ho et al. 'A Search for Extragalactic Fast Blue Optical Transients in ZTF and the Rate of AT2018cow-like Transients'. In: *The Astrophysical Journal* 949.2 (June 2023), p. 120. DOI: 10.3847/1538-4357/acc533. (Visited on 10/26/2024) (cited on page 24).

[105] Kohta Murase et al. 'New Class of High-Energy Transients from Crashes of Supernova Ejecta with Massive Circumstellar Material Shells'. In: *Phys. Rev. D* 84 (2011), p. 043003. DOI: 10.1103/PhysRevD.84.043003 (cited on page 24).

[106] V. N. Zirakashvili and V. S. Ptuskin. 'Type IIn Supernovae as Sources of High Energy Astrophysical Neutrinos'. In: *Astroparticle Physics* 78 (May 2016), pp. 28–34. DOI: 10.1016/j.astropartphys.2016.02.004. (Visited on 10/17/2024) (cited on pages 24, 70).

[107] Rachel J. Bruch et al. 'The Prevalence and Influence of Circumstellar Material around Hydrogen-rich Supernova Progenitors'. In: *The Astrophysical Journal* 952 (Aug. 2023), p. 119. DOI: 10.3847/1538-4357/acd8be. (Visited on 07/31/2023) (cited on page 25).

[108] R. Abbasi et al. 'Constraining High-energy Neutrino Emission from Supernovae with IceCube'. In: *The Astrophysical Journal Letters* 949.1 (May 2023), p. L12. DOI: 10.3847/2041-8213/acd2c9. (Visited on 06/13/2023) (cited on pages 25, 26).

[109] Tetyana Pitik et al. 'Optically Informed Searches of High-Energy Neutrinos from Interaction-Powered Supernovae'. In: *Monthly Notices of the Royal Astronomical Society* 524.3 (Sept. 2023), pp. 3366–3384. DOI: 10.1093/mnras/stad2025. (Visited on 10/17/2024) (cited on page 25).

[110] Nicholas Senno, Kohta Murase, and Peter Mészáros. 'Choked Jets and Low-Luminosity Gamma-Ray Bursts as Hidden Neutrino Sources'. In: *Phys. Rev. D* 93.8 (Apr. 2016), p. 083003. DOI: 10.1103/PhysRevD.93.083003 (cited on pages 25, 26).

[111] T. J. Galama et al. 'An Unusual Supernova in the Error Box of the γ-Ray Burst of 25 April 1998'. In: *Nature* 395.6703 (Oct. 1998), pp. 670–672. DOI: 10.1038/27150. (Visited on 10/18/2024) (cited on page 25).

[112] S. E. Woosley and J. S. Bloom. 'The Supernova Gamma-Ray Burst Connection'. In: *Ann. Rev. Astron. Astrophys.* 44 (2006), pp. 507–556. DOI: 10.1146/annurev.astro.43.072103.150558 (cited on pages 25, 26).

[113] Eli Waxman and John Bahcall. 'High Energy Neutrinos from Cosmological Gamma-Ray Burst Fireballs'. In: *Physical Review Letters* 78.12 (Mar. 1997), pp. 2292–2295. DOI: 10.1103/PhysRevLett.78.2292. (Visited on 10/18/2024) (cited on pages 25, 27).

[114] R. Abbasi et al. 'Searches for Neutrinos from Gamma-Ray Bursts Using the IceCube Neutrino Observatory'. In: *The Astrophysical Journal* 939.2 (Nov. 2022), p. 116. DOI: 10.3847/1538-4357/ac9785. (Visited on 10/18/2024) (cited on pages 25, 27).

[115] R. Abbasi et al. 'Search for 10–1000 GeV Neutrinos from Gamma-Ray Bursts with IceCube'. In: *The Astrophysical Journal* 964.2 (Mar. 2024), p. 126. DOI: 10.3847/1538-4357/ad220b. (Visited on 10/18/2024) (cited on pages 25, 27).

[116] 'Gamma-Ray Burst Afterglows'. In: *Gamma-Ray Bursts: The Brightest Explosions in the Universe*. Ed. by Gilbert Vedrenne and Jean-Luc Atteia. Berlin, Heidelberg: Springer, 2009, pp. 259–329. DOI: 10.1007/978-3-540-39088-6_6. (Visited on 11/10/2024) (cited on page 25).

[117] Eric Burns et al. 'GRB 221009A: The BOAT'. In: *The Astrophysical Journal Letters* 946.1 (Mar. 2023), p. L31. DOI: 10.3847/2041-8213/acc39c. (Visited on 10/18/2024) (cited on page 25).

[118] R. Abbasi et al. 'Limits on Neutrino Emission from GRB 221009A from MeV to PeV Using the IceCube Neutrino Observatory'. In: *The Astrophysical Journal Letters* 946.1 (Mar. 2023), p. L26. DOI: 10.3847/2041-8213/acc077. (Visited on 10/18/2024) (cited on page 25).

[119] Peter Mészáros and Eli Waxman. 'TeV Neutrinos from Successful and Choked Gamma-Ray Bursts'. In: *Phys. Rev. Lett.* 87.17 (Oct. 2001), p. 171102. DOI: 10.1103/PhysRevLett.87.171102 (cited on page 26).

[120] Stephen J. Smartt. 'Progenitors of Core-Collapse Supernovae'. In: *Annual Review of Astronomy and Astrophysics* 47.1 (Sept. 2009), pp. 63–106. DOI: 10.1146/annurev-astro-082708-101737 (cited on page 26).

[121] Nicholas Senno, Kohta Murase, and Peter Mészáros. 'Constraining High-Energy Neutrino Emission from Choked Jets in Stripped-Envelope Supernovae'. In: *Journal of Cosmology and Astroparticle Physics* 2018.1 (Jan. 2018), p. 025. DOI: 10.1088/1475-7516/2018/01/025. (Visited on 04/05/2023) (cited on page 26).

[122] Po-Wen Chang et al. 'High-Energy Neutrinos from Choked-Jet Supernovae: Searches and Implications'. In: *Physical Review D* 109.10 (May 2024), p. 103041. DOI: 10.1103/PhysRevD.109.103041. (Visited on 10/17/2024) (cited on page 26).

[123] Simeon Reusch et al. 'IceCube-231004A: One Candidate Counterpart from the Zwicky Transient Facility'. In: *GRB Coordinates Network* 34810 (Oct. 2023), p. 1 (cited on pages 26, 81).

[124] Robert Stein et al. 'IC231004A: Classification of AT2023uqf/ZTF23abidzvf as a Rapidly-Evolving Supernova with CSM Interaction'. In: *GRB Coordinates Network* 34837 (Oct. 2023), p. 1 (cited on pages 26, 82).

[125] P. S. Cowperthwaite et al. 'The Electromagnetic Counterpart of the Binary Neutron Star Merger LIGO/Virgo GW170817. II. UV, Optical, and Near-infrared Light Curves and Comparison to Kilonova Models'. In: *The Astrophysical Journal Letters* 848.2 (Oct. 2017), p. L17. DOI: 10.3847/2041-8213/aa8fc7. (Visited on 10/23/2024) (cited on page 26).

[126] Danielle Frostig et al. 'An Infrared Search for Kilonovae with the WINTER Telescope. I. Binary Neutron Star Mergers'. In: *The Astrophysical Journal* 926.2 (Feb. 2022), p. 152. DOI: 10.3847/1538-4357/ac4508. (Visited on 10/23/2024) (cited on page 26).

[127] Will Sutherland et al. 'The Visible and Infrared Survey Telescope for Astronomy (VISTA): Design, Technical Overview, and Performance'. In: *Astronomy & Astrophysics* 575 (Mar. 2015), A25. DOI: 10.1051/0004-6361/201424973. (Visited on 10/23/2024) (cited on page 26).

[128] David Eichler et al. 'Nucleosynthesis, Neutrino Bursts and γ-Rays from Coalescing Neutron Stars'. In: *Nature* 340.6229 (July 1989), pp. 126–128. DOI: 10.1038/340126a0. (Visited on 10/23/2024) (cited on page 26).

[129] A. Albert et al. 'Search for High-energy Neutrinos from Binary Neutron Star Merger GW170817 with ANTARES, IceCube, and the Pierre Auger Observatory'. In: *The Astrophysical Journal Letters* 850.2 (Nov. 2017), p. L35. DOI: 10.3847/2041-8213/aa9aed. (Visited on 10/22/2024) (cited on page 27).

[130] Zi-Hang Zhou and Kai Wang. 'High-Energy Neutrino Emission Associated with GWs from Binary Black Hole Mergers in AGN Accretion Disks'. In: *The Astrophysical Journal Letters* 958.1 (Nov. 2023), p. L12. DOI: 10.3847/2041-8213/ad096f. (Visited on 10/24/2024) (cited on page 27).

[131] Zhi-Peng Ma and Kai Wang. 'High-Energy Neutrinos from Outflows Powered by the Kicked Remnants of Binary Black Hole Mergers in Active Galactic Nucleus Accretion Disks'. In: *The Astrophysical Journal* 970 (Aug. 2024), p. 127. DOI: 10.3847/1538-4357/ad5678. (Visited on 10/24/2024) (cited on page 27).

[132] Matthew J. Graham et al. 'A Light in the Dark: Searching for Electromagnetic Counterparts to Black Hole–Black Hole Mergers in LIGO/Virgo O3 with the Zwicky Transient Facility'. In: *The Astrophysical Journal* 942.2 (Jan. 2023), p. 99. DOI: 10.3847/1538-4357/aca480. (Visited on 10/22/2024) (cited on page 27).

[133] R. Abbasi et al. 'IceCube Search for Neutrinos Coincident with Gravitational Wave Events from LIGO/Virgo Run O3'. In: *The Astrophysical Journal* 944.1 (Feb. 2023), p. 80. DOI: 10.3847/1538-4357/aca5fc. (Visited on 10/23/2024) (cited on page 27).

[134] Jessie Thwaites et al. 'Searches for IceCube Neutrinos Coincident with Gravitational Wave Events'. In: *Proceedings of 38th International Cosmic Ray Conference — PoS(ICRC2023)*. Vol. 444. 2023, p. 1484. DOI: 10.22323/1.444.1484 (cited on page 27).

[135] Eli Waxman and John Bahcall. 'High Energy Neutrinos from Astrophysical Sources: An Upper Bound'. In: *Physical Review D* 59.2 (Dec. 1998), p. 023002. DOI: 10.1103/PhysRevD.59.023002. (Visited on 10/04/2024) (cited on page 29).

[136] J. A. Formaggio and G. P. Zeller. 'From eV to EeV: Neutrino Cross Sections across Energy Scales'. In: *Reviews of Modern Physics* 84.3 (Sept. 2012), pp. 1307–1341. DOI: 10.1103/RevModPhys.84.1307. (Visited on 10/02/2024) (cited on pages 29, 30).

[137] Sheldon L. Glashow. 'Resonant Scattering of Antineutrinos'. In: *Physical Review* 118.1 (Apr. 1960), pp. 316–317. DOI: 10.1103/PhysRev.118.316. (Visited on 10/03/2024) (cited on page 30).

[138] M. G. Aartsen et al. 'Detection of a Particle Shower at the Glashow Resonance with IceCube'. In: *Nature* 591.7849 (Mar. 2021), pp. 220–224. DOI: 10.1038/s41586-021-03256-1. (Visited on 10/03/2024) (cited on page 30).

[139] M. G. Aartsen et al. 'Energy Reconstruction Methods in the IceCube Neutrino Telescope'. In: *Journal of Instrumentation* 9.03 (Mar. 2014), P03009. DOI: 10.1088/1748-0221/9/03/P03009. (Visited on 06/14/2023) (cited on pages 30, 34, 37, 41–43).

[140] John G. Learned and Karl Mannheim. 'High-Energy Neutrino Astrophysics'. In: *Annual Review of Nuclear and Particle Science* 50.1 (2000), pp. 679–749. DOI: 10.1146/annurev.nucl.50.1.679 (cited on page 30).

[141] John David Jackson. *Klassische Elektrodynamik*. De Gruyter, Nov. 2011. (Visited on 10/03/2024) (cited on page 30).

[142] Stephen G. Warren. 'Optical Constants of Ice from the Ultraviolet to the Microwave'. In: *Applied Optics* 23.8 (Apr. 1984), pp. 1206–1225. DOI: 10.1364/AO.23.001206. (Visited on 10/03/2024) (cited on page 30).

[143] Jakob van Santen. 'Neutrino Interactions in IceCube above 1 TeV: Constraints on Atmospheric Charmed-Meson Production and Investigation of the Astrophysical Neutrino Flux with 2 Years of IceCube Data Taken 2010–2012'. PhD thesis. Wisconsin U., Madison, Nov. 2014 (cited on pages 30, 53).

[144] Paul H. Barrett et al. 'Interpretation of Cosmic-Ray Measurements Far Underground'. In: *Reviews of Modern Physics* 24.3 (July 1952), pp. 133–178. DOI: 10.1103/RevModPhys.24.133. (Visited on 09/06/2024) (cited on pages 31, 105).

[145] Dmitry Chirkin and Wolfgang Rhode. 'Propagating Leptons through Matter with Muon Monte Carlo (MMC)'. In: *arXiv e-prints* (July 2004), hep–ph/0407075 (cited on page 31).

[146] M. G. Aartsen et al. 'All-Sky Search for Time-integrated Neutrino Emission from Astrophysical Sources with 7 Yr of IceCube Data'. In: *The Astrophysical Journal* 835.2 (Jan. 2017), p. 151. DOI: 10.3847/1538-4357/835/2/151. (Visited on 06/19/2023) (cited on pages 31, 35, 36, 38).

[147] M. G. Aartsen et al. 'The IceCube Neutrino Observatory: Instrumentation and Online Systems'. In: *Journal of Instrumentation* 12.03 (Mar. 2017), P03012. DOI: 10.1088/1748-0221/12/03/P03012. (Visited on 06/14/2024) (cited on pages 32–35, 38, 39, 50).

[148] R. Abbasi et al. 'The Design and Performance of IceCube DeepCore'. In: *Astroparticle Physics* 35.10 (May 2012), pp. 615–624. DOI: 10.1016/j.astropartphys.2012.01.004. (Visited on 10/06/2024) (cited on page 32).

[149] R. Abbasi et al. 'IceTop: The Surface Component of IceCube'. In: *Nuclear Instruments and Methods in Physics Research Section A: Accelerators, Spectrometers, Detectors and Associated Equipment* 700 (Feb. 2013), pp. 188–220. DOI: 10.1016/j.nima.2012.10.067. (Visited on 10/06/2024) (cited on page 33).

[150] IceCube Collaboration et al. 'Measurement of the Cosmic Ray Energy Spectrum with IceTop-73'. In: *Physical Review D* 88.4 (Aug. 2013), p. 042004. DOI: 10.1103/PhysRevD.88.042004. (Visited on 10/06/2024) (cited on page 33).

[151] R. Abbasi et al. 'Calibration and Characterization of the IceCube Photomultiplier Tube'. In: *Nuclear Instruments and Methods in Physics Research Section A: Accelerators, Spectrometers, Detectors and Associated Equipment* 618.1 (June 2010), pp. 139–152. DOI: 10.1016/j.nima.2010.03.102. (Visited on 06/14/2024) (cited on page 34).

[152] R. Abbasi et al. 'The IceCube Data Acquisition System: Signal Capture, Digitization, and Timestamping'. In: *Nuclear Instruments and Methods in Physics Research Section A: Accelerators, Spectrometers, Detectors and Associated Equipment* 601.3 (Apr. 2009), pp. 294–316. DOI: 10.1016/j.nima.2009.01.001. (Visited on 06/14/2024) (cited on pages 34, 35).

[153] Federica Bradascio. 'Searches for Cross-Correlations between IceCube Neutrinos and Active Galactic Nuclei Selected in Various Bands of the Electromagnetic Spectrum'. doctoralThesis. Humboldt-Universität zu Berlin, July 2021. DOI: 10.18452/22871. (Visited on 06/19/2024) (cited on page 35).

[154] R. Abbasi et al. 'IceCube Sensitivity for Low-Energy Neutrinos from Nearby Supernovae'. In: *Astronomy & Astrophysics* 535 (Nov. 2011), A109. DOI: 10.1051/0004-6361/201117810. (Visited on 11/11/2024) (cited on page 35).

[155] M. Ackermann et al. 'Optical Properties of Deep Glacial Ice at the South Pole'. In: 111.D13 (2006), p. D13203. DOI: 10.1029/2005JD006687 (cited on pages 35, 36).

[156] P. Buford Price and Lars Bergström. 'Optical Properties of Deep Ice at the South Pole: Scattering'. In: *Applied Optics* 36.18 (June 1997), pp. 4181–4194. DOI: 10.1364/AO.36.004181. (Visited on 10/09/2024) (cited on page 35).

[157] IceCube Collaboration et al. 'A Calibration Study of Local Ice and Optical Sensor Properties in IceCube'. In: *Proceedings of 37th International Cosmic Ray Conference — PoS(ICRC2021)*. Vol. 395. SISSA Medialab, Mar. 2022, p. 1023. DOI: 10.22323/1.395.1023. (Visited on 10/09/2024) (cited on page 36).

[158] M. G. Aartsen et al. 'Measurement of South Pole Ice Transparency with the IceCube LED Calibration System'. In: *Nuclear Instruments and Methods in Physics Research Section A: Accelerators, Spectrometers, Detectors and Associated Equipment* 711 (May 2013), pp. 73–89. DOI: 10.1016/j.nima.2013.01.054. (Visited on 06/14/2024) (cited on page 36).

[159] Gustav Mie. 'Beiträge Zur Optik Trüber Medien, Speziell Kolloidaler Metallösungen'. In: *Annalen der Physik* 330.3 (1908), pp. 377–445. DOI: 10.1002/andp.19083300302. (Visited on 10/09/2024) (cited on page 36).

[160] Rasha Abbasi et al. 'In Situ Estimation of Ice Crystal Properties at the South Pole Using LED Calibration Data from the IceCube Neutrino Observatory'. In: *The Cryosphere* 18.1 (Jan. 2024), pp. 75–102. DOI: 10.5194/tc-18-75-2024. (Visited on 06/14/2024) (cited on pages 36, 54).

[161] The IceCube Collaboration. 'South Pole Glacial Climate Reconstruction from Multi-Borehole Laser Particulate Stratigraphy'. In: *Journal of Glaciology* 59.218 (Jan. 2013), pp. 1117–1128. DOI: 10.3189/2013JoG13J068. (Visited on 10/10/2024) (cited on page 36).

[162] IceCube Collaboration et al. 'Observation of the Cosmic-Ray Shadow of the Moon with IceCube'. In: *Physical Review D* 89.10 (May 2014), p. 102004. DOI: 10.1103/PhysRevD.89.102004. (Visited on 10/10/2024) (cited on page 36).

[163] Thomas Kintscher. 'Rapid Response to Extraordinary Events: Transient Neutrino Sources with the IceCube Experiment'. doctoralThesis. Humboldt-Universität zu Berlin, Oct. 2020. DOI: 10.18452/21948. (Visited on 06/19/2024) (cited on page 38).

[164] M. G. Aartsen et al. 'Search for Steady Point-like Sources in the Astrophysical Muon Neutrino Flux with 8 Years of IceCube Data'. In: *The European Physical Journal C* 79.3 (Mar. 2019), p. 234. DOI: 10.1140/epjc/s10052-019-6680-0. (Visited on 09/11/2024) (cited on page 38).

[165] M. G. Aartsen et al. 'Time-Integrated Neutrino Source Searches with 10 Years of IceCube Data'. In: *Physical Review Letters* 124.5 (Feb. 2020), p. 051103. DOI: 10.1103/PhysRevLett.124.051103. (Visited on 06/19/2024) (cited on pages 38, 103).

[166] Trevor Hastie, Robert Tibshirani, and Jerome Friedman. 'Boosting and Additive Trees'. In: *The Elements of Statistical Learning: Data Mining, Inference, and Prediction*. Ed. by Trevor Hastie, Robert Tibshirani, and Jerome Friedman. New York, NY: Springer, 2009, pp. 337–387. DOI: 10.1007/978-0-387-84858-7_10. (Visited on 11/11/2024) (cited on page 38).

[167] S. S. Keerthi et al. 'Improvements to Platt's SMO Algorithm for SVM Classifier Design'. In: *Neural Computation* 13.3 (Mar. 2001), pp. 637–649. DOI: 10.1162/089976601300014493. (Visited on 11/11/2024) (cited on page 38).

[168] Tessa Carver. 'Time Integrated Searches for Astrophysical Neutrino Sources Using the IceCube Detector and Gender in Physics Studies for the Genera Project'. PhD thesis. Jan. 2019. (Visited on 04/25/2023) (cited on page 38).

[169] M. G. Aartsen et al. 'Observation of High-Energy Astrophysical Neutrinos in Three Years of IceCube Data'. In: *Physical Review Letters* 113.10 (Sept. 2014), p. 101101. DOI: 10.1103/PhysRevLett.113.101101 (cited on page 38).

[170] IceCube Collaboration et al. 'IceCube High-Energy Starting Event Sample: Description and Flux Characterization with 7.5 Years of Data'. In: *Physical Review D* 104.2 (July 2021), p. 022002. DOI: 10.1103/PhysRevD.104.022002. (Visited on 10/31/2024) (cited on page 38).

[171] IceCube Collaboration et al. 'Constraints on Ultrahigh-Energy Cosmic-Ray Sources from a Search for Neutrinos above 10 PeV with IceCube'. In: *Physical Review Letters* 117.24 (Dec. 2016), p. 241101. DOI: 10.1103/PhysRevLett.117.241101. (Visited on 10/08/2024) (cited on page 38).

[172] V. J. Stenger. *Track Fitting For Dumand-II Octagon Array (Technical Report)*. Tech. rep. University of Hawaii at Manoa, 1990 (cited on page 39).

[173] Kai Schatto. 'Stacked Searches for High-Energy Neutrinos from Blazars with IceCube'. PhD thesis. Mainz: Johannes Gutenberg-Universität Mainz, 2014. DOI: 10.25358/openscience-2897 (cited on pages 39, 40).

[174] Roger Barlow. 'Extended Maximum Likelihood'. In: *Nuclear Instruments and Methods in Physics Research Section A: Accelerators, Spectrometers, Detectors and Associated Equipment* 297.3 (Dec. 1990), pp. 496–506. DOI: 10.1016/0168-9002(90)91334-8. (Visited on 09/06/2024) (cited on page 39).

[175] Michael Soiron. 'Untersuchungen Zur Verbesserung Der Myonenspur-Rekonstruktion in IceCube'. PhD thesis. RWTH Aachen, Oct. 2012 (cited on page 40).

[176] Nathan Whitehorn, Jakob van Santen, and Sven Lafebre. 'Penalized Splines for Smooth Representation of High-Dimensional Monte Carlo Datasets'. In: *Computer Physics Communications* 184.9 (Sept. 2013), pp. 2214–2220. DOI: 10.1016/j.cpc.2013.04.008. (Visited on 06/19/2024) (cited on page 40).

[177] Giacomo Sommani et al. 'Towards a More Robust Reconstruction Method for IceCube's Real-Time Program'. In: *Proceedings of 38th International Cosmic Ray Conference — PoS(ICRC2023)*. Vol. 444. 2023, p. 1186. DOI: 10.22323/1.444.1186 (cited on pages 41, 99).

[178] K. M. Górski et al. 'HEALPix: A Framework for High-Resolution Discretization and Fast Analysis of Data Distributed on the Sphere'. In: *The Astrophysical Journal* 622.2 (Apr. 2005), p. 759. DOI: 10.1086/427976. (Visited on 06/20/2024) (cited on page 41).

[179] Till Neunhoffer. 'Estimating the Angular Resolution of Tracks in Neutrino Telescopes Based on a Likelihood Analysis'. In: 25 (2006), pp. 220–225. DOI: 10.1016/j.astropartphys.2006.01.002 (cited on page 41).

[180] R. Abbasi et al. 'An Improved Method for Measuring Muon Energy Using the Truncated Mean of dE/Dx'. In: *Nuclear Instruments and Methods in Physics Research A* 703 (Mar. 2013), pp. 190–198. DOI: 10.1016/j.nima.2012.11.081. (Visited on 03/28/2023) (cited on pages 42, 43).

[181] Thorsten Glüsenkamp. 'Search for a Cumulative Neutrino Flux from 2LAC-blazar Populations Using 3 Years of IceCube Data'. PhD thesis. Humboldt-Universität zu Berlin, Mathematisch-Naturwissenschaftliche Fakultät, 2016. DOI: http://dx.doi.org/10.18452/17462 (cited on page 44).

[182] Jerzy Neyman, Egon Sharpe Pearson, and Karl Pearson. 'IX. On the Problem of the Most Efficient Tests of Statistical Hypotheses'. In: *Philosophical Transactions of the Royal Society of London. Series A, Containing Papers of a Mathematical or Physical Character* 231.694-706 (Jan. 1997), pp. 289–337. DOI: 10.1098/rsta.1933.0009. (Visited on 07/04/2023) (cited on pages 45, 51).

[183] S. S. Wilks. 'The Large-Sample Distribution of the Likelihood Ratio for Testing Composite Hypotheses'. In: *Annals Math. Statist.* 9.1 (1938), pp. 60–62. DOI: 10.1214/aoms/1177732360 (cited on pages 45, 51, 159).

[184] M. G. Aartsen et al. 'The IceCube Realtime Alert System'. In: *Astroparticle Physics* 92 (June 2017), pp. 30–41. DOI: 10.1016/j.astropartphys.2017.05.002. (Visited on 06/14/2024) (cited on page 50).

[185] Christian Haack, Christopher Wiebusch, and on behalf of the IceCube Collaboration. 'A Measurement of the Diffuse Astrophysical Muon Neutrino Flux Using Eight Years of IceCube Data.' In: *Proceedings of 35th International Cosmic Ray Conference — PoS(ICRC2017)*. Vol. 301. SISSA Medialab, Aug. 2018, p. 1005. DOI: 10.22323/1.301.1005. (Visited on 06/17/2024) (cited on page 50).

[186] E. Kankare et al. 'Search for Transient Optical Counterparts to High-Energy IceCube Neutrinos with Pan-STARRS1'. In: *Astronomy & Astrophysics* 626 (June 2019), A117. DOI: 10.1051/0004-6361/201935171. (Visited on 06/14/2023) (cited on pages 52, 53).

[187] Rasha Abbasi et al. 'Studies of Systematic Uncertainty Effects on IceCube's Real-Time Angular Uncertainty'. In: *Proceedings of 37th International Cosmic Ray Conference — PoS(ICRC2021)*. Vol. 395. 2021, p. 1045. DOI: 10.22323/1.395.1045 (cited on page 52).

[188] Cristina Lagunas Gualda. 'Realtime Detection of High-Energy Neutrinos and Search for Correlations with Candidate Source Classes'. PhD thesis. Berlin: Humboldt-Universität zu Berlin, Jan. 2024 (cited on pages 53–55, 57).

[189] R. Abbasi et al. 'LeptonInjector and LeptonWeighter: A Neutrino Event Generator and Weighter for Neutrino Observatories'. In: *Computer Physics Communications* 266 (Sept. 2021), p. 108018. DOI: 10.1016/j.cpc.2021.108018. (Visited on 07/01/2024) (cited on page 53).

[190] J. -H. Koehne et al. 'PROPOSAL: A Tool for Propagation of Charged Leptons'. In: *Computer Physics Communications* 184.9 (Sept. 2013), pp. 2070–2090. DOI: 10.1016/j.cpc.2013.04.001. (Visited on 07/01/2024) (cited on page 53).

[191] M. G. Aartsen et al. 'Efficient Propagation of Systematic Uncertainties from Calibration to Analysis with the SnowStorm Method in IceCube'. In: *Journal of Cosmology and Astroparticle Physics* 2019.10 (Oct. 2019), p. 048. DOI: 10.1088/1475-7516/2019/10/048. (Visited on 07/01/2024) (cited on pages 53, 54).

[192] Jannis Necker et al. 'ASAS-SN Follow-up of IceCube High-Energy Neutrino Alerts'. In: *Monthly Notices of the Royal Astronomical Society* 516 (Oct. 2022), pp. 2455–2469. DOI: 10.1093/mnras/stac2261. (Visited on 11/21/2022) (cited on page 65).

[193] K. Hart et al. *ASAS-SN Sky Patrol V2.0*. Apr. 2023. DOI: 10.48550/arXiv.2304.03791. (Visited on 09/18/2024) (cited on page 66).

[194] T. M. Brown et al. 'Las Cumbres Observatory Global Telescope Network'. In: *Publications of the Astronomical Society of the Pacific* 125.931 (Sept. 2013), p. 1031. DOI: 10.1086/673168 (cited on page 65).

[195] B. J. Shappee et al. 'The Man behind the Curtain: X-Rays Drive the UV through NIR Variability in the 2013 Active Galactic Nucleus Outburst in NGC 2617'. In: *The Astrophysical Journal* 788.1 (June 2014), p. 48. DOI: 10.1088/0004-637X/788/1/48 (cited on pages 65, 67, 132).

[196] T. de Jaeger et al. 'ASAS-SN Search for Optical Counterparts of Gravitational-Wave Events from the Third Observing Run of Advanced LIGO/Virgo'. In: *Monthly Notices of the Royal Astronomical Society* 509.3 (Jan. 2022), pp. 3427–3440. DOI: 10.1093/mnras/stab3141 (cited on pages 65, 66).

[197] C. Alard. 'Image Subtraction Using a Space-Varying Kernel'. In: *Astronomy and Astrophysics Supplement Series* 144.2 (June 2000), pp. 363–370. DOI: 10.1051/aas:2000214. (Visited on 09/24/2024) (cited on page 66).

[198] C. Alard and Robert H. Lupton. 'A Method for Optimal Image Subtraction'. In: *The Astrophysical Journal* 503.1 (Aug. 1998), p. 325. DOI: 10.1086/305984. (Visited on 09/24/2024) (cited on page 66).

[199] E. Bertin and S. Arnouts. 'SExtractor: Software for Source Extraction'. In: *Astronomy and Astrophysics Supplement Series* 117.2 (June 1996), pp. 393–404. DOI: 10.1051/aas:1996164. (Visited on 09/24/2024) (cited on pages 66, 78).

[200] C. S. Kochanek et al. 'The All-Sky Automated Survey for Supernovae (ASAS-SN) Light Curve Server v1.0'. In: *Publications of the Astronomical Society of the Pacific* 129.980 (Oct. 2017), p. 104502. DOI: 10.1088/1538-3873/aa80d9 (cited on page 67).

[201] E. Blaufuss. 'ICECUBE-160427A Neutrino Candidate Event: Updated Direction Information.' In: *GCN Circular* 19363 (Apr. 2016) (cited on page 69).

[202] I. Taboada. 'IceCube-161103: IceCube Observation of a Very-High-Energy Neutrino.' In: *GCN Circular* 20119 (Nov. 2016) (cited on page 69).

[203] E. Blaufuss. 'IceCube-161210: IceCube Observation of a High-Energy Neutrino Candidate Event.' In: *GCN Circular* 20247 (Dec. 2016) (cited on page 69).

[204] E. Blaufuss. 'IceCube-170312A - IceCube Update on a High-Energy Neutrino Candidate Event.' In: *GCN Circular* 20857 (Mar. 2017), p. 1 (cited on page 69).

[205] E. Blaufuss. 'IceCube-170321A - IceCube Observation of a High-Energy Neutrino Candidate Event.' In: *GCN Circular* 20929 (Mar. 2017) (cited on page 69).

[206] C. Kopper and E. Blaufuss. 'IceCube-170922A - IceCube Observation of a High-Energy Neutrino Candidate Event.' In: *GCN Circular* 21916 (Sept. 2017) (cited on page 69).

[207] I. Taboada. 'IceCube-171106A - IceCube Observation of a High-Energy Neutrino Candidate.' In: *GCN Circular* 22105 (Nov. 2017) (cited on page 69).

[208] E. Blaufuss. 'IceCube-181023A - IceCube Observation of a High-Energy Neutrino Candidate Event'. In: *GCN Circular* 23375 (Oct. 2018) (cited on page 69).

[209] C. Kopper. 'IceCube-190104A - IceCube Observation of a High-Energy Neutrino Candidate Event'. In: *GCN Circular* 23605 (Jan. 2019) (cited on page 69).

[210] Icecuce Collaboration. 'IceCube-190221A - IceCube Observation of a High-Energy Neutrino Candidate Event.' In: *GRB Coordinates Network* 23918 (Jan. 2019), p. 1. (Visited on 09/23/2024) (cited on page 69).

[211] C. Kopper. 'IceCube-190331A - IceCube Observation of a High-Energy Neutrino Candidate Event.' In: *GCN Circular* 24028 (Mar. 2019) (cited on page 69).

[212] E. Blaufuss. 'IceCube-190503A - IceCube Observation of a High-Energy Neutrino Candidate Event'. In: *GCN Circular* 24378 (May 2019) (cited on page 69).

[213] E. Blaufuss. 'IceCube-190619A - IceCube Observation of a High-Energy Neutrino Candidate Event'. In: *GCN Circular* 24854 (June 2019) (cited on page 69).

[214] E. Blaufuss. 'IceCube-190629A - IceCube Observation of a High-Energy Neutrino Candidate Event'. In: *GCN Circular* 24910 (June 2019) (cited on page 69).

[215] M. Santander. 'IceCube-190704A - IceCube Observation of a High-Energy Neutrino Candidate Event'. In: *GCN Circular* 24981 (July 2019) (cited on page 69).

[216] E. Blaufuss. 'IceCube-190712A - IceCube Observation of a High-Energy Neutrino Candidate Event'. In: *GCN Circular* 25057 (July 2019) (cited on page 69).

[217] R. Stein. 'IceCube-190730A - IceCube Observation of a High-Energy Neutrino Candidate Event'. In: *GCN Circular* 25225 (July 2019) (cited on pages 69, 72).

[218] Erik Blaufuss. 'IceCube-190922B - IceCube Observation of a High-Energy Neutrino Candidate Event'. In: *GCN Circular* 25806 (Sept. 2019) (cited on page 69).

[219] R. Stein. 'IceCube-191001A - IceCube Observation of a High-Energy Neutrino Candidate Event'. In: *GCN Circular* 25913 (Oct. 2019) (cited on page 69).

[220] E. Blaufuss. 'IceCube-191122A - IceCube Observation of a High-Energy Neutrino Candidate Event'. In: *GCN Circular* 26276 (Nov. 2019) (cited on page 69).

[221] R. Stein. 'IceCube-191204A - IceCube Observation of a High-Energy Neutrino Candidate Event'. In: *GCN Circular* 26341 (Dec. 2019) (cited on page 69).

[222] R. Stein. 'IceCube-191215A - IceCube Observation of a High-Energy Neutrino Candidate Event'. In: *GCN Circular* 26435 (Dec. 2019) (cited on page 69).

[223] M. Santander. 'IceCube-191231A: IceCube Observation of a High-Energy Neutrino Candidate Event'. In: *GCN Circular* 26620 (Dec. 2019) (cited on page 69).

[224] R. Stein. 'IceCube-200107A: IceCube Observation of a High-Energy Neutrino Candidate Event'. In: *GCN Circular* 26655 (Jan. 2020) (cited on page 69).

[225] R. Stein. 'IceCube-200109A: IceCube Observation of a High-Energy Neutrino Candidate Event'. In: *GCN Circular* 26696 (Jan. 2020) (cited on page 69).

[226] C. Lagunas Gualda. 'IceCube-200117A: IceCube Observation of a High-Energy Neutrino Candidate Event'. In: *GCN Circular* 26802 (Jan. 2020) (cited on page 69).

[227] R. Stein. 'IceCube-200410A: IceCube Observation of a High-Energy Neutrino Candidate Event'. In: *GCN Circular* 27534 (Apr. 2020) (cited on page 69).

[228] M. Santander. 'IceCube-200425A: IceCube Observation of a High-Energy Neutrino Candidate Event'. In: *GCN Circular* 27651 (Apr. 2020) (cited on page 69).

[229] C. Lagunas Gualda. 'IceCube-200512A: IceCube Observation of a High-Energy Neutrino Candidate Event'. In: *GCN Circular* 27719 (May 2020) (cited on page 69).

[230] E. Blaufuss. 'IceCube-200523A: IceCube Observation of a High-Energy Neutrino Candidate Event'. In: *GCN Circular* 27787 (May 2020) (cited on page 69).

[231] R. Stein. 'IceCube-200530A: IceCube Observation of a High-Energy Neutrino Candidate Event'. In: *GCN Circular* 27865 (May 2020) (cited on page 69).

[232] E. Blaufuss. 'IceCube-200614A: IceCube Observation of a High-Energy Neutrino Candidate Event'. In: *GCN Circular* 27941 (June 2020) (cited on page 69).

[233] C. Lagunas Gualda. 'IceCube-200615A: IceCube Observation of a High-Energy Neutrino Candidate Event'. In: *GCN Circular* 27950 (June 2020) (cited on page 69).

[234] M. Santander. 'IceCube-200620A: IceCube Observation of a High-Energy Neutrino Candidate Event'. In: *GCN Circular* 27997 (June 2020) (cited on page 69).

[235] C. Lagunas Gualda. 'IceCube-200911A: IceCube Observation of a High-Energy Neutrino Candidate Event'. In: *GCN Circular* 28411 (Sept. 2020) (cited on page 69).

[236] E. Blaufuss. 'IceCube-200916A - IceCube Observation of a High-Energy Neutrino Candidate Track-like Event'. In: *GCN Circular* 28433 (Sept. 2020) (cited on page 69).

[237] C. Lagunas Gualda. 'IceCube-200926A: IceCube Observation of a High-Energy Neutrino Candidate Event'. In: *GCN Circular* 28504 (Sept. 2020) (cited on pages 69, 70).

[238] C. Lagunas Gualda. 'IceCube-200929A: IceCube Observation of a High-Energy Neutrino Candidate Event'. In: *GCN Circular* 28532 (Sept. 2020) (cited on page 69).

[239] M. Santander. 'IceCube-201007A - IceCube Observation of a High-Energy Neutrino Candidate Track-like Event'. In: *GCN Circular* 28575 (Oct. 2020) (cited on page 69).

[240] C. Lagunas Gualda. 'IceCube-201021A: IceCube Observation of a High-Energy Neutrino Candidate Event'. In: *GCN Circular* 28715 (Oct. 2020) (cited on page 69).

[241] E. Blaufuss. 'IceCube-201114A - IceCube Observation of a High-Energy Neutrino Candidate Event'. In: *GCN Circular* 28887 (Nov. 2020) (cited on page 69).

[242] C. Lagunas Gualda. 'IceCube-201115A: IceCube Observation of a High-Energy Neutrino Candidate Event'. In: *GCN Circular* 28889 (Nov. 2020) (cited on page 69).

[243] C. Lagunas Gualda. 'IceCube-201120A: IceCube Observation of a High-Energy Neutrino Candidate Event'. In: *GCN Circular* 28927 (Nov. 2020) (cited on page 69).

[244] C. Lagunas Gualda. 'IceCube-201130A: IceCube Observation of a High-Energy Neutrino Candidate Event'. In: *GCN Circular* 28969 (Nov. 2020) (cited on page 69).

[245] C. Lagunas Gualda. 'IceCube-201209A: IceCube Observation of a High-Energy Neutrino Candidate Event'. In: *GCN Circular* 29012 (Dec. 2020) (cited on page 69).

[246] E. Blaufuss. 'IceCube-201221A: IceCube Observation of a High-Energy Neutrino Candidate Event'. In: *GCN Circular* 29102 (Dec. 2020) (cited on page 69).

[247] E. Blaufuss. 'IceCube-201222A: IceCube Observation of a High-Energy Neutrino Candidate Event'. In: *GCN Circular* 29120 (Dec. 2020) (cited on page 69).

[248] C. Lagunas Gualda. 'IceCube-210210A: IceCube Observation of a High-Energy Neutrino Candidate Event'. In: *GCN Circular* 29454 (Feb. 2021) (cited on page 69).

[249] M. Santander. 'IceCube-210503A: IceCube Observation of a High-Energy Neutrino Candidate Event'. In: *GCN Circular* 29951 (May 2021) (cited on page 69).

[250] M. Santander. 'IceCube-210510A - IceCube Observation of a High-Energy Neutrino Candidate Track-like Event'. In: *GCN Circular* 29976 (May 2021) (cited on page 69).

[251] C. Lagunas Gualda. 'IceCube-210608A: IceCube Observation of a High-Energy Neutrino Candidate Track-like Event'. In: *GCN Circular* 30153 (June 2021) (cited on page 69).

[252] M. Santander. 'IceCube-210629A: IceCube Observation of a High-Energy Neutrino Candidate Track-like Event'. In: *GCN Circular* 30342 (June 2021) (cited on page 69).

[253] C. Lagunas Gualda. 'IceCube-210717A: IceCube Observation of a High-Energy Neutrino Candidate Track-like Event'. In: *GCN Circular* 30468 (July 2021), p. 1 (cited on page 69).

[254] M. Santander. 'IceCube-210811A - IceCube Observation of a High-Energy Neutrino Candidate Track-like Event'. In: *GCN Circular* 30627 (Aug. 2021), p. 1 (cited on page 69).

[255] D. Cowen. 'IceCube 160806A EHE Neutrino Candidate Event'. In: *GCN Circular* 19787 (Aug. 2016), p. 1 (cited on page 70).

[256] E. Blaufuss. 'IceCube-171015A - IceCube Observation of a High-Energy Neutrino Candidate Event.' In: *GCN Circular* 22016 (Oct. 2017) (cited on page 70).

[257] E. Blaufuss. 'IceCube-180908A - IceCube Observation of a High-Energy Neutrino Candidate Event'. In: *GCN Circular* 23214 (Sept. 2018) (cited on page 70).

[258] I. Taboada. 'IceCube-181014A - IceCube Observation of a High-Energy Neutrino Candidate Event'. In: *GCN Circular* 23338 (Oct. 2018) (cited on page 70).

[259] E. Blaufuss. 'IceCube-190124A - IceCube Observation of a High-Energy Neutrino Candidate Event'. In: *GCN Circular* 23785 (Jan. 2019) (cited on page 70).

[260] M. Santander. 'IceCube-190819A - IceCube Observation of a High-Energy Neutrino Candidate Event'. In: *GCN Circular* 25402 (Aug. 2019) (cited on page 70).

[261] R. Stein. 'IceCube-190922A - IceCube Observation of a High-Energy Neutrino Candidate Event'. In: *GCN Circular* 25802 (Sept. 2019) (cited on page 70).

[262] E. Blaufuss. 'IceCube-191119A - IceCube Observation of a High-Energy Neutrino Candidate Event'. In: *GCN Circular* 26258 (Nov. 2019) (cited on page 70).

[263] IceCube Collaboration. 'IceCube-200421A - IceCube Observation of a High-Energy Neutrino Candidate Event'. In: *GRB Coordinates Network* 27612 (Apr. 2020), p. 1. (Visited on 09/23/2024) (cited on page 70).

[264] R. Stein. 'IceCube-200806A: IceCube Observation of a High-Energy Neutrino Candidate Event'. In: *GCN Circular* 28210 (Aug. 2020) (cited on page 70).

[265] C. Lagunas Gualda. 'IceCube-200921A: IceCube Observation of a High-Energy Neutrino Candidate Event'. In: *GCN Circular* 28468 (Sept. 2020) (cited on page 70).

[266] E. Blaufuss. 'IceCube-201014A - IceCube Observation of a High-Energy Neutrino Candidate Track-like Event'. In: *GCN Circular* 28616 (Oct. 2020) (cited on page 70).

[267] M. Santander. 'IceCube-210516A - IceCube Observation of a High-Energy Neutrino Candidate Track-like Event'. In: *GCN Circular* 30026 (May 2021) (cited on page 70).

[268] M. Santander. 'IceCube-210730A - IceCube Observation of a High-Energy Neutrino Candidate Track-like Event'. In: *GCN Circular* 30559 (July 2021), p. 1 (cited on page 70).

[269] Robert Stein et al. 'A Tidal Disruption Event Coincident with a High-Energy Neutrino'. In: *Nature Astronomy* 5 (Feb. 2021), pp. 510–518. DOI: 10.1038/s41550-020-01295-8. (Visited on 03/06/2023) (cited on pages 70, 83, 84).

[270] Simeon Reusch et al. 'Candidate Tidal Disruption Event AT2019fdr Coincident with a High-Energy Neutrino'. In: *Physical Review Letters* 128.22 (June 2022), p. 221101. DOI: 10.1103/PhysRevLett.128.221101. (Visited on 08/26/2022) (cited on pages 70, 76, 83, 84, 96, 130).

[271] J. Nordin et al. 'ZTF Transient Discovery Report for 2019-01-24'. In: *Transient Name Server Discovery Report* 2019–1231 (Jan. 2019), p. 1 (cited on page 70).

[272] A. Dahiwale and C. Fremling. 'ZTF Transient Classification Report for 2020-02-22'. In: *Transient Name Server Classification Report* 2020–601 (Feb. 2020), p. 1 (cited on page 70).

[273] Kohta Murase et al. 'High-Energy Emission from Interacting Supernovae: New Constraints on Cosmic-Ray Acceleration in Dense Circumstellar Environments'. In: *The Astrophysical Journal* 874.1 (Mar. 2019), p. 80. DOI: 10.3847/1538-4357/ab0422 (cited on page 70).

[274] R. Cartier. 'Transient Classification Report for 2018-07-04'. In: *Transient Name Server Classification Report* 2018–927 (July 2018), p. 1 (cited on page 70).

[275] K. Z. Stanek. 'ASAS-SN Transient Discovery Report for 2018-06-16'. In: *Transient Name Server Discovery Report* 2018–828 (June 2018), p. 1 (cited on page 72).

[276] J. Brimacombe et al. 'Discovery of Eight ASAS-SN Supernovae'. In: *The Astronomer's Telegram* 10967 (Nov. 2017), p. 1 (cited on page 72).

[277] J. Tonry et al. 'ATLAS Transient Discovery Report for 2019-05-24'. In: *Transient Name Server Discovery Report* 2019–844 (May 2019), p. 1 (cited on page 72).

[278] Frank J. Masci et al. 'The Zwicky Transient Facility: Data Processing, Products, and Archive'. In: *Publications of the Astronomical Society of the Pacific* 131.995 (Jan. 2019), p. 018003. DOI: 10.1088/1538-3873/aae8ac (cited on pages 72, 78).

[279] S. Abdollahi et al. 'Fermi Large Area Telescope Fourth Source Catalog'. In: *The Astrophysical Journal Supplement* 247.1 (Mar. 2020), p. 33. DOI: 10.3847/1538-4365/ab6bcb (cited on page 72).

[280] J. Ballet et al. 'Fermi Large Area Telescope Fourth Source Catalog Data Release 2'. In: *arXiv e-prints* (May 2020), arXiv:2005.11208 (cited on page 72).

[281] A. Franckowiak et al. 'Patterns in the Multiwavelength Behavior of Candidate Neutrino Blazars'. In: *The Astrophysical Journal* 893.2 (Apr. 2020), p. 162. DOI: 10.3847/1538-4357/ab8307 (cited on page 72).

[282] R. Stein et al. 'Optical Follow-up of IceCube-190730A with ZTF'. In: *The Astronomer's Telegram* 12974 (July 2019) (cited on page 72).

[283] D. Steeghs et al. 'IceCube 190730A: No Counterpart Candidates or Blazar Activity in GOTO Observations'. In: *GRB Coordinates Network* 25255 (Aug. 2019), p. 1 (cited on page 72).

[284] Robert Stein et al. 'Neutrino Follow-up with the Zwicky Transient Facility: Results from the First 24 Campaigns'. In: *Monthly Notices of the Royal Astronomical Society* 521.4 (June 2023), pp. 5046–5063. DOI: 10.1093/mnras/stad767. (Visited on 05/09/2023) (cited on pages 72, 73, 75, 79).

[285] D D Desai et al. 'Supernova Rates and Luminosity Functions from ASAS-SN I: 2014–2017 Type Ia SNe and Their Sub-Types'. In: *Monthly Notices of the Royal Astronomical Society* (Feb. 2024), stae606. DOI: 10.1093/mnras/stae606. (Visited on 04/15/2024) (cited on page 73).

[286] Barbara Ryden. *Introduction to Cosmology*. 2nd ed. Cambridge: Cambridge University Press, 2016 (cited on pages 74, 108).

[287] Amy Lien et al. 'Probing the Cosmic Gamma-Ray Burst Rate with Trigger Simulations of the Swift Burst Alert Telescope'. In: *The Astrophysical Journal* 783.1 (Mar. 2014), p. 24. DOI: 10.1088/0004-637X/783/1/24 (cited on page 74).

[288] Louis-Gregory Strolger et al. 'The Rate of Core Collapse Supernovae to Redshift 2.5 from the CANDELS and CLASH Supernova Surveys'. In: *The Astrophysical Journal* 813.2 (Nov. 2015), p. 93. DOI: 10.1088/0004-637X/813/2/93 (cited on page 74).

[289] D. A. Kann et al. 'The Afterglows of Swift-era Gamma-Ray Bursts. I. Comparing Pre-Swift and Swift Era Long/Soft (Type II) GRB Optical Afterglows'. In: *Astrophys. J.* 720 (2010), pp. 1513–1558. DOI: 10.1088/0004-637X/720/2/1513 (cited on page 74).

[290] A. Nyholm et al. 'Type IIn Supernova Light-Curve Properties Measured from an Untargeted Survey Sample'. In: *åp* 637 (May 2020), A73. DOI: 10.1051/0004-6361/201936097 (cited on page 74).

[291] Željko Ivezić et al. 'LSST: From Science Drivers to Reference Design and Anticipated Data Products'. In: *The Astrophysical Journal* 873.2 (Mar. 2019), p. 111. DOI: 10.3847/1538-4357/ab042c. (Visited on 05/03/2024) (cited on pages 75, 150).

[292] P. Giommi et al. '3HSP J095507.9+355101: A Flaring Extreme Blazar Coincident in Space and Time with IceCube-200107A'. In: *Astron. Astrophys.* 640 (2020), p. L4. DOI: 10.1051/0004-6361/202038423 (cited on page 76).

[293] Vaidehi S. Paliya et al. 'Multifrequency Observations of the Candidate Neutrino-emitting Blazar BZB J0955+3551'. In: *The Astrophysical Journal* 902.1 (Oct. 2020), p. 29. DOI: 10.3847/1538-4357/abb46e (cited on page 76).

[294] R. G. Harrington. 'The 48-Inch Schmidt-type Telescope at Palomar Observatory'. In: *Publications of the Astronomical Society of the Pacific* 64 (Dec. 1952), p. 275. DOI: 10.1086/126494. (Visited on 09/26/2024) (cited on page 77).

[295] Bernhard Schmidt. 'Ein Lichtstarkes Komafreies Spiegelsystem'. In: *Mitteilungen der Hamburger Sternwarte in Bergedorf* 7 (Jan. 1938), pp. 15–17. (Visited on 09/26/2024) (cited on page 77).

[296] Richard Dekany et al. 'The Zwicky Transient Facility: Observing System'. In: *Publications of the Astronomical Society of the Pacific* 132.1009 (Jan. 2020), p. 038001. DOI: 10.1088/1538-3873/ab4ca2. (Visited on 09/26/2024) (cited on pages 77, 78).

[297] Eric C. Bellm, Shrinivas R. Kulkarni, Tom Barlow, et al. 'The Zwicky Transient Facility: Surveys and Scheduler'. In: *Publications of the Astronomical Society of the Pacific* 131.1000 (June 2019), p. 068003. DOI: 10.1088/1538-3873/ab0c2a (cited on pages 77, 78).

[298] Eric C. Bellm. 'Volumetric Survey Speed: A Figure of Merit for Transient Surveys'. In: *Publications of the Astronomical Society of the Pacific* 128.966 (Aug. 2016), p. 084501. DOI: 10.1088/1538-3873/128/966/084501 (cited on page 77).

[299] Eric C. Bellm et al. 'The Zwicky Transient Facility: System Overview, Performance, and First Results'. In: *Publications of the Astronomical Society of the Pacific* 131.995 (Dec. 2018), p. 018002. DOI: 10.1088/1538-3873/aaecbe. (Visited on 05/13/2024) (cited on page 78).

[300] A. G. A. Brown et al. 'Gaia Data Release 1 - Summary of the Astrometric, Photometric, and Survey Properties'. In: *Astronomy & Astrophysics* 595 (Nov. 2016), A2. DOI: 10.1051/0004-6361/201629512. (Visited on 09/29/2024) (cited on page 78).

[301] K. C. Chambers et al. 'The Pan-STARRS1 Surveys'. In: *ArXiv e-prints* (Dec. 2016) (cited on page 78).

[302] Barak Zackay, Eran O. Ofek, and Avishay Gal-Yam. 'Proper Image Subtraction—Optimal Transient Detection, Photometry, and Hypothesis Testing'. In: *The Astrophysical Journal* 830.1 (Oct. 2016), p. 27. DOI: 10.3847/0004-637X/830/1/27. (Visited on 09/29/2024) (cited on page 78).

[303] Ashish Mahabal et al. 'Machine Learning for the Zwicky Transient Facility'. In: *Publications of the Astronomical Society of the Pacific* 131.997 (Jan. 2019), p. 038002. DOI: 10.1088/1538-3873/aaf3fa. (Visited on 09/26/2024) (cited on page 78).

[304] Maria T. Patterson et al. 'The Zwicky Transient Facility Alert Distribution System'. In: *Publications of the Astronomical Society of the Pacific* 131.995 (Nov. 2018), p. 018001. DOI: 10.1088/1538-3873/aae904. (Visited on 09/26/2024) (cited on page 79).

[305] Simeon Reusch, Robert Stein, and Jakob van Santen. *Simeonreusch/Planobs: Release 0.7.3*. Zenodo. Sept. 2023. DOI: 10.5281/zenodo.8308182 (cited on page 79).

[306] Robert Stein, Simeon Reusch, and Jannis Necker. *Desy-Multimessenger/Nuztf: V2.1.0 Release*. Zenodo. Aug. 2021. DOI: 10.5281/zenodo.5217976. (Visited on 09/30/2024) (cited on page 79).

[307] Yutaro Tachibana and A. A. Miller. 'A Morphological Classification Model to Identify Unresolved PanSTARRS1 Sources: Application in the ZTF Real-time Pipeline'. In: *Publications of the Astronomical Society of the Pacific* 130.994 (Nov. 2018), p. 128001. DOI: 10.1088/1538-3873/aae3d9. (Visited on 09/12/2022) (cited on page 79).

[308] Daniel Stern et al. 'Mid-Infrared Selection of Active Galactic Nuclei with the Wide-Field Infrared Survey Explorer. I. Characterizing WISE-Selected Active Galactic Nuclei in COSMOS'. In: *The Astrophysical Journal* 753.1 (June 2012), p. 30. DOI: 10.1088/0004-637X/753/1/30. (Visited on 02/29/2024) (cited on pages 79, 92, 131).

[309] E. Blaufuss et al. 'The Next Generation of IceCube Real-time Neutrino Alerts'. In: *36th International Cosmic Ray Conference (ICRC2019)*. Vol. 36. International Cosmic Ray Conference. July 2019, p. 1021 (cited on page 80).

[310] J. Xavier Prochaska et al. *Pypeit/PypeIt: Release 1.0.0*. Zenodo. Apr. 2020. DOI: 10.5281/zenodo.3743493. (Visited on 09/30/2024) (cited on page 80).

[311] J. Xavier Prochaska et al. 'PypeIt: The Python Spectroscopic Data Reduction Pipeline'. In: *Journal of Open Source Software* 5.56 (Dec. 2020), p. 2308. DOI: 10.21105/joss.02308. (Visited on 09/30/2024) (cited on page 80).

[312] IceCube Collaboration. 'IceCube-220405A - IceCube Observation of a High-Energy Neutrino Candidate Track-like Event'. In: *GRB Coordinates Network* 31839 (Apr. 2022), p. 1. (Visited on 11/10/2024) (cited on page 81).

[313] Jannis Necker et al. 'IceCube-220405B: No Candidate Counterparts from the Zwicky Transient Facility'. In: *GRB Coordinates Network* 31842 (Apr. 2022), p. 1 (cited on page 81).

[314] Jannis Necker et al. 'IceCube-220405B - ZTF19aavnpjv Unrelated'. In: *GRB Coordinates Network* 32004 (May 2022), p. 1 (cited on page 81).

[315] IceCube Collaboration. 'IceCube-220624A - IceCube Observation of a High-Energy Neutrino Candidate Track-like Event'. In: *GRB Coordinates Network* 32260 (June 2022), p. 1. (Visited on 11/10/2024) (cited on page 81).

[316] Arthur N Cox. *Allen's Astrophysical Quantities*. Fourth Edition. New York, NY: Springer / SpringerLink (Online service), 1999 (cited on page 81).

[317] Robert Stein et al. 'IceCube-220624A: Classification of AT2022nit as a Type Ia Supernova and AT2021bei as an AGN'. In: *GRB Coordinates Network* 32357 (July 2022), p. 1 (cited on page 81).

[318] IceCube Collaboration. 'IceCube-231004A - IceCube Observation of a High-Energy Neutrino Candidate Track-like Event'. In: *GRB Coordinates Network* 34797 (Oct. 2023), p. 1. (Visited on 11/10/2024) (cited on page 81).

[319] J. B. Oke et al. 'The Keck Low-Resolution Imaging Spectrometer'. In: *Publications of the Astronomical Society of the Pacific* 107.710 (Apr. 1995), p. 375. DOI: 10.1086/133562. (Visited on 11/09/2024) (cited on page 82).

[320] M. Nicholl et al. 'ePESSTO+ Classification of Optical Transients'. In: *The Astronomer's Telegram* 12752 (May 2019), p. 1. (Visited on 10/01/2024) (cited on page 83).

[321] R. Chornock et al. 'Transient Classification Report for 2019-06-15'. In: *Transient Name Server Classification Report* 2019–1016 (June 2019), p. 1. (Visited on 10/01/2024) (cited on page 83).

[322] Tetyana Pitik et al. 'Is the High-energy Neutrino Event IceCube-200530A Associated with a Hydrogen-rich Superluminous Supernova?' In: *The Astrophysical Journal* 929.2 (Apr. 2022), p. 163. DOI: 10.3847/1538-4357/ac5ab1. (Visited on 10/09/2023) (cited on page 83).

[323] Sara Frederick et al. 'A Family Tree of Optical Transients from Narrow-line Seyfert 1 Galaxies'. In: *The Astrophysical Journal* 920.1 (Oct. 2021), p. 56. DOI: 10.3847/1538-4357/ac110f. (Visited on 04/11/2024) (cited on pages 84, 130).

[324] Walter Winter and Cecilia Lunardini. 'A Concordance Scenario for the Observed Neutrino from a Tidal Disruption Event'. In: *Nature Astronomy* 5.5 (May 2021), pp. 472–477. DOI: 10.1038/s41550-021-01305-3. (Visited on 10/01/2024) (cited on page 84).

[325] M. J. Rees et al. 'Infrared Radiation from Dust in Seyfert Galaxies'. In: *Nature* 223.5208 (Aug. 1969), pp. 788–791. DOI: 10.1038/223788a0. (Visited on 08/22/2024) (cited on pages 89–91).

[326] G. H. Rieke. 'The Infrared Emission of Seyfert Galaxies.' In: *The Astrophysical Journal* 226 (Dec. 1978), pp. 550–558. DOI: 10.1086/156639. (Visited on 08/21/2024) (cited on pages 89, 91).

[327] Richard Barvainis. 'Hot Dust and the Near-Infrared Bump in the Continuum Spectra of Quasars and Active Galactic Nuclei'. In: *The Astrophysical Journal* 320 (Sept. 1987), p. 537. DOI: 10.1086/165571. (Visited on 05/03/2024) (cited on pages 89–91).

[328] Ari Laor and Bruce T. Draine. 'Spectroscopic Constraints on the Properties of Dust in Active Galactic Nuclei'. In: *The Astrophysical Journal* 402 (Jan. 1993), p. 441. DOI: 10.1086/172149. (Visited on 08/21/2024) (cited on page 89).

[329] Maia Nenkova, Željko Ivezić, and Moshe Elitzur. 'Dust Emission from Active Galactic Nuclei'. In: *The Astrophysical Journal* 570.1 (Apr. 2002), p. L9. DOI: 10.1086/340857. (Visited on 08/22/2024) (cited on pages 89, 90).

[330] D. Bollea and A. Cavaliere. 'The Spectrum of IR Radiation from Dust Clouds.' In: *Astronomy and Astrophysics* 49 (June 1976), pp. 313–319. (Visited on 08/22/2024) (cited on page 89).

[331] E. Waxman and B. T. Draine. 'Dust Sublimation by Gamma-ray Bursts and Its Implications'. In: *The Astrophysical Journal* 537 (July 2000), pp. 796–802. DOI: 10.1086/309053. (Visited on 07/29/2024) (cited on page 89).

[332] S. van Velzen et al. 'Discovery of Transient Infrared Emission from Dust Heated by Stellar Tidal Disruption Flares'. In: *The Astrophysical Journal* 829.1 (Sept. 2016), p. 19. DOI: 10.3847/0004-637X/829/1/19. (Visited on 01/06/2024) (cited on pages 89, 91, 127, 128).

[333] Edward A. Pier and Julian H. Krolik. 'Infrared Spectra of Obscuring Dust Tori around Active Galactic Nuclei. I. Calculational Method and Basic Trends'. In: *The Astrophysical Journal* 401 (Dec. 1992), p. 99. DOI: 10.1086/172042. (Visited on 08/22/2024) (cited on page 90).

[334] Edward A. Pier and Julian H. Krolik. 'Infrared Spectra of Obscuring Dust Tori around Active Galactic Nuclei. II. Comparison with Observations'. In: *The Astrophysical Journal* 418 (Dec. 1993), p. 673. DOI: 10.1086/173427. (Visited on 08/22/2024) (cited on page 90).

[335] Wenbin Lu, Pawan Kumar, and Neal J. Evans II. 'Infrared Emission from Tidal Disruption Events – Probing the Pc-Scale Dust Content around Galactic Nuclei'. In: *Monthly Notices of the Royal Astronomical Society* 458.1 (May 2016), pp. 575–581. DOI: 10.1093/mnras/stw307. (Visited on 01/05/2024) (cited on pages 90, 91).

[336] Ning Jiang et al. 'The WISE Detection of an Infrared Echo in Tidal Disruption Event ASASSN-14li'. In: *The Astrophysical Journal* 828 (Sept. 2016), p. L14. DOI: 10.3847/2041-8205/828/1/L14. (Visited on 01/30/2023) (cited on page 91).

[337] Liming Dou et al. 'Long Fading Mid-Infrared Emission in Transient Coronal Line Emitters: Dust Echo of a Tidal Disruption Flare'. In: *The Astrophysical Journal* 832.2 (Nov. 2016), p. 188. DOI: 10.3847/0004-637X/832/2/188. (Visited on 04/19/2024) (cited on page 91).

[338] Ning Jiang et al. 'Infrared Echoes of Optical Tidal Disruption Events: ~1% Dust-covering Factor or Less at Subparsec Scale'. In: *The Astrophysical Journal* 911.1 (Apr. 2021), p. 31. DOI: 10.3847/1538-4357/abe772. (Visited on 08/20/2024) (cited on pages 91, 100).

[339] J. Fritz, A. Franceschini, and E. Hatziminaoglou. 'Revisiting the Infrared Spectra of Active Galactic Nuclei with a New Torus Emission Model'. In: *Monthly Notices of the Royal Astronomical Society* 366.3 (Mar. 2006), pp. 767–786. DOI: 10.1111/j.1365-2966.2006.09866.x. (Visited on 08/23/2024) (cited on page 91).

[340] Rivay Mor, Hagai Netzer, and Moshe Elitzur. 'Dusty Structure Around Type-I Active Galactic Nuclei: Clumpy Torus, Narrow-Line Region, and Near-Nucleus Hot Dust'. In: *The Astrophysical Journal* 705.1 (Oct. 2009), p. 298. DOI: 10.1088/0004-637X/705/1/298. (Visited on 08/23/2024) (cited on page 91).

[341] I. G. Roseboom et al. 'IR-derived Covering Factors for a Large Sample of Quasars from WISE–UKIDSS–SDSS'. In: *Monthly Notices of the Royal Astronomical Society* 429.2 (Feb. 2013), pp. 1494–1501. DOI: 10.1093/mnras/sts441. (Visited on 08/23/2024) (cited on page 91).

[342] Yuhan Yao et al. 'Tidal Disruption Event Demographics with the Zwicky Transient Facility: Volumetric Rates, Luminosity Function, and Implications for the Local Black Hole Mass Function'. In: *The Astrophysical Journal Letters* 955.1 (Sept. 2023), p. L6. DOI: 10.3847/2041-8213/acf216. (Visited on 08/20/2024) (cited on page 92).

[343] S Sazonov et al. 'First Tidal Disruption Events Discovered by SRG/eROSITA: X-ray/Optical Properties and X-ray Luminosity Function at z < 0.6'. In: *Monthly Notices of the Royal Astronomical Society* 508.3 (Dec. 2021), pp. 3820–3847. DOI: 10.1093/mnras/stab2843. (Visited on 08/26/2024) (cited on page 92).

[344] Megan Masterson et al. 'A New Population of Mid-infrared-selected Tidal Disruption Events: Implications for Tidal Disruption Event Rates and Host Galaxy Properties'. In: *The Astrophysical Journal* 961.2 (Jan. 2024), p. 211. DOI: 10.3847/1538-4357/ad18bb. (Visited on 02/08/2024) (cited on pages 92, 96, 131, 134, 137, 139, 143, 171, 172).

[345] S. Mattila et al. 'A Dust-Enshrouded Tidal Disruption Event with a Resolved Radio Jet in a Galaxy Merger'. In: *Science* 361.6401 (Aug. 2018), pp. 482–485. DOI: 10.1126/science.aao4669. (Visited on 05/31/2024) (cited on page 91).

[346] Tinggui Wang et al. 'Long-Term Decline of the Mid-Infrared Emission of Normal Galaxies: Dust Echo of Tidal Disruption Flare?' In: *Monthly Notices of the Royal Astronomical Society* 477.3 (July 2018), pp. 2943–2965. DOI: 10.1093/mnras/sty465. (Visited on 04/19/2024) (cited on page 91).

[347] E C Kool et al. 'AT 2017gbl: A Dust Obscured TDE Candidate in a Luminous Infrared Galaxy'. In: *Monthly Notices of the Royal Astronomical Society* 498.2 (Sept. 2020), pp. 2167–2195. DOI: 10.1093/mnras/staa2351. (Visited on 05/31/2024) (cited on pages 91, 144).

[348] Ning Jiang et al. 'Mid-Infrared Outbursts in Nearby Galaxies (MIRONG). I. Sample Selection and Characterization'. In: *The Astrophysical Journal Supplement Series* 252.2 (Feb. 2021), p. 32. DOI: 10.3847/1538-4365/abd1dc. (Visited on 08/25/2023) (cited on pages 91, 123, 135, 137, 143, 171, 172).

[349] Kevin Schawinski et al. 'The Green Valley Is a Red Herring: Galaxy Zoo Reveals Two Evolutionary Pathways towards Quenching of Star Formation in Early- and Late-Type Galaxies'. In: *Monthly Notices of the Royal Astronomical Society* 440.1 (May 2014), pp. 889–907. DOI: 10.1093/mnras/stu327. (Visited on 10/27/2024) (cited on page 91).

[350] Erica Hammerstein et al. 'Tidal Disruption Event Hosts Are Green and Centrally Concentrated: Signatures of a Post-merger System'. In: *The Astrophysical Journal* 908 (Feb. 2021), p. L20. DOI: 10.3847/2041-8213/abdcb4. (Visited on 09/01/2022) (cited on pages 91, 142).

[351] Yibo Wang et al. 'Mid-Infrared Outbursts in Nearby Galaxies (MIRONG). II. Optical Spectroscopic Follow-up'. In: *The Astrophysical Journal Supplement Series* 258.1 (Jan. 2022), p. 21. DOI: 10.3847/1538-4365/ac33a6. (Visited on 08/20/2024) (cited on pages 92, 110).

[352] T. M. Reynolds et al. 'Energetic Nuclear Transients in Luminous and Ultraluminous Infrared Galaxies'. In: *Astronomy & Astrophysics* 664 (Aug. 2022), A158. DOI: 10.1051/0004-6361/202243289. (Visited on 08/20/2024) (cited on page 92).

[353] Dustin Lang. 'unWISE: Unblurred Coadds of the WISE Imaging'. In: *The Astronomical Journal* 147.5 (Apr. 2014), p. 108. DOI: 10.1088/0004-6256/147/5/108. (Visited on 08/27/2024) (cited on page 92).

[354] A. M. Meisner, D. Lang, and D. J. Schlegel. 'Time-Resolved WISE/NEOWISE Coadds'. In: *The Astronomical Journal* 156.2 (July 2018), p. 69. DOI: 10.3847/1538-3881/aacbcd. (Visited on 08/27/2024) (cited on page 92).

[355] Kishalay De et al. 'Palomar Gattini-IR: Survey Overview, Data Processing System, On-sky Performance and First Results'. In: *Publications of the Astronomical Society of the Pacific* 132.1008 (Jan. 2020), p. 025001. DOI: 10.1088/1538-3873/ab6069. (Visited on 08/27/2024) (cited on page 92).

[356] David O. Cook et al. 'Census of the Local Universe (CLU) Narrowband Survey. I. Galaxy Catalogs from Preliminary Fields'. In: *The Astrophysical Journal* 880.1 (July 2019), p. 7. DOI: 10.3847/1538-4357/ab2131. (Visited on 02/20/2024) (cited on pages 92, 135).

[357] Christopher P. Ahn et al. 'The Ninth Data Release of the Sloan Digital Sky Survey: First Spectroscopic Data from the SDSS-II Baryon Oscillation Spectroscopic Survey'. In: *The Astrophysical Journal Supplement Series* 203.2 (Nov. 2012), p. 21. DOI: 10.1088/0067-0049/203/2/21. (Visited on 08/27/2024) (cited on page 94).

[358] P. M. Veres et al. 'Significant Re-Brightening of the Candidate Tidal Disruption Event AT2019aalc'. In: *Transient Name Server AstroNote* 194 (July 2023), p. 1. (Visited on 08/27/2024) (cited on page 94).

[359] Patrik Milán Veres et al. *Back from the Dead: AT2019aalc as a Candidate Repeating TDE in an AGN*. Aug. 2024. DOI: 10.48550/arXiv.2408.17419. (Visited on 09/02/2024) (cited on page 94).

[360] Ning Jiang et al. 'Two Candidate Obscured Tidal Disruption Events Coincident with High-energy Neutrinos'. In: *The Astrophysical Journal Letters* 953.1 (Aug. 2023), p. L12. DOI: 10.3847/2041-8213/acebe3. (Visited on 08/25/2023) (cited on pages 94, 96).

[361] Walter Winter and Cecilia Lunardini. 'Interpretation of the Observed Neutrino Emission from Three Tidal Disruption Events'. In: *The Astrophysical Journal* 948.1 (May 2023), p. 42. DOI: 10.3847/1538-4357/acbe9e. (Visited on 03/11/2024) (cited on pages 100, 102, 110, 111).

[362] Thomas Gaisser et al. 'Seasonal Variation of Atmospheric Muons in IceCube'. In: *Proceedings of 36th International Cosmic Ray Conference — PoS(ICRC2019)*. Vol. 358. SISSA Medialab, July 2021, p. 894. DOI: 10.22323/1.358.0894. (Visited on 09/06/2024) (cited on page 105).

[363] R. Abbasi et al. 'Observation of Seasonal Variations of the Flux of High-Energy Atmospheric Neutrinos with IceCube'. In: *The European Physical Journal C* 83.9 (Sept. 2023), p. 777. DOI: 10.1140/epjc/s10052-023-11679-5. (Visited on 09/06/2024) (cited on page 105).

[364] R. Abbasi et al. 'Search for Continuous and Transient Neutrino Emission Associated with IceCube's Highest-energy Tracks: An 11 Yr Analysis'. In: *The Astrophysical Journal* 964.1 (Mar. 2024), p. 40. DOI: 10.3847/1538-4357/ad18d6. (Visited on 10/24/2024) (cited on page 108).

[365] S. van Velzen. 'On the Mass and Luminosity Functions of Tidal Disruption Flares: Rate Suppression Due to Black Hole Event Horizons'. In: *The Astrophysical Journal* 852.2 (Jan. 2018), p. 72. DOI: 10.3847/1538-4357/aa998e. (Visited on 09/05/2024) (cited on pages 110, 111).

[366] Hui Sun, Bing Zhang, and Zhuo Li. 'Extragalactic High-Energy Transients: Event Rate Densities and Luminosity Functions'. In: *The Astrophysical Journal* 812.1 (Oct. 2015), p. 33. DOI: 10.1088/0004-637X/812/1/33. (Visited on 01/29/2024) (cited on pages 110, 111, 142).

[367] Cecilia Lunardini and Walter Winter. 'High Energy Neutrinos from the Tidal Disruption of Stars'. In: *Phys. Rev. D* 95.12 (June 2017), p. 123001. DOI: 10.1103/PhysRevD.95.123001 (cited on page 111).

[368] Jannis Necker et al. 'Search for High-Energy Neutrinos from TDE-like Flares with IceCube'. In: *Proceedings of 38th International Cosmic Ray Conference — PoS(ICRC2023)*. Vol. 444. SISSA Medialab, July 2023, p. 1478. DOI: 10.22323/1.444.1478. (Visited on 01/05/2024) (cited on page 113).

[369] Jannis Necker et al. *Flaires: A Comprehensive Catalog of Dust-Echo-like Infrared Flares*. July 2024. DOI: 10.48550/arXiv.2407.01039. (Visited on 07/19/2024) (cited on page 113).

[370] Mark F. Larsen and Scott H. Schick. 'Wide-Field Infrared Survey Explorer Science Payload Overview'. In: *Cryogenic Optical Systems and Instruments XI*. Vol. 5904. SPIE, Aug. 2005, pp. 166–177. DOI: 10.1117/12.615346. (Visited on 11/04/2024) (cited on pages 113, 114).

[371] Edward L. Wright et al. 'The Wide-Field Infrared Survey Explorer (WISE): Mission Description and Initial On-Orbit Performance'. In: *The Astronomical Journal* 140.6 (Nov. 2010), p. 1868. DOI: 10.1088/0004-6256/140/6/1868. (Visited on 04/26/2024) (cited on pages 113, 114).

[372] A. Mainzer et al. 'Initial Performance of the NEOWISE Reactivation Mission'. In: *The Astrophysical Journal* 792.1 (Aug. 2014), p. 30. DOI: 10.1088/0004-637X/792/1/30. (Visited on 02/08/2024) (cited on pages 114, 115, 123).

[373] Edward L. Wright. *Wide-Field Infrared Survey Explorer (WISE)*. https://www.astro.ucla.edu/~wright/WISE/. (Visited on 11/04/2024) (cited on pages 114, 145).

[374] A. S. Eddington. 'On a Formula for Correcting Statistics for the Effects of a Known Probable Error of Observation'. In: *Monthly Notices of the Royal Astronomical Society* 73.5 (Mar. 1913), pp. 359–360. DOI: 10.1093/mnras/73.5.359. (Visited on 04/29/2024) (cited on pages 115, 122).

[375] Vladislav Khramtsov, Volodymyr Akhmetov, and Peter Fedorov. 'The Northern Extragalactic WISE × Pan-STARRS (NEWS) Catalogue - Machine-learning Identification of 40 Million Extragalactic Objects'. In: *Astronomy & Astrophysics* 644 (Dec. 2020), A69. DOI: 10.1051/0004-6361/201834122. (Visited on 09/12/2022) (cited on pages 115, 116).

[376] D. E. Rumelhart, G. E. Hinton, and R. J. Williams. 'Learning Internal Representations by Error Propagation'. In: *Parallel Distributed Processing, Volume 1: Explorations in the Microstructure of Cognition: Foundations*. The MIT Press, July 1986. DOI: 10.7551/mitpress/5236.003.0012 (cited on page 116).

[377] Vladimir Naumovich Vapnik. 'The Nature of Statistical Learning Theory'. In: *The Nature of Statistical Learning Theory*. New York, 1995 (cited on page 116).

[378] B. W. Matthews. 'Comparison of the Predicted and Observed Secondary Structure of T4 Phage Lysozyme'. In: *Biochimica et Biophysica Acta (BBA) - Protein Structure* 405.2 (Oct. 1975), pp. 442–451. DOI: 10.1016/0005-2795(75)90109-9. (Visited on 08/01/2024) (cited on page 116).

[379] Róbert Beck, S Curt Dodds, and István Szapudi. 'WISE-PS1-STRM: Neural Network Source Classification and Photometric Redshifts for WISE×PS1'. In: *Monthly Notices of the Royal Astronomical Society* 515.4 (Oct. 2022), pp. 4711–4721. DOI: 10.1093/mnras/stac1714. (Visited on 03/09/2023) (cited on page 116).

[380] D. O. Cook et al. 'Completeness of the NASA/IPAC Extragalactic Database (NED) Local Volume Sample'. In: *The Astrophysical Journal Supplement Series* 268.1 (Aug. 2023), p. 14. DOI: 10.3847/1538-4365/acdd06. (Visited on 09/04/2023) (cited on pages 116, 136, 157, 158).

[381] Leland McInnes and John Healy. 'Accelerated Hierarchical Density Based Clustering'. In: *2017 IEEE International Conference on Data Mining Workshops (ICDMW)*. Nov. 2017, pp. 33–42. DOI: 10.1109/ICDMW.2017.12. (Visited on 10/04/2023) (cited on page 118).

[382] Fabian Pedregosa et al. 'Scikit-Learn: Machine Learning in Python'. In: *The Journal of Machine Learning Research* 12.null (Nov. 2011), pp. 2825–2830 (cited on page 118).

[383] T. H. Jarrett et al. 'The Spitzer–WISE Survey of the Ecliptic Poles'. In: *The Astrophysical Journal* 735.2 (June 2011), p. 112. DOI: 10.1088/0004-637X/735/2/112. (Visited on 12/21/2023) (cited on page 119).

[384] Jannis Necker and Sarah Mechbal. *JannisNe/Timewise: V0.4.10*. Zenodo. Jan. 2024. DOI: 10.5281/zenodo.10473347. (Visited on 06/04/2024) (cited on page 119).

[385] Jeffrey D. Scargle et al. 'Studies in Astronomical Time Series Analysis. VI. Bayesian Block Representations'. In: *The Astrophysical Journal* 764.2 (Feb. 2013), p. 167. DOI: 10.1088/0004-637X/764/2/167. (Visited on 08/28/2023) (cited on pages 119, 120).

[386] The Astropy Collaboration et al. 'The Astropy Project: Sustaining and Growing a Community-oriented Open-source Project and the Latest Major Release (v5.0) of the Core Package*'. In: *The Astrophysical Journal* 935.2 (Aug. 2022), p. 167. DOI: 10.3847/1538-4357/ac7c74. (Visited on 12/23/2023) (cited on page 119).

[387] J. Nordin et al. 'Transient Processing and Analysis Using AMPEL: Alert Management, Photometry, and Evaluation of Light Curves'. In: *Astronomy & Astrophysics* 631 (Nov. 2019), A147. DOI: 10.1051/0004-6361/201935634. (Visited on 12/23/2023) (cited on page 120).

[388] Jannis Necker. *Timewise-Sup: The Timewise Subtraction Pipeline v0.5.0*. Zenodo. May 2024. DOI: 10.5281/zenodo.11446250. (Visited on 06/03/2024) (cited on page 122).

[389] Daniel W. Weedman. *Quasar Astronomy*. Cambridge Astrophysics. Cambridge: Cambridge University Press, 1986 (cited on pages 122, 138).

[390] Maciej Bilicki et al. 'WISE × SuperCOSMOS Photometric Redshift Catalog: 20 Million Galaxies Over 3π Steradians'. In: *The Astrophysical Journal Supplement Series* 225.1 (July 2016), p. 5. DOI: 10.3847/0067-0049/225/1/5. (Visited on 01/11/2024) (cited on page 123).

[391] M. Brescia, S. Cavuoti, and G. Longo. 'Automated Physical Classification in the SDSS DR10. A Catalogue of Candidate Quasars'. In: *Monthly Notices of the Royal Astronomical Society* 450.4 (July 2015), pp. 3893–3903. DOI: 10.1093/mnras/stv854. (Visited on 01/11/2024) (cited on pages 123, 129).

[392] G Dálya et al. 'GLADE: A Galaxy Catalogue for Multimessenger Searches in the Advanced Gravitational-Wave Detector Era'. In: *Monthly Notices of the Royal Astronomical Society* 479.2 (Sept. 2018), pp. 2374–2381. DOI: 10.1093/mnras/sty1703. (Visited on 01/11/2024) (cited on page 123).

[393] Kenneth J Duncan. 'All-Purpose, All-Sky Photometric Redshifts for the Legacy Imaging Surveys Data Release 8'. In: *Monthly Notices of the Royal Astronomical Society* 512.3 (May 2022), pp. 3662–3683. DOI: 10.1093/mnras/stac608. (Visited on 01/11/2024) (cited on page 123).

[394] C. A. Beichman et al. 'Infrared Astronomical Satellite (IRAS) Catalogs and Atlases.Volume 1: Explanatory Supplement.' In: *Infrared astronomical satellite (IRAS) catalogs and atlases. Volume 1: Explanatory supplement* 1 (Jan. 1988). (Visited on 04/29/2024) (cited on page 123).

[395] B. T. Draine and H. M. Lee. 'Optical Properties of Interstellar Graphite and Silicate Grains'. In: *The Astrophysical Journal* 285 (Oct. 1984), p. 89. DOI: 10.1086/162480. (Visited on 05/02/2024) (cited on page 123).

[396] Daniel Foreman-Mackey et al. 'Emcee: The MCMC Hammer'. In: *Publications of the Astronomical Society of the Pacific* 125.925 (Feb. 2013), p. 306. DOI: 10.1086/670067. (Visited on 01/10/2024) (cited on page 124).

[397] A. Sokal. 'Monte Carlo Methods in Statistical Mechanics: Foundations and New Algorithms'. In: *Functional Integration: Basics and Applications*. Ed. by Cecile DeWitt-Morette, Pierre Cartier, and Antoine Folacci. NATO ASI Series. Boston, MA: Springer US, 1997, pp. 131–192. DOI: 10.1007/978-1-4899-0319-8_6. (Visited on 01/19/2024) (cited on page 124).

[398] Christos Panagiotou et al. 'A Luminous Dust-obscured Tidal Disruption Event Candidate in a Star-forming Galaxy at 42 Mpc'. In: *The Astrophysical Journal* 948 (May 2023), p. L5. DOI: 10.3847/2041-8213/acc02f. (Visited on 11/21/2023) (cited on pages 125, 134, 171, 172).

[399] Ning Jiang et al. 'Rapid Infrared Variability of Three Radio-Loud Narrow-Line Seyfert 1 Galaxies: A View from the Wide-Field Infrared Survey Explorer'. In: *The Astrophysical Journal Letters* 759.2 (Oct. 2012), p. L31. DOI: 10.1088/2041-8205/759/2/L31. (Visited on 05/03/2024) (cited on page 127).

[400] Neng-Hui Liao et al. 'Multi-Wavelength Variability Properties of CGRaBS J0733+0456: Identifying a Distant Gamma-Ray Blazar at z = 3.01'. In: *The Astrophysical Journal Letters* 879.1 (July 2019), p. L9. DOI: 10.3847/2041-8213/ab2893. (Visited on 05/03/2024) (cited on page 127).

[401] Eric Wim Flesch. 'The Million Quasars (Milliquas) Catalogue, V8'. In: *The Open Journal of Astrophysics* 6 (Dec. 2023), p. 49. DOI: 10.21105/astro.2308.01505. (Visited on 02/01/2024) (cited on page 127).

[402] S. Komossa. 'Tidal Disruption of Stars by Supermassive Black Holes: Status of Observations'. In: *Journal of High Energy Astrophysics*. Swift 10 Years of Discovery, a Novel Approach to Time Domain Astronomy 7 (Sept. 2015), pp. 148–157. DOI: 10.1016/j.jheap.2015.04.006. (Visited on 06/03/2024) (cited on page 128).

[403] J. A. Baldwin, M. M. Phillips, and R. Terlevich. 'Classification Parameters for the Emission-Line Spectra of Extragalactic Objects'. In: *Publications of the Astronomical Society of the Pacific* 93.551 (Feb. 1981), p. 5. DOI: 10.1086/130766. (Visited on 04/10/2024) (cited on page 129).

[404] J M M Neustadt et al. 'To TDE or Not to TDE: The Luminous Transient ASASSN-18jd with TDE-like and AGN-like Qualities'. In: *Monthly Notices of the Royal Astronomical Society* 494.1 (Mar. 2020), pp. 2538–2560. DOI: 10.1093/mnras/staa859. (Visited on 03/13/2024) (cited on page 129).

[405] M. W. Ochmann et al. *The Transient Event in NGC 1566 from 2017 to 2019. I. An Eccentric Accretion Disk and a Turbulent, Disk-Dominated Broad-Line Region Unveiled by Double-Peaked Ca II and O I Lines*. Feb. 2024. (Visited on 02/20/2024) (cited on pages 130, 134, 171, 172).

[406] J. Brimacombe et al. 'Discovery of Six ASAS-SN Supernovae'. In: *The Astronomer's Telegram* 10652 (Aug. 2017), p. 1. (Visited on 04/11/2024) (cited on page 130).

[407] I. Arcavi et al. 'FLOYDS Classification of ASASSN-17jz/AT 2017fro as an AGN'. In: *The Astronomer's Telegram* 10668 (Aug. 2017), p. 1. (Visited on 04/11/2024) (cited on page 130).

[408] A. J. Drake et al. 'The Discovery and Nature of the Optical Transient CSS100217:102913+404220'. In: *The Astrophysical Journal* 735.2 (June 2011), p. 106. DOI: 10.1088/0004-637X/735/2/106. (Visited on 04/11/2024) (cited on page 130).

[409] Thomas W.-S. Holoien et al. 'Investigating the Nature of the Luminous Ambiguous Nuclear Transient ASASSN-17jz'. In: *The Astrophysical Journal* 933.2 (July 2022), p. 196. DOI: 10.3847/1538-4357/ac74b9. (Visited on 04/11/2024) (cited on page 130).

[410] A. Malyali et al. 'AT 2019avd: A Novel Addition to the Diverse Population of Nuclear Transients'. In: *Astronomy & Astrophysics* 647 (Mar. 2021), A9. DOI: 10.1051/0004-6361/202039681. (Visited on 04/09/2024) (cited on pages 130, 134, 171, 172).

[411] Jin-Hong Chen, Li-Ming Dou, and Rong-Feng Shen. 'AT 2019avd: A Tidal Disruption Event with a Two-phase Evolution'. In: *The Astrophysical Journal* 928 (Mar. 2022), p. 63. DOI: 10.3847/1538-4357/ac558d. (Visited on 04/11/2024) (cited on page 130).

[412] Yanan Wang et al. 'The Radio Detection and Accretion Properties of the Peculiar Nuclear Transient AT 2019avd'. In: *Monthly Notices of the Royal Astronomical Society* 520.2 (Apr. 2023), pp. 2417–2435. DOI: 10.1093/mnras/stad101. (Visited on 04/24/2024) (cited on page 130).

[413] I. Arcavi et al. 'FLOYDS Classification of AT 2018dyk/ZTF18aajupnt as a Possible Tidal Disruption Event'. In: *The Astronomer's Telegram* 11953 (Aug. 2018), p. 1. (Visited on 04/11/2024) (cited on page 130).

[414] Sara Frederick et al. 'A New Class of Changing-look LINERs'. In: *The Astrophysical Journal* 883.1 (Sept. 2019), p. 31. DOI: 10.3847/1538-4357/ab3a38. (Visited on 04/11/2024) (cited on page 130).

[415] A. Reguitti. 'Padova-Asiago Transient Classification Report for 2022-10-28'. In: *Transient Name Server Classification Report* 2022–3144 (Oct. 2022), p. 1. (Visited on 04/11/2024) (cited on page 130).

[416] Samaporn Tinyanont et al. 'A Systematic Study of Mid-infrared Emission from Core-collapse Supernovae with SPIRITS'. In: *The Astrophysical Journal* 833.2 (Dec. 2016), p. 231. DOI: 10.3847/1538-4357/833/2/231. (Visited on 04/29/2024) (cited on page 131).

[417] E. Falco et al. 'Spectroscopic Classification of ASASSN-18am, ASASSN-18ao, and ASASSN-18ap'. In: *The Astronomer's Telegram* 11180 (Jan. 2018), p. 1. (Visited on 04/12/2024) (cited on page 131).

[418] Melina Thévenot et al. 'Mid-Infrared Detections of Type I Supernovae and Unclassified Possible Supernovae with NEOWISE'. In: *Research Notes of the AAS* 5.3 (Mar. 2021), p. 58. DOI: 10.3847/2515-5172/abf120. (Visited on 04/29/2024) (cited on page 131).

[419] Yibo Wang et al. *ASASSN-18ap: A Dusty Tidal Disruption Event Candidate with an Early Bump in the Light Curve*. Mar. 2024. DOI: 10.48550/arXiv.2312.12015. (Visited on 04/09/2024) (cited on page 131).

[420] M. A. Tucker. 'SCAT Transient Classification Report for 2021-02-11'. In: *Transient Name Server Classification Report* 2021–433 (Feb. 2021), pp. 1–433. (Visited on 04/12/2024) (cited on page 131).

[421] M. Thévenot, M. Kabatnik, and J. M. Gantier. 'Supernovae Detected in NEOWISE-R 2021'. In: *Transient Name Server AstroNote* 212 (Aug. 2021), pp. 1–212. (Visited on 04/29/2024) (cited on page 131).

[422] A. Dahiwale and C. Fremling. 'ZTF Transient Classification Report for 2020-06-02'. In: *Transient Name Server Classification Report* 2020–1667 (June 2020), p. 1. (Visited on 04/12/2024) (cited on page 131).

[423] C. Fremling and Y. Sharma. 'ZTF Transient Classification Report for 2018-06-22'. In: *Transient Name Server Classification Report* 2018–873 (June 2018), p. 1. (Visited on 04/12/2024) (cited on page 131).

[424] Xinghan Zhang et al. 'SN 2018hfm: A Low-Energy Type II Supernova with Prominent Signatures of Circumstellar Interaction and Dust Formation'. In: *Monthly Notices of the Royal Astronomical Society* 509.2 (Jan. 2022), pp. 2013–2032. DOI: 10.1093/mnras/stab3007. (Visited on 04/12/2024) (cited on page 131).

[425] C. Fremling, A. Dugas, and Y. Sharma. 'ZTF Transient Classification Report for 2019-02-01 2018kly, SN2018kly, SN 2018kly, 2019kg, SN2019kg, SN 2019kg, 2019uo, SN2019uo, SN 2019uo, 2019ui, SN2019ui, SN 2019ui, 2019us, SN2019us, SN 2019us, 2018kyt, SN2018kyt, SN 2018kyt, 2018lan, SN2018lan, SN 2018lan, 2018lfb, SN2018lfb, SN 2018lfb, 2019abv, SN2019abv, SN 2019abv, 2018lev, SN2018lev, SN 2018lev, 2019vv, SN2019vv, SN 2019vv, 2019abk, SN2019abk, SN 2019abk, 2018khn, SN2018khn, SN 2018khn, 2018ktv, SN2018ktv, SN 2018ktv, 2019bq, SN2019bq, SN 2019bq, 2019aas, SN2019aas, SN 2019aas, 2019ail, SN2019ail, SN 2019ail, 2018kkv, SN2018kkv, SN 2018kkv, 2018liq, SN2018liq, SN 2018liq'. In: *Transient Name Server Classification Report* 2019–188 (Feb. 2019), p. 1. (Visited on 04/12/2024) (cited on page 131).

[426] M. Lacy et al. 'The Spitzer Mid-infrared AGN Survey. II. The Demographics and Cosmic Evolution of the AGN Population'. In: *The Astrophysical Journal* 802 (Apr. 2015), p. 102. DOI: 10.1088/0004-637X/802/2/102. (Visited on 06/03/2024) (cited on page 136).

[427] T. Kettlety et al. 'Galaxy and Mass Assembly (GAMA): The Consistency of GAMA and WISE Derived Mass-to-Light Ratios'. In: *Monthly Notices of the Royal Astronomical Society* 473 (Jan. 2018), pp. 776–783. DOI: 10.1093/mnras/stx2379. (Visited on 01/26/2024) (cited on pages 137, 138).

[428] B. Röck et al. 'Stellar Population Synthesis Models between 2.5 and 5 Mm Based on the Empirical IRTF Stellar Library'. In: *Monthly Notices of the Royal Astronomical Society* 449.3 (May 2015), pp. 2853–2874. DOI: 10.1093/mnras/stv503. (Visited on 08/19/2024) (cited on page 137).

[429] Xiao-Qing Wen et al. 'The Stellar Masses of Galaxies from the 3.4 Mm Band of the WISE All-Sky Survey'. In: *Monthly Notices of the Royal Astronomical Society* 433.4 (Aug. 2013), pp. 2946–2957. DOI: 10.1093/mnras/stt939. (Visited on 08/19/2024) (cited on page 137).

[430] Sharon E. Meidt et al. 'Reconstructing the Stellar Mass Distributions of Galaxies Using S^4G IRAC 3.6 and 4.5 Mm Images. II. The Conversion from Light to Mass'. In: *The Astrophysical Journal* 788.2 (June 2014), p. 144. DOI: 10.1088/0004-637X/788/2/144. (Visited on 08/19/2024) (cited on page 137).

[431] Mark A. Norris et al. 'Being Wise II: Reducing the Influence of Star Formation History on the Mass-to-Light Ratio of Quiescent Galaxies'. In: *The Astrophysical Journal* 832.2 (Dec. 2016), p. 198. DOI: 10.3847/0004-637X/832/2/198. (Visited on 08/19/2024) (cited on page 137).

[432] Mark A. Norris et al. 'Being Wise. I. Validating Stellar Population Models and $M^\star/L$ Ratios at 3.4 and 4.6 Mm'. In: *The Astrophysical Journal* 797.1 (Nov. 2014), p. 55. DOI: 10.1088/0004-637X/797/1/55. (Visited on 08/19/2024) (cited on page 137).

[433] A. Bongiorno et al. 'The MBH-M* Relation for X-ray-obscured, Red QSOs at $1.2 < z < 2.6$'. In: *Monthly Notices of the Royal Astronomical Society* 443.3 (Sept. 2014), pp. 2077–2091. DOI: 10.1093/mnras/stu1248. (Visited on 08/19/2024) (cited on page 137).

[434] Mauricio Cisternas et al. 'Secular Evolution and a Non-Evolving Black-Hole-to-Galaxy Mass Ratio in the Last 7 Gyr'. In: *The Astrophysical Journal Letters* 741.1 (Oct. 2011), p. L11. DOI: 10.1088/2041-8205/741/1/L11. (Visited on 08/19/2024) (cited on page 137).

[435] Knud Jahnke et al. 'Massive Galaxies in Cosmos: Evolution of Black Hole Versus Bulge Mass but Not Versus Total Stellar Mass Over the Last 9 Gyr?' In: *The Astrophysical Journal* 706.2 (Nov. 2009), p. L215. DOI: 10.1088/0004-637X/706/2/L215. (Visited on 08/19/2024) (cited on page 137).

[436] A. Merloni et al. 'On the Cosmic Evolution of the Scaling Relations Between Black Holes and Their Host Galaxies: Broad-Line Active Galactic Nuclei in the zCOSMOS Survey'. In: *The Astrophysical Journal* 708.1 (Dec. 2009), p. 137. DOI: 10.1088/0004-637X/708/1/137. (Visited on 08/19/2024) (cited on page 137).

[437] Mouyuan Sun et al. 'Evolution in the Black Hole–Galaxy Scaling Relations and the Duty Cycle of Nuclear Activity in Star-Forming Galaxies'. In: *The Astrophysical Journal* 802.1 (Mar. 2015), p. 14. DOI: 10.1088/0004-637X/802/1/14. (Visited on 08/19/2024) (cited on page 137).

[438] Christopher N. A. Willmer. 'The Absolute Magnitude of the Sun in Several Filters'. In: *The Astrophysical Journal Supplement Series* 236.2 (June 2018), p. 47. DOI: 10.3847/1538-4365/aabfdf. (Visited on 04/30/2024) (cited on page 138).

[439] J. B. Oke and Allan Sandage. 'Energy Distributions, K Corrections, and the Stebbins-Whitford Effect for Giant Elliptical Galaxies'. In: *The Astrophysical Journal* 154 (Oct. 1968), p. 21. DOI: 10.1086/149737. (Visited on 08/06/2024) (cited on page 138).

[440] David W. Hogg et al. 'The Luminosity Density of Red Galaxies'. In: *The Astronomical Journal* 124.2 (Aug. 2002), p. 646. DOI: 10.1086/341392. (Visited on 08/18/2024) (cited on page 138).

[441] Michael R. Blanton and Sam Roweis. 'K-Corrections and Filter Transformations in the Ultraviolet, Optical, and Near-Infrared'. In: *The Astronomical Journal* 133.2 (Jan. 2007), p. 734. DOI: 10.1086/510127. (Visited on 08/16/2024) (cited on page 138).

[442] Piero Madau and Mark Dickinson. 'Cosmic Star Formation History'. In: *Annual Review of Astronomy and Astrophysics* 52 (2014), pp. 415–486. DOI: 10.1146/annurev-astro-081811-125615 (cited on page 142).

[443] C. S. Kochanek. 'Tidal Disruption Event Demographics'. In: *Monthly Notices of the Royal Astronomical Society* 461.1 (Sept. 2016), pp. 371–384. DOI: 10.1093/mnras/stw1290. (Visited on 05/29/2024) (cited on page 142).

[444] Iair Arcavi et al. 'A Continuum of H- to He-Rich Tidal Disruption Candidates with a Preference for E+A Galaxies'. In: *The Astrophysical Journal* 793.1 (Sept. 2014), p. 38. DOI: 10.1088/0004-637X/793/1/38. (Visited on 06/05/2024) (cited on page 142).

[445] K. Decker French, Iair Arcavi, and Ann Zabludoff. 'Tidal Disruption Events Prefer Unusual Host Galaxies'. In: *The Astrophysical Journal Letters* 818.1 (Feb. 2016), p. L21. DOI: 10.3847/2041-8205/818/1/L21. (Visited on 06/04/2024) (cited on page 142).

[446] Vivienne Wild et al. 'The Evolution of Post-Starburst Galaxies from Z=2 to 0.5'. In: *Monthly Notices of the Royal Astronomical Society* 463.1 (Nov. 2016), pp. 832–844. DOI: 10.1093/mnras/stw1996. (Visited on 06/05/2024) (cited on page 142).

[447] *NASA Mission Concludes After Years of Successful Asteroid Detections - NASA*. https://www.nasa.gov/news-release/nasa-mission-concludes-after-years-of-successful-asteroid-detections/. (Visited on 08/19/2024) (cited on page 145).

[448] Rachel Akeson et al. *The Wide Field Infrared Survey Telescope: 100 Hubbles for the 2020s*. Feb. 2019. DOI: 10.48550/arXiv.1902.05569. (Visited on 08/16/2024) (cited on pages 145, 150).

[449] Ryan Foley et al. 'WFIRST: Enhancing Transient Science and Multi-Messenger Astronomy'. In: *Bulletin of the AAS* 51.3 (May 2019). (Visited on 08/16/2024) (cited on page 145).

[450] *About | Rubin Observatory*. https://rubinobservatory.org/about. (Visited on 11/07/2024) (cited on page 150).

[451] *Roman - NASA Science*. https://science.nasa.gov/mission/roman-space-telescope/. (Visited on 11/07/2024) (cited on page 150).

[452] Y. Shvartzvald et al. 'ULTRASAT: A Wide-field Time-domain UV Space Telescope'. In: *The Astrophysical Journal* 964.1 (Mar. 2024), p. 74. DOI: 10.3847/1538-4357/ad2704. (Visited on 11/11/2024) (cited on page 150).

[453] *Project Timeline | ULTRASAT*. https://www.weizmann.ac.il/ultrasat/project-and-technology/project-timeline. (Visited on 11/07/2024) (cited on page 150).

[454] M. Actis et al. 'Design Concepts for the Cherenkov Telescope Array CTA: An Advanced Facility for Ground-Based High-Energy Gamma-Ray Astronomy'. In: *Experimental Astronomy* 32.3 (Dec. 2011), pp. 193–316. DOI: 10.1007/s10686-011-9247-0. (Visited on 11/07/2024) (cited on page 150).

[455] Francis Halzen. 'Pionic Photons and Neutrinos from Cosmic Ray Accelerators'. In: *Astroparticle Physics*. Seeing the High-Energy Universe with the Cherenkov Telescope Array - The Science Explored with the CTA 43 (Mar. 2013), pp. 155–162. DOI: 10.1016/j.astropartphys.2011.10.003. (Visited on 11/07/2024) (cited on page 150).

[456] Kazuki Abe et al. 'First Science Results from CTA LST-1 Telescope and Status of LST-2-4'. In: *Proceedings of 38th International Cosmic Ray Conference — PoS(ICRC2023)*. Vol. 444. 2023, p. 731. DOI: 10.22323/1.444.0731 (cited on page 151).

[457] S. Adrián-Martínez et al. 'Letter of Intent for KM3NeT 2.0'. In: *Journal of Physics G: Nuclear and Particle Physics* 43.8 (June 2016), p. 084001. DOI: 10.1088/0954-3899/43/8/084001. (Visited on 11/07/2024) (cited on page 151).

[458] A. D. Avrorin et al. 'Status of the Early Construction Phase of Baikal-GVD'. In: *Nuclear and Particle Physics Proceedings*. 37th International Conference on High Energy Physics (ICHEP) 273–275 (Apr. 2016), pp. 314–320. DOI: 10.1016/j.nuclphysbps.2015.09.044. (Visited on 11/07/2024) (cited on page 151).

[459] Rastislav Dvornicky. 'Large Neutrino Telescope Baikal-GVD: Recent Status'. In: *Proceedings of 38th International Cosmic Ray Conference — PoS(ICRC2023)*. Vol. 444. 2023, p. 976. DOI: 10.22323/1.444.0976 (cited on page 151).

[460] Thijs van Eeden and Aart Heijboer. 'Astronomy Potential of KM3NeT/ARCA230'. In: *Proceedings of 38th International Cosmic Ray Conference — PoS(ICRC2023)*. Vol. 444. 2023, p. 1075. DOI: 10.22323/1.444.1075 (cited on page 151).

[461] J. A. Aguilar et al. *Design and Sensitivity of the Radio Neutrino Observatory in Greenland (RNO-G)*. July 2024. DOI: 10.48550/arXiv.2010.12279. (Visited on 11/07/2024) (cited on page 151).

[462] M. G. Aartsen et al. 'IceCube-Gen2: The Window to the Extreme Universe'. In: *Journal of Physics G Nuclear Physics* 48.6 (June 2021), p. 060501. DOI: 10.1088/1361-6471/abbd48 (cited on page 151).

[463] Carlos Rodrigo, Enrique Solano, and Amelia Bayo. *SVO Filter Profile Service Version 1.0*. Tech. rep. Oct. 2012, p. 1015. DOI: 10.5479/ADS/bib/2012ivoa.rept.1015R. (Visited on 09/17/2024) (cited on page 155).

[464] C. Rodrigo and E. Solano. 'The SVO Filter Profile Service'. In: *Conference Name: XIV.0 Scientific Meeting (Virtual) of the Spanish Astronomical Society*. July 2020, p. 182. (Visited on 09/17/2024) (cited on page 155).

[465] David W. Hogg. *Distance Measures in Cosmology*. Dec. 2000. DOI: 10.48550/arXiv.astro-ph/9905116. (Visited on 01/31/2024) (cited on page 157).

[466] P. Schechter. 'An Analytic Expression for the Luminosity Function for Galaxies.' In: *The Astrophysical Journal* 203 (Jan. 1976), pp. 297–306. DOI: 10.1086/154079. (Visited on 08/06/2024) (cited on page 157).

[467] D. Heath Jones et al. 'Near-Infrared and Optical Luminosity Functions from the 6dF Galaxy Survey'. In: *Monthly Notices of the Royal Astronomical Society* 369.1 (June 2006), pp. 25–42. DOI: 10.1111/j.1365-2966.2006.10291.x. (Visited on 08/02/2024) (cited on page 157).

[468] M. F. Skrutskie et al. 'The Two Micron All Sky Survey (2MASS)'. In: *The Astronomical Journal* 131.2 (Feb. 2006), p. 1163. DOI: 10.1086/498708. (Visited on 08/06/2024) (cited on page 158).

[469] C. Forbes et al. *Statistical Distributions*. Wiley, 2011 (cited on pages 159, 160).

Notation

ln	Natural logarithm
log	Used interchangeably with ln
$\log_x$	Logarithm with the base x
sqd	square degree
c	Speed of light in a vacuum inertial frame
d_{L}	Luminosity distance
h	Planck constant
k_{B}	Boltzmann constant
$X_{\odot}$	The value of X for the sun

Glossary

AGN	active galactic nucleus. 17–22, 27, 28, 79, 81, 91
ALFOSC	*Alhambra Faint Object Spectrograph and Camera*. 80–82
AMPEL	*Alert Management, Photometry, and Evaluation of Lightcurves*, an analysis framekwork for high-throughput surveys designed for streamed data. 79, 120
ASAS-SN	*All-Sky Automated Survey for SuperNovae*. 2, 65–68, 70, 72, 74–76, 79, 132, 149, 155
BDT	Boosted Decision Tree. 38
CCD	charge-coupled device. 65, 77
CCSN	Core-collapse Supernova. 23, 24, 26
CDF	cumulative distribution function. 40, 45, 51, 59, 74
charge	Number of detected Photoelectrons. 34, 54, 56, 97
CMB	cosmic microwave background. 8, 11–14
covering factor f_c	Encodes how much radiation is absorbed by dust. Because the absorption efficiency is assumed to be 1, in this work it is a geometric factor. 145
CR	cosmic ray. 7–15, 149
CSM	circumstellar material. 24–26, 70, 82
CTA	*Cherenkov Telescope Array*. 150
CV	cataclysmic variable. 81
DAQ	data acquisition. 34, 35, 37
DOM	*Digital Optical Module*. 32–41, 43, 53, 54, 57, 97
DSNB	diffuse supernova background. 13
dust echo	Delayed emission in the MIR due to re-processing of incident radiation by dust. 149, 150
dust layer	A layer of dust embedded in the ice in IceCube. 36, 57, 96, 97
EHE	*Extremely High Energy*. 38, 50
EM	electromagnetic. 1, 2, 19, 20, 25–27, 76, 91, 97, 99, 105, 151
FBOT	Fast Blue Optical Transient. 24, 26
FoV	field-of-view. 1, 49, 65, 77, 113, 116, 150
FSRQ	Flat Spectrum Radio Quasar. 72
FWHM	full width at half maximum. 117
GCN	*General Coordinates Network*. 49–51, 66, 68
GFU	*Gamma-ray Follow-Up*. 38, 50
GRB	gamma-ray burst. 25–27, 49, 74, 150
GZK	*Greisen-Zatsepin-Kuzmin*. 8, 9, 14, 151
HESE	*High-Energy Starting Events*. 38, 50, 96
Hills Mass	Mass limit for a SMBH to allow a TDE of a solar type star, $\approx 10^8 M_\odot$. 20, 137, 138, 143, 144

ICL	*IceCube Lab*. 33–35
iGRB	isotropic gamma-ray background. 10, 12
IR	infrared. 11, 22, 26, 89, 101, 109, 150
ISM	interstellar medium. 21
KAGRA	*Kamioka Gravitational Wave Detector*. 16, 49
kinematic angle	The angle between the incident neutrino and the outgoing lepton. 30, 36, 42
LIGO	*Laser Interferometer Gravitational-Wave Observatory*. 16, 27, 49
LISA	*Laser Interferometer Space Antenna*. 16
livetime	Time during which the detector is operational. 105
LRIS	*Low-Resolution Imaging Spectrograph*. 82
LST	*Large Size Telescope*. 150
MC	Monte-Carlo. 40, 46, 54
MCMC	Markov-Chain Monte-Carlo. 124, 125
MIR	mid-infrared. 11, 12, 20, 113, 149, 150, 203
MIRONG	*Mid-infrared Outbursts in Nearby Galaxies*. 91, 92, 94, 96, 110, 134, 135, 137, 143, 166
ML	maximum likelihood. 39, 40, 124
MPE	Multi-Photoelectron. 40
NANOGrav	*North American Nanohertz Observatory for Gravitational Waves*. 16
NED-LVS	*Local Volume Sample from the NASA Extragalactic Database*. 116, 157, 158
NEWS	*The Northern Extragalactic WISE × Pan-STARRS catalogue*. 115, 116
NOT	*Nordical Optical Telescope*. 80
OUV	optical and ultraviolet. 20–22, 83, 90, 101, 129, 130, 149
Pan-STARRS	*Panoramic Survey Telescope And Rapid Response System*. 78, 79, 115, 133
PAO	*Pierre Auger Observatory*. 8, 10
PDF	probability density function. 39, 40, 44, 46, 94, 104, 105
PE	photoelectron. 34, 40, 42, 43
PMT	Photo-Multiplier Tube. 34, 35
PSF	point spread function. 115, 117
RNO-G	*Radio Neutrino Observatory in Greenland*. 151
SDSS	*Sloan Digital Sky Survey*. 91
SED	spectral energy distribution. 84
SESN	Stripped-envelope Supernova. 24–26
SFR	star formation rate. 74
signalness	Probability of being an astrophysical neutrino for individual neutrino alert events. 50, 73, 79
SLSN	superluminous supernova. 24, 83

SMBH	supermassive black hole. 2, 11, 16, 17, 20, 22, 27, 81, 83, 89, 129, 137, 150
SN	supernova. 11, 13, 22, 24–26, 150
SPICE	*South Pole Ice*. 36, 53, 54
TA	*Telescope Array*. 8, 10
TDE	tidal disruption event. 2, 3, 15, 20–22, 27, 77, 81–83, 90, 91, 100, 109–111, 149, 150
TNS	*Transient Name Server*. 12, 129
ToO	Target-of-Opportunity. 66, 67, 81
UHECR	Ultra-High Energy Cosmic Ray. 8–10, 12, 14, 19–21
ULIRG	ultra luminous infrared galaxy. 92
Virgo	*Virgo interferometer*. 16, 27, 49
VRO	*Vera Rubin Observatory*. 75, 150
WISE	*Wide-Field Infrared Survey Explorer*. 84, 91, 113, 114, 150, 155, 157, 159
WTP	*WISE Transient Pipeline*. 92, 134, 169
ZTF	*Zwicky Transient Facility*. 2, 20, 27, 72, 75–77, 93, 94, 135, 149, 155
ZTF AF	*Zwicky Transient Facility Accretion Flares*. 94, 96, 135, 137, 169

Acknowledgements

I would like to extend a very big *mercinger* to:

Prof. Marek Kowalski for giving me the opportunity to write this thesis, for supervising me, for always having helpful comments, for much energy in times of scientific excitement, for baiting me into astronomy as a Bachelor student!

Prof. Anna Franckowiak for also supervising me, for many helpful comments and suggestions, for much support, for hosting me in Bochum, for baiting me into astroparticle physics as a master student!

Robert Stein for teaching me essentially everything about IceCube, ZTF and astrophysics in general.

Simeon Reusch for being such an automation fan that ZTF follow-up observations became a butten press.

Jakob van Santen and Jakob Nordin for always being an encyclopedia of solutions for AMPEL or IceCube related technical problems.

Eleni Graikou for being a great office mate and for helping to get the infrared flare sample off the ground.

Teresa for continuing the dust echo work.

Giacomo, Simeon, Alice, Neha, Leander, Sofia, Massimiliano, and Robert for reading parts of this thesis, catching my many typos, giving valuable feedback. I would guess that the quality went up by approximately 18345818246%.

the IceCube, ZTF, ASAS-SN, and GROWTH collaborations for creating a lovely, collaborative research environment.

My friends and family for being the most supporting hammock I could ever have wished for.

Sarah for being a bright star.

This work would never have been possible without you.

Selbstständigkeitserklärung

Hiermit erkläre ich, die Dissertation selbstständig und nur unter Verwendung der angegebenen Hilfen und Hilfsmittel angefertigt zu haben. Ich habe mich nicht anderwärts um einen Doktorgrad in dem Promotionsfach beworben und besitze keinen entsprechenden Doktorgrad. Die Promotionsordnung der Mathematisch-Naturwissenschaftlichen Fakultät, veröffentlicht im Amtlichen Mitteilungsblatt der Humboldt-Universität zu Berlin Nr. 42 am 11. Juli 2018, habe ich zur Kenntnis genommen.

I declare that I have completed the thesis independently using only the aids and tools specified. I have not applied for a doctor's degree in the doctoral subject elsewhere and do not hold a corresponding doctor's degree. I have taken due note of the Faculty of Mathematics and Natural Sciences PhD Regulations, published in the Official Gazette of Humboldt-Universität zu Berlin no. 42 on July 11 2018.

Jannis Necker, 11.11.2024